

# **Low-energy ion irradiation and thermal annealing of supported 2D materials**

Inaugural-Dissertation  
zur  
Erlangung des Doktorgrades  
der Mathematisch-Naturwissenschaftlichen Fakultät  
der Universität zu Köln

vorgelegt von  
**M. Sc. Philipp Valerius**  
aus Wickede (Ruhr)

Köln 2020

Erster Berichterstatter: Prof. Dr. Thomas Michely  
Zweiter Berichterstatter: Assoz. Prof. Dr. Jani Kotakoski

Vorsitzender der Prüfungskommission: Prof. Dr. Klas Lindfors  
Tag der mündlichen Prüfung: 30.04.2020

# Abstract

---

In the recent years, two-dimensional materials such as graphene, monolayers of hexagonal boron nitride, and monolayers of molybdenum disulfide have moved drastically into the research spotlight due to their extraordinary and unique properties. This thesis aims to investigate the phenomena that occur during low-energy ion irradiation of atomically thin sheets of 2D materials resting on a metallic substrate. By combining scanning tunneling microscopy, -spectroscopy, and low-energy electron diffraction the resulting surface morphologies are studied, whereas X-ray photoelectron spectroscopy and temperature programmed desorption provide chemical information. The experimental data is corroborated by atomistic simulations to further decipher the microscopic mechanisms involved in the damage formation and their thermal annealing. The ion-induced damage formation in graphene on Ir(111) has been intensively studied in the past. It has been shown that through thermal annealing this 2D material has excellent capability to reorganize its crystal lattice and even completely restore its initial shape at sufficient temperatures. Therefore, it is important to investigate the recrystallization possibility also for other members of the fast growing family of 2D materials.

In this manner, we first study the recovery of highly damaged hexagonal boron nitride. We uncover that lattice restoration of monolayer h-BN exposed to large ion doses is feasible, although bond rotation is energetically unfavorable, due to its hetero-elemental composition. Annealing of a monolayer of hexagonal boron nitride destroyed by  $\text{Xe}^+$  ion irradiation gives rise to rich structural phenomena. We find: selective pinning of vacancy clusters at a single specific location within the moiré formed by hexagonal boron nitride and the Ir substrate; crystalline Xe of monolayer and bilayer thickness sealed inside hexagonal boron nitride blisters at room temperature; standalone blisters bound only to the metal at temperatures at which hexagonal boron nitride on Ir(111) decomposes; a pronounced threefold symmetry of all morphological features, due to the preferential formation of boron-terminated zigzag edges that firmly bind to the substrate. The investigations give clear insight into the relevance of the substrate to damage creation and annealing in a two-dimensional layered material.

Secondly, this thesis will focus on the damage production by low-energy  $\text{Xe}^+$  ions interacting with monolayers of  $\text{MoS}_2$ , a transition metal dichalcogenide.  $\text{MoS}_2$  is a semiconductor with a band gap of about 2.5 eV. The  $\text{MoS}_2$  layer is epitaxially grown on graphene/Ir(111) and analyzed before and after irradiation *in-situ* under ultra-high vacuum conditions. Through optimized irradiation conditions using low-energy ions with grazing trajectories, amorphization of the monolayer is induced already

at low ion fluences and without inducing damage underneath the MoS<sub>2</sub> layer. A comprehensive picture of the structural and electronic response of a monolayer of MoS<sub>2</sub> to 500 eV Xe<sup>+</sup> irradiation is obtained, by using low-energy electron diffraction and scanning tunneling microscopy measurements. Molecular dynamics simulation uncover that upon ion impact mainly top-layer-sulfur is sputtered from the crystal lattice, and significant structural disorder is induced at the impact site. Surprisingly, the crystalline-to-amorphous transformation is accompanied by changes in the electronic properties from semiconductor-to-metal and an extinction of photoluminescence. The MoS<sub>2</sub> lattice recrystallizes upon thermal annealing accompanied with the restoration of the semiconducting properties. However, residual defects prevent the recovery of photoluminescence.

In addition, we study the formation of an ordered array of nanoscopic pores in hexagonal boron nitride on Ir(111). 2D materials such as graphene are chemically and mechanically inert, flexible, and ultimately thin. Combined with the introduction of nanopores, a graphene sheet can easily outperform state-of-the-art filtration membranes. By using low-energy ion irradiation at elevated temperatures it has been shown that graphene yields nanopore lattices with pore sizes in the nm-range, a critical pore size that is predicted to be suitable for water purification purposes. However, a high density of holes accompanied with a well-defined size distribution is a requirement that still lacks experimental realization. With combined ion beam studies and *ab initio* density functional theory calculations we report on the nanomesh formation mechanism in hexagonal boron nitride on Ir(111) - an ordered array of vacancy clusters that is superior to the graphene one. We make use of the moiré superstructure formed by hexagonal boron nitride and the Ir(111) substrate and show that the introduction of vacancies is susceptible to the moiré landscape. This superlattice is well-ordered with a periodicity at the nanometer scale. First, we observe that vacancies agglomerate only at one specific site of the moiré unit cell, which is the valley region. This opens a path to controllable position each vacancy cluster. Then, we observe that the vacancy clusters exhibit a size selective stability, that does not change even for larger ion doses. Additionally, the nanopore lattice displays a high thermal stability. Using DFT, we can explain the variation of vacancy cluster binding strength in the moiré unit cell with position and uncover a size-selective stability.

Finally, graphene on Ir(111) is irradiated with small fluences of 500 eV He<sup>+</sup> ions at temperatures close to its chemical vapor deposition growth temperature. The ion irradiation experiments explore whether it is possible to suppress the formation of wrinkles in graphene during growth. We have found that the release of thermal mismatch strain by wrinkle formation can be entirely suppressed for an irradiation temperature of 1150 K. A model for the ion beam induced suppression of wrinkle formation in supported graphene is presented and underpinned by experiments varying the irradiation temperature and involving intercalation subsequent to irradiation.

# Deutsche Kurzzusammenfassung

## *(German Abstract)*

---

Aufgrund ihrer außergewöhnlichen Eigenschaften haben 2D Materialien wie Graphen, einlagiges hexagonales Bornitrid, und Monolagen Molybdädisulfid jüngst das Augenmerk der Wissenschaft und Forschung auf sich gezogen. Die vorliegende Dissertation widmet sich der Untersuchung der auftretenden Phänomene, wenn 2D Materialien, die auf einem metallischen Substrat ruhen, niederenergetischer Ionenstrahlung ausgesetzt werden. Durch Kombination von Rastertunnelmikroskopie, -spektroskopie und niederenergetischer Elektronenbeugung wird die resultierende Oberflächenmorphologie untersucht, wohingegen Röntgenphotoelektronenspektroskopie und Temperatur-programmierte Desorption chemische Einsicht liefern. Die experimentellen Daten werden durch atomistische Simulationen und Berechnungen vervollständigt, um ein aufschlussreiches Bild über die vorliegenden mikroskopischen Mechanismen zu erlangen. Die Ioneninduzierte Produktion von Gitterbeschädigungen in Graphen auf Ir(111) wurde intensiv untersucht. Interessanterweise konnte durch ein thermisches Ausheilen eine exzellente Reorganisation der Kristallstruktur beobachtet werden, welche sich für genügend hohe Ausheiltemperaturen kaum von einer unbeschädigten Probe unterscheiden konnte. Daher ist es von großem Interesse, die Möglichkeit dieser Rekristallisierung auf weitere Strukturen der schnell wachsenden Kristallklasse der 2D Materialien zu erweitern.

In diesem Sinne haben wir zunächst die kristallinische Reorganisation in Ionen-beschossenen hexagonalem Bornitrid untersucht und herausgefunden, dass ein Heilungsprozess des Kristallgitters realisierbar ist, obwohl Bindungsrotationen durch die hetero-elementare Komposition energetisch deutlich eingeschränkt sind. Durch Ausheilen einer von  $\text{Xe}^+$  Ionen beschossenen Monolage hexagonalen Bornitrids entstehen vielfältige strukturelle Phänomene. Wir haben die örtlich-selektive Bindung von angesammelten Fehlstellen an einer einzigen bestimmten Position innerhalb der Moirézelle beobachtet; die Entstehung von kristallinem Xe bei Raumtemperatur, welches in Blasen von Bornitrid gefangen war; freistehende Blasen von Bornitrid, welche bei Temperaturen an denen Bornitrid sich längst zersetzt fest an das Metallsubstrat gebunden sind; und schließlich eine deutliche dreifach Symmetrie bei allen Oberflächenstrukturen, welches auf die zigzag Bor-Terminierung der Kristallkanten zurückzuführen ist. Eine klare Folgerung über die Relevanz des Substrats für die Schadensproduktion und Selbstheilung in einem 2D Material wird gezogen.

Anschließend werden wir uns in dieser Arbeit auf die Schadensproduktion niederenergetischer Xe Ionen in einer Monolage  $\text{MoS}_2$  konzentrieren, einem Übergangsmetall-Dichalkogenid, welcher darüber

hinaus ein Halbleiter ist. Die MoS<sub>2</sub> Lage wird epitaktisch auf Graphen/Ir(111) gewachsen und sowohl vor als auch nach dem Beschuss *in-situ* unter Ultrahochvakuum Bedingungen analysiert. Anhand von niederenergetischer Elektronenbeugung und Rastertunnelmikroskopie Messungen können wir beobachten, dass bei streifendem Beschuss von 500 eV Xe<sup>+</sup>, die kristalline Phase in einen amorphen Zustand übergeht und erhalten somit ein eindeutiges Bild von der strukturellen und elektronischen Reaktion der Monolage MoS<sub>2</sub>. Durch optimierte Beschussbedingungen für niederenergetische Ionen unter streifenden Beschussbahnen ist die Amorphisierung einer Monolage schon bei kleinen Ionenfluenzen möglich, ohne dass ein Schaden im Substrat induziert wird. Der kristalline-zu-amorphe Übergang ist begleitet von Veränderungen in den elektronischen Eigenschaften, von halbleitend-zu-metallisch, und dem Verlust der Photolumineszenz.

Darüber hinaus haben wir die Bildung eines geordneten Gitters aus Nanoporen in hexagonalem Bornitrid auf Ir(111) untersucht. 2D Materialien, wie Graphen, zeigen außergewöhnlich hohe chemische und mechanische Stabilität, Flexibilität, und sind ultimativ dünn. Durch die Zuführung von Nanoporen könnte Graphen als Filtermembran eingesetzt werden, welcher eine bis dato unerreichte Leistung vorausgesagt wird. Durch niederenergetische Ionenstrahlung bei erhöhten Temperaturen wurde gezeigt, dass Graphen ein dichtes Netz aus Nanoporen ausbildet. Diese Nanoporen besitzen Durchmesser unter einem Nanometer, eine kritische Größe, welche das Filtern von Trinkwasser ermöglichen soll. Dennoch bleibt eine experimentelle Realisierung einer dichten Lochmembran begleitet von geordneten und Größen-selektiven Poren aus. Durch die Kombination aus Ionenstrahl-Experimenten und *ab initio* Berechnungen, beschreiben wir die Bildung von einer Lochgittermembran in Bornitrid auf Ir(111) - ein Lochgitter, welches hinsichtlich der Ordnung sogar dem in Gr deutlich überlegen ist. Somit ist die Möglichkeit gegeben, ein geordnetes Gitter von zu Cluster angesammelten Fehlstellen herzustellen. Das Lochgitter ist sowohl thermisch stabil als auch Größen-selektiv. Basierend auf atomistischen Berechnungen können wir die positionsabhängige Bindungsvariation und Größenspezifische Stabilität für Fehlstellen auf die lokalen Bindungskonfigurationen innerhalb der Moirézelle zurückführen.

Schließlich haben wir Graphen auf Ir(111) mit kleinen Fluenzen von 500 eV He<sup>+</sup> Ionen auf erhöhten Temperaturen, welche der Wachstumstemperatur von CVD Graphen gleicht, beschossen. Durch die hier aufgeführten Ionenstrahlexperimente erschließen wir die Möglichkeit, die Ausbildung von Falten in Graphen während der Wachstumsphase zu unterbinden. Wie wir feststellen können, kann die Freigabe von thermischer Zugspannung bei einer Beschusstemperatur von 1150 K durch Faltenbildung gänzlich unterdrückt werden. Wir präsentieren ein Modell für die Ionenstrahl-induzierte Faltenunterdrückung und unterstützen unsere These durch weitere Experimente, bei denen Temperatur variiert oder Fremdspezies nach dem Beschuss interkaliert werden.

## Frequently used Symbols and Abbreviations

<b>2D</b>	-	two-dimensional
<b>3D</b>	-	three-dimensional
<b>BL</b>	-	bilayer
<b>BZ</b>	-	Brillouin zone
<b>CVD</b>	-	chemical vapor deposition
<b>DFT</b>	-	density functional theory
<b>(L)DOS</b>	-	(local) density of states
<b>FFT</b>	-	fast Fourier transformation
<b>Gr</b>	-	graphene
<b>GNM</b>	-	graphene nanomesh
<b>h-BN</b>	-	hexagonal boron nitride
<b>L</b>	-	Langmuir, $1 \text{ L} = 1 \times 10^{-6} \text{ Torr} \cdot \text{s} \approx 1.33 \times 10^{-6} \text{ mbar} \cdot \text{s}$
<b>LEED</b>	-	low-energy electron diffraction
<b>MBE</b>	-	molecular beam epitaxy
<b>MD</b>	-	molecular dynamics
<b>ML</b>	-	monolayer
<b>MoS<sub>2</sub></b>	-	molybdenum disulfide
<b>MLE</b>	-	monolayer equivalent, $1 \text{ MLE} = 1.57 \times 10^{15} \text{ particles per cm}^2$
<b>PL</b>	-	photoluminescence
<b>STM</b>	-	scanning tunnelling microscopy
<b>STS</b>	-	scanning tunnelling spectroscopy
<b>TDS</b>	-	thermal desorption spectroscopy
<b>TMDC</b>	-	transition metal dichalcogenide
<b>UHV</b>	-	ultra-high vacuum
<b>vdW</b>	-	van der Waals
<b>w.r.t.</b>	-	with respect to
<b>XPS</b>	-	x-ray photoelectron spectroscopy
<b>Y</b>	-	sputtering yield, removed atoms per impinging ion
$\theta, \vartheta$	-	polar angle of ion beam with respect to the surface normal
$\phi, \varphi$	-	azimuthal angle of ion beam with respect to the sample surface



# Contents

<b>Abstract</b>	<b>iii</b>
<b>Deutsche Kurzzusammenfassung (<i>German Abstract</i>)</b>	<b>v</b>
<b>Frequently used Symbols and Abbreviations</b>	<b>vii</b>
<b>I Introduction</b>	<b>1</b>
<b>II Fundamentals</b>	<b>5</b>
<b>1 Low-energy ion interactions with supported 2D materials</b>	<b>7</b>
1.1 Ion surface interactions . . . . .	7
1.2 2D materials . . . . .	13
1.3 Ion interactions with 2D materials . . . . .	16
1.4 Growth of supported 2D materials . . . . .	20
1.5 Ion interactions with 2D materials supported by a substrate . . . . .	25
<b>2 Experimental methods</b>	<b>27</b>
2.1 Scanning tunnelling microscopy . . . . .	27
2.2 Low-energy electron diffraction . . . . .	28
2.3 Raman spectroscopy . . . . .	30
2.4 Photoluminescence spectroscopy . . . . .	31
2.5 X-ray photoelectron spectroscopy . . . . .	31
<b>3 Experimental setups, procedures, and theoretical modeling</b>	<b>33</b>
3.1 UHV system ATHENE . . . . .	33
3.2 X-ray undulator beamline I311 at MAX-LAB . . . . .	34
3.3 Sample preparation . . . . .	35
3.4 Sample analysis . . . . .	37
3.5 Theoretical modeling . . . . .	38

<b>III Results</b>	<b>41</b>
<b>4 Annealing of ion-irradiated hexagonal boron nitride on Ir(111)</b>	<b>43</b>
4.1 Motivation . . . . .	43
4.2 Amorphization and recrystallization . . . . .	44
4.3 Xe Trapping . . . . .	51
4.4 Blistering and shape evolution . . . . .	54
4.5 Low-energy ion irradiation . . . . .	59
4.6 Influence of the substrate upon thermal annealing . . . . .	60
4.7 Thermal decomposition of h-BN and formation of borophene on Ir(111) . . . . .	63
4.8 Discussion . . . . .	68
4.9 Conclusion . . . . .	71
<b>5 Reversible crystalline-to-amorphous phase transition in MoS<sub>2</sub></b>	<b>73</b>
5.1 Motivation . . . . .	73
5.2 Amorphization and recrystallization . . . . .	74
5.3 Molecular dynamics simulations . . . . .	80
5.4 Evolution of electronic and optical properties . . . . .	84
5.5 Conclusions . . . . .	88
<b>6 Self-limited vacancy cluster growth in 2DM moirés</b>	<b>91</b>
6.1 Motivation . . . . .	91
6.2 Vacancy cluster arrays in h-BN and Gr on Ir(111) . . . . .	92
6.3 Mechanism of vacancy cluster array formation in h-BN/Ir(111) . . . . .	96
6.4 Influence of the ion fluence and temperature on the nanomesh formation . . . . .	98
6.5 Influence of ion species and grazing incidence on the nanomesh formation . . . . .	105
6.6 Low-energy He <sup>+</sup> ion irradiation of h-BN on Pt(111) at elevated temperatures . . . . .	108
6.7 Intercalation of a h-BN sheet on Ir(111) . . . . .	110
6.8 Bubbling transfer of nanomesh membranes on Ir(111) . . . . .	114
6.9 Conclusions . . . . .	117
<b>7 Suppression of wrinkle formation in graphene</b>	<b>119</b>
7.1 Motivation . . . . .	119
7.2 High temperature Gr growth and wrinkle formation . . . . .	121
7.3 Effect of high temperature He <sup>+</sup> ion irradiation on wrinkle formation . . . . .	122
7.4 Unpinning of irradiated Gr by Eu intercalation . . . . .	125
7.5 Conclusions . . . . .	126

<b>IV</b>	<b>Summary and Outlook</b>	<b>127</b>
<b>V</b>	<b>Appendix</b>	<b>133</b>
<b>A</b>	<b>Scientific Appendix</b>	<b>135</b>
	A.1 Low-energy Xe <sup>+</sup> ion irradiation and thermal annealing of Gr on Ir(110) . . . . .	135
	A.2 DFT calculated vacancy cluster configurations in h-BN on Ir(111) . . . . .	138
<b>B</b>	<b>Appendix</b>	<b>141</b>
	B.1 3D rendered interpretation of the Gr/Ir(111) moiré based metal cluster superlattice .	141
	B.2 Interference effects of visible light in PMMA/Gr-membranes transferred on SiO <sub>2</sub> . . .	141
<b>C</b>	<b>Liste der Teilpublikationen (<i>List of Publications</i>)</b>	<b>144</b>
	<b>Bibliography</b>	<b>147</b>
	<b>Danksagung (<i>Acknowledgements</i>)</b>	<b>167</b>
	<b>Erklärung gemäß Promotionsordnung</b>	<b>169</b>
	<b>Lebenslauf (<i>Curriculum Vitae</i>)</b>	<b>170</b>



## **PART I**

---

# **Introduction**



---

In recent years, two-dimensional (2D) atomic crystals have gained extensive publicity in the field of fundamental as well as application-oriented research. Since then, the class of two dimensional materials (2DM) is vastly growing with over 700 examples already predicted to be stable [1]. Although still in the early phase, the global market is open for devices based on 2DM, with the size of the graphene (Gr) market around 55 million US\$ in 2019 [2], with strong indications of significant expansion in the next years. Looking at graphene-branded products, such as touch screens, batteries, and sensors [3,4], one might think that successful applications of fundamental research were found. In any case, graphene is becoming a strong marketing tool based on the hype factor surrounding it. The growing interest in 2DM stems from their unique physical properties which differ from those of their three-dimensional (3D) counterparts. The 2DM themselves, and also when combined into van der Waals (vdW) stacked hetero-structures, exhibit exceptional properties, such as the recently measured superconductivity in twisted bilayer Gr [5,6]. The choice of different layers and their respective orientation in heterostructures provides a playground in which to develop new electronic and optoelectronic devices [7].

The most prominent member of the family of 2DM is Gr, a one-atom thick layer of carbon arranged in a honeycomb lattice. With remarkable electron mobility [8], it is a promising component for future nanoelectronic devices. Still, Gr is lacking applicability for semiconductor-based electronics because it lacks a band gap. However, the large number of recently explored 2DM offer a large variety of electronic properties. A monolayer of hexagonal boron nitride (h-BN<sup>1</sup>), also referred to as white graphene, is isoelectronic and isostructural to Gr. But while Gr is a zero band gap semiconductor, h-BN is an excellent insulator with a band gap of about 5 eV [9]. The distinct properties stem from two inequivalent basis atoms. Another prevalent 2DM is monolayer MoS<sub>2</sub>, a triple layered structure, where Mo atoms are sandwiched in between planes of sulfide atoms. MoS<sub>2</sub>, a member of the largest 2DM family, the transition metal dichalcogenides (TMDC), is a direct band gap ( $E_{\text{gap}} = 2.5$  eV) semiconductor [10,11].

All three 2DM mentioned above are established as key components in vertical vdW-stacked heterostructures [12–14]. The tuning of their physical properties is highly desirable and can also be achieved by a controlled introduction of defects and doping effects, e.g., by using ion beam techniques. Through energetic impacts of charged particles with the atomic lattice, point defects such as substitutional defects or vacancy defects can be created. In MoS<sub>2</sub> the controlled introduction of S-vacancies was demonstrated by exposing MoS<sub>2</sub> to an Ar plasma [15]. It has been reported that ion induced defects in MoS<sub>2</sub> can beneficially alter the electronic properties by lowering contact resistances, and therefore give rise to improved device performance [16].

Apart from the field of electronic applications more fundamental issues may be solved by 2D materials. One key property of graphene and other 2DM is the possibility of hosting nanopores in the lattice while offering atomic thicknesses. Theoretical [17–19] and experimental [20–25] investigations

---

<sup>1</sup>In this work h-BN always refers to a monolayer of h-BN.

---

predict a huge impact of graphene on filter membranes, as it provides high permeance, high selectivity, while being chemically, mechanically and thermally stable. In order to create such perforations, surface science tools have proven to be very helpful. For example, low-energy ion irradiation of metal supported Gr at elevated temperatures has led to the formation of a nanomesh, a Gr layer hosting a dense array of nanopores ordered with the Gr/Ir(111) moiré [26]. The nanopores have diameters in the range of 1 nm, which is a critical pore size necessary for molecular sieving processes [27]. The implementation of such filter membranes would be a milestone for water purification purposes.

At the same time, Gr can act as a protective cover that prevents the metal substrate underneath from sputtering. Remarkably, the ion-induced damage and lattice disorder in Gr self-repair efficiently when annealed at temperatures in the range of the chemical vapor deposition (CVD) growth of Gr [28–30]. This qualifies Gr as a self-sustaining protective coating against ion irradiation. For h-BN, the non-equivalence of the two basis atoms in the  $sp^2$  hybridized honeycomb has also a profound effect on damage formation and annealing. While Gr displays a high flexibility in bond reorganization h-BN does not. Therefore, damage annealing in h-BN is assumed to be substantially impaired.

The main objective of this thesis is to study the response of 2D materials, such as epitaxial Gr, h-BN, and monolayer  $MoS_2$  grown on an Ir(111) substrate, to ion irradiation. More specifically, we focus on damage annealing, underlining the outstanding capability of these 2DM to recover from a largely destroyed state. Ion irradiation is a versatile tool to locally transfer high amounts of energy via particle impacts which drives the 2DM far out of thermodynamic equilibrium. This exposes the binding configurations within a 2DM to structural changes. Stable defect structures are formed when the impact energy dissipates. The emerging structures might host exciting new properties worth exploring.

In the following the content of this work is outlined. In Part II the basic concepts of ion surface interactions and the fundamental properties of Gr, h-BN, and  $MoS_2$  are introduced as well as defect structures and their generation in these 2DM. Additionally, the experimental techniques used in this thesis are described, while the corresponding setups and procedures are reviewed. Part III presents the results achieved in this work, where we investigate the physical phenomena that occur when energetic ions interact with 2D materials. We explicitly focus on low-energy ion irradiation and thermal annealing of Gr, h-BN, and  $MoS_2$  that we grow under ultra-high vacuum conditions on atomically clean metal surfaces. Finally, in Part IV the results are summarized and an outlook to future research is given.

## **PART II**

---

# **Fundamentals**



# CHAPTER 1

## Low-energy ion interactions with supported 2D materials

In this chapter, selected topics about 2D materials interacting with energetic particles are reviewed. Firstly, an overview of ion-surface interactions will be given. Then, 2D materials investigated in this thesis will be introduced. Subsequently, the interaction of 2D materials with energetic particles will be reviewed. Finally, supported 2D materials on metals are introduced, while an overview about their distinct interactions with energetic ions will be presented.

### 1.1 Ion surface interactions

When an energetic particle collides with a target material it will transfer some of its initial kinetic energy. For example, an impinging energetic ion is decelerated after a collision with a surface atom of a target material and the loss of energy can be described by the stopping power  $S(E)$  as shown by Eq. 1.1. The energy transfer can be induced by displacement of the target nuclei, excitation of the target electronic system, and initiation of nuclear reactions within the target atoms.

$$N \times S(E) = - \left( \frac{dE}{dx} \right)_d - \left( \frac{dE}{dx} \right)_e - \left( \frac{dE}{dx} \right)_n \quad (1.1)$$

$dE/dx$  describes the energy loss per unit path length and  $N$  the number density of substrate atoms. Nuclear stopping (index  $d$ ) is an elastic scattering process, electronic stopping (index  $e$ ) and nuclear reactions (index  $n$ ) are inelastic scattering processes. For ion energies as used in this thesis ( $E_{ion} < 10 \text{ keV}$ ) the electronic stopping ( $E_{ion} \approx \text{MeV}$ ) or nuclear reaction ( $E_{ion} \gg 1 \text{ MeV}$ ) can be neglected. For lower ion energies ( $E_{ion} \approx \text{keV}$ ), the Coulomb repulsion between ion nucleus with charge  $Z_1e$  and the target nucleus with charge  $Z_2e$  and the screening of the nucleus by the surrounding electrons has to be taken into account. The interaction potential of the scattered particles with the target material can be approximated by using the Coulomb potential multiplied by the screening function  $\Phi(r)$ :

$$V(r) = \frac{Z_1 Z_2 e^2}{r} \Phi(r). \quad (1.2)$$

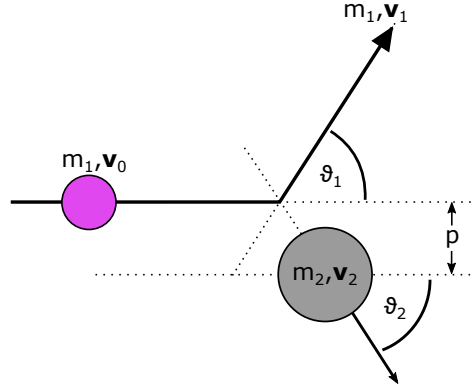


**Figure 1.1:** Schematics of a binary collision of an incident ion (purple) and a target atom (grey). The ion with mass  $m_1$  and initial velocity  $\mathbf{v}_0$  hits a particle at rest with mass  $m_2$ . The impact parameter is denoted with  $p$ . After the collision, the ion is deflected under a scattering angle  $\vartheta_1$  with a final velocity  $\mathbf{v}_1$ . The target atom recoils at an angle  $\vartheta_2$  with a velocity  $\mathbf{v}_2$ .

While a variety of screening functions have been derived, the potentials of this form are frequently used for numerical calculations of trajectories and scattering cross-sections [31]. The fractional term itself describes the case of Rutherford scattering for swift ions ( $E_{ion} \approx \text{MeV}$ ). The differential cross-section (formula of Rutherford)  $d\sigma/d\Omega$  describes the probability density of an ion scattered over a certain scattering angle:

$$\frac{d\sigma}{d\Omega} = \left( \frac{Z_1 e Z_2 e^2}{4E_0} \right)^2 \frac{1}{\sin^4(\vartheta_1/2)} g(\vartheta_1, m_1, m_2), \quad (1.3)$$

where  $g$  is a factor transforming the center of mass to the laboratory frame. As highlighted by Eq. 1.3, the scattering intensity strongly increases for heavy ions and targets.

### Binary collision

In first approximation, the interaction of a charged particle with a solid can be described by classical elastic binary collisions between the incident ion and a target surface atom for ion energies in the keV range. Here, the interaction time for a collision is short and the kinetic energy of the ions exceeds the interatomic binding energies. As shown in Figure 1.1, the incident ion with initial velocity of  $\mathbf{v}_0$  is scattered at an angle  $\vartheta_1$  with its final velocity of  $\mathbf{v}_1$ . Energy is transferred to the target atom, initially at rest, is scattered at an angle of  $\vartheta_2$  and final velocity of  $\mathbf{v}_2$ . By considering the conservation laws of energy and momentum, the energy of the scattered projectile  $E_1$  can be calculated using Eq. 1.4 and of the recoil atom  $E_2$  using Eq. 1.5.

$$E_1 = E_0 \left( \frac{m_1 \cos\vartheta_1 \pm \sqrt{m_2^2 - m_1^2 \sin^2\vartheta_1}}{m_1 + m_2} \right)^2 \quad (1.4)$$

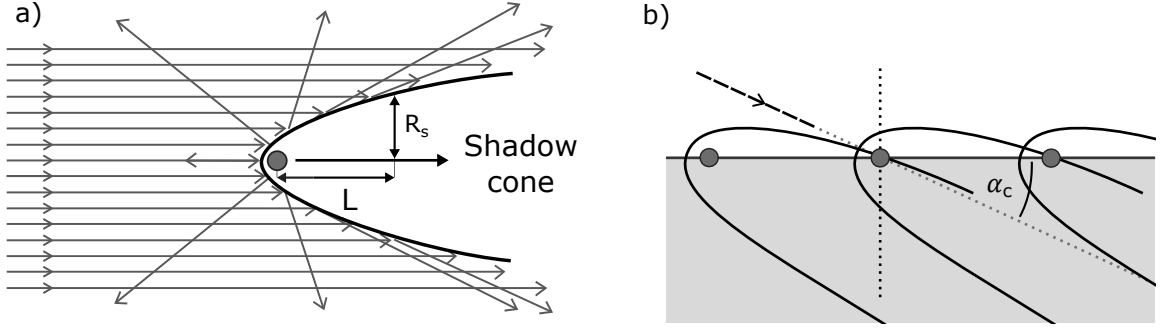


**Figure 1.2:** Schematics of shadowing. (a) Scattering trajectories from projectile ions scattered from a target atom form a shadow cone - a region totally free of trajectories. (b) Shadow cone of surface atom under grazing ion incidence. The critical angle  $\alpha_c$ , where direct impact of neighboring atoms are blocked, is indicated. Redrawn after Ref. 32.

$$E_2 = E_0 \frac{4m_1 m_2 \cos^2 \vartheta_2}{(m_1 + m_2)^2} \quad (1.5)$$

If the projectile is heavier than the target mass ( $m_1 > m_2$ ) only forward scattering with angles smaller than  $\vartheta_{1,\max} = \arcsin(m_2/m_1)$  is possible. The fraction of transferred energy is small if mass differences are large. Using Eq. 1.4 and Eq. 1.5 one can obtain direct information on the masses of atomic species present at the surface, e.g., as used for surface elemental analysis. Common methods are ion scattering spectroscopy (ISS) or Rutherford backscattering spectroscopy (RBS).

### Shadowing and blocking

As depicted by Figure 1.2(a), a parallel beam of projectile ions is scattered according to the repulsive interaction potential from the target atom. Based on the Coulomb repulsion, a shadow cone is formed behind the target atom, a region completely free of trajectories, where impinging ions are not able to enter. The excluded trajectories accumulate at the edges of the cone (called focusing effect). In case of an unscreened Coulomb potential the shadow cone has a shape of a paraboloid with radius  $R_s$  at a certain distance  $L$  from the target nucleus (see Eq. 1.6).

$$R_s = 2\sqrt{\frac{Z_1 Z_2 e^2 L}{E_0}} \quad (1.6)$$

The energy of the impinging ion is denoted with  $E_0$ . From Eq. 1.6 the shadow cone size drastically increases for low-energy ions. However, for lower-energetic ions screening effects become important. If atoms are located inside the cone, they are shielded from the impinging ions. For surface atoms, the shadowing effect becomes relevant for grazing ion incidence. As shown in Figure 1.2(b), for an critical angle  $\alpha_c$ , between the surface and impinging ion trajectory, the neighboring atom enters the shadow cone and a direct impact between the impinging ion beam and the neighboring target atom

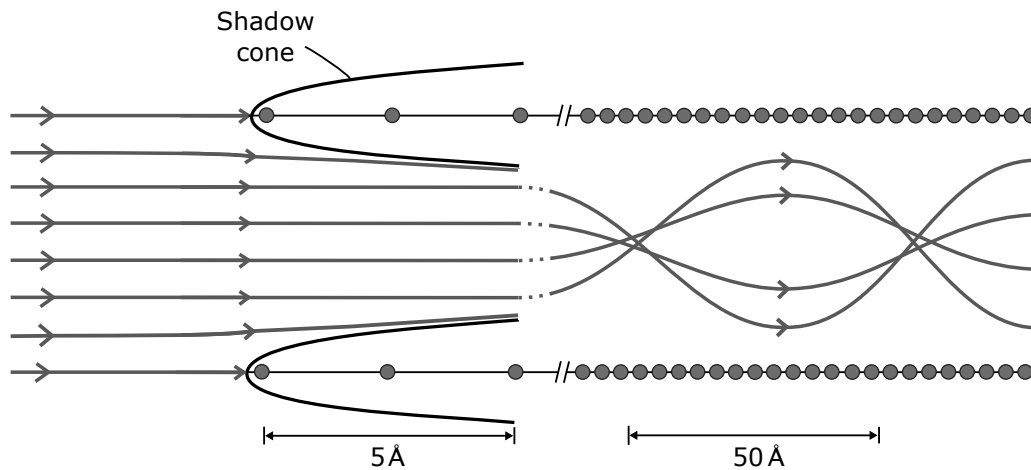


**Figure 1.3:** Schematics of the channeling effect. Particles of a well-aligned ion beam are scattered at the surface atoms of the target material and perform channeling along the atomic rows of the crystal. The length scale on the right side is compressed in order to highlight the trajectories undergoing channeling. Redrawn after Ref. 32.

is blocked. The critical angle depends on the spacing between the surface atoms, as well as on the width of the cone. Both critical angle  $\alpha_c$  and cone width will substantially decrease with increasing ion energies [33]. It should be noted that for projectiles lighter than the target atom ( $m_1 < m_2$ ) the shadowing is complete, for ( $m_1 > m_2$ ) shadowing is incomplete and some trajectories may enter the cone. However, the density of allowed trajectories within the cone is still heavily reduced, and the focusing effect still holds.

### Channeling

When the ion beam direction is well-aligned with major symmetry directions of a monocrystalline target material, the stopping power of the particle can be much lower. The particles will only do small-angle scattering as it passes through the crystal mimicking an oscillatory motion in channels formed by the rows of atoms. This oscillatory trajectories have wavelength of up to several hundred Ångströms. The motion along the crystal channel is commonly referred to as channelling [34]. As previously discussed, due to the repulsive Coulomb potential, ion trajectories are excluded within the shadow cone of a target atom. If the width of the shadow cone is small compared to the interatomic distance, *i.e.*, for light or high-energy ions, the particles can enter in-between the atomic rows as shown in Figure 1.3.

For grazing-incidence ions, channeling can also occur within the topmost layers of a material. Ions that penetrate the topmost crystal layer along a major symmetry direction will move almost parallel to the planes of the surface atom rows. The ion is trapped in between the two topmost layers where it only performs small angle binary collisions, called subsurface channeling [35]. Trails of defects, such as surface vacancies and adatoms are formed along the ion path, whenever the projectile scatters at the topmost crystal layer but from below. Due to under-coordination of surface atoms,

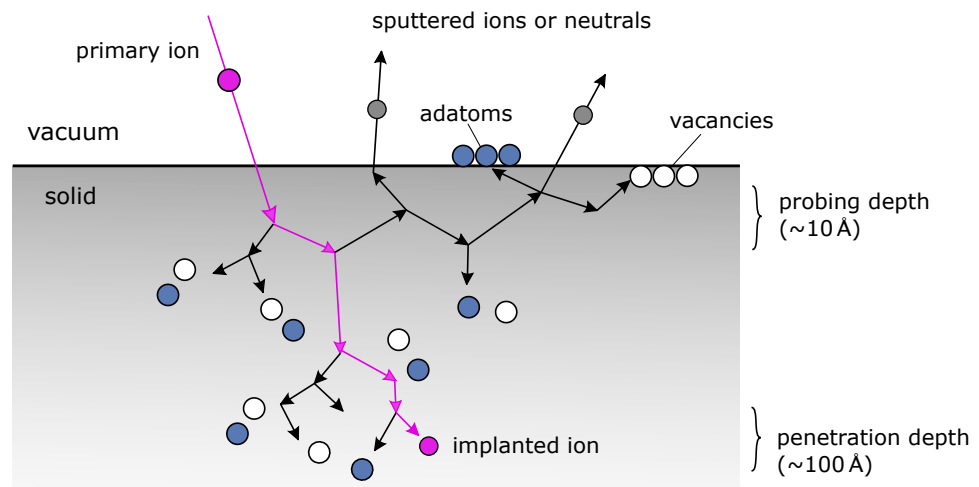


**Figure 1.4:** Schematic representation of a collision cascade. Upon penetration of the impinging ion induces different processes in the solid. The cascade of collisions results in the formation of Frenkel pairs, surface adatoms, sputtering of target atoms (probing depth of  $\sim 10 \text{ \AA}$ ), and ion implantation (penetration depth of  $\sim 100 \text{ \AA}$ ). Vacancies are shown in white, sputtered atoms in grey, and adatoms in blue. The path of the impinging ion is highlighted in purple. Redrawn after Ref. [37].

the energy threshold for damage formation at the surface by ion impacts from below is strongly reduced compared to bulk defects [36].

### Defect formation and evolution

When the impinging ion is not scattered out of the sample through elastic collisions, it may enter deep into the bulk, while dissipating its kinetic energy through a series of collisions until it comes to rest. Heavy or highly energetic ions ( $1 - 10^3 \text{ keV}$ ) can initiate a collision cascade. A schematic representation of such is given in Figure 1.4. As a result of energy transfer from the impinging ion into target atoms within the solid, the atoms gain enough energy to be displaced from their original lattice site and generate recoil cascades. Collision cascades from a probing depth of about  $10 \text{ \AA}$ , may terminate at the surface, causing target atoms to leave the crystal as sputtered ions or neutrals. A surface atom becomes sputtered if the energy transferred to it has a component normal to the surface which is larger than the surface binding energy. The impinging ion may come to rest deep in the solid up to penetration depths of about  $100 \text{ \AA}$ , while producing stable vacancy-interstitial pairs (called Frenkel pairs), throughout its path.

The development of the collision cascade is only the first out three stages of the damage evolution. Secondly, it terminates into the thermal spike, a liquid like zone, followed by a recovery phase. The duration of this whole process is in the range of picoseconds. In the initial  $0.1 - 0.3 \text{ ps}$  the primary knock-on atom (a lattice atom with enough transferred energy to enable its displacement) is decelerated by subsequent recoils producing several branches of collision cascades until the energy

of all moving atoms has dropped below the displacement energy. During this sequence the distance between each collision decreases. After about 0.25 ps, the kinetic energy at the impact site is distributed fast between many atoms in a small volume leading to a collective motion called thermal spike. Based on simulations, the temperature in this region is predicted to be well above the melting temperature, while the local atomic density is reduced by up to 20% and compressed material is found in the surrounding [38]. After 3 ps stable interstitials are produced outside the molten zone while the core area recrystallizes after about 10 ps, where interstitials annihilate with nearby vacancies.

### Sputtering

The removal of target atoms from the solid is called sputtering. The sputtering yield is defined as the average number of removed atoms per incident ion. In general, the sputtering yield depends on several important factors, such as the incidence angle of impinging ions at which collisions with the surface takes place, the amount of kinetic energy they strike it with, their masses, the masses of the target atoms, the target's surface binding energy, and the crystallographic orientation. With increasing incident ion energy, the sputtering yield increases rapidly, when the binding energy threshold is exceeded. It is proportional to the nuclear stopping power  $(dE/dx)_n$  (compare Eq. 1.1), which, as discussed above, refers to the elastic collisions between the projectile ion and target atoms. Sputtering then continues to grow with energy ( $E < 100$  keV), and finally slightly decreases [39]. At high energies ( $E > 100$  keV), the cross sections and interaction times for energy transfer to target atoms are small and the ranges of energetic particles in the solid are large. Here,  $(dE/dx)_n$  is small and  $(dE/dx)_e$  becomes more relevant. Ions with greater mass have greater sputtering efficiency. With increasing incidence angle  $\theta$  from the surface normal, the penetration depth decreases, resulting in a concentration of collision cascades closer to the surface region, and therefore, an increase in sputtering by  $1/\cos \theta$ . For  $\theta$  greater than  $80^\circ$ , ions impinge the surface at grazing incidence and are mostly scattered off the surface without penetrating into the solid. As only a small portion of kinetic energy of the grazing incident ions are transferred, they are reflected from the atomically smooth terraces, resulting in a steep decrease of the sputtering yield. However, grazing incidence ions impinge on rising atomic steps with significant momentum and energy transfer to the substrate, and thus cause sputtering at the step edges. Compared to an atomically flat surface the step edge sputtering yield can be higher by a factor of 100. This process is also referred to as step edge sputtering [40]. As shown by Figure 1.5, ions that are reflected from the lower terrace, within a maximum distance  $x_c$  from a rising step edge, are redirected towards small angle collision, and therefore have a high impact. Sputtering is applied, for example, in sputter ion sources, for obtaining atomically clean surfaces. The detection and identification of sputtered particles from a surface gives information about its elemental composition and is used for surface analysis, such as secondary ion mass spectroscopy (SIMS). Additionally, by successively removing atomic layers by sputtering, insights in the subsurface composition as a function of depth can be gained (depth ion profiling).

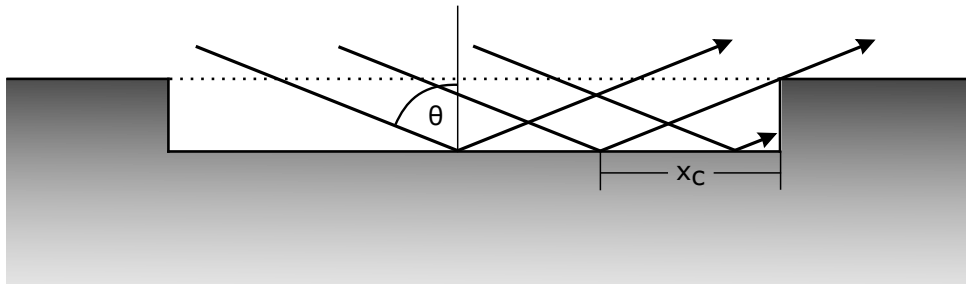


**Figure 1.5:** Schematic side view of the step edge sputtering process. A surface with an atomic step edge is exposed to grazing incidence ions. Ions entering the upper terrace level (dashed line) at a maximum distance of  $x_c$  from the the ascending step are scattered from the lower terrace and directly collide with the step. Redrawn after Ref. 40.

### Amorphization

The passage of an energetic ion through a crystal lattice initiates a sequence of displacement events that leads to defect production and, at sufficiently high doses, to an amorphous lattice transformation of the irradiated area. Radiation effects in crystalline solids, such as a crystalline-to-amorphous phase transformation, is an active area of research in the semiconductor industry. Irradiation induced amorphization can be assigned to chemical disordering or volumetric expansion of the crystal [41,42] and sets in when the free energy of the damaged crystalline phase is higher than that of the amorphous phase. Amorphization by ion implantation is the result of a critical balance between the damage generation and its annihilation. Collision cascades generate different damage configurations going from isolated point defects and defect clusters to amorphous pockets, which can be correlated to an overlap of isolated damaged regions (heterogeneous amorphization) or via the build-up of simple defects (homogeneous amorphization). Thermal processing is required to anneal the induced damage [43]. While the formation of an amorphous phase can be beneficial, *e.g.*, because it limits ion channeling, annealing can drastically improve crystal ordering resulting in a low defect density in the recrystallized volume. Usually, annealing temperatures far above 1000 K are required to remove extended defects in the irradiated region and place foreign species into substitutional positions.

## 1.2 2D materials

The exploration of new materials is an everlasting field of research as it ensures technological advances and breakthroughs. Recently, the class of two-dimensional materials is expanding with many new members exhibiting different properties [1]. Their variety becomes even larger through the combination of 2DM in (vdW) stacked hetero-structures. 2DM have an extended planar crystal structure, with strong covalent bonds within the plane and weak vdW-forces normal to the plane. Based on the weak interlayer bonding, single layers can be easily obtained by breaking the vdW bonds, without

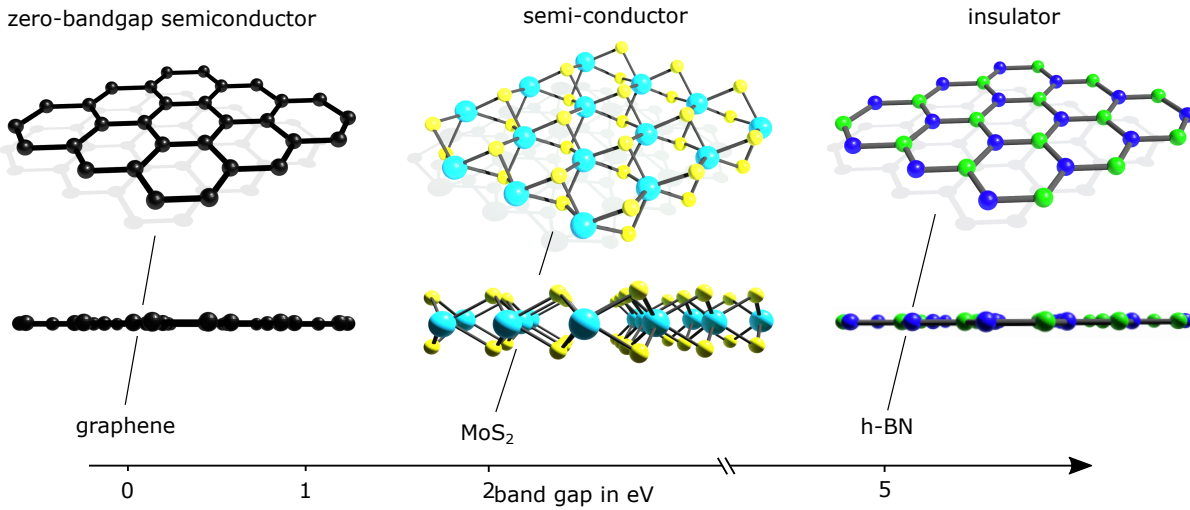


**Figure 1.6:** Top and side view of atomic models for different 2D materials as used in this thesis. Left: Graphene has a honeycomb lattice made of C atoms (black balls) with no band-gap. Middle: Monolayer MoS<sub>2</sub> is a semi-conducting member of TMDCs and consists of a triple layered structure consisting of sulfur (yellow) and molybdenum (cyan). Right: h-BN is a large band gap insulator with a honeycomb lattice of alternating nitrogen (green) and boron (blue) atoms.

disturbing the crystal structure, *e.g.*, through exfoliation by the scotch-tape method [44]. Figure 1.6 depicts the crystal structure of the 2D materials as investigated in this thesis, namely graphene, hexagonal boron nitride, and monolayer molybdenum disulfide. Gr and h-BN are 2D crystals made of a honeycomb lattice of either pure carbon or alternating nitrogen and boron atoms, respectively. The strong in-plane bonding is based on  $sp^2$  hybridization, where each atom forms three  $\sigma$  bonds from the  $s$ ,  $p_x$ , and  $p_y$  orbitals. The  $p_z$  orbitals of each atom overlap and form the delocalized  $\pi$ -electron system, which dominates the electronic properties of the materials<sup>1</sup>. Although Gr is the most investigated 2DM and has useful electronic properties, it is lacking applicability for semi-conducting based electronics because of its missing band gap. A monolayer of h-BN is isoelectronic and isostructural to Gr. It is distinct from Gr as its basis is formed by two inequivalent atoms, in place of two equivalent C atoms as for Gr. This gives rise to a fundamental difference in the electronic properties, as h-BN is a large band gap insulator [9]. Additionally, monolayers of MoS<sub>2</sub>, a semiconductor in the family of TMDC, is a direct band gap semiconductor<sup>2</sup> consisting of a triple layered structure, where Mo atoms are sandwiched in between planes of sulfide atoms (compare Figure 1.6), forming an equilateral prism, with S atoms at the bottom and top corners of the prism. The 2H configuration is the most common stacking order for MoS<sub>2</sub>. Single-layer MoS<sub>2</sub> does not have an inversion center in contrast to even-numbered stacks of 2H-MoS<sub>2</sub>, which show inversion symmetry. Further members of the TMDC show not only similar semiconducting properties such as WS<sub>2</sub>, MoSe<sub>2</sub>, and WSe<sub>2</sub> [45] with band gaps of 1 to 2.5 eV, but also metallic and even superconducting such as NbSe<sub>2</sub> and TaS<sub>2</sub> [46–48].

<sup>1</sup>The overlapped  $p_z$ -orbitals form the bonding  $\pi$  and antibonding  $\pi^*$  bands, which are the bands closest to the Fermi-level and, therefore, make up the valence and conduction band.

<sup>2</sup>Bulk MoS<sub>2</sub> in the 2H-phase is an indirect band gap semiconductor ( $E_{\text{gap}} = 1.23$  eV), transitioning into a direct band gap ( $E_{\text{gap}} = 2.5$  eV) semiconductor when thinned down to a monolayer [10].

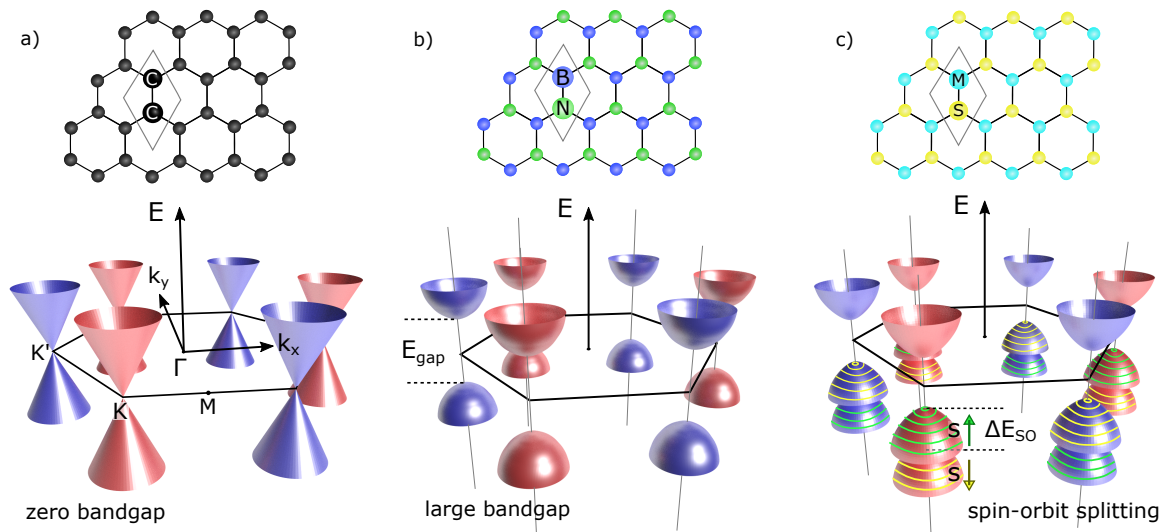


**Figure 1.7:** Crystal structures with highlighted unit cell and electronic band dispersion near the K(red)- and K'(blue)-points for (a) Gr, (b) h-BN, and (c) MoS<sub>2</sub>. The hexagonal Brillouin zone is indicated. The valence bands of MoS<sub>2</sub> are spin split. The colored circles of the valence band in (c) indicate electron spin configuration within the bands, with green (yellow) holds for spin-up (spin-down) configuration.

Because of its inertness, flatness, structural perfection, and insulating character, cleaved bulk hexagonal boron nitride or monolayers of h-BN are now widely used as substrates for organic molecules [49, 50], topological insulators [51], and Gr [52]. Gr and h-BN both combine high mechanical strength, low friction, excellent heat conductivity, resistance against degradation at high temperatures, and the ability to produce them as nanosheets or wires [53]. This moves their application for water cleaning [54], gas separation [55], or as components in high-strength composite materials [56] into reach. Bulk layered MoS<sub>2</sub> and individual sheets have found applications in tribology [57, 58], catalysis [15, 59, 60], and as an electronic [61, 62], opto-electronic [63, 64] or spintronic material [65].

Figure 1.7 depicts the electronic bands at the K-points of the investigated 2DMs. Although all three materials show a similar hexagonal crystal structure and symmetries, their electronic properties differ significantly. Based on quantum mechanics the band structure of graphene shows relativistic behavior at the K- and K'-points of the Brillouin zone. As shown in Figure 1.7(a), the electron energy is linear with  $\mathbf{k}$ . The movement of these quasiparticles is similar to massless particles but with a constant Fermi-velocity of  $v_F = 10^6$  m/s, about a factor of 300 smaller than the speed of light. As seen in Figure 1.7(b) and (c) the inversion symmetry of the hexagonal lattice in the unit cell of h-BN and MoS<sub>2</sub> is broken, which results in the formation of a band gap with parabolic bands at the K- and K'-points. In the case of h-BN the size of the band gap is about 5 eV and for MoS<sub>2</sub> it is about 2.5 eV [11, 66]. Additionally, due to loss of Kramer's degeneracy the valence band of MoS<sub>2</sub> is spin-split induced by spin-orbit coupling. The valence band maxima are populated with inverted spin-configuration in the neighboring valleys [67]. Therefore, selective spin excitation (up or down)

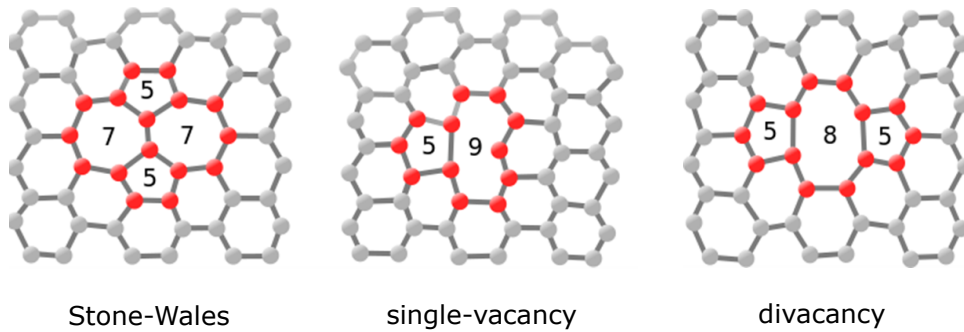


**Figure 1.8:** Atomic models of vacancy structure in graphene illustrating that possible defect structures in  $sp^2$ -lattices are diverse. The Stone-Wales defect involves the formation of two 5- and 7-membered C rings, a pentagon-nonagon pair is formed after the removal of one C atom, and a 5-8-5 defect configuration evolves upon ejection of two C atoms.

will excite only one the valley (K or K') [68], resulting in optically induced valley polarization and spin Hall effects [69, 70]. The combination of 2D materials in a vertical stack is a promising way to alter their properties. All three 2DM discussed above are established as key components in vertical vdW heterostructures [12–14], with their integration, *e.g.* in light emitting diodes, claimed to have a huge potential for light sources and displays. Furthermore, the combination of two graphene sheets rotated under a certain angle with respect to each other was found to induce superconductivity in so-called twisted bilayer graphene [5, 6].

### 1.3 Ion interactions with 2D materials

Due to their unique electronic and structural properties, 2D materials have attracted substantial interest and are dealt as promising candidates for nanotechnological applications. The presence of structural defects within these materials influence their intrinsic properties and may deteriorate their performance. In semiconductor production, the intentional introduction of impurity atoms or defects into an intrinsic semiconductor is used to modulate its electrical, optical and structural properties. Ion irradiation is a useful technique to introduce defects into 2D materials in a controlled manner that may open a path to beneficially design their properties and is of high priority to be explored. In this chapter, structural defects which may appear during growth or are introduced by energetic particle irradiation are reviewed. As defect structures appear at the atomic-scale, advanced imaging techniques are required, such as transmission electron microscopy (TEM) or scanning tunneling microscopy/spectroscopy (STM/STS), to image their atomic structure, together with their electronic structure such as band gap or defect related states [71].

#### Structural defects in Gr, h-BN, and MoS<sub>2</sub>

CVD is a practical technique for large-scale synthesis of graphene [72]. However, this preparation method inevitably introduces atomic defects, which influence the intrinsic material properties such

as mechanical, electronic, thermal, chemical, and even magnetic properties. For instance defects might act as scattering centers for phonons, and therefore affect thermal transport [73], or as charge trapping centers, thereby affecting electronic transport [74,75]. The  $sp^2$ -hybridized atoms in Gr and h-BN are able to rearrange themselves into a variety of polygons. For freestanding Gr, a whole zoo of defect structures involving 5- and 7-membered C rings, such as the Stone-Wales defect, have been observed in electron irradiation studies using a TEM [76–81]. Some of the most relevant defect structures are depicted in the atomic models in Figure 1.8. A single vacancy reconstructs into a 5-9 defect (a paired configuration of a 5- and a 9-membered C-ring), and a double vacancy into a 5-8-5 defect. However, the number of structural defects is essentially infinite. Upon ion impacts with the Gr lattice, defects beyond single and double vacancies are formed via in-plane recoils. The types and concentrations of defects can be controlled via tuning the ion energy [82,83]. Interstitial or impurity atoms often exist in as-prepared crystal samples due to the complexity of the synthesis. Adatoms within the planar 2D crystal are energetically very costly, which is why additional atoms might induce out of plane bonding and bending of the Gr sheet. For example, the energetically favored position for a C adatom in freestanding Gr is the bridge site, *i.e.*, on top of a C-C bond. Adatoms can form covalent bonds to the 2D layer with binding energies of the order of 1.5 - 2 eV for freestanding Gr [84]. The incorporation of foreign atoms as substitutional impurities, such as the replacement of C atoms by B, N, or Si atoms, leads to doping of Gr [85,86]. Although a perfect graphene sheet is known to be nonmagnetic, intrinsic vacancies or external dopants may induce local magnetism. Gr with an overall paramagnetic, and also ferromagnetic behavior was reported in Refs. [87,88], where hysteresis loops of graphene were measured.

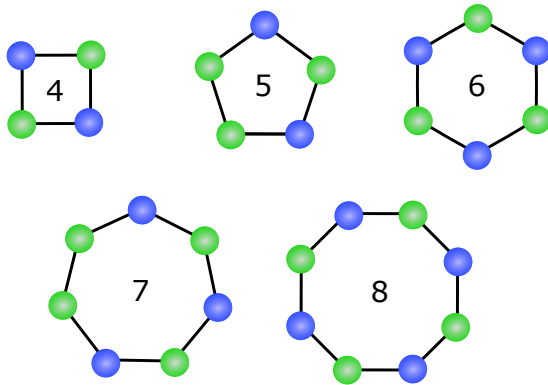


**Figure 1.9:** Atomic models for different polygonal configurations in h-BN. The formation of uneven numbered rings involves the formation of energetically unfavored homo-elemental bonds between N-N or B-B atoms.

As depicted in Figure 1.9, formation of 5- and 7- membered rings in h-BN involves homo-elemental bonds which are substantially weaker and thus unfavorable. Therefore, single vacancies in freestanding h-BN are unreconstructed. Continued electron irradiation of h-BN causes only the ejection of atoms, but no bond reorganization [89,90]. Bond rotations, *e.g.*, necessary in vacancy migration processes, are energetically more costly compared to in Gr. The mono-vacancy migration energy in freestanding Gr is about 1.4 eV [91], while in h-BN it is 2.6 eV for a B and 5.8 eV for an N vacancy [92].

A different type of a macroscopically defective Gr sheet is the graphene nanomesh (GNM), a periodic arrangement of holes within the atomic lattice. The extended 2D defect structure significantly modifies the electronic structure of graphene, turning the semi-metallic graphene sheet into a semiconductor [93,94]. GNMs with a lattice constant on the order of 100 nm have been realized using reactive ion etching [95], lithography [96], or ion

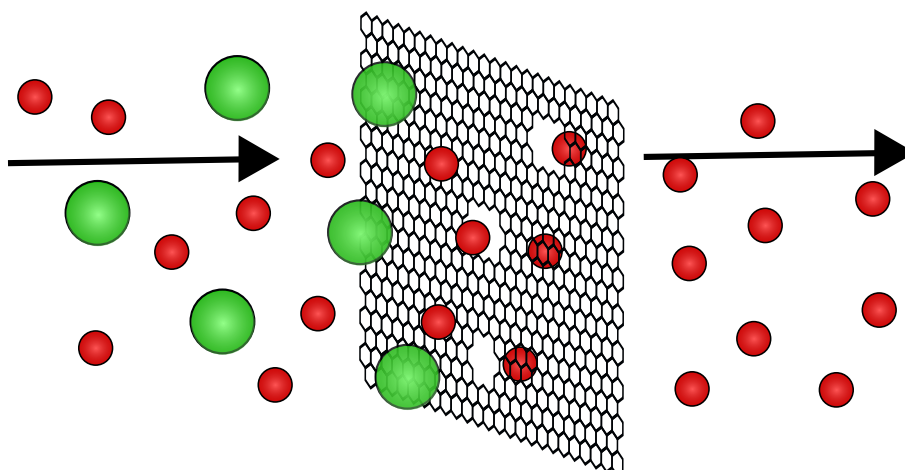


**Figure 1.10:** Schematic of a molecular sieving membrane. A graphene membrane with well defined holes is a promising filter membrane for size selective mass separation processes. Pressure applied to a solution of differently sized molecules (left), *e.g.*, salt ions in water, drives the smaller molecules (red spheres) through the graphene membrane, while bigger molecules (green spheres) are blocked. Redrawn after Ref. 98.

bombardment [97], varying significantly in hole sizes and band areas between holes. Apart from tuning the intrinsic properties, a holey 2D sheet can be considered as the ultimately thin filter membrane, enabling size selective mass transport which is essential for a wide field of applications as reviewed in Ref. [27]. As implied by Figure 1.10, a solution of differently sized molecules can be efficiently separated by a graphene membrane with well-defined hole sizes. A significant filtering process would be the desalination of water, and based on theoretical predictions a Gr membrane with hole sizes smaller than 1 nm would be a very promising candidate [98]. However, the experimental realization of a Gr membrane with a dense array of holes with well defined diameters, especially smaller than 1 nm, is still an open challenge for research.

Considering semiconducting materials, such as  $\text{MoS}_2$ , the removal of atoms or introducing of foreign species can have detrimental effects on the electronic properties. The electron mobility [99] in CVD-grown  $\text{MoS}_2$  is significantly lower than in mechanically exfoliated  $\text{MoS}_2$ . Such large discrepancies may arise from charge-carrier scattering centers such as point defects or grain boundaries. Sulfur vacancies in  $\text{MoS}_2$  include monovacancy and double-vacancy with one or two S atoms missing from the sulfur sublattice site, respectively. Extended Mo vacancies were also observed, where the central Mo atom and its neighboring S atoms are absent. Upon removal of single S atoms, distinct states appear within the band gap, and with increasing vacancy density, these may even induce metallic behavior [15]. Common defects and impurities in CVD and MBE grown  $\text{MoS}_2$  include vacancies [100], antisite defects [101], substitutional atoms [102], and adatoms [103]. Furthermore, line defects such as grain boundaries, which form between two differently oriented grains of  $\text{MoS}_2$ , exhibit interesting physical properties [11, 104].

### Ion induced generation of structural defects

The tuning of the physical properties of 2D materials is highly desirable. Ion irradiation is an elegant tool in order to induce structural and doping effects in a controlled manner. Energetic impacts of charged particles, such as ions or electrons, with the atomic lattice can lead to the formation of point defects such as substitutional, Stone-Wales defects, and vacancies. Whenever enough kinetic energy is transferred from the impinging particle to overcome the threshold energy for displacement, atoms are ejected from the crystal lattice. The displacement threshold for C atoms in Gr is 18–20 eV [105–107], for N and B atoms in h-BN it is 19 eV and 23 eV [105], respectively. For S atoms in MoS<sub>2</sub> it is 7 and 8 eV for top or bottom-layer S, respectively and for Mo atoms it is 20 eV [108].

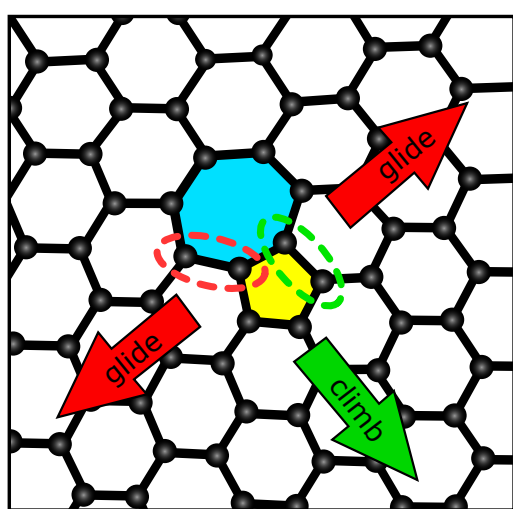


**Figure 1.11:** Schematic diagram showing the possible migration directions for dislocations in graphene. A dislocation can migrate along the gliding plane via bond rotations (indicated by red arrows) or climb perpendicularly to the gliding plane via the removal of a two C atoms (green arrow). Reproduced with permission from Ref. 109, © 2015 ACS.

Particle irradiation can also directly transfer energy to existing defects and activate their mobility. The migration barrier for vacancies is significantly lower than the displacement threshold for atom ejection in Gr, resulting in a heavily favored vacancy migration in Gr compared to atoms being removed from the lattice. Continued electron irradiation of Gr transforms the honey-comb lattice into 2D amorphous carbon, consisting of a random arrangement of polygons, predominantly 5-, 6-, and 7-membered C rings. As for very large ion doses the Gr lattice can adopt a large variety of defect configurations until a complete loss of its long range crystal order. This amorphization process was shown by successive electron bombardment in an TEM [78]. Defect migration can take place in form of vacancy climb and glide motion, when exposed to energetic particle irradiation. As indicated by Figure 1.11, a dislocation can migrate along the gliding plane via bond rotations (indicated by red arrows), while the activation energy for a bond rotation is calculated to be about 5–10 eV. The climb motion is perpendicular to the glide plane and requires the removal of a pair of carbon atoms, as highlighted by the green ellipse. Electron microscopy work has demonstrated dislocation climb, under conditions where vacancies are created through electron impacts [80, 109, 110]. The successive creation of vacancies leads not to an accumulation of defects, but only to the climb motion of the dislocation core together with the creation of tensile strain.

Ion implantation at relatively low energies has been widely used to modify the properties of 2D materials. For 2D materials, low-energy ions typically below 1 keV are efficient for modifying the surface morphology [111], because the interaction time and thus the nuclear stopping power decreases for higher ion energies. Ion irradiation at higher energies up to tens of keV is usually applied to realize defect engineering as discussed above. Distinct ions, such as B or N can be incorporated in the Gr

lattice and induce doping effects [112]. In the case of highly-charged ions, the ion-target interaction is dominated by fast electronic transitions. These ions have low velocities (150-450 keV) and high charge states<sup>3</sup> due to the loss of many or most of their bound electrons. Once the ion is in close proximity with the target material, electron emission towards the ion sets in. As for Gr, highly-charged ion irradiation has been utilized to generate defects [114] or to investigate the electronic response of a freestanding Gr sheet to localized and large electric fields [113]. Furthermore, swift heavy ions<sup>4</sup> were used for defect creation in 2D materials. For heavy ions with an energy of a few hundred MeV, nanostructures are produced in MoS<sub>2</sub> due to single-ion impacts on the target materials [115].

The hexagonal lattice structure of monolayer h-BN was directly imaged using high-resolution aberration-corrected TEM [89, 90, 105], where single B vacancies were frequently observed. The binary binding configuration leads to suppression of vacancy migration, while the knock-out of atoms becomes energetically favorable. Under electron beam exposure, the formation of single boron vacancies is feasible, even at a low electron energies of 80 keV. The threshold of atom knock out is quite low for edge atoms at existing vacancy defects. Therefore, with continuing irradiation, large holes of triangular shape appear in h-BN which are composed of three equivalent N-terminated zigzag edges [90, 116]. The remaining sp<sup>2</sup>-lattice is still of perfect crystallinity. As bond reorganization is heavily suppressed, no vacancy reconstruction is found in the h-BN lattice. This indicates an instability of homo-elemental B–B or N–N bonds. A structural amorphization of the h-BN lattice is therefore not feasible [78, 90]. The introduction of vacancies in h-BN monolayers is predicted to form localized defect states within the intrinsic band gap [117].

In MoS<sub>2</sub>, the controlled introduction of S-vacancies was demonstrated by exposure to an Ar plasma [15]. Additionally, few-layer MoS<sub>2</sub> was amorphized using 30 keV He<sup>+</sup> irradiation [118]. It has been reported that ion induced defects in MoS<sub>2</sub> can beneficially alter the electronic properties, giving rise to improved device performance. This is presumably due to the introduction of defects [16], causing a reduction of the contact resistance. Additionally, a phase transition from the stable, semiconducting 2H phase into the meta-stable metallic 1T phase was observed upon weak Ar<sup>+</sup> ion beam exposure [119]. However, this transition is only locally induced, with resulting domain sizes of a few nanometers, and can only be stabilized through point defects.

### 1.4 Growth of supported 2D materials

Andre Geim and Konstantin Novoselov initially used adhesive tape to split graphite into graphene. Exfoliated flakes are deposited on a silicon wafer and crystallites larger than 1 mm, visible to the naked eye, can be obtained [120]. Besides exfoliation, *e.g.*, from highly-oriented pyrolytic graphite (HOPG), CVD growth on catalytically active metal surfaces leads to the formation of well-defined monolayers [121]. CVD synthesis is a common form of epitaxy and a straightforward way to produce high-quality large-area graphene sheets. This growth method is based on the thermal crack-

<sup>3</sup>For highly charged ion irradiation of single-layer Gr Xe<sup>+x</sup>, charge states of q= 20 - 35 were used [113].

<sup>4</sup>Ions with typical kinetic energies in the MeV or GeV range. They have sufficient energy and mass to penetrate solids on a straight line.

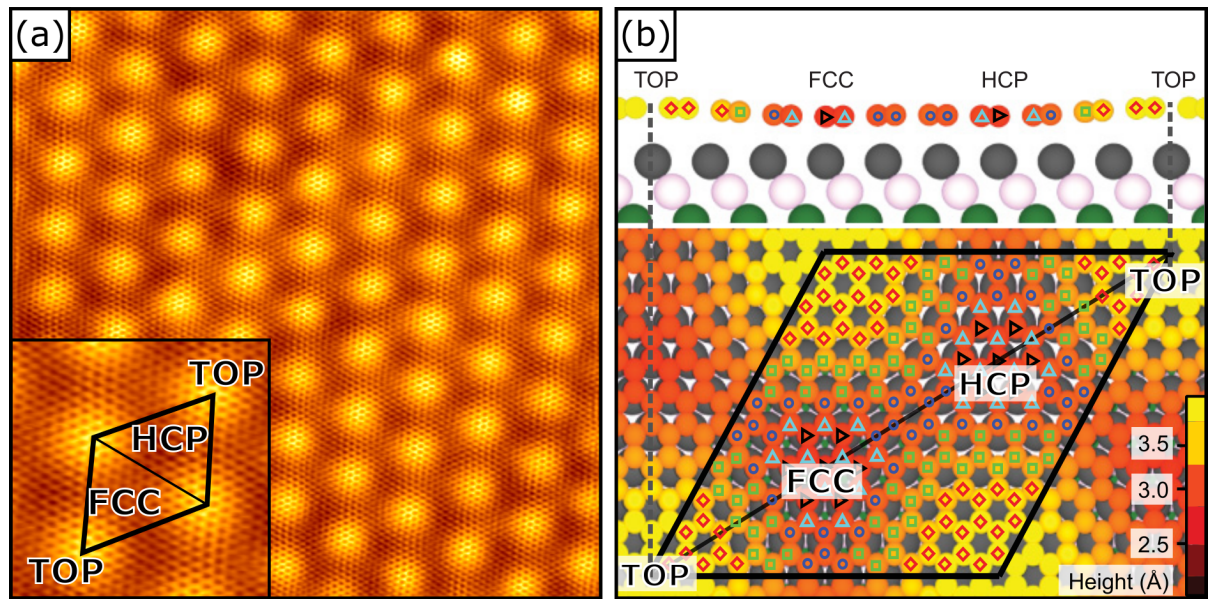


**Figure 1.12:** (a) Atomically resolved STM topographs of Gr on Ir(111). The large topograph shows the moiré lattice of Gr/Ir(111). The inset shows a zoom. Image sizes are 23 nm  $\times$  23 nm and 6 nm  $\times$  6 nm for the inset. (b) Atomic model of the commensurate moiré supercell of (10 $\times$ 10) Gr on (9 $\times$ 9) Ir cells based of DFT calculations. The moiré unit cell is indicated by the black rhombus. The TOP region is located at the edged of the rhombus. The local height differences become apparent from the side view, which is cut plane along the diagonal of the rhombus. The atomic model is reproduced with permission from Ref. [136], © 2012 APS.

ing of gaseous precursors on metal surfaces. Common metal surfaces for graphene growth are Pt(111) [122,123], Ir(111) [124–127], Ni(111) [128,129], Ru(0001) [130,131], Cu(111) [72,132,133], and Rh(111) [134, 135]. When grown on iridium(111), graphene of exceptional quality can be obtained by a combination of a temperature-programmed growth (TPG) step combined with a CVD step, using ethylene (C<sub>2</sub>H<sub>4</sub>) as a precursor. Ethylene decomposes on the surface and the resulting carbon atoms, adsorbed on the surface, form a self-limiting graphene monolayer [124,126,137,138]. The Gr layer is weakly bound to the iridium substrate and, due to a slight mismatch of the lattice constant of Gr and Ir, a moiré superlattice with a periodicity of 25 Å forms [see Figure 1.12(a)]. Within a moiré unit cell the graphene layer is corrugated by about 0.3 Å, due to varying atomic interactions with the underlying substrate atoms<sup>5</sup>. As apparent from Figure 1.12(b), three distinct regions emerge, according to whether the center of the carbon ring is positioned above on top of a surface metal atom (TOP), on the fcc hollow site (FCC), or a hcp hollow site (HCP) of the underlying Ir surface [136, 139]. In the TOP regions the carbon-metal interaction is typically weak and the graphene sheet is the farthest away from the metal surface. In the HCP and FCC sites the carbon atoms are positioned over the surface metal atoms. Here, strong interactions lead to lower adsorption heights of the graphene sheet (valley site). The binding of defects [26, 140], or adsorption

<sup>5</sup>Gr on Pt(111) is also weakly with a small corrugation of <0.5 Å. Ru(0001), Rh(111), and Ni(111) are strong interacting systems with corrugations >1 Å.

of foreign atoms [141–143], clusters [139, 144–146], and molecules [147–153] depend significantly on the position within a moiré unit cell. While the TOP-site is rather non-reactive, metal and non-metal adsorbates are strongly bound within the HCP and FCC region of the moiré [126, 136, 139]. The site selective binding opens a path to produce highly-ordered cluster lattices. As apparent from the LEEM image in Figure 1.13 of Gr/Ir(111), wrinkles are a persistent type of defect on the macroscopic scale in Gr grown by CVD. Wrinkles typically appear in the form of networks with a characteristic separation on the order of  $\mu\text{m}$  [154–156]. They originate from the mismatch of thermal expansion coefficients of substrate and graphene, as the latter displays only a marginal thermal expansion over an extended temperature range [157]. Wrinkles deteriorate the electrical properties of Gr [158, 159], and affect thermal properties of Gr, reducing the thermal conductivity [160–162].

Similar to graphene, single layers of h-BN can be grown by exposing catalytic metal surfaces to borazine ( $\text{B}_3\text{N}_3\text{H}_6$ ). Examples are epitaxial h-BN layers on Rh(111) [163, 164, 164–169], Ru(0001) [170–172], Ni(111) [166, 173–176], Cu(111) [177–181], Pt(111) [166, 182–184], and Ir(111) [185–191]. The CVD growth of h-BN on Ir(111) results in monolayers including two domain orientations rotated by  $180^\circ$  [185]. The two distinct rotational domains emerge from each other by interchanging the locations of B and N atoms. Since their energy difference is small, they typically nucleate with close to equal probability during h-BN growth. A domain boundary forms at the location where two rotational domains touch, which is well recognized in the STM topograph in Figure 1.14(a) (also compare Refs. 175, 185, 190). A slight lattice mismatch of h-BN and Ir results in a moiré superlattice with a periodicity of  $29 \text{ \AA}$  [190]. The h-BN and Ir(111) lattices are aligned with their dense-packed rows. On average  $(11.7 \times 11.7)$  h-BN unit cells rest on  $(10.7 \times 10.7)$  Ir(111) unit cells [190]. A DFT model for the commensurate  $(12 \times 12)$  on  $(11 \times 11)$  moiré supercell is presented in Figure 1.14(b). The valley represents a high symmetry region of the moiré cell where the N atom sits on top of an Ir atom and B atoms in a threefold hollow-site of hcp type (short:  $\text{N}_{\text{top}}\text{B}_{\text{hcp}}$ ) [190, 192]. In the chemisorbed valley region, the separation of the h-BN layer and the Ir(111) substrate is only  $2.2 \text{ \AA}$ , while in the physisorbed mesa<sup>6</sup> it is  $3.7 \text{ \AA}$  [190]. The adsorption distances from the Ir substrate

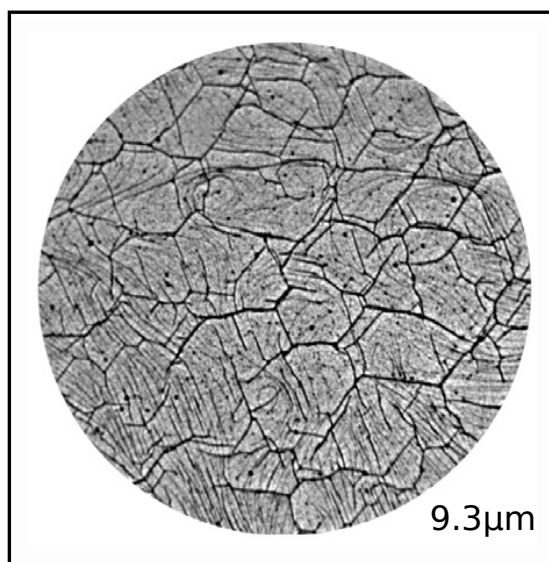


**Figure 1.13:** Low-energy electron microscopy (LEEM) image of Gr on Ir(111). Due to the thermal mismatch of Gr and Ir, excess C is stored within wrinkles in Gr when the sample is cooled down. The wrinkles are visible as dark thick lines, which form extended hexagonal networks. Thin dark lines running from top left to bottom right represent Ir substrate steps. The field of view is  $9.3 \mu\text{m}$ . Reproduced with permission from Ref. [154], © 2015 Elsevier.

<sup>6</sup>Sometimes the flat mesa is referred to as the TOP or WIRE region, but due to the hetero-elemental composition of

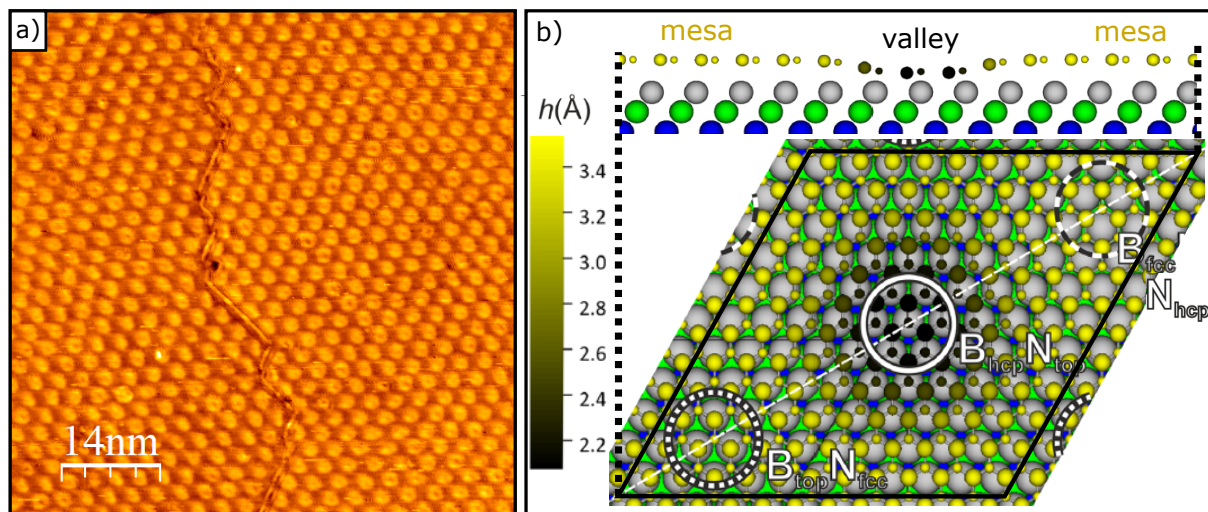


**Figure 1.14:** (a) STM topograph showing the surface morphology of CVD grown h-BN on Ir(111). The periodic moiré superstructure is visible. A grain boundary merges where the two mirrored h-BN domain meet. (b) Atomic model of the commensurate ( $12 \times 12$ ) on ( $11 \times 11$ ) moiré supercell based on DFT. The side view highlights the corrugation. Reproduced with permission from [190], © 2012 ACS.

vary by  $1.55 \text{ \AA}$ , classifying h-BN/Ir(111) as a strongly corrugated system [190, 193]. Compared to Ir(111), the h-BN layers are flat on Cu(111) and Pt(111) surfaces [179, 184], and similar or even stronger corrugated on Ni(111) [194], Rh(111) and Ru(0001) [187, 195]. Also, the moirés of a monolayer h-BN with noble metal surfaces can host regular arrays of molecules [50, 196, 197] and metal clusters [173, 192, 198–201], where the adsorbed species are chemisorbed at the valley site of the moiré cell. Furthermore, h-BN/Ir(111) exhibits a local work function variation within the moiré superstructure, resulting in a bias-dependent contrast inversion of the apparent height corrugation of the moiré in STM images. This inversion is mainly determined by electronic effects, despite the considerable geometric corrugation. Although strongly bound, the valley sites correspond to areas of lowest local work function [189].

Considering MoS<sub>2</sub>, micro-mechanical exfoliation [202] is widely employed to prepare atomic layers. Additionally, CVD enables production of monolayer or few-layer MoS<sub>2</sub> up to the wafer-scale [203]. For the CVD synthesis, molybdenum oxides are reduced to MoS<sub>2</sub> under the flow of S vapor. These methods are *ex-situ* and are lacking cleanliness. In order to get atomically clean surfaces, *in-situ* growth would be necessary. In a different approach, MoS<sub>2</sub> on Au(111) is synthesized under UHV conditions by depositing metallic Mo from an electron-beam evaporator in an ultra-pure H<sub>2</sub>S atmosphere [204]. Although the resulting epitaxy on noble metal surfaces is excellent, the TMDC is significantly influenced by the metal substrates [205]. Recent developments have shown drastic improvements considering cleanliness, defect density, and epitaxy, when growing TMDCs by molecular beam epitaxy (MBE) on an inert substrate [206]. Here, the two reactants, *e.g.* Mo and S,

h-BN, these regions cannot be uniquely identified. Still, the regions with the atomic configuration of B<sub>fcc</sub>N<sub>hcp</sub> and B<sub>top</sub>N<sub>fcc</sub> share very similar chemical behavior and reactivity, which is why they both can be referred to as the flat mesa.

## Chapter 1 Low-energy ion interactions with supported 2D materials

---

are co-evaporated from the vapor phase under UHV conditions onto a Gr/Ir(111) substrate. The resulting TMDC layer is quasi freestanding and the remaining interaction between the forming MoS<sub>2</sub> layer with the substrate is only of van der Waals-type.

### 1.5 Ion interactions with 2D materials supported by a substrate

As most of the irradiation studies shown before were carried out on freestanding 2D sheets, the influence of a substrate on the defect structure was largely ignored. However, as large scale production of 2D sheets becomes more and more feasible on catalytic metal surfaces, the investigation of ion-induced damage and their thermal annealing of 2D sheets supported by a metal substrate is of high interest. It has been shown that the morphology and electronic signature of the defects are altered when a substrate comes into play. The creation of defects upon low-energy ion irradiation of supported graphene has been widely studied [207, 208]. While for weak interacting substrates such as Gr on HOPG, the substrate effect is negligible [209], metal supports such as Ir(111) and Pt(111) induce fundamental changes. For instance, the metal substrate surface atoms stabilize vacancy type defects by saturating created dangling bonds of the 2D sheet [26]. Consequently, the entire adhesion of the graphene layer with the metal substrate strongly increases when single C vacancies are introduced. By making extensive use of the underlying substrate, a controlled structuring of graphene becomes possible. Additionally, the presence of a support enables defect modeling via guided thermal annealing. Standop *et al.* implemented a new route towards the fabrication of a graphene nanomesh by ion irradiation of Gr supported by Ir(111) [26]. Small vacancy defects within a largely destroyed Gr sheet resting on Ir(111), detach during annealing from their preferential binding sites and aggregate to large vacancy islands [29]. The resulting Gr is nearly defect free. This process shows that 2D materials have a remarkable self-healing capability, activated by the catalytic substrate. More findings in the field of ion irradiation of supported Gr was interface channeling [26]; damage evolution with ion energy [112]; and sputter protection of the substrate through a Gr cover [28].

Moreover, it has been shown that supported 2D sheets exposed to noble gas irradiation with kinetic energies in range of a few keV, exhibit a remarkable trapping capability over a large ion fluence and temperature range. Examples are the trapping of single noble gas ions under Gr on Ru(0001) [210] or the formation of highly pressurized gas blisters under Gr on Pt(111) [211], Ir(111) [29, 212, 213], Ir(100) [214], and Ni(111) [30, 215] upon annealing subsequent to noble gas implantation. In these studies, room-temperature irradiated Gr demonstrated a remarkable ability to self-repair upon annealing, which one might relate to the flexible bond reorganization in this material. Upon irradiation at very low energies of h-BN on Rh(111) and their annealing [216–219] a stable trapping of single Ar atoms was found, complemented by the theoretical modeling of Iannuzzi [220]. Ar atoms are trapped underneath the h-BN cover on Rh(111), becoming mobile and aggregating to small blisters upon annealing, while created vacancies assemble at a specific location of the moiré. Additionally, the formation of small cut-out flakes after annealing to 900 K was observed, appearing as bright bumps in STM [216].



## CHAPTER 2

# Experimental methods

The experimental methods used in this thesis are STM/STS, low-energy electron diffraction (LEED), X-ray photoelectron spectroscopy (XPS), Raman spectroscopy, and photoluminescence spectroscopy (PL). For theoretical modeling molecular dynamics (MD) simulations and density functional theory (DFT) calculation were used.

### 2.1 Scanning tunnelling microscopy

The STM is a surface science tool used to produce real space images of a surface down to the atomic scale using the quantum mechanical tunneling effect. It was developed in 1980s by Gerd Binnig and Heinrich Rohrer, who were honored for their invention with the Noble Prize in Physics in 1986 [221]. The operational principle of the technique is to scan the surface with a probing tip and measure the local topography and electronic structure. The atomically sharp tip is placed in close distance ( $\sim 5 - 10 \text{ \AA}$ ) to the probed surface so that the wave functions of the closest tip atom and surface atom overlap. When a tunneling bias voltage  $U$  is applied between tip and surface, a tunneling current  $I$  will flow through the gap, depending exponentially on the tip-surface distance  $d$ . The tunneling barrier height is determined by the work functions of tip and sample. Typically, changing the distance  $d$  by  $1 \text{ \AA}$  changes the conductivity by an order of magnitude, indicating the extremely high vertical resolution. The lateral resolution is determined by the fact that about 90 % of the current flows through the the "last" atom of the tip and the closest atom of the surface, with which separations down to  $2 \text{ \AA}$  can be resolved. Using a piezodrive, the height of the tip ( $z$ ) and its lateral position ( $x, y$ ) can be precisely controlled. An equilibrium current that defines the  $z$ -position is established through the feedback loop. As the tip scans over the  $xy$ -plane, a 2D array of  $z$ -positions, representing the topographic image, is obtained. However, it should be noted that STM is primarily sensitive to the convolution of the local density of electronic states (LDOS) of tip and sample ( $\rho_t, \rho_s$ ) rather than atomic positions. The tunneling current  $I$  is given by

$$I \propto \int_{-\infty}^{+\infty} |M|^2 [f(E - eU) - f(E)] \rho_s(E_F - eU) \rho_t(E_F) dE \quad (2.1)$$

## Chapter 2 Experimental methods

---

where  $f(E)$  is the Fermi function and  $M$  the tunnelling matrix element [222]. In a simplified theory<sup>1</sup> [223] this equation can be approximated by

$$I \propto U \rho_t(E_F) \rho_s(\vec{r}_s, E_F - eU) \quad (2.2)$$

where  $\rho_s(\vec{r}_s, E_F - eU)$  is the density of states of the sample surface at the position of the tip. Since the tunneling current is determined by summing over electron states in the energy range set by the bias voltage  $U$ , additional information on the local density of states can be obtained when  $U$  is varied. Either by measuring a set of constant current images of the same surface area for different values and polarities of  $U$ , or by STS, where tunneling current  $I$  versus bias voltage  $U$  is scanned at a fixed pixel. For the measured  $I$ - $U$  (also  $I$ - $V$ ) curves, one can calculate  $(dI/dU)/(I/U)$ , which corresponds to the density of states of the sample. Equation 2.2 shows that the tip LDOS must be known for the measurement to have meaning. However, under the assumption that the tip LDOS is constant, the density of states is directly proportional to the differential conductivity by

$$\frac{dI}{dU} \propto \rho_s(\vec{r}_s, E_F - eU). \quad (2.3)$$

Therefore, STS is a useful tool to probe electronic properties of a local area and gain spectroscopic information of an energy gap, band bending, or to distinguish the individual chemical nature of adatoms/molecules at the surface [32].

## 2.2 Low-energy electron diffraction

Diffraction techniques provide a complementary view of the surface structure of a crystal, using elastic scattered waves or particles. The spatial distribution of diffracted beams is related to the crystal structure and the intensity thereof gives information on the atomic arrangement within a unit cell. The diffraction pattern of scattered electrons is directly related to the reciprocal crystal lattice by the Laue condition

$$\mathbf{k} - \mathbf{k}_0 = \mathbf{G}_{hkl} \quad (2.4)$$

where  $\mathbf{k}_0$  is the incidence wave vector and  $\mathbf{G}_{hkl}$  the reciprocal lattice vector. Due to energy conservation, as scattering is elastic,

$$|\mathbf{k}| = |\mathbf{k}_0|. \quad (2.5)$$

---

<sup>1</sup>If the tip wave functions are arbitrarily localized, then the matrix element is simply proportional to the amplitude of  $\rho_s(\psi_\nu)$  at the position  $\vec{r}_0$  of the probe [222].

This diffraction conditions are graphically represented by the Ewald construction. In LEED, a collimated beam of electrons with typical energies of 30-200 eV is accelerated towards the sample surface. The de Broglie wavelength of electrons

$$\lambda = \frac{h}{\sqrt{2mE}}, \quad \lambda[\text{\AA}] = \sqrt{\frac{150}{E(\text{eV})}}, \quad (2.6)$$

that satisfy the diffraction condition with energies of 30-200 eV, is about 1-2 Å, so of the order of interatomic distances. They scatter with a very short mean free path of a few atomic layers. Therefore, the most diffracted intensity stems from the topmost layer of the sample. The sample surface can be considered as a 2D atomic structure, lacking the crystal periodicity in the direction normal to the surface. The Ewald construction modified for diffraction on a 2D crystal is shown in Figure 2.1. The lattice rods correspond to the reciprocal lattice points of the 2D lattice. The reciprocal lattice points along the normal direction become infinitely dense, thus forming the rods. The incidence wave vector  $k_0$  terminates at the lattice rod. The intercepts of the Ewald sphere with the lattice rods define the scattered wave vector  $k$  for diffraction.

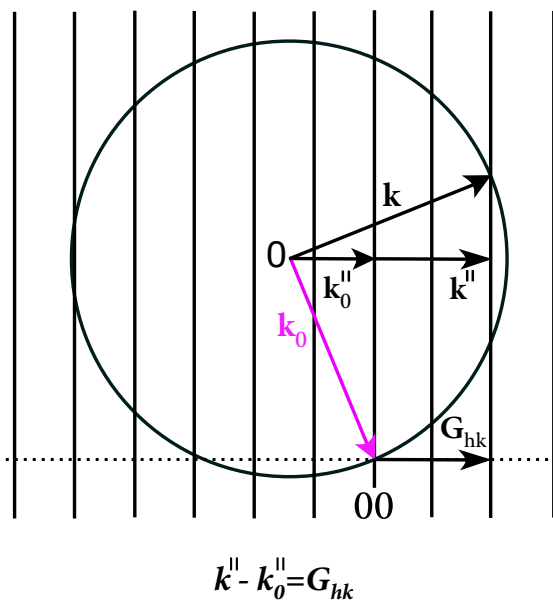


**Figure 2.1:** Ewald construction for diffraction on a 2D surface lattice. Redrawn after Ref. 32.

The resulting diffraction condition in 2D is given in Figure 2.1. It describes the conservation of momentum given by the scattering vector component parallel to the surface,  $(k^{\parallel} - k_0^{\parallel})$ , which must be equal to the 2D surface reciprocal lattice vector  $G_{hk}$ . Finally, elastic scattered electrons are accelerated onto a hemispherical fluorescent screen with the sample at the center of curvature, where the diffraction pattern can be observed. A highly ordered structure gives rise to very sharp and intense diffraction spots, and vice versa, defects and crystallographic imperfection broaden and weaken the spot intensity. The LEED pattern of a threefold rotational symmetric fcc (111) surface is shown in Figure 3.2(a). Here, six spots can be clearly recognized. The reciprocal unit cell vector is indicated. The diameter of the electron beam is about 1 mm<sup>2</sup> and the resulting LEED pattern is thus an average

over a large surface area. An absence of a LEED pattern indicates an amorphous or disordered surface. The reader is referred to Ref. 32 for a more detailed description of LEED.

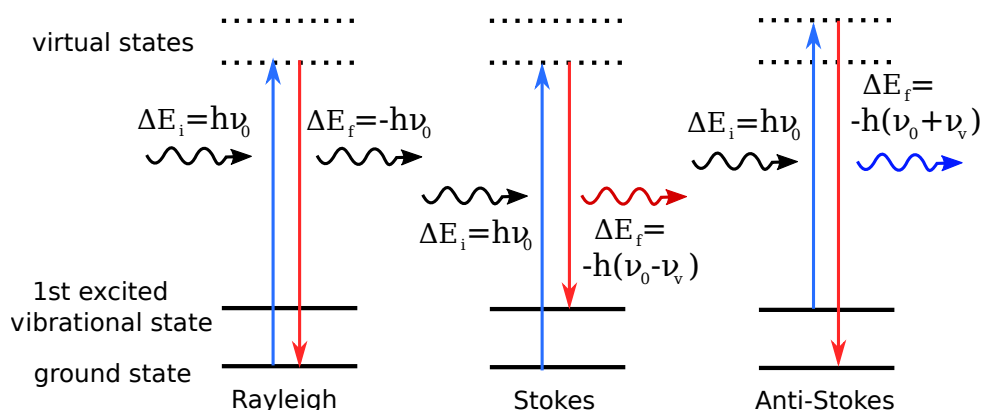


**Figure 2.2:** Schematics for Rayleigh scattering (incident and scattered photons have the same energy), Stokes Raman scattering (scattered photon has less energy, highlighted by red wave) and anti-Stokes Raman scattering (scattered photon has more energy than the incident photon, highlighted by blue wave).

## 2.3 Raman spectroscopy

Raman spectroscopy is a technique to probe vibrational modes or characteristic phonon modes of molecules or solids and is commonly used to provide a chemical fingerprint. It is based on inelastic scattering of photons, also known as Raman scattering. For the work on scattering of light Sir Chandrashekhara V. Raman received the Nobel Prize in Physics in 1930.

In solids, incoming photons are scattered inelastically at the atomic lattice by interacting with phonons, which results in an energy change for the photon. The Raman effect correlates with the polarizability of the material by phonons. The lattice vibrations induce a modulation of the polarizability. Raman scattering involves the excitation of a vibrational mode to a virtual energy level, where the energy difference equals the energy of the exciting laser light. The scattered light is typically collected and dispersed by a spectrograph. The re-emission of the photon can either happen by Raman or Rayleigh scattering (compare Figure 2.2). The final state is higher in vibrational energy in the case of Stokes Raman scattering or lower in the case of anti-Stokes Raman scattering.<sup>2</sup> The re-emitted photon has therefore less energy for Stokes and more energy (anti-Stokes) compared to the initial photon. The energy difference between incoming and scattered light corresponds to the frequency shift  $\Delta\nu$ , or Raman shift. The Raman spectrum shows the intensity of scattered light as a function of  $\Delta\nu$  and is typically given in wavenumbers [ $cm^{-1}$ ], which is directly related to the energy. By analyzing the peak position (frequency) and intensity information can be obtained about the crystallinity and defect density.

<sup>2</sup>As the inelastic scattering probability is by a factor of  $10^3 - 10^4$  smaller than the elastic Rayleigh-scattering, the elastic scattered light will be filtered out during the measurements. Additionally, Raman scattering requires high-intensity laser light.

## 2.4 Photoluminescence spectroscopy

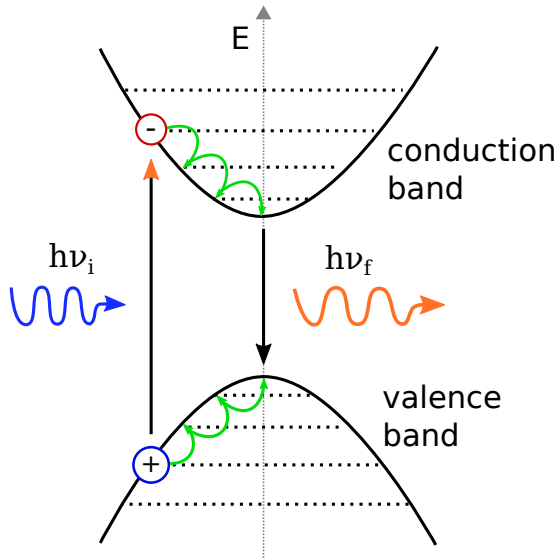


**Figure 2.3:** Schematics of the excitation and relaxation process of photoluminescence at a direct band gap. The incoming light wave (yellow) excites an electron. The relaxation of the electron (hole) via phonons to the top (bottom) of the valence (conduction) band is depicted by the green curve. The radiative recombination is shown by the orange light wave. Redrawn after Ref 224.

In photoluminescence spectroscopy (PL) the emitted light of an investigated material, which was electronically excited by the absorption of a photon, is analyzed and information about the electronic structure of the material can be obtained. It is a highly sensitive method to detect intrinsic or defect related electronic transitions in semiconductors and insulators.

In photoluminescence of a semiconductor, electrons are excited from the valence band to the conduction band by absorbing a photon with energy  $h\nu_i$  larger than the size of the bandgap  $E_g$  (see sketch in Figure 2.3). The excited charge carriers relax non radiatively to the bottom or top of the conduction or valence band, respectively, by interacting with phonons. These electron-hole pairs recombine under the emission of a photon with energy  $h\nu_f \leq E_g$ . This process it is called phosphorescence (long timescales) or fluorescence (short timescales). From Figure 2.3 it is obvious that photoluminescence require a

direct bandgap. The transition from a semiconductor to metal can be nicely observed using PL spectroscopy, as in metals, the electron-hole-pair recombination is purely non-radiatively. Here the emission of phonons is favored since that process is faster than radiative recombination. Typically a laser with enough energy ( $h\nu > E_g$ ) is used to excite the investigated material. The laser light is focused on a cooled sample, stored in cryostat, to obtain sharp PL due to longer lifetimes of the excitons. Finally, the emitted light is analyzed in a dispersive spectograph. For further information about the optical measurement techniques used in this thesis the reader is referred to Ref [225].

## 2.5 X-ray photoelectron spectroscopy

X-ray photoelectron spectroscopy is an analytical technique to probe the electronic structure of occupied states at the surface region of the sample. Based on the photoelectric effect, the electron with binding Energy  $E_B$  absorbs a photon of energy  $\hbar\omega$  and leaves the solid with resulting kinetic energy

$$E_{kin} = \hbar\omega - E_B - \phi, \quad (2.7)$$

## Chapter 2 Experimental methods

---

where  $\phi$  is the work function of the material. For XPS the photon energy is in the range of 100 eV - 10 keV (corresponding to  $\lambda = 100 \text{ \AA} - 1 \text{ \AA}$ ), consequently XPS measures atomic core levels of the investigated material. These core levels appear as sharp peaks in the XPS spectra, with locations defined by the electron binding energies, which are characteristic for the atomic species. Therefore, the XPS spectrum is a fingerprint of the chemical surface composition of the investigated sample. The intensity of a peak is a measure for the amount of a specific element. Additionally, the spectra are highly sensitive to changes in the chemical environment of an element, i.e., depending on chemical bond configuration of an element, the binding energy of the core electron can shift [so called core level shift (CLS)]. Therefore, by investigating shifts in binding energies, bond configurations of the investigated element can be determined. Additionally, with high-energy resolution the fine structure of core levels such as spin-orbit splitting can be well resolved. As XPS also provides information on the chemical fingerprint and bonding configuration it is also called electron spectroscopy for chemical analysis (ESCA). For the development in the field of high-resolution electron spectroscopy the founder Kai M. Siegbahn was awarded the Noble Prize in Physics in 1981.

## CHAPTER 3

# Experimental setups, procedures, and theoretical modeling

The experimental techniques are employed either in ultra-high vacuum<sup>1</sup> setups in Cologne (STM, Raman, PL and LEED) or at the I311 beamline of the Max IV Laboratory in Lund (XPS). This chapter is dedicated to the introduction of the experimental setups, justifying the usage of UHV, as well as providing a detailed description on how to prepare atomically clean crystal surfaces and epitaxially grow 2D materials.

### 3.1 UHV system ATHENE

To gain insight on the atomic level of a solid surface, the surface composition should remain unchanged for the duration of an experiment. Therefore, the rate of reactive species arriving at the surface needs to be low and, thus, vacuum is required. The flux  $I$  of impinging molecules is given by the kinetic theory of gases [32]

$$I = \frac{p}{\sqrt{2\pi mk_B T}}, \quad (3.1)$$

where  $p$  is the pressure,  $m$  the mass of the molecule/atom,  $k_B$  the Boltzmann's constant, and  $T$  the temperature. To ensure that the surface is not covered by foreign species by more than a few percent of a monolayer during the time of the experiment (2 - 3 hours) a base pressure of the UHV chamber around  $1 \times 10^{-10}$  mbar is necessary. Figure 3.1 depicts the schematics of such a UHV system, with a side view (left) and cross sectional view (right) provided. A basic concept of the vacuum system is the gas flow from the chamber to the pump in response of a pressure difference. The base pressure is reached using a combination of a turbomolecular pump (1), an ion getter pump (2), and a titanium sublimation pump (3). During measurements the pressure can be further reduced to  $5 \times 10^{-11}$  mbar by filling a cooling trap (4) with liquid nitrogen. The sample-holder (8), can be transferred into the system via a transfer load lock (6) without sustaining a loss of the vacuum. The sample-holder is

---

<sup>1</sup>Vacuum regimes with pressures lower than  $1 \times 10^{-9}$  are conventionally defined as ultra-high vacuum

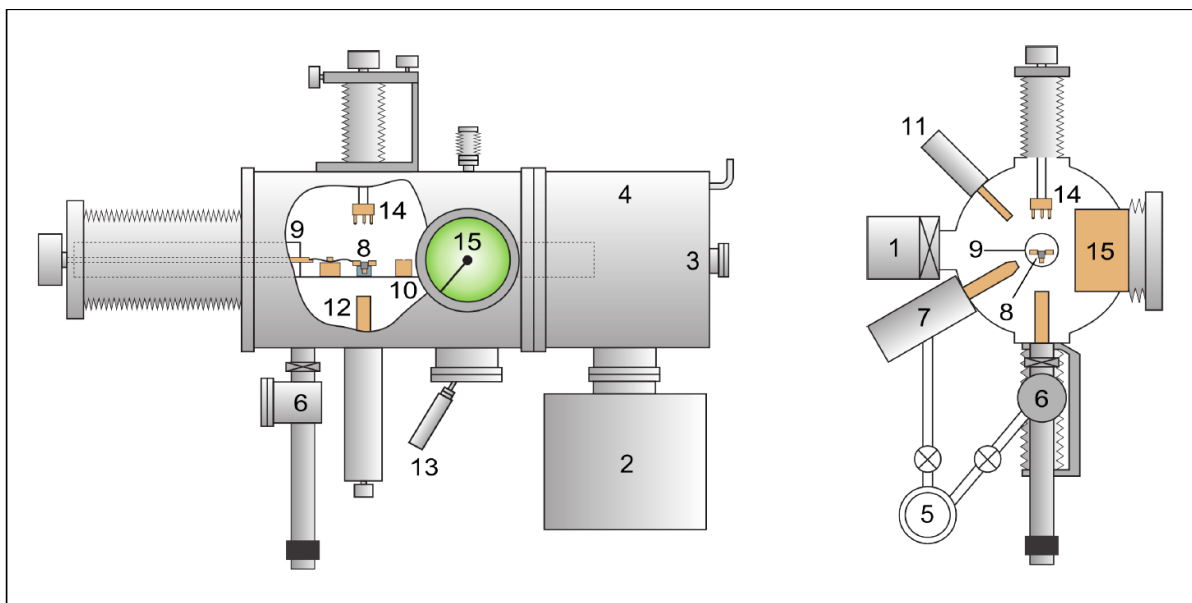


**Figure 3.1:** Sketch of the UHV system ATHENE at the University of Cologne. Side view (left) and cross-sectional view (right) of the chamber. See text for declaration of the numerations. Redrawn after Ref. 226.

placed in the manipulator (9), which is rotatable by  $360^\circ$  and horizontally translatable. Additionally, it provides a built-in heating station through electron bombardment, with which the sample can be heated up to 1600 K. The differentially pumped ion source (7) is used to clean the sample and conduct the ion irradiation experiments. The ion current is measured through a Faraday cup (10). Gases can be supplied onto the sample via different leak valves with dosing tubes, which increase the local pressure at the position of the sample by about a factor of 80. For deposition of high purity foreign species, such as metal atoms, evaporators are used. There, the evaporated material is heated either by electron bombardment (e-beam evaporator [12]) or by direct heating (Knudsen cell [13]). For analyzing the samples the chamber is equipped with a scanning tunneling microscope (14) and a low-energy electron diffraction instrument (15).

### 3.2 X-ray undulator beamline I311 at MAX-LAB

XPS is an analytical technique to probe the binding energies of electrons at the surface region of the sample based on the photoelectric effect. The photon energy is in the range of 100 eV - 10 keV. For the XPS measurements performed during this thesis photon energies in the range of 120 eV up to 860 eV were used. The measurements were performed at the synchrotron MAX IV in Lund (Sweden) at beamline I311. Here, the synchrotron radiation is generated through an undulator, where electrons are forced on sinusoidal path by magnets. The spectrum of an undulator can be tuned by changing the gap between two magnetic arrays. The radiation is monochromized and focused by gratings, mirrors, and X-ray optics. The experimental end-station is used for high resolution photoemission

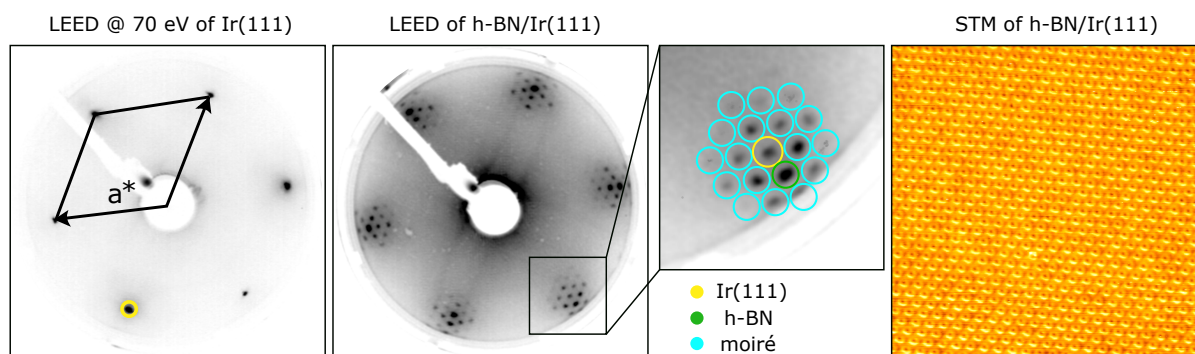


**Figure 3.2:** LEED patterns of Ir(111) and h-BN on Ir(111) of samples as used in this thesis. LEED energy is 70 eV and represents the kinetic energy of the incoming electrons. The diffraction spots are marked by colors depending on their origin, where Ir(111) is highlighted in yellow, h-BN in green, first and second order moiré in cyan. STM topograph shows h-BN/Ir(111) with visible moiré pattern. Image size is 60 nm  $\times$  60 nm.

(XPS) and photo absorption spectroscopy (XAS) on solids, especially on surfaces and interfaces. The experimental chamber consists of separated analyzer and preparation chambers in a vertical mount with base pressures in the range of  $10^{-10}$  mbar. The chambers are accessible via a long-travel manipulator. The preparation chamber includes the usual equipment for sample preparation, such as an ion sputtering gun, a heating station, gas-inlets, and a LEED setup for characterization of the prepared crystal surfaces. A hemispherical electron energy analyzer (SCIENTA-SES200) is used to record the spectra of the photoemission electrons with high resolution [227].

### 3.3 Sample preparation

#### Preparation of Ir(111)

In order to achieve an atomically clean surface, the Ir(111) is prepared *in-situ* before each experiment. Surface contaminants are sputtered off (together with the substrate top layers) by cycles of noble gas ion (in this thesis  $\text{Xe}^+$  and  $\text{Ar}^+$ ) bombardment. Noble gas atoms are admitted through a leak valve into the ion gun, where they are ionized via electron impact and finally accelerated to the desired energy ( $\approx 2 - 4$  keV). As the sample surface degrades through the sputtering process, subsequent annealing is required to restore the surface crystallography and remove implanted noble gas atoms. The sputtering process was performed at room temperature or 970 K and was followed by subsequent annealing steps at 1570 K. Additionally, the sample was frequently processed using a chemical treatment, where the sample is heated *in-situ* at low  $\text{O}_2$  pressures ( $1 \times 10^{-7}$  mbar). The gas reacts with impurities to convert them into weakly bound compounds, *e.g.*, to get rid of carbon (C converts into CO). A LEED pattern of an as prepared Ir(111) sample is shown in Figure 3.2.

### Growth of 2D materials on Ir(111)

A well oriented, closed monolayer of h-BN was grown by exposing Ir(111) to borazine ( $B_3N_3H_6$ ) at a chamber pressure of  $1 \times 10^{-8}$  mbar for 300 s at 1250 K. Through the gas dosing tube the local sample pressure is enhanced by about a factor of 80. The borazine is stored in a glass vial, cooled to 270 K by a water-cooled peltier element. Before each growth step, the borazine was cleaned using freeze and pump cycles directly at the borazine. A typical LEED pattern and STM topograph of this sample is shown in Figure 3.2. The magnified view of the LEED pattern in the inset highlights the substrate (yellow), the h-BN (green), and the moiré reflexes (cyan). The STM topograph shows the typical moiré pattern of h-BN/Ir(111) and depicts the high epitaxial quality and cleanness of the h-BN layer. Single crystal epitaxial Gr was grown on Ir(111) by room temperature exposure to ethylene ( $C_2H_4$ ) till saturation, subsequent thermal decomposition at 1470 K, followed by ethylene exposure through a gas dosing tube at 1220 K [228] for  $\approx 600$  s and with a pressure of  $1 \times 10^{-7}$  mbar measured by a distant ion gauge. This growth procedure leads to a full layer of Gr on Ir(111) of high perfection [137]. However, due to the high temperature during CVD large wrinkle networks form within the Gr layer [155].  $MoS_2$  was grown on Gr/Ir(111) by MBE, following the recipe detailed in Ref. 206. Mo was deposited at 330 K with a flux of  $F_{Mo} = 2.6 \times 10^{16} m^{-2} s^{-1}$  for 500 s, while S was simultaneously sublimated from  $FeS_2$ . The S flux was controlled through the S pressure set to  $\approx 5 \times 10^{-9}$  mbar. Finally, the sample was annealed at 1050 K in a sulfur pressure of  $2.5 \times 10^{-9}$  mbar for 500 s. The resulting  $MoS_2$  coverage was  $\approx 0.70$  ML. The coverage is specified in monolayers (ML), where 1 ML corresponds to full geometrical coverage with a single  $MoS_2$  layer. Single-layer islands of boron related structures (borophene) were grown by dosing borazine at sample temperatures of 1400 K, resulting in the formation of a well oriented h-BN layer. The h-BN is subsequently annealed at 1600 K, where it decomposes into B atoms, which form stable 2D boron structures on the Ir(111) surface. At the same time nitrogen becomes volatile and desorbs from the surface in the form of  $N_2$ .

### Irradiation experiments

For each irradiation experiment the ion flux was adjusted with a Faraday cup moved to the sample position before the sample itself was irradiated. The ion fluence was set by the irradiation time at a given ion flux and is given in monolayer equivalents (MLE), where 1 MLE corresponds to the surface atomic density of Ir(111), *i.e.*,  $1.57 \times 10^{15}$  particles per  $cm^2$ .  $He^+$  and  $Xe^+$  ions were used for irradiation experiments with ion energies from 0.5 keV up to 5 keV. Typically, ion irradiation was performed at normal incidence, except for chapter 5 where  $\theta = 75^\circ$  with respect to the surface normal and if not stated otherwise. The sample temperature during irradiation was held at room temperature, except for chapter 6 where ion irradiation was performed at elevated temperatures ( $\approx 1000$  K), and if not stated otherwise. For the experiments in chapter 5 the projection of the ion beam onto the surface is within  $\pm 5^\circ$  parallel to a dense-packed [110] direction and aligned with the  $MoS_2$  zigzag direction. The ion fluence was set to  $1.5 \times 10^{14}$  ions per  $cm^2$  for 500 eV  $Xe^+$ , *i.e.*, in average 1 out of 7  $MoS_2$  cells is struck by an ion during irradiation.

## 3.4 Sample analysis

### Scanning tunneling microscopy and spectroscopy

STM imaging was conducted at room temperature. A typical sample bias of  $U_b \approx -1.4$  V and tunneling current  $I_t \approx 1$  nA are used. Otherwise, the values are specified for each topograph in the corresponding caption, especially if imaging of the sample is bias sensitive. For spectroscopy,  $I - V$  curves were recorded at room temperature, while the tip was stabilized at a chosen sample position with  $I_{\text{stab}} = 2$  nA and  $U_{\text{stab}} = -2.5$  V. Each given spectrum was averaged over 20 single point spectra. The  $I - V$  curves were numerically derived to obtain the  $dI/dV(E)$  spectra. The STM data were post-processed using WSxM [229] and SPIP.

### X-ray photoelectron spectroscopy

In chapter 4, the XPS measurements were performed at beamline I311, MAX-lab, Lund University [227]. All spectra were recorded at room temperature. The B 1s and N 1s core levels were probed with a photon energy of 284 eV and 500 eV and a total energy resolution of 72 meV and 155 meV, respectively. The Ir 4f spectra were measured with a photon energy of 120 eV with an energy resolution better than 45 meV. Using the software IGOR the XPS data were post-processed with a polynomial background subtraction of 5th order and fitted with Doniach-Šunjić line shapes using the Levenberg-Marquardt minimization algorithm. This function includes an asymmetry parameter and a Lorentzian full width at half maximum (LFWHM) taking electron-hole pair creation and the limited lifetime of the core hole into account. The fitting parameters are listed in Table 4.1 in chapter 4. Binding energies were calibrated to the Fermi edge and normalized to the Ir 4s peak. The Ir 4f spectra were normalized to the Ir 4  $f_{7/2}$  bulk peak.

### Photoluminescence and Raman spectroscopy

In chapter 5, the MoS<sub>2</sub> sample used for PL and Raman spectroscopy was synthesized in a separate UHV system according to the growth recipe outlined above. After synthesis, it was transferred with a vacuum suitcase to the UHV analysis chamber with a base pressure in the  $10^{-10}$  mbar range [230,231]. Characterization by LEED, PL, and Raman spectroscopy was conducted prior and after 500 eV Xe<sup>+</sup> ion irradiation with  $\theta = 75^\circ$ , as well as after annealing of the irradiated sample in S-vapor. PL and Raman spectra were acquired at 10 K using a 532 nm laser. PL spectroscopy was conducted with 6.8 mW laser power to avoid heating, while for Raman spectra we utilized 70 mW for good statistics. The laser was focused with a long-working distance  $\times 50$  objective onto the sample. The energies in Raman and PL spectra were calibrated using the sharp oxygen peak at  $1556 \text{ cm}^{-1}$ , which appears in the spectra due to the part of the laser path outside the vacuum. In chapter 6, we characterize a transferred Gr membrane on SiO<sub>2</sub> by Raman spectroscopy using the 532 nm laser with a power of only 6.8 mW in order to avoid damage. The laser was focused on the Gr/SiO<sub>2</sub> sample *ex situ* at room temperature.

### 3.5 Theoretical modeling

#### Density functional theory calculations

Density functional theory is a computational modelling method used to determine the quantum mechanical ground state of a many-body system by evaluating the spatially dependent electron density. DFT is used to gain insight into the electronic or atomic structure of atoms, molecules, solids, and particular binding energies or bond distances [232]. Contemporary DFT techniques evaluate the electronic structure using a potential acting on the system's electrons. The potentials are solely determined by the structure, the elemental composition of the system, and an effective potential, which defines the inter-electronic interactions. In this way a system with  $n$ -electrons can be evaluated by a set of  $n$  one-electron Schrödinger-equations (Kohn-Sham-theory). For his development of the density functional theory Walter Kohn was awarded with the Nobel Prize in Chemistry in 1998.

In this thesis, *ab initio* calculations, based on DFT [233], have been performed by employing the projector augmented wave method [234] to describe electron-ion interactions as implemented in the VASP code [235–237]. The PAW pseudopotentials used in this study were generated with the Perdew-Burke-Ernzerhof (PBE) exchange-correlation energy functional [238] while the cut-off energy that determines the size of the planewave basis was set to 500 eV. Additionally, the vdW interactions that bind the h-BN islands to the Ir(111) surface were taken into account by using the non-local correlation energy functional vdW-DF2 [239] together with the exchange energy functional developed by Hamada [240]. Furthermore, the relaxed geometries of the h-BN islands/Ir(111) configurations considered in this study were obtained when the calculated forces were smaller than a threshold value of 10 meV/Å. The adsorption energies of the h-BN nanoflakes are the system energy minus the sum of the energies of the Ir(111) slab, the single Xe atoms and the freestanding h-BN nanoflake. Three layers of Ir and a vacuum height of 10 Å were used in the calculations. The VESTA software was used to visualize the atomic models and to determine the inter-atomic distances in the relaxed atomic configurations [241].

#### MD simulations

Molecular dynamics (MD) is a computer based simulation in molecular modelling, where interactions between atoms and molecules and their resulting spatial positions and movement are iteratively calculated, providing a dynamic view of the evolution of the investigated system. Usually, when complex systems with many atoms are considered, semi-empirical methods or force fields are used, and trajectories of particles are determined by numerically solving Newton's equations. The computing time for *ab initio* calculations of such systems would exceed any appropriate limit [242].

In this thesis, analytical potential molecular dynamics simulations were performed to extract the defect production statistics under Xe<sup>+</sup> ion bombardment of MoS<sub>2</sub> supported by graphene on Ir(111) using the LAMMPS [243] code. The defect production of 500 eV Xe<sup>+</sup> is assessed by averaging over at least 380 impact points in the irreducible area [244–246] for each angular configuration. A

modified Stillinger-Weber potential [247] with a smooth transition to the Ziegler-Biersack-Littmark (ZBL) potential [248] for small distances was used for MoS<sub>2</sub>. Interactions of carbon atoms in graphene and iridium atoms were accounted for by Tersoff [249] and the embedded-atom method (EAM) [250] potentials, respectively. An attractive interaction between the layers is modeled by a shallow Lennard-Jones potential (Mo-C, C-Ir interaction only), thereby the interlayer distance is maintained. The repulsive part dominating in high-energetic collisions was taken into account by the ZBL potential for all species. The simulated system consisted of about 12,000 atoms, in a simulation box of  $128 \times 74 \times 26 \text{ \AA}^3$  with periodic boundary conditions in the x-y direction. The supercell consists of graphene [1806 formula units (f.u.)] stacked on three Ir(111) layers (1466 f.u. per layer) forming a Ir(111)/Gr=(9×9)/(10×10) supercell with 0.01 % strain on graphene. On top of that  $42 \times 28$  unit cells of MoS<sub>2</sub> (1176 f.u.) were placed, which yields 0.08 % strain on the MoS<sub>2</sub>. It was checked that for the 500 eV Xe<sup>+</sup> ion under grazing incidence the ion cannot pass the relatively thin substrate. The equations of motion were integrated using an adaptive time step with a maximal size of 0.1 fs and the maximum distance criterion set to 0.001 Å. 50,000 time steps were performed for each ion impact simulation.



## **PART III**

---

# **Results**



## CHAPTER 4

# Annealing of ion-irradiated hexagonal boron nitride on Ir(111)

*This chapter is based on the manuscript published in Phys Rev B **96**, 235410 (2017) and its supplement [251]. It contains contributions from P. Valerius, C. Herbig, M. Will, M. A. Arman, J. Knudsen, V. Caciuc, N. Atodiresei, and T. Michely. The experiments were designed by me together with T. Michely and C. Herbig. I carried out most of the STM, LEED, TDS measurements and data analysis under the guidance of C. Herbig, and wrote the draft of the manuscript with T. Michely. M. Will measured the STM data of Figure 4.5. I did all XPS measurements with assistance from J. Knudsen and M. A. Arman. DFT calculations were provided by V. Caciuc and N. Atodiresei.*

*Section 4.7 are preliminary results in collaboration with M. Petrovic and F. Meyer zu Heringdorf. This work is not yet published, but publication is planned [252]. Experiments were designed by me and M. Petrovic. Data acquisition and analysis was performed by me and P. Bampoulis.*

### 4.1 Motivation

The non-equivalence of the two basis atoms in h-BN forming the  $sp^2$  hybridized honeycomb causes not only a qualitative difference in the electronic structure to Gr, but also influences damage formation and annealing. For freestanding Gr, a variety of defect structures has been observed [79, 80, 90, 105, 110, 253]. Continued electron irradiation of Gr transforms the honeycomb lattice into 2D amorphous carbon. The graphene is still  $sp^2$  bonded, but consists out of a random arrangement of polygons [105]. As discussed above, in h-BN, formation of 5- and 7-membered rings would involve homo-elemental bonds which are unfavorable. This results in a monovacancy migration energy that is substantially larger in freestanding h-BN compared to in Gr [91, 92]. Therefore, damage annealing in h-BN must be assumed to be substantially impaired. In the past few years ion-induced damage and annealing of Gr on a metal substrate has been intensely investigated [26, 26, 28–30, 112, 210–215]. In these studies room temperature irradiated Gr demonstrated a remarkable ability of self-repair. Far less work has been conducted for h-BN grown on a metal substrate, thus a conclusive picture of ion-induced damage and annealing is still missing. Only irradiation at very low energies, just above the displacement

threshold and at extremely low fluences has been conducted for h-BN on Rh(111) [216–218, 220]. These studies found stable trapping of single Ar atoms underneath the h-BN cover and investigated their behavior upon annealing.

To date, a one-to-one comparison of irradiation and annealing of supported h-BN versus Gr, with parameters kept identical, is missing. It would provide insight into whether the large difference found in radiation damage of freestanding h-BN and Gr through TEM studies is also reflected in the radiation damage and annealing of metal supported h-BN and Gr. Thereby insights into the generality of the observed phenomena and the relevance of the substrate in damage formation and annealing within a 2D layer material would be obtained. Here, we present a study that contributes to this goal. We conduct ion irradiation of an epitaxial h-BN monolayer on Ir(111) under the same conditions as used for previous work on ion irradiation of Gr on Ir(111) (see Ref. 29). The similarities in the damage evolution of h-BN and Gr on Ir(111) enabled us to uncover the decisive importance of the substrate and its interaction with the 2D layer for recovery of irradiation damage. However, also striking differences in the reorganization of the 2D materials become apparent: h-BN on Ir(111) recovers in triangular shapes, a fact that is linked to the two non-equivalent atoms in the unit cell of h-BN. Additional remarkable observations are the direct imaging of crystalline Xe in blisters and the finding that tiny vacancy clusters in h-BN on Ir(111) are pinned up to 1300 K to the valley in the moiré of h-BN with its substrate.

## 4.2 Amorphization and recrystallization

### The structure of h-BN/Ir(111)

For reference, Figure 4.1(a) displays the morphology of pristine h-BN after growth. The moiré superlattice has a periodicity of 2.91 nm [190] as recognized in Figure 4.1(a) through the periodicity of the dark valleys. The corrugation between the chemisorbed valleys and physisorbed mesa is about 1.5 Å, much larger than the apparent corrugation measured by STM: The line profile in Figure 4.1(a) depicts an apparent corrugation of at most 0.5 Å. For the insulator h-BN, the STM contrast and corrugation depend strongly on the tunneling parameters, *e.g.*, the valleys can even appear as protrusions [177, 189].

### Morphology of h-BN/Ir(111) after ion irradiation

After h-BN growth, the sample shown in Figure 4.1(a) was exposed to 0.1 MLE 3 keV Xe<sup>+</sup> irradiation at normal incidence and 300 K. Figure 4.1(b) shows an STM topograph of the morphology directly after ion irradiation. The surface is rough, the high density of protrusions and depressions on the nm-scale lead to a total corrugation of 4 Å. No sign of the moiré can be recognized. The roughness is partly due to the damage created in the Ir substrate in consequence of irradiation, *e.g.*, Ir adatoms and surface vacancies (compare Ref. 29). However, a large part of the corrugation must be due to

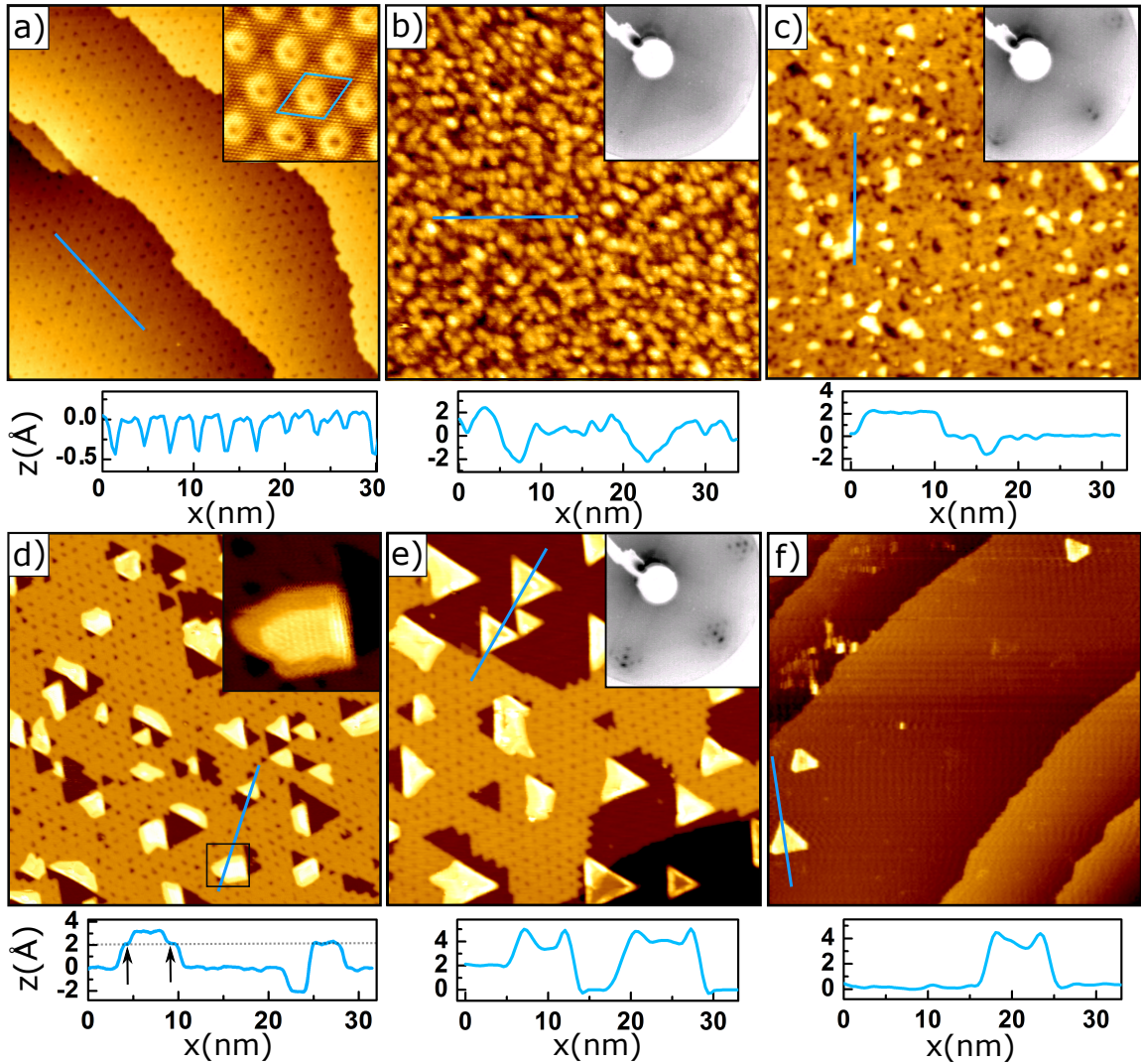


**Figure 4.1:** STM topographs of (a) pristine h-BN/Ir(111), (b) after exposure of the sample in (a) to 0.1 MLE of 3 keV Xe<sup>+</sup> at 300 K, (c) additional annealing at 1000 K, (d) at 1300 K, (e) at 1500 K, and (f) at 1550 K. Height profiles are along the blue lines indicated in the topographs. In (d) and (e) the contrast is chosen to highlight the vacancy clusters and the corrugation in the h-BN layer. The inset in (a) is an atomically resolved zoom-in. The rhomb indicates the moiré unit cell. The insets in (b), (c), and (e) are 68 eV LEED patterns taken after the corresponding annealing step. The inset in (d) is a contrast enhanced zoom-in of the area indicated by the black frame in (d) highlighting a blister with two layers of stacked Xe. Tunneling parameters are (a)  $U_b = -1.97$  V,  $I_t = 1$  nA [inset:  $U_b = +0.2$  V,  $I_t = 1$  nA], (b)  $U_b = -1.21$  V,  $I_t = 0.39$  nA, (c)  $U_b = -1.42$  V,  $I_t = 0.06$  nA, (d)  $U_b = -1.19$  V,  $I_t = 0.09$  nA, (e)  $U_b = -0.91$  V,  $I_t = 0.23$  nA and (f)  $U_b = -1.33$  V,  $I_t = 0.15$  nA. Image size is always 90 nm  $\times$  90 nm. Size of inset in (a) is 12 nm  $\times$  12 nm and in (d) is 16 nm  $\times$  16 nm.

Xe atoms and small assemblies thereof resting underneath h-BN. This statement is based on our X-ray photoelectron spectroscopy experiments that display a huge increase of the Xe 3d signal after irradiation, only when an h-BN cover is present (for more information see Figure 4.3). Because of the substantial fluence of primary ions penetrating the h-BN sheet and the energized Ir recoil atoms

hitting the h-BN sheet from below, it must be assumed that the structural integrity of the h-BN layer is severely disturbed. In fact, the LEED pattern after 0.1 ML 3 keV Xe<sup>+</sup> irradiation shown as inset in Figure 4.1(b) displays almost invisible first-order diffraction spots of the Ir(111) substrate, but none of the h-BN layer. The h-BN layer appears amorphous in LEED.

### Irradiated h-BN/Ir(111) annealed to 1000 K

The sample shown in Figure 4.1(b) was additionally annealed to 1000 K and the resulting morphology is represented in Figure 4.1(c). A well-defined base level appears to be restored, but the moiré is only faintly visible. A large number of protrusions emerges above the base level, of which the larger ones display a flat top with a height of about 2 Å [compare height profile in Figure 4.1(c)]. Also, depressions with a frequent separation of  $\approx 3$  nm are present, a distance reminiscent of the moiré. The larger ones possess a depth of about 2 Å. We interpret the morphology as follows: A flat Ir(111) surface is restored under the h-BN layer after annealing at 1000 K. This happens because Ir adatoms and clusters are mobile well below 1000 K and thus recombine with surface vacancies [26]. We interpret the depressions as vacancy clusters (small, size below 2 nm) and vacancy islands (large, size above 2 nm) within the h-BN layer. The vacancy structures emerge because nitrogen and boron were sputtered during irradiation. As the vacancy islands result from aggregation, their separation and small lateral expansion imply a limited mobility of irradiation-induced vacancies at 1000 K on a length scale of 2 nm. We interpret protrusions as Xe filled blisters at the interface of the h-BN layer and the Ir(111) substrate. The well-defined apparent height of the large blisters indicates a monolayer thickness of the encapsulated Xe. The Xe blisters aggregate from smaller Xe entities present at 300 K, since larger blisters minimize strain and delamination energies in the h-BN [29, 214, 218]. The LEED pattern shown as inset in Figure 4.1(c) displays again first order Ir and h-BN reflexes, indicating the restoration of the substrate and h-BN layer. However, the moiré reflexes are hardly visible, assuming a poor long-range order of the h-BN layer, in agreement with the STM topographies.

### Irradiated h-BN/Ir(111) annealed to 1300 K

The next annealing step takes the sample to 1300 K, and the corresponding morphology is shown in Figure 4.1(d). The STM topograph displays a well-ordered moiré pattern, from which it is evident that the h-BN lattice structure is restored to perfection. The blisters ripened further, as obvious from their number decrease and size increase, with their lateral dimension now being in the order of 5 nm. The blisters tend to display triangular shapes, specifically when adjacent to a vacancy island. Most of the blisters display a two-level structure with apparent heights of 2 Å and 3.5 Å, as shown in the inset of Figure 4.1(d). It shows a zoom-in of the blister in the black box and highlights the two-level structure (also, compare corresponding height profile). Below we provide evidence that the two-level appearance of the blisters is linked to a two-layer structure of the encapsulated Xe.

The vacancy aggregates display a bimodal distribution: Large aggregates – vacancy islands – extend over the area of several moiré unit cells and possess a tendency for triangular shapes. Small

aggregates – vacancy clusters – are pinned to the moiré at the location of the valleys. Vacancy clusters and valleys are not always easy to distinguish, as for smaller vacancy clusters, the blunt STM tip does not reach down to the substrate, resulting in a variety of depths between  $\approx 2 \text{ \AA}$  and  $0.5 \text{ \AA}$ . Nevertheless, the situation is unambiguous for larger vacancy clusters, and a close inspection reveals that about 25 % of the valley locations are indeed populated by a vacancy cluster.

The pinning of vacancy clusters precisely at the location of the valley, as well as their large number are remarkable findings. We interpret them as follows: The configuration of a vacancy cluster at the valley location must be a deep energetic minimum for the lateral position of the vacancy cluster. If not, the energy of vacancy clusters at other locations would not differ much, and consequently, the clusters would be mobile at 1300 K and coalesce with each other. Note that by assuming a standard pre-exponential factor, a temperature of 1300 K is sufficient to overcome activation energies of more than 3 eV on a time scale of seconds. So why does the valley location define such a deep energetic minimum for a vacancy cluster? By removing the core of the valley, the edge atoms of the resulting vacancy cluster still bind strongly to the substrate, as they are chemisorbed to Ir(111). Removing a similar sized vacancy cluster outside the valley region implies weaker edge atom bonds to the substrate, as their original height was about  $3.7 \text{ \AA}$  above Ir, instead of  $2.2 \text{ \AA}$  at the valley location. This makes it energetically costly to bend down to the substrate to form bonds, if bond formation is possible at all. Thus, due to the inferior edge atom bonding to the substrate, vacancy clusters outside the valleys are strongly disfavored. Since the edge atom binding energy to the substrate in a favorable geometry is of the order of 2 eV per atom [190], the enormous stability of the vacancy clusters becomes understandable. We note that similar pinning of vacancy clusters to specific moiré sites was also found for graphene on Ir(111) [26,212]. However, for graphene on Ir(111) the vacancy agglomeration site within the moiré unit cell is not uniquely defined. In fact, the graphene moiré unit cell on Ir(111) has *two* distinct preferential locations for a vacancy cluster, which are both populated.

Image analysis of topographs after annealing at 1300 K, like the one shown in Figure 4.1(d), gives on average for the removed h-BN layer an area fraction of 13.8 %. Assuming this loss to result from sputtering, a joint boron and nitrogen sputtering yield of  $Y_{\text{h-BN,Ir}} = 3.3$  atoms/ion is obtained. This yield is much larger than the yield for 3 keV Xe of freestanding h-BN. It amounts to  $Y_{\text{h-BN,free}} = 1.2$  atoms/ion as estimated from the molecular dynamics data of Lehtinen *et al.* [83]. As there is no sign of h-BN decomposition after annealing at 1300 K, we consider this value – though certainly subject to substantial errors – as a realistic estimate for the yield. Thus,  $Y_{\text{h-BN,Ir}}$  being almost three times larger than  $Y_{\text{h-BN,free}}$  is a remarkable quantitative difference. We attribute this difference to the additional sputtering of h-BN caused by recoiling Ir atoms created in the collision cascade in the substrate and to recoiling primary ions, as it was found for Gr/Ir(111) [254].

### Irradiated h-BN/Ir(111) annealed to 1500 K

The next annealing step is at 1500 K and the resulting morphology is presented in Figure 4.1(e). The most remarkable change is the absence of vacancy clusters pinned to the moiré. Evidently, vacancy clusters dissolved and ripened to large vacancy islands. The moiré does not anymore represent an obstacle for vacancy diffusion. The area of vacancy islands is about twice as large as the summed area of vacancy islands and clusters at 1300 K. This is a first indication for the partial decomposition of the h-BN layer at 1500 K. Blisters ripened also in this annealing step, with a decrease in number and an increase in size. The remaining blisters are mostly triangular in shape. Blisters not bound to the rest of the h-BN layer and bound with their edges only to the Ir(111) substrate (stand-alone blisters) are present within large vacancy islands [compare blisters in the vacancy island in the upper part of Figure 4.1(e)]. As the height profile in Figure 4.1(e) indicates, these blisters are often not uniformly curved outward (negative curvature), but display a depression in their center. This issue will be discussed below in more detail. Remarkably, in the lower right part of Figure 4.1(e) a blister extends over an Ir substrate step. It highlights the flexibility of the blister, which enables efficient trapping of Xe underneath, even when its baseline is not bound to an atomically flat plane. The inset of Figure 4.1(e) displays the LEED pattern after annealing to 1500 K, (indistinguishable from the 1300 K pattern which is not shown). At least two orders of moiré reflexes are visible indicating the perfect long-range order of the h-BN layer. The quality of the LEED patterns is comparable to as grown h-BN on Ir(111) [compare Ref. 190]. This implies the complete recovery of the h-BN lattice and the absence of defects on the length scale of the order of the LEED transfer width of around 10 nm, in perfect agreement with the STM topographs.

### Irradiated h-BN/Ir(111) annealed to 1550 K

The final annealing step of the 3 keV Xe<sup>+</sup> irradiated h-BN/Ir(111) sample is at 1550 K. The STM topograph of Figure 4.1(f) makes plain that the h-BN layer decomposed almost completely during this annealing step, such that bare Ir terraces are present nearly in the entire topograph. Just a few, small stand-alone blisters have survived this thermal treatment. A possible explanation for this finding: As h-BN on Ir decomposes first in the valleys [190], this decay channel is blocked by the Xe filling of the blisters. Direct contact between the h-BN and the Ir substrate is only present at the edges. The Xe filling will strain these edge bonds and make close approach of the B or N edge atoms to the Ir substrate atoms more difficult, thereby diminishing the decay rate. The fact that after annealing at 1550 K the blisters are much smaller than at 1500 K indicates that they are already the result of a shrinking process, presumably due to the loss of h-BN from the blister edges. Irradiation damage and annealing morphology of the h-BN layer – including the phenomena of amorphization, blister formation, vacancy cluster trapping, emergence of stand-alone blisters, and the evolution of triangular shapes – are obtained also for other ion energies and depend only quantitatively on ion energy, fluence, and species. An example for a 500 eV Xe<sup>+</sup> irradiation sequence is provided in Figure 4.8 of chapter 4.5.

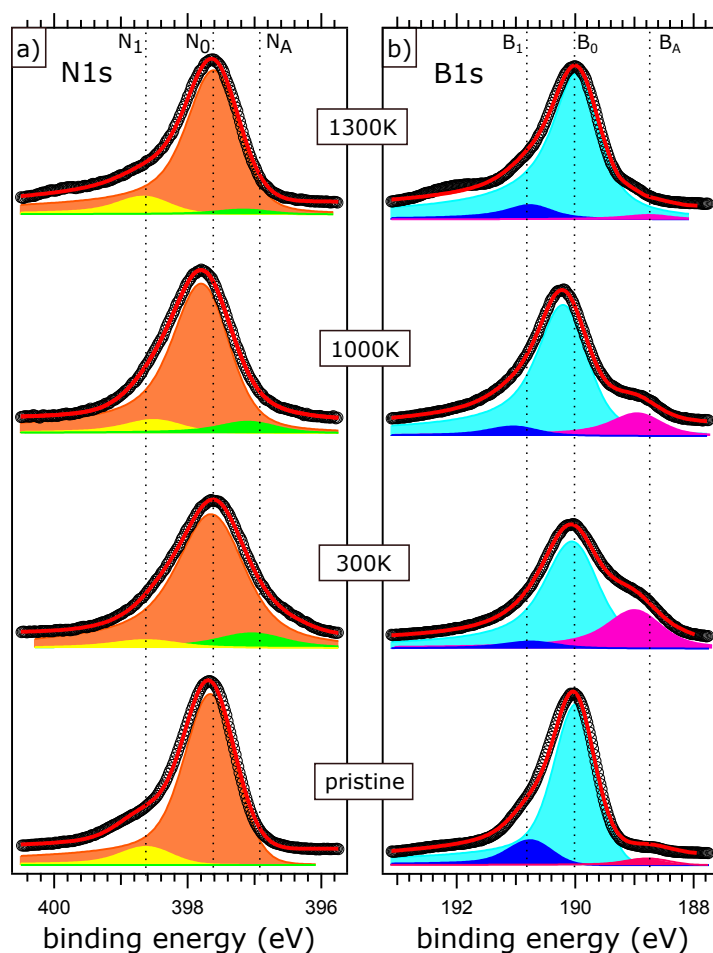


**Figure 4.2:** XPS analysis of the (a) N 1s and (b) B 1s of h-BN on Ir(111) after the exposure to 3 keV  $\text{Xe}^+$  ions at 300 K and subsequent annealing to 1000 K and 1300 K. The associated spectra of pristine h-BN/Ir(111) can be found at the bottom. Binding energies, full width at half maximum and normalized areas of the fit components are given in Table 4.1.

### X-ray photoelectron spectroscopy

To obtain complementary insight into the radiation damage and annealing process, we conducted XPS experiments. XP spectra of N 1s and B 1s core levels of pristine h-BN (lowest spectra), h-BN irradiated at 300 K (second lowest spectra) and h-BN annealed to 1000 K and 1300 K (upper spectra) are displayed in Figure 4.2. Consistent with literature [185, 190], N 1s and B 1s of pristine h-BN on Ir(111) reveal a similar peak structure, each with a main component  $N_0$  or  $B_0$  and a small side component  $N_1$  or  $B_1$  shifted to higher binding energy by about 0.8 eV to 1.0 eV. The two components represent the contributions of B and N physisorbed ( $N_0$  and  $B_0$ ) and chemisorbed in the valley region ( $N_1$  and  $B_1$ ).

The relevant parameters characterizing the components of the B 1s and N 1s XP spectra in Figure 4.3 after 3 keV  $\text{Xe}^+$  irradiation and subsequent annealing are presented in Table 4.1. They

comprise the binding energy, the total full width at half maximum (FWHM), and the normalized area under of each component. Consistent with the literature, we allowed also asymmetric line shapes for the components [185], which in fact gave the best fit results. This relaxation appears reasonable, due to the chemisorption and substantial hybridization of the h-BN with Ir(111), giving rise to a non-negligible density of states of h-BN at the Fermi level [185,190], and due to the multitude of slightly different chemical environments of the atoms within the groups formed by the components [245].

After irradiation at room temperature the two component structure of the two species [ $N_0$  and  $N_1$  as well as  $B_0$  and  $B_1$ ) is essentially lost and the N 1s and B 1s peak is substantially broadened. Evidently, this implies the absence of the moiré with its distinct binding areas. Instead a broad distribution of small chemical shifts, caused by a broad distribution of binding geometries in the heavily damaged layer, is likely. Since the main peaks are not shifted in their position with respect to the pristine case, it is not implausible to assume that the main amount of B and N atoms are still part of a disordered  $sp^2$  network.

New components  $N_A$  and  $B_A$  also emerge at lower binding energy with respect to the main peaks. Consistent with literature, we attribute this intensity to atomic species [185,188,255] detached by energetic collisions from the network, but still bound to the Ir substrate. It is obvious from the spectra in Figure 4.2 that the adatom peak  $N_A$  is less pronounced compared to the adatom peak  $B_A$ . While B atoms are firmly bound to Ir, N atoms detached from the network will be able to combine to  $N_2$  and desorb [256,257], if they are not trapped underneath the damaged sheet, which is apparently the case to a significant extent.

Annealing the sample to 1000 K diminishes the amount of atomic species, narrows the main components  $N_0$  and  $B_0$  and implies a recovery of the chemisorption components  $N_1$  and  $B_1$ . After annealing to 1300 K the spectra are still broadened compared to the pristine case, but the chemisorption components have further recovered and the characteristics for the atomic species  $N_A$  and  $B_A$  have disappeared. In view of the morphology of Figure 4.1(d) and Figure 4.5, the presence of the large number of vacancy clusters pinned to the moiré and the large vacancy islands imply a considerable number of edge atoms and near-edge atoms, which are likely to be the main cause for the residual broadening of the spectra. They could also give rise to the hump around 192 eV in the B 1s spectrum at 1300 K which is not accounted for in our fit by an own component.

**Table 4.1:** Binding energy, total full width at half maximum (FWHM), and normalized area for each component of the XPS spectrum fits in Figure 5 of the manuscript.

core level	T (K)	peak component	FWHM (eV)	binding energy (eV)	normalized area
N1s	pristine	N <sub>0</sub>	0.94	397.6	0.89
		N <sub>1</sub>		398.6	0.11
		N <sub>A</sub>		396.2	0.00
N1s	300	N <sub>0</sub>	1.24	397.6	0.83
		N <sub>1</sub>		398.6	0.06
		N <sub>A</sub>		397.0	0.11
N1s	1000	N <sub>0</sub>	1.04	397.7	0.84
		N <sub>1</sub>		398.5	0.09
		N <sub>A</sub>		397.0	0.07
N1s	1300	N <sub>0</sub>	0.96	397.6	0.86
		N <sub>1</sub>		398.5	0.11
		N <sub>A</sub>		397.1	0.03
B1s	pristine	B <sub>0</sub>	0.99	190.0	0.88
		B <sub>1</sub>		190.7	0.12
		B <sub>A</sub>		188.7	0.00
B1s	300	B <sub>0</sub>	1.11	190.0	0.59
		B <sub>1</sub>		190.7	0.06
		B <sub>A</sub>		188.9	0.35
B1s	1000	B <sub>0</sub>	1.05	190.2	0.76
		B <sub>1</sub>		191.0	0.07
		B <sub>A</sub>		189.0	0.17
B1s	1300	B <sub>0</sub>	1.02	189.9	0.87
		B <sub>1</sub>		190.7	0.09
		B <sub>A</sub>		188.7	0.04

### 4.3 Xe Trapping

A substantial amount of the noble gas ions impinging on a monolayer of h-BN on Ir(111) is trapped underneath the 2D-layer and partly retained there up to very high temperatures. This statement is concluded from our XPS experiments conducted at the XPS beamline I311 of the MAX IV Laboratory in Lund with comparable sample preparation and irradiation conditions as for the STM experiments. The XP spectra were recorded at 300 K and in normal emission with a photon energy of 1000 eV. The total resolution of light and analyzer was better than 400 meV. After polynomial background subtraction, the spectra were normalized to the Ir 4s peak. For reference, we first exposed a bare Ir(111) sample to an ion fluence of 0.1 MLE of 0.5 keV Xe<sup>+</sup> at 300 K and conducted successive annealing at 1000 K and 1300 K [purple spectra in Figure 4.3(a)]. The XP spectra display the Ir 4s core level peak at 690 eV together with the Xe 3d<sub>3/2</sub>/Xe 3d<sub>5/2</sub> doublet at 683.2 eV/669.7 eV,

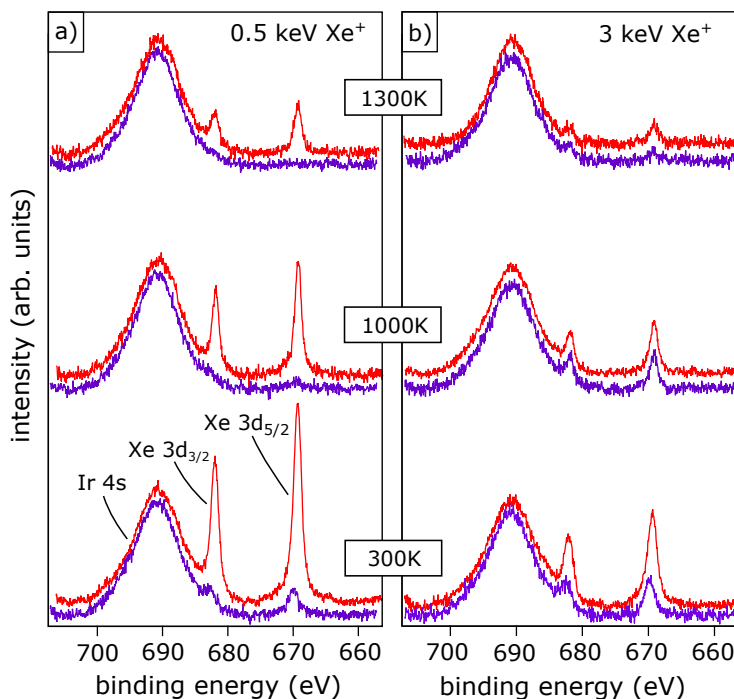


**Figure 4.3:** XP-spectra of the Ir 4s, Xe 3d<sub>3/2</sub> and Xe 3d<sub>5/2</sub> core levels of bare Ir(111) (purple) and h-BN covered Ir(111) (red) after exposure to 0.1 MLE of (a) 0.5 keV Xe<sup>+</sup> and (b) 3.0 keV Xe<sup>+</sup> at room temperature (bottom panels) and subsequent annealing at the indicated temperatures (upper panels).

consistent with the peak positions found in our previous XPS experiments for Xe trapping through Gr/Ir(111) [29]. For better comparison, all spectra were normalized to the Ir 4s peak height.

Since Xe does not adsorb on Ir(111) at 300 K [29], the Xe 3d signal obtained for the bare Ir case [purple bottom spectrum in Figure 4.3(a)] must be attributed to Xe implanted into the metal within the XPS probing depth of about 2.3 nm [258–260]. Upon annealing at 1000 K the Xe 3d signal diminishes and has vanished to good approximation after annealing at 1300 K [middle and top spectra in Figure 4.3(a)]. Consistent with similar studies for noble gas irradiation of other metals [261, 262] and our irradiation studies of Gr/Ir(111) [29], we explain these changes as follows: Upon heating, the Xe diffuses from its capture sites in the crystal bulk to the surface, and finally desorbs into the vacuum, such that barely (1000 K) or no (1300 K) Xe is left in the sample.

The same experiment was repeated, but now with Ir(111) covered by a full monolayer of h-BN resulting in the red spectra of Figure 4.3(a). The result is remarkably different. After Xe bombardment at room temperature, the integrated Xe 3d<sub>5/2</sub> intensity is about a factor of 8 higher than for the uncovered Ir. All additional intensity must thus be due to Xe trapped at the interface of h-BN/Ir(111). Heating the sample to 1000 K decreases the Xe 3d intensity, but still after annealing at 1300 K there is a significant amount of trapped Xe underneath the h-BN cover. In conclusion, the h-BN layer gives rise to efficient noble gas trapping during room temperature irradiation and hinders its release during annealing.

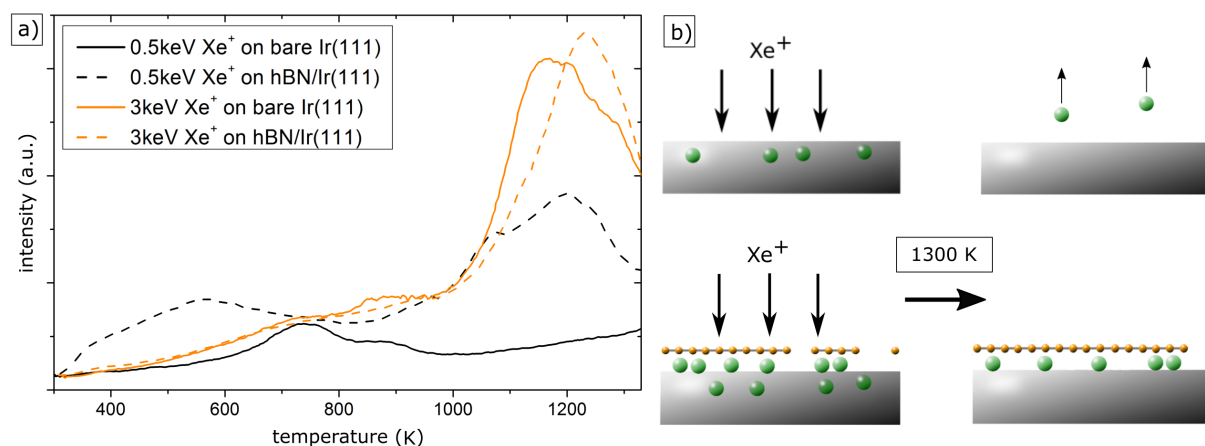


**Figure 4.4:** (a) TDS of Xe (131 amu) after exposure of bare Ir(111) and h-BN/Ir(111) to 0.1 MLE Xe<sup>+</sup> at 300 K. Solid black line: 0.5 keV, bare Ir(111); dashed black line: 0.5 keV, h-BN/Ir(111); solid orange line: 3 keV, bare Ir(111); dashed orange line: 3 keV, h-BN/Ir(111). Heating rate 5K/s. (b) Sketch of trapping and annealing mechanisms of Xe in 500 eV Xe<sup>+</sup> irradiated bare Ir(111) and h-BN/Ir(111).

The situation for 3 keV Xe<sup>+</sup> irradiation, analyzed by precisely the same experiments, is visualized in Figure 4.3(b). More Xe is implanted into the bare Ir sample and more Xe remains in the crystal upon annealing. Molecular dynamics simulations for Xe irradiation of Pt(111) show that by changing from 0.5 keV ions to 3 keV Xe, the implantation probability increases from a marginal value to about 0.4 (see supplement of Ref. 29 for reference). The larger penetration depth of the ions and the more violent collision cascade, producing a substantial amount of subsurface vacancies that stably trap noble gas [261], give rise to the better Xe retention in the Ir crystal after 3 keV irradiation. Moreover, for the 3 keV Xe<sup>+</sup> case, the h-BN cover implies a substantial enhancement of the integrated Xe 3d<sub>5/2</sub> intensity. After room temperature irradiation, the Xe 3d<sub>5/2</sub> peak is larger by about a factor of three compared to bare Ir(111), again indicating trapping of a substantial amount of Xe at the interface. As for the 0.5 keV case, annealing releases some of the trapped Xe, but still after annealing at 1300 K Xe is present under the h-BN cover. The lower trapping efficiency may be rationalized by considering that the 3 keV ions create much more violent collision cascades within the Ir substrate, whereby energized Ir atoms recoiling to the h-BN contribute to damage formation in and sputtering of the h-BN layer. Thereby the cover is more defective and perforated and thus less effective in trapping.

To get complementary insight into the Xe trapping, we conducted thermal desorption spectroscopy (TDS) measurements, as shown in Figure 4.4(a). TDS quantifies Xe leaving the sample after irradiation through thermal activation. The solid black line in Figure 4.4(a) shows the thermal desorption of Xe after 0.5 keV irradiation of bare Ir(111) with similar parameters as used for the XPS experiment. A double-peak structure is seen with peak desorption temperatures of 745 K and 880 K, which is in good agreement to TDS data of Xe<sup>+</sup> irradiated Ir(111) shown by Herbig et al. in Ref 29. Beyond 1000 K, the desorption rate gradually increases up to the end of the heating ramp

at 1330 K. The integrated intensity of Xe after irradiation of h-BN/Ir(111) is strongly enhanced compared to bare Ir. However, the TDS data for h-BN/Ir(111) (dashed black curve) shows that Xe already desorbs below 745 K and the peak positions shift to 1080 K and 1200 K. This confirms the efficient trapping, as more Xe is in the sample. Also, there is a loss of Xe during heating.

The sketch in Figure 4.4(b) is a simplified visualization of the trapping mechanism, and the annealing behavior of bare and h-BN covered Ir after 500 eV Xe<sup>+</sup> ion exposure. Impinging Xe ions are trapped in the Ir bulk. Upon annealing, the Xe atoms diffuse from the bulk to the surface and finally desorb into the vacuum. In the case of h-BN covered Ir, a substantially larger amount of Xe is trapped after ion irradiation at room temperature. The additional Xe is trapped in the interface region of h-BN and Ir. Even after annealing, a considerable amount of Xe is still left in the sample. While the h-BN sheet itself recovers from irradiation damage during the annealing process, it is capable of trapping diffusive Xe at the interface of h-BN/Ir(111). We note that upon 3 keV Xe<sup>+</sup> irradiation there is still Xe left in the uncovered sample after annealing to 1300 K.

## 4.4 Blistering and shape evolution

### Shape evolution and step edges

One of the most remarkable features in the erosion morphology of h-BN/Ir(111) is the evolution of pronounced triangular shapes, which we will attribute in the following to result from the energetic preference of a specific step edge type. The topograph represented by Figure 4.5(a) highlights the morphology after annealing at 1300 K on a larger scale and in more detail. Several interesting features are observable: (i) Blisters and vacancy islands display a strong preference for triangular shapes. (ii) The edges of triangular blisters and vacancy islands are parallel to the dense-packed  $[1\bar{1}0]$  directions of Ir(111) [compare white arrow in Figure 4.5(a)]. (iii) There is a vertical dark band in the middle of the topograph, which is a vacancy island stripe crossing the image. (iv) Neighboring blisters and vacancy islands tend to have opposing triangular orientations, *i.e.*, the triangular shapes of blisters and vacancy islands are rotated by 180° with respect to each other [compare also Figure 4.5(b) and (c)]. (v) Left and right of the vacancy island stripe the orientations of triangular blisters are rotated by 180° with respect to each other, just as the orientations of triangular vacancy islands. (vi) The most equilateral triangular blister shapes are observed for freestanding blisters surrounded by bare Ir(111), *i.e.*, for blisters disconnected from the h-BN sheet and located in a large vacancy island structure. This feature highlighted by the two zooms is shown in Figure 4.5(b) and (c) [also compare Figure 4.1(e)]. (vii) There is a clear tendency of finding blisters next to vacancy islands and vice versa. The two defect features are apparently correlated to each other.

Since edges in the dense-packed directions of h-BN (zigzag edges) are aligned with the dense-packed substrate directions  $[190]$ , the first two observations (i) and (ii) imply that the edges of h-BN - that formed during annealing - have a strong preference for zigzag edges. This holds for

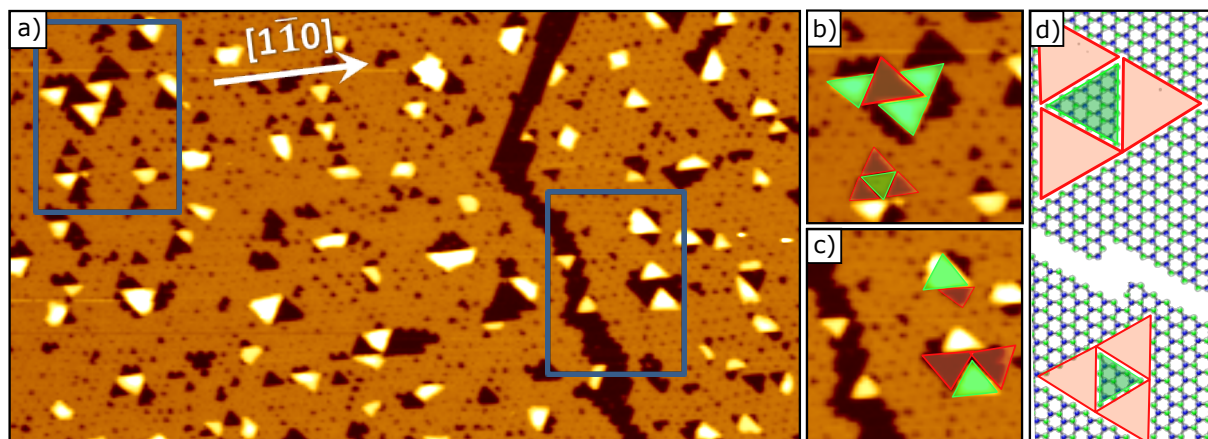


**Figure 4.5:** (a) Large scale STM topograph after 3 keV  $\text{Xe}^+$  bombardment and subsequent annealing at 1300 K. Image size:  $300 \text{ nm} \times 100 \text{ nm}$ ,  $U_b = -1.19 \text{ V}$ ,  $I_t = 0.09 \text{ nA}$ . (b) and (c) show zoom-ins ( $36 \text{ nm} \times 36 \text{ nm}$ ) of the blue boxes in (a). (d) Ball model of the h-BN layer on Ir(111) with vacancy islands, h-BN adatom islands, and a  $180^\circ$  rotational domain boundary (Blue, green, and yellow balls represent nitrogen, boron, and Ir atoms, respectively). Corresponding triangular vacancy structures and small h-BN islands are highlighted with red or green triangles, respectively. See text.

blisters as well as vacancy island edges. The vertical dark stripe separating Figure 4.5(a) in two parts [observation (iii)] is indicating the former position of a rotational domain boundary [175, 186, 190]. The internal structure of a domain boundary between two opposite domains is an intriguing problem that is not yet solved. Evidently, it is a high energy defect and thus, similar to an existing h-BN island edge, a sink for migrating vacancies. As we never observed such vacancy stripes after irradiation at room temperature, we conclude that during annealing vacancies precipitate at the domain boundary and thereby form a vacancy island stripe.

Through DFT calculations, Farwick zum Hagen *et al.* [190] identified that the boron terminated h-BN zigzag step edge on Ir(111) is preferred in energy compared to the N terminated zigzag edge. Therefore, it can be expected that all step edges forming the triangular structures are boron terminated. Considering this, the triangular shapes forming blisters and vacancy islands must be rotated by  $180^\circ$ , as observed in (iv). Likewise, this also implies that the shapes of blisters in the two different rotational domains are rotated by  $180^\circ$ , as derived by observation (v). The same holds for the shapes of vacancy islands. Since the triangular shapes are driven by step edge energy minimization, it is clear that blisters do not display a triangular shape when located within the h-BN sheet. The triangular shape is observed only for blisters in contact with h-BN step edges and is better developed, the less contact the blister has with the surrounding h-BN sheet. This explains observation (vi). Finally, the tendency for a positional correlation of blisters and vacancy island edges [observation(vii)] is not as straightforward to understand, as the other features. The explanation starts with the observation that a line profile through a blister within the h-BN plane needs to start from zero slope, curves away from its base (positive curvature), changes the sign of

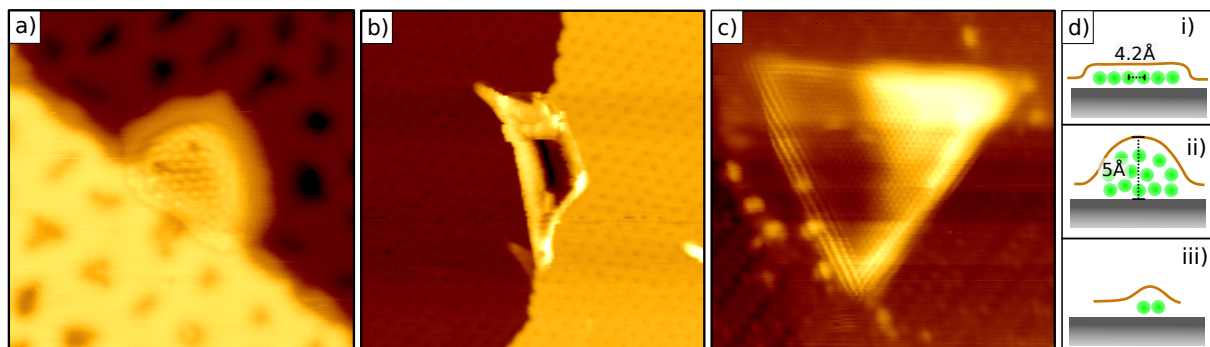


**Figure 4.6:** Typically sized blister after 500 eV ion beam exposure of h-BN/Ir(111) and annealing to (a) 1000 K, (b) 1500 K, and (c) 1600 K. Image sizes are (a) 16 nm × 16 nm, (b) 50 nm × 50 nm, and (c) 12 nm × 12 nm.

curvature at the protrusion top (negative curvature) and must turn to positive curvature again to match the zero slope of the h-BN plane on the other side. In contrast, when a blister is bound to an island edge, the need to merge the blister with zero slope into the h-BN layer is lifted. An h-BN edge may bind with non-zero slope to the Ir substrate. This is even likely to be energetically favorable, as for an inclined h-BN sheet less bond deformation is necessary to match the dangling  $sp^2$  edge bonds to the substrate. The need for bending with positive curvature next to the base of the protrusion is released and consequently bending energy is saved. We thus assume blisters are present preferentially at vacancy island edges, because their deformation energy is lower as compared to blisters of same volume, but entirely within the h-BN plane.

### Xe filled blisters and Xe nano-crystals

For blisters formed in consequence of noble gas irradiation of Gr, it has been proposed several times that these blisters are pressurized [29, 30, 214, 215]. Zamborlini *et al.* [214] and Larciprete *et al.* [30] even proposed solid Ar in Gr blisters on a metal substrate, when at room temperature. This inference was based on estimates of the pressure inside the blister. Here we will provide direct evidence for the solid state of Xe in blisters at room temperature. The size of the blister is changing, *e.g.*, by a ripening process if the sample is annealed to higher temperatures. Figure 4.6(a-c) presents high-resolution STM topographs of typically sized Xe filled blisters for annealing temperatures of 1000 K, 1500 K and 1600 K, respectively. In 4.6(a) solid Xe is imaged through the h-BN layer. Such atomic resolution imaging through a 2D-layer cover is by now a standard technique to obtain information on the substrate and intercalation layers [263–266]. Figure 4.6(a) displays flat blisters after 0.5 keV irradiation and subsequent annealing at 1000 K. Their height is  $\approx 2 \text{ \AA}$ . An additional hexagonal superstructure [with an average periodicity of  $(4.2 \pm 0.1) \text{ \AA}$ ], aligned to the blister edges is visible. The superstructure is not linked to the h-BN lattice, which would give a periodicity of  $\approx 2.5 \text{ \AA}$ . It is interpreted as a single layer of compressed Xe on Ir(111) [compare sketch (i) in Figure 4.6(d)]. The measured nearest neighbor distance is consistent with a compressed Xe phase. Xe crystallizes as an

fcc crystal with a nearest neighbor distance of 4.384 Å [267] in the crystalline state below 161.7 K at ambient pressures [268]. At 300 K it is only solid for pressures above of 0.5 GPa [269].

We observed the superstructure indicative of solid Xe under a variety of conditions, including also ion exposure at elevated temperature and without additional annealing. Nevertheless, two conditions need to be fulfilled: The blisters possess a certain lateral size enabling the organization of the enclosed Xe – the superstructure is not observed after room temperature irradiation – and the pressure inside the blisters is large enough to crystallize Xe. The large blisters formed after annealing at 1500 K possess a substantially lower pressure, as it will be discussed in more detail below, it is consistent that we were not able to detect a Xe-induced superstructure in them. Figure 4.6(b) displays a large blister, with an increased height of about 5 Å. The areal size increased from about 31 nm<sup>2</sup> to 190 nm<sup>2</sup>. However, as evident from the STM topograph in Fig 4.6(b), the large blister exhibits a deep dip in its center. Since h-BN is a large band-gap insulator, the tunneling current is dominated by the density of states of the Ir(111) surface [189]. Therefore, in constant current mode, and while the STM tip is scanning on top of a large blister, the tip is further away from the Ir surface compared to smaller blisters (compare sketch of Figure 4.6(d)). In order to reach the set current it will push the blister down in its center to get closer to the Ir substrate, resulting in a dark depression.

Figure 4.6(c) highlights a triangular blister after annealing at 1600 K, which is partly laminated to the Ir substrate. The atomically resolved structure with a periodicity of about 2.5 Å corresponds to the h-BN lattice. We assume that at around 1600 K the blisters are fully developed triangles and are purely curved outward (only negative curvature). Their curvature and volume at 1600 K is determined by the quasi-equilibrium between pV-work (to be done upon compression), strain energy (gained upon compression), and adhesion of h-BN to Ir(111) (gained upon relamination associated with compression). Upon cooling, the pressure in the blisters lowers - it would drop by a factor of 5 for an ideal gas - and the energy balance favors relamination to the substrate, until the gain of adhesion energy is again balanced by pV-work done. The drop in pressure causes blister to partly relaminate, leaving the characteristic triangular blister shape still visible [compare sketch (iii) in Figure 4.6(d)].

#### DFT calculations of Xe filled h-BN blisters

To gain insight into the stability and energetics of Xe-filled h-BN blisters sealed to Ir(111), we performed *ab initio* calculations based on DFT. The experimentally observed triangular h-BN blisters of 5-10 nm edge length cannot be simulated from first principles with acceptable computational effort. Therefore the h-BN island investigated in our simulations has an edge length of only  $\approx 20$  Å and it is without a chemisorption valley in its interior. The pristine triangular h-BN island binds to the iridium substrate via its zigzag edges – as experimentally observed. Our previous DFT calculations found the B-termination of the zigzag edge to be energetically strongly preferred over the N-termination [190]. The h-BN island consists of 45 N atoms and 52 B atoms, of which 3 N atoms and 24 B-atoms are located at the edge. As depicted in Figure 4.7(a), the inner B and N atoms are far away from the Ir

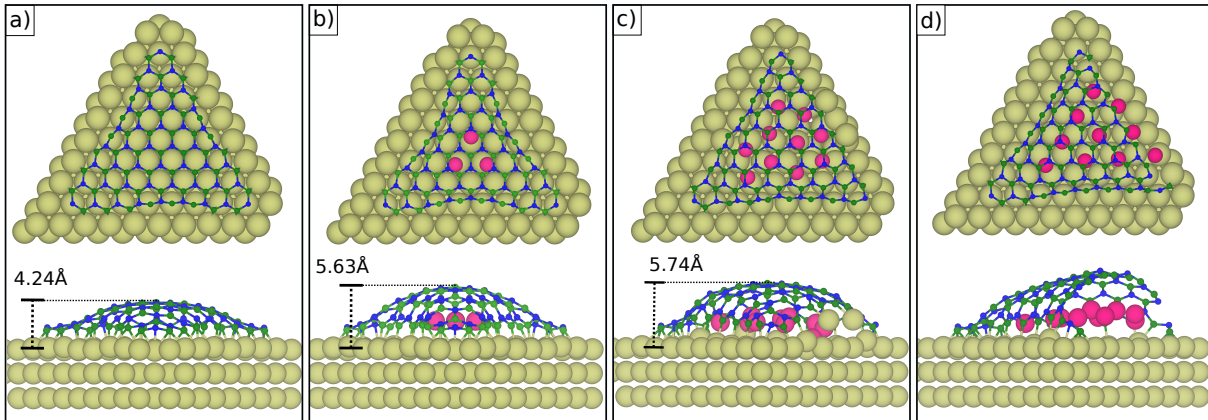


**Figure 4.7:** Ball model representations (top and side view) for the relaxed DFT calculated structures of a triangular, boron terminated h-BN island on Ir(111) without or with intercalated Xe. (a) h-BN island without intercalated Xe. (b) h-BN blister consisting of an h-BN island intercalated by three Xe atoms. (c) same as (b) but intercalated by 10 Xe atoms. (d) same as (c) but intercalated by 13 Xe atoms. Small green balls: B atoms; small, blue balls: N atoms; magenta balls: Xe atoms; large, light green balls: Ir atoms.

substrate (up to  $\approx 4.2 \text{ \AA}$ ) and do not chemically interact with the iridium surface. On the contrary, the edge atoms of the nanoisland are only  $\approx 2.1 \text{ \AA}$  above Ir(111) indicating the formation of strong B(N)-Ir chemical bonds consistent with the large calculated binding energies of  $E_{\text{B-edge}} = -2.0 \text{ eV}$  and  $E_{\text{N-edge}} = -1.6 \text{ eV}$  (see Ref. 190). The large adsorption energy  $E_{\text{ads}} = -58.8 \text{ eV}$  evaluated for the pristine h-BN island on the Ir surface is dominated by the edge bonds, but has also contributions from the energy required to deform the h-BN from its flat isolated geometry and from the van der Waals interaction of inner B and N atoms with the substrate.

In a next step we theoretically investigated the effect of filling the h-BN island with 3 Xe atoms. The resulting blister is shown in Figure 4.7(b). The Xe atoms take positions, which are  $3.64 \text{ \AA}$  apart and consistent with the triangular symmetry of the h-BN island. The calculated adsorption energy of  $E_{\text{ads}} = -56.0 \text{ eV}$  indicates a slightly weaker binding as compared to the pristine case. The reduced magnitude of  $E_{\text{ads}}$  is attributed to the energetic cost of additional deformation of the intercalated h-BN nanoflake and the repulsive interaction between the

Xe atoms. It is important to note that the average distance between the edge atoms and Ir surface atoms is practically the same as in the pristine h-BN nanoflake. The feature underlines the strong bonds between h-BN boron edge atoms and Ir surface ones. Nevertheless, the inner B and N atoms are up to  $\approx 1.4 \text{ \AA}$  further away from the substrate as compared to the pristine nanoisland in order to accommodate the Xe. Based on DFT calculations for the similar case of intercalated Xe penetrating

**Table 4.2:** Calculated adsorption energies and Xe-Xe nearest neighboring distances for the h-BN nanoflakes on Ir, depending on the number of intercalated Xe atoms.

Xe-atoms	$E_{\text{ads}}$ [eV]	Xe-Xe distance [ $\text{\AA}$ ]
0	-58.8	-
3	-56.0	3.644
4	-51.5	3.663
5	-48.1	3.467

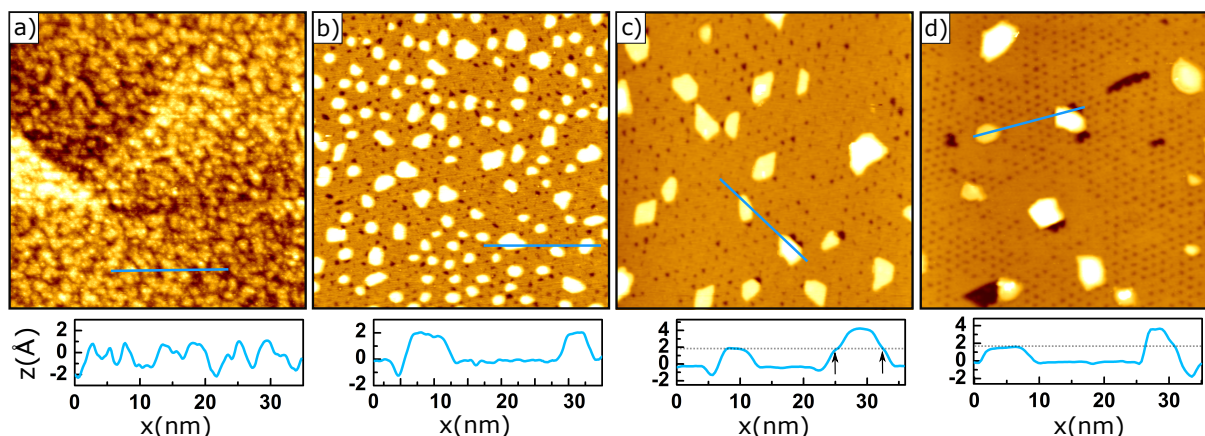


**Figure 4.8:** (a) STM topograph after exposure of h-BN/Ir(111) to 0.1 MLE of 0.5 keV Xe<sup>+</sup> at 300 K and subsequent annealing at (b) 1000 K, (c) 1300 K, and (d) 1500 K. Image size is always 90 nm × 90 nm.

the edge of an adsorbed Gr island [29], two edge bonds must be broken temporarily for the release of one Xe atom. This process requires about 2 eV per bond, or in total an activation energy of about 4 eV. This estimate makes it plausible, why Xe can be retained under h-BN blisters up to the highest annealing temperature of 1550 K.

Intercalation up to 5 Xe atoms under the 97 atom h-BN island hardly changes the overall picture, with the adsorption energy becoming only somewhat less negative (compare table 4.2). When we overfill the h-BN nanoflake with 10 intercalated Xe atoms, Ir atoms are ripped out from the surface layer by the h-BN edge atoms as shown in Figure 4.7(c) implying that the h-BN blister cannot anymore confine the intercalated Xe properly. This effect becomes stronger for 13 intercalated Xe atoms where the edge B atoms start to detach from Ir(111), enabling the escape of Xe atoms (compare Figure 4.7(d)). In conclusion, our calculations for a small h-BN nanoisland with different Xe fillings indicate a very high stability of h-BN blisters and are consistent with highly pressurized Xe, unable to escape even at the highest annealing temperatures.

## 4.5 Low-energy ion irradiation

This section is dedicated to highlight the discrepancies and similarities after ion irradiation of the h-BN covered Ir(111) sample with lower energy ions - 0.5 keV instead of 3 keV Xe<sup>+</sup>. In Figure 4.8 an overview of h-BN/Ir(111) after irradiation at room temperature and its subsequent annealing is shown. Globally, the room temperature 0.5 keV irradiation morphology and its evolution with temperature are rather similar to the 3 keV case. The rough room temperature morphology displayed in Figure 4.8(a) is almost indistinguishable from the 3 keV morphology in Figure 1(b). Just the lateral length scale of the rough sample is somewhat finer, as expected after impingement of lower energy and less violent ions. As shown in Figure 4.8(b), upon annealing at 1000 K blisters of 2 Å height (due to the monolayer Xe incorporated) appear on a flat reestablished base level, just as for the 3 keV

case. In comparison to Figure 1(c) for the 3 keV case, the blisters are larger. In distinction to the 3 keV case, the moiré can already be well recognized again, as the vacancies resulting from sputtering form only small vacancy clusters, which are pinned to the moiré valleys.

After annealing at 1300 K some two layer high blister are present [compare height profile in Figure 4.8(c)], but in distinction to the 3 keV case shown in Figure 1(c), most blisters are still of single-layer height. Annealing to 1500 K, as represented by Figure 4.8(d), leads to a detachment of the vacancy clusters from their pinning sites causing the formation of larger vacancy islands and to blister ripening, similar to the 3 keV case. In contrast to the 3 keV case, at both temperatures blisters do not display triangular shapes and even vacancy islands rarely do [compare Figure 1(d) and (e)]. The two most remarkable differences of the 0.5 keV case compared to the 3 keV one are the much smaller area of vacancy islands resulting at high annealing temperatures and the almost complete absence of triangular shapes.

The smaller area of vacancy islands is a consequence of the lower ion energy, which in turn implies a lower sputtering yield. This is surprising in view of the fact that the calculated yield of 0.5 keV Xe<sup>+</sup> for freestanding h-BN is  $Y_{\text{h-BN,free}} = 1.8$  atoms/ion [83] and thus larger than the calculated 3 keV yield of  $Y_{\text{h-BN,free}} = 1.2$  atoms/ion. This apparent discrepancy resolves when considering that the majority of sputtered boron and nitrogen atoms stems from collisions with recoiling substrate atoms, which are more abundant and higher in energy for the 3 keV case. Moreover, our yield estimate based on image analysis for 0.5 keV of  $Y_{\text{h-BN,Ir}} \approx 0.5$  atoms/ion is also much smaller than the calculated 0.5 keV yield of  $Y_{\text{h-BN,free}} = 1.2$  atoms/ion. As most probable explanation, we consider here that at 0.5 keV the detachment of atoms in forward direction is hampered by the substrate, such that detached atoms are mostly not displaced from the Ir surface, making reincorporation during annealing possible. The absence of triangular shapes in the morphology after 0.5 keV is intimately linked to the smaller eroded amount: As shown before, formation of triangular shapes requires the presence of island edges in the h-BN layer and thus of substantial erosion.

## 4.6 Influence of the substrate upon thermal annealing

### The structure of h-BN/Pt(111)

As apparent from the previous chapters, the substrate plays a crucial role in the annealing behaviour of the 2D material, ultimately enabling recrystallization of an amorphized h-BN sheet. Here, the effect of a different metal substrate will be shortly addressed. Depending on the choice of substrate the strength of interaction varies. For a weak interacting substrate such as Pt(111) the recrystallization process might be hindered [187], or not possible at all. Therefore, a comparable annealing series to chapter 4.2 of Xe<sup>+</sup> irradiated h-BN on Pt(111) is presented in Figure 4.9.

## 4.6 Influence of the substrate upon thermal annealing

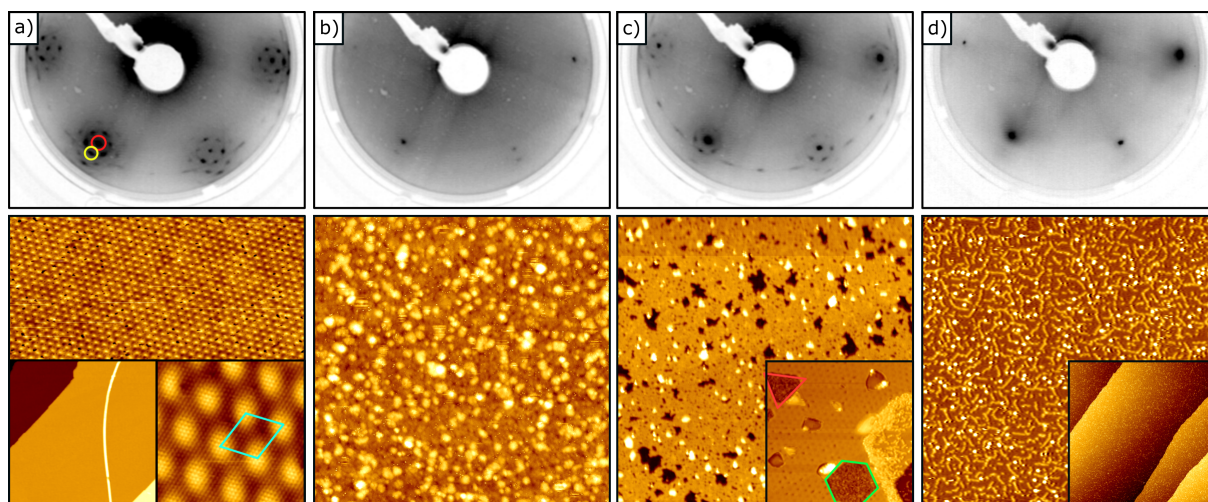


**Figure 4.9:** LEED measurement and STM topographs of (a) pristine h-BN/Pt(111), (b) after exposure to 0.1 MLE of 0.5 keV Xe<sup>+</sup> at 300 K and subsequent annealing at (c) 1200 K, 1300 K [inset in (c)], and (d) 1400 K. Insets show (a) a large scale topograph of same sample; an atomically resolved moiré superlattice; (c) the surface morphology after annealing at 1300 K; (d) a large scale topograph of same sample. Red triangle and green hexagon highlight different vacancy structures. LEED energies are 80 eV and image sizes are 90 nm × 90 nm and for insets in (a) it is 720 nm × 720 nm left and 9 nm × 9 nm right; in (c) 50 nm × 50 nm; in (d) 360 nm × 360 nm.

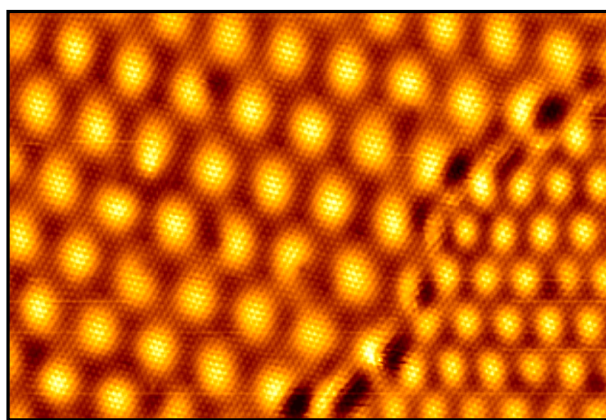


**Figure 4.10:** Atomically resolved STM topograph of h-BN/Pt(111) displaying a domain boundary connecting an aligned h-BN domain and a 15° rotated domain w.r.t. the Pt(111) substrate. Image size is 28 nm × 19 nm

The LEED pattern and morphology of pristine h-BN after growth is shown in Figure 4.9(a). The LEED image shows sharp h-BN spots (yellow) and Pt substrate spots (red) and surrounding moiré satellites up to second-order, indicating a long-range ordered superlattice. Additionally, sharp h-BN reflexes appear at 15° and 30° and circular intensity between 0° and 15° rotation with respect to the Pt(111) substrate spot, indicating the formation of differently oriented domains of the h-BN layer - activated by the weaker substrate interaction compared to Ir(111) [also compare Figure 4.10]. The STM topograph in Figure 4.9(a) shows a well ordered h-BN/Ir(111) moiré lattice of the most common

domain of 0° rotation w.r.t. Pt(111). Small black spots are electronic artifacts due to loss of tunneling current (compare Ref. 182). A zoom-in of the moiré reveals the atomically resolved superlattice with a mean periodicity of about  $a_M = 2.5$  nm. It should be noted that differently oriented domains of h-BN/Pt(111) have different moiré lattice constants, but will not be further addressed in this chapter. Based on the LEED measurement and the atomically resolved STM image, the moiré

## Chapter 4 Annealing of ion-irradiated hexagonal boron nitride on Ir(111)

---

unit cell can be determined. Dividing the distances in reciprocal space of the h-BN and Pt reflexes yields a lattice ratio of about  $\frac{d_{\text{hBN}}}{d_{\text{Pt}}} = 1.11$ , which corresponds to a ratio 10:9 of h-BN to Pt unit cells. Additionally, the atomically resolved STM topograph counts 10 h-BN unit cells per moiré cell with a measured lattice constant of about  $a_{\text{hBN}} = 2.5 \text{ \AA}$ , which is in good agreement with the literature [182, 270, 271]. Furthermore, we observed the formation of wrinkles in h-BN on Pt(111) [compare left inset in Figure 4.9(a)], which are completely absent in h-BN/Ir(111) and is due to the weaker substrate interaction.

### Ion irradiation and annealing of h-BN/Pt(111)

The sample shown in Figure 4.9(a) was exposed to 0.1 MLE 0.5 keV  $\text{Xe}^+$  ions at 300 K. The LEED pattern shown in Figure 4.9(b) displays only weak first-order diffraction spots of h-BN but no moiré satellites. The STM topograph shows a rough surface, with a high density of protrusions as well as depressions on the nm-scale. No moiré superlattice can be recognized. Similar to the previous chapter 4.2, the roughness correlates to the damage created in the Pt substrate in consequence of irradiation, and Xe atoms and small assemblies thereof resting underneath h-BN. Based on the LEED pattern and morphology, we assume that the structural integrity of the h-BN layer is severely disturbed.

The sample shown in Figure 4.9(b) was subsequently annealed to 1200 K, and the resulting morphology is represented in Figure 4.9(c). The LEED pattern displays again first order Ir and h-BN reflexes of rotated domains as well as moiré satellites, indicating the restoration of the substrate, the h-BN layer, and their moiré superlattice. STM topograph reveals a well-defined base level, but the moiré is only faintly visible. Protrusions emerge, which can be correlated to formed gas blisters, as well as depressions, that are interpreted as vacancy clusters and vacancy islands within the h-BN layer. As shown by the inset in Figure 4.9(c), after annealing at 1300 K, vacancy islands agglomerate and grow in size. They exhibit distinct geometric structures of triangular (red) and hexagonal (green) shapes. The revealed Pt surface free of h-BN is covered by a high amount of adsorbates or fractions of decomposed h-BN. The restoration of the h-BN/Pt(111) moiré can now clearly be seen. After the next annealing step at 1400 K, the LEED pattern shown in Figure 4.9(d) does not reveal any h-BN intensity, instead only the Pt substrate spots are clearly visible indicating a complete thermal decomposition of the h-BN layer. The corresponding morphology is shown in the STM topograph below and displays a Pt surface which is largely covered by worm-like structures. We assume that these structures are based on boron rich residuals, which stay on the surface while nitrogen might desorb from the surface in form of  $\text{N}_2$ . The absence of any additional intensity in LEED might be due to a too low coverage or the formation of a  $(1 \times 1)$  isomorphous structure w.r.t. the Pt(111).

## 4.7 Thermal decomposition of h-BN and formation of borophene on Ir(111)

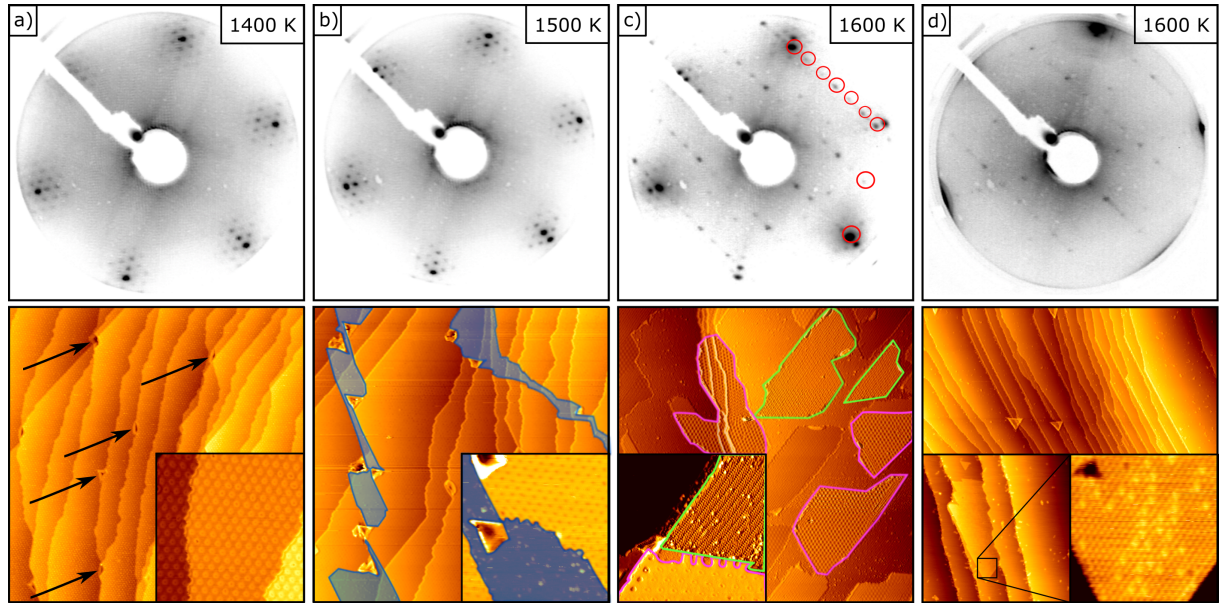


**Figure 4.11:** LEED and STM topographs of h-BN/Ir(111) after (a) growth at 1400 K for 420 s, (b) annealing at 1500 K for 150 s, (c) flash at 1600 K, and (d) 80 s at 1600 K. LEED energies are 78 eV, except for (d) it is 68 eV. Insets show topographs of increased resolution to highlight specific structures of the sample. Some blister are highlighted by black arrows. Vacancy islands are highlighted by a blue color filter. Undisturbed h-BN and stripe-patterned islands are highlighted with pink and green color, respectively. Image sizes are 250 nm  $\times$  250 nm, for insets it is 35 nm  $\times$  35 nm, except for (d) it is 50 nm  $\times$  50 nm left and 5 nm  $\times$  5 nm right.

## 4.7 Thermal decomposition of h-BN and formation of borophene on Ir(111)

As apparent from previous annealing series of irradiated h-BN on Ir(111) in section 4.2 and on Pt(111) in section 4.6, h-BN disintegrates at high annealing temperatures. As for Pt(111), no h-BN was left on the surface after annealing at 1400 K, while h-BN on Ir(111) decomposes only around 1500 K. In this section, we systematically investigate the thermal decomposition of h-BN on Ir(111), by increasing the annealing temperature step-wise until h-BN is completely decomposed. H-BN splits up into boron and nitrogen containing substructures or atoms. While N can easily form  $N_2$  and desorb into vacuum [256,257], B stays on the surface ultimately forming boron-based structures as it was shown in Refs. 251 and 191. As the formation of a boron-phase was already observed at synthesis temperatures of about 1400 K [191], we carried out an h-BN growth step at 1400 K, resulting in the LEED image shown in Figure 4.11(a). The h-BN, Ir substrate, and moiré spots are clearly visible, indicating the formation of well ordered h-BN layer. As opposed to the boron phase observed in Ref. 191, the absence of a superstructure in our data indicates that formation of the boron phase is only locally visible (*e.g.*,  $\mu$ -LEED setup). The corresponding STM topograph shows a closed layer of h-BN, covering the stepped Ir(111) surface area. Additionally, large blisters formed

## Chapter 4 Annealing of ion-irradiated hexagonal boron nitride on Ir(111)

---

due to the high growth temperature (follow black arrows), show a dark interior probably because of the lack of LDOS and the large geometrical separation from the Ir substrate. The blisters have formed without exposing the h-BN layer to Xe irradiation. The trapped Xe stems from implanted Xe in the Ir bulk due to our UHV cleaning procedure. The inset shows a close-up topography of the same sample, revealing a highly ordered moiré superlattice.

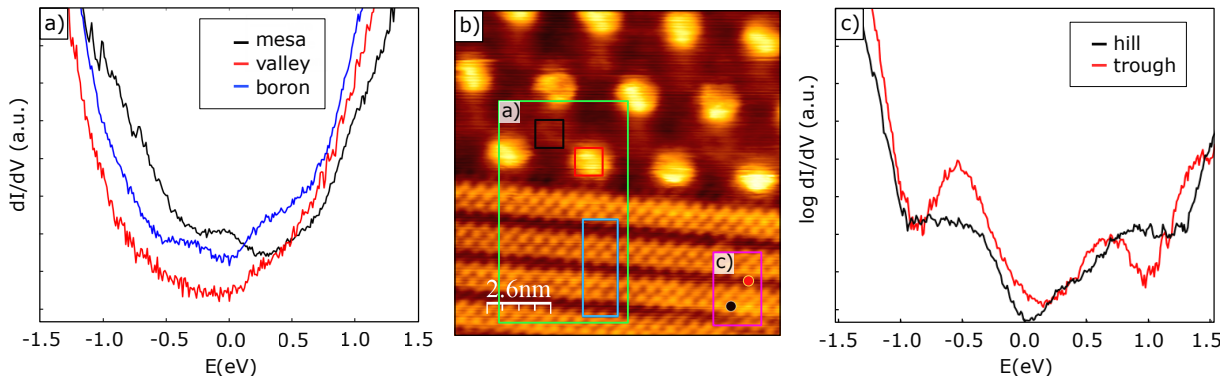
The sample shown in (a) was additionally annealed at 1500 K for 150 s, which resulted in the LEED pattern shown in Figure 4.11(b). Except from a slight increase in intensity of the Ir substrate spot, there are no other visible changes in the LEED pattern. This increase might indicate the onset of thermal decomposition. Indeed, as shown in the STM topograph, large grooves appear in the h-BN layer, revealing areas of bare Ir(111), indicating a disintegration of the h-BN layer. The LEED image in Figure 4.11(c) corresponds to the sample shown in (b), which was flash annealed to 1600 K. Strikingly, additional spots appear which correspond to a  $(6 \times 2)$  superstructure with respect to the Ir substrate (compare red circles). Additionally, the intensity of the moiré satellites has drastically reduced, indicating a further disintegration of the h-BN layer and the formation of a boron phase. Although theoretical studies have examined 2D boron sheets with various boron-based structures, the general class of 2D boron sheets are referred to as borophene [272]. The STM topograph shows various islands, some of which show the typical h-BN/Ir(111) moiré superlattice (pink), some show a striped pattern (green), and others show the coexistence of both. The h-BN flake in the inset shows signs of degradation at its top part, while the striped borophene phase covers the area above. The stripes are interpreted as a 1D moiré with the Ir(111) surface. Based on their measured real space periodicities of 0.53 nm inner row- and 1.48 nm inter-row-distance, the ribbons indeed correspond to the  $(6 \times 2)$  structure found by Petrović *et al.* in consequence of h-BN decomposition on Ir(111) [191] after growth at 1370 K. H-BN decomposition on Ir(111) at the same temperature and the presence of a decomposition related B 1s XPS component was already noticed by Usachov *et al.* [188]. According to the data of Petrović *et al.* [191], the ribbons organize upon cool-down at around 1220 K, either through condensation of B adatoms or segregation of B that dissolved in the selvage after h-BN decomposition. The borophene sheets realized through boron molecular beam epitaxy on Ag(111) display a similar striped appearance as the boron phase observed here, hinting at a similar structure [272, 273].

Figure 4.11(d) presents the LEED pattern after annealing at 1600 K for 80 s. No h-BN diffraction spots are visible, while only intensity at the Ir substrate spots and the  $(6 \times 2)$  boron phase are visible, indicating a complete thermal decomposition of the h-BN layer. The morphology is shown in the corresponding STM topograph. It displays a largely uncovered Ir substrate, sparsely covered with triangular blisters, which survived the annealing process, as Xe filling can act as a thermal buffer layer and prevent the h-BN from decomposition [251]. We note, that the Ir step edges transform into straight step segments, which are decorated by a line approximately 0.5 Å higher than the upper terrace corresponding to the boron phase. The inset left shows a triangular-shaped island with a

#### 4.7 Thermal decomposition of h-BN and formation of borophene on Ir(111)

---

(1×1) superstructure with respect to Ir(111) (compare atomically resolved STM topograph in the right inset), which can be associated with a reconstructed borophene phase [191].



**Figure 4.12:** Scanning tunneling spectroscopy of borophene (a) averaged  $dI/dV$  spectra of h-BN/Ir(111) and the striped boron phase at locations as shown in green box of the STM topograph in (b). The black, red, and blue box mark the flat mesa, valley, and the boron region, respectively. Image size is  $13 \text{ nm} \times 13 \text{ nm}$ . (c) Point spectra of different locations within the boron phase as marked in pink box in (b). Black, and red mark the hill, and the trough region, respectively. STS parameters are in (a)  $U_{\text{stab}}=-2.0 \text{ V}$ ,  $I_{\text{stab}}=0.5 \text{ nA}$  and (c)  $U_{\text{stab}}=-2.0 \text{ V}$ ,  $I_{\text{stab}}=0.5 \text{ nA}$ .

### Borophene phase and properties

Ab initio calculations have predicted stable boron configurations and nanostructures, such as puckered monolayer sheets [274]. The stability of these sheets is enhanced by inducing vacancies [275] or out-of-plane buckling [276]. Borophene is predicted to be metallic [277], or semimetallic [276] and shows anisotropic growth [272, 273] when adsorbed on noble-metal substrates. However, bonding between boron atoms is even more complex than for carbon, resulting in various bulk and 2D allotropes of boron. Due to the large variety of 2D boron allotropes, literature is still lacking insights of the exact structural configurations of the borophene phases. In order to get additional insights in the electronic properties of the borophene phase we, conducted scanning tunneling spectroscopy measurements. As experimentally shown by Mannix *et al.* in Ref [272], borophene on Ag(111) shows clear metallic features, with highly anisotropic conductivity along the chains. Figure 4.12 presents STS data of h-BN and borophene on Ir(111). In Figure 4.12(a)  $dI/dV$  spectra<sup>1</sup> of the regions as marked in the green box in (b) are shown. The red and black curves show spectra of h-BN at the mesa and the valley site, respectively. The red and black curves cross at a positive bias around 0.4 eV, which causes the contrast inversion in STM topographies of h-BN/Ir(111) when changing the bias polarity [189]. As h-BN is a large band-gap insulator with a gap of about 5 eV, all intensity in the  $dI/dV$  spectra recorded on top of the h-BN layer stem from h-BN modulated density of states of the Ir substrate. The blue curve shows an averaged  $dI/dV$  spectrum of the boron phase as marked by the blue box in Figure 4.12(b). The curve exhibits a V-shaped DOS at the Fermi level, with two distinct states located left and right of the Fermi level. The  $\log(dI/dV)$  spectra in Figure 4.12(c) provide additional details on the DOS of the B-phase. Strikingly, the two different regions within the borophene, *i.g.*,

<sup>1</sup>The shown spectra correspond to measured  $I(V)$  point-spectra at room temperature that were averaged over several spectra recorded within the marked areas in Figure 4.12(b). Subsequently, they were numerically differentiated.

## 4.7 Thermal decomposition of h-BN and formation of borophene on Ir(111)

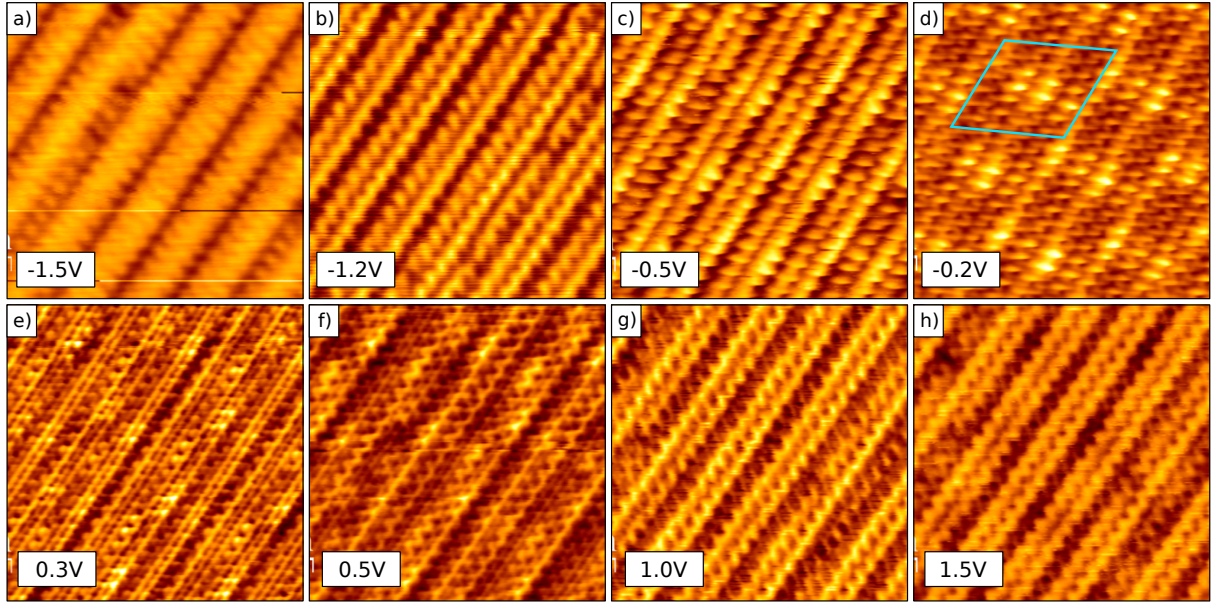


**Figure 4.13:** Tunneling bias dependency of STM topographs of borophene/Ir(111). (a-h) show STM topographs of the same region depending on the tunneling bias  $U_t$ , stated in the respective image. Image sizes are  $14 \text{ nm} \times 14 \text{ nm}$ .

the hill and trough sites [compare red and black dot in the pink box of Figure 4.12(b)], reveal distinct differences in their corresponding DOS. The LDOS of the troughs shows pronounced peaks around  $-0.5 \text{ eV}$ ,  $0.7 \text{ eV}$ , and  $1.3 \text{ eV}$ . The hills show less intensity at  $-0.5 \text{ eV}$  and a peak around  $1 \text{ eV}$ . Note that both regions show finite DOS at  $E_{\text{fermi}}$ , consistent with the superposition between the Ir(111) surface and the predicted filled state population in borophene [272] pointing towards a metallic origin. The clear difference in the DOS through the STS data for different regions within the borophene yields striking transitions in the borophene structure, as shown by STM topographs in Figure 4.13, with changing tunneling biases  $U_t$ . For example, at negative  $U_t$  the borophene shows a dot-like phase (compare upper row of Figure 4.13). For very small  $U_t$  a moiré pattern becomes visible, as marked by the blue box. It resembles the one of the former h-BN/Ir(111) with a slightly smaller periodicity of about  $2.7 \text{ nm}$ . For positive biases the dot-like phase changes into straight line for  $U_t=0.3 \text{ V}$  and sharp zigzag lines for  $U_t=0.5 \text{ V}$  and higher.

To sum up, we have presented the formation of borophene phases upon thermal disintegration of h-BN on Ir(111). The onset of disintegration is around  $1500 \text{ K}$ , where large vacancy islands form at grain boundaries of the h-BN layer. At  $1600 \text{ K}$ , we observe the formation of a  $(6 \times 2)$  superstructure that we attribute to a borophene phase on Ir(111). Additionally, we observe the formation of a  $(1 \times 1)$  superstructure, which corresponds to a second phase of the borophene forming on Ir(111).

### 4.8 Discussion

As outlined in the introduction, upon electron irradiation of freestanding h-BN and Gr, the two materials display a very different damage evolution. When comparing our results for h-BN on Ir(111) to those obtained under the same conditions for Gr on Ir(111) (compare Refs. 26, 29 and related SM), we find the damage evolution to be in several aspects quite similar: (i) Room temperature ion irradiation destroys both materials. Upon annealing they (ii) reestablish their lattice and moiré to perfection, (iii) form highly pressurized blisters that ripen, display a transition from 2D to 3D blisters and a preferred blister attachment to 2D-layer edges, (iv) develop a nanomesh with trapping of vacancies at specific locations of the moiré that is (v) eventually lost by the formation of large vacancy islands. We attribute this fundamental similarity to the strong influence of the substrate on the damage formation and annealing. Both materials form strong bonds between the 2D-layer edges and the substrate, which is the basis (1) to retain and reincorporate detached atoms of N, B, and C into the 2D-layer, (2) to develop a nanomesh through the inhomogeneity of this bonding within the moiré, and (3) to keep the implanted Xe under the 2D-layer by preventing out-diffusion at the 2D-layer edges. The differences in the annealing behavior between h-BN and Gr are:

**(I)** In h-BN vacancy clusters are pinned at a single preferential location, where N atoms are atop of Ir atoms. Whereas in graphene, vacancy clusters are pinned at two locations, the HCP and the FCC areas [26]. **(II)** For h-BN, the ordering of the vacancy clusters is not yet fully achieved at 1000 K, while detachment of vacancy clusters from the moiré already takes place at 1300 K. Therefore, the optimum annealing temperature to prepare a nanomesh in h-BN must lie somewhere inside of this temperature interval. Additional work to determine this temperature is highly desirable to optimize the h-BN nanomesh. For Gr, the ordered positioning of vacancy clusters is optimal at considerable lower temperatures, that is between 850 K and 950 K [26]. It is yet unclear why ordering of clusters in h-BN requires higher temperatures. The dissolution of vacancy clusters as an entity is most likely given through emission of single or double vacancies. We speculate that the higher stability of vacancy clusters may reflect a higher migration barrier of vacancy species for h-BN, because migration in h-BN involves homo-elemental bond formation. For future work, the single pinning location and the high thermal stability of the vacancy clusters in h-BN make the determination of the optimum parameters for creation of an ordered nanomesh without large vacancy islands a very attractive topic. A removal of the nanomesh from the substrate, e.g., through the hydrogen bubbling method [278, 279], would evolve the irradiated and annealed h-BN sheet into a membrane with a very high hole density of about  $1.3 \times 10^{17} \text{ m}^{-2}$  (as defined by the moiré), with narrow size distribution, and sizes below 1 nm. Such a membrane with controllable pore sizes would be well suitable for water desalination or gas filtration [17, 55, 280]. Even on the substrate, it is also worthwhile to explore the templating effect of an ordered array of vacancy clusters in h-BN on Ir(111), *i.e.*, a periodic array of tiny patches of metallic Ir in the insulating h-BN sheet.

**(III)** H-BN on Ir(111) thermally decomposes at an annealing temperature around 1500 K, while for Gr on Ir(111) this is not the case. This difference is closely linked to the inability to grow

high quality h-BN layers above 1300 K [188], while an excellent quality Gr layer can be grown at 1500 K on Ir(111) [281]. The limiting factor for the stability of h-BN is the onset for detachment of B and N species from the sheet, and adatom gas formation at high temperatures. Once present, atomic N on Ir(111) readily recombines to N<sub>2</sub> which desorbs immediately at the temperatures under concern [256]. Thus, no quasi-equilibrium between a 2D gas phase of its constituents and the h-BN layer on Ir(111) can be established. On the contrary, C monomers and small C clusters stably bind to Ir(111) without any chance to desorb [212]. Therefore there is a temperature regime extending beyond the stability range of h-BN, where small adsorbed carbon entities coexist with the Gr sheet. Only at higher temperatures, the onset of noticeable C solubility terminates the stability of Gr on Ir(111) [282, 283]. It is noteworthy that upon h-BN decomposition the remaining B forms 2D structures on Ir(111) [compare Figure 4.11(c,d)]. The fact that we observe stand-alone h-BN blisters at high temperatures is closely linked to the thermal decomposition of h-BN on Ir(111). Stand-alone blisters, though not triangular, were also observed for Gr on Ni(111) by Späth *et al.* [215] and by Larciprete *et al.* [30] under conditions, where the Gr dissolves into the Ni bulk. The stand-alone blisters emerge due to the slower decay rate of the 2D-layer separated by a gas cushion from the substrate. This mechanism may be of general relevance and we speculate that annealing Gr/Ir(111) irradiated by noble gas to temperatures beyond 1500 K, where the dissolution of Gr into the Ir bulk sets in, would also allow to observe stand-alone blisters.

**(IV)** For h-BN, we were able to image the Xe nanocrystals within the blisters after annealing at 1000 K and 1300 K, while no superstructure indicating a solid Xe state could be resolved within Gr blisters. A simple order of magnitude estimate for the pressure inside a blister, neglecting strain effects, is obtained by equating the  $pV$ -work done upon compression with the gained adhesion per unit area  $\gamma$  between h-BN and Ir. This yields  $p = \gamma/h$ , where  $h$  is the height of the blister. Since h-BN adheres more strongly to Ir(111) than to Gr [190], the Xe in an h-BN blister may be under higher pressure, thus crystalline and visible for STM. Though this argument is highly speculative, it is also in line with another difference between blisters under the two materials. H-BN displays also blisters with a two-layer structure, while for Gr flat monolayer blisters directly evolve into curved ones. **(V)** While for h-BN on Ir(111) vacancy islands and blisters display a clear triangular shape, for Gr on Ir(111) the corresponding shapes are less pronounced and mostly hexagonal [29]. For both materials zigzag edges binding to Ir(111) are energetically preferred. However, the hetero-elemental composition reduces the symmetry – B-terminated h-BN edges binding to Ir are strongly preferred – and implies the threefold symmetric shapes for h-BN. This feature is not a unique in consequence of ion erosion on Ir(111), but has also been observed for h-BN growth on Ir(111) or Ni(111) [175, 190]. Also, in TEM – electron irradiation (non-equilibrium conditions) experiments for freestanding h-BN results in triangular shapes [89, 90], but the edges were – for reasons not entirely clear – N-terminated rather than B-terminated. In any case, the threefold symmetric morphology of blisters and vacancy islands, also highlighting just by shape different rotational domains, is an appealing aspect of the irradiation morphology and so far unique to h-BN on a metal.

## Chapter 4 Annealing of ion-irradiated hexagonal boron nitride on Ir(111)

---

The state of the h-BN layer after 0.1 MLE 3 keV Xe<sup>+</sup> irradiation needs a brief additional discussion. Given the large ion dose, the efficient energy deposition in the topmost layers, and a sputtering yield of 6.5 for 3 keV Xe<sup>+</sup> on bare Ir(111) estimated with SRIM [31], we must assume severe damage of the h-BN layer as well as roughening of the underlying Ir(111) substrate. This inference is consistent with the h-BN layer being *LEED amorphous* [no h-BN diffraction spots in the inset of Figure 4.1(b)] and only very faint Ir(111) spots. To the extreme, one might assume to have a melange of B, N, Xe, and Ir atoms at the surface, including the absence of an sp<sup>2</sup> bonded network. Though the XPS N 1s and B 1s peaks substantially broaden upon ion irradiation, it appears that the majority of B and N atoms do not shift into a new chemical state, implying the preservation of the sp<sup>2</sup> bonded network. The presence of an sp<sup>2</sup> bonded network is also suggested by the ability of the sample to trap the impinging Xe efficiently (compare also Figure 4.3) as well as N atoms. The apparent contradiction is resolved when considering the STM data of Figure 4.1(b), which displays a rough surface with a characteristic length scale of a few nm and an RMS roughness of a few Å. Since LEED is not only sensitive to lateral disorder, but also vertical disorder, the absence of the h-BN diffraction spots does not imply the absence of a disordered sp<sup>2</sup> bonded h-BN network. Though a precise characterization of the h-BN/Ir(111) system after irradiation is close to impossible, the data presented here appear to be consistent with a disordered and defective primarily sp<sup>2</sup> bonded network, which covers atomic species of Xe, N, B, and Ir. The preserved sp<sup>2</sup> network with strong edge bonds to Ir, makes plausible that the h-BN layer can recover without the entire loss of nitrogen. It appears that the substrate not only stabilizes the sp<sup>2</sup> bonded network upon room temperature irradiation, but also catalyzes diffusion processes in the network during annealing. This helps to repair the network and is not possible in freestanding h-BN monolayers - only at much higher temperatures. To the authors' best knowledge, to date, the only other irradiation data for h-BN on a metal substrate is by Cun *et al.* [216–219] complemented by the theoretical modeling of Iannuzzi [220]. The used irradiation parameters are very different and include extremely low ion fluences, very low ion energies of the order of 100 eV, and Ar<sup>+</sup> instead of Xe<sup>+</sup>. However, several similarities to our work can be noted: (i) Ar atoms are trapped underneath the h-BN sheet on Rh(111) and upon annealing they become mobile and aggregate to small blisters. (ii) Vacancies created at room temperature aggregate upon annealing and assemble at a specific location of the moiré. (iii) Above 1000 K the vacancy clusters unpin from the moiré and aggregate to larger islands (for h-BN on Ir(111) unpinning takes place above 1300 K). The disappearance of noble gas related protrusions already at 900 K [216] is at variance with our findings. It is hard to reconcile with the fact that blisters are the objects of highest thermal stability for h-BN on Ir(111), objects that even survive the decomposition of h-BN in direct contact with Ir(111). Also at variance with our results is the observation of small cut-out flakes after annealing to 900 K. They appear as bright bumps in STM [216]. A unified view on the phenomena in h-BN on the two metals would emerge, if the bright bumps would be interpreted as blisters, rather than as cut-out flakes.

## 4.9 Conclusion

Our investigations show that the global damage and annealing morphology of h-BN and Gr on Ir(111) have strong similarities, involving irradiation-induced structural disintegration, reestablishment of lattice and moiré pattern, blister formation, and final collapse of the vacancy clusters to large vacancy islands at the highest annealing temperature. Despite the dissimilarity of the electron irradiation damage of the freestanding materials, these similarities for the supported materials arise from the strong bonding of the 2D-layer edges to the Ir(111) substrate. We believe this feature to be of general relevance and expect for any 2D-layer on a substrate, to which its edges bind strongly, a similar set of phenomena after irradiation and annealing, as described here. Presumably, due to the stronger adhesion and thus comparatively higher pressure in h-BN blisters as compared to Gr ones, we were able to directly image solid Xe of monolayer and bilayer thickness through the blister cover. We thereby provide direct proof for the high pressures in irradiation-induced noble gas blisters under 2D-layers on a metal. At sufficiently high annealing temperatures, stand-alone blisters only sealed to the metal substrate form. We identified the onset of 2D-layer decomposition as the key condition for the creation of stand-alone blisters. Additionally, the disintegration of h-BN leads to the formation of borophene phases exhibiting a  $(6 \times 2)$  and a  $(1 \times 1)$  superstructure on Ir(111). Visually, an appealing effect of the hetero-elemental binding in h-BN is the development of pronounced triangular shapes in the entire morphology, which is traced back to the strong and preferential binding of B-terminated zigzag edges to Ir(111). We found that each moiré unit cell can trap just one vacancy cluster at a specific location, namely the chemisorbed valley region of the h-BN layer. This uniqueness of vacancy cluster pinning makes h-BN on Ir(111) from the fundamental point of view superior to Gr/Ir(111). It may thus enable the formation of much better ordered arrays of vacancy clusters.



## CHAPTER 5

# Reversible crystalline-to-amorphous phase transition in monolayer MoS<sub>2</sub> under grazing ion irradiation

*This chapter is based on the manuscript published in 2D Materials 07, 025005 (2020) and its supplement [284] and contains contributions from P. Valerius, S. Kretschmer, B. V. Senkovskiy, J. Hall, A. Herman, N. Ehlen, S. Wu, A. Grüneis, M. Ghorbani-Asl, A. V. Krasheninnikov, and T. Michely. The experiments were designed by me and T. Michely. I carried out most of the STM, STS, and LEED measurements and analyzed all data, and wrote the draft of the manuscript with T. Michely. J. Hall assisted during sample preparation. A. Herman measured the STM data of Figure 5.3. DFT calculations and MD simulations were provided by A. V. Krasheninnikov, S. Kretschmer, and M. Ghorbani-Asl. PL and Raman measurements were provided by B. V. Senkovskiy, N. Ehlen, S. Wu, and A. Grüneis.*

### 5.1 Motivation

MoS<sub>2</sub> is a semiconductor in the family of TMDC. Bulk layered MoS<sub>2</sub> and individual sheets have found applications in tribology [57, 58], catalysis [15, 59, 60], and as an electronic [61, 62], optoelectronic [63, 64] or spintronic material [65]. Controlled introduction of defects into a single sheet of MoS<sub>2</sub> by ion beam irradiation is a powerful tool to alter its morphology [15, 115, 118, 119, 285–293] and the associated changes in the material properties can be beneficial or detrimental, depending on the applications. Examples for beneficial effects are: (i) introduction of S-vacancies created by an Ar plasma dramatically increases the turn-over frequency in the basal plane of MoS<sub>2</sub> for the hydrogen evolution reaction [15]; (ii) low-energy Ar ion irradiation [286] or Ar plasma treatment [119] of MoS<sub>2</sub> prior to metal contact formations gives rise to improved device performance, presumably due to the introduction of defects that short-circuit the metal-MoS<sub>2</sub> Schottky barrier [16] causing thereby a reduction of the contact resistance.

Larger fluence particle irradiation induces dramatic changes in the structure and properties of TMDC. Upon 30 keV He<sup>+</sup> irradiation in a helium ion microscope, Fox *et al.* [118] amorphized few-layer of MoS<sub>2</sub> with doses of 10<sup>17</sup> – 10<sup>18</sup> ions/cm<sup>2</sup>, whereby the material became metallic. Using the same tool, similar observations were reported by Stanford *et al.* [294] for few-layer WSe<sub>2</sub>. Also Zhu

*et al.* [119] observed local phase transformations in MoS<sub>2</sub> under mild Ar plasma treatment from the thermodynamically stable and semiconducting 2H-phase to the metallic 1T-phase. In reverse, Bayer *et al.* [295] reported electron beam induced crystallization of thin amorphous MoS<sub>2</sub>. Ion-irradiation-induced changes in the atomic structure and properties of MoS<sub>2</sub> were noticed already in early studies of the bulk material. Lince *et al.* [296] showed that, after 1 keV Ne<sup>+</sup> ion irradiation with a fluence of  $4 \times 10^{16}$  ions/cm<sup>2</sup>, the surface of a bulk MoS<sub>2</sub> sample transforms into an amorphous S-depleted state in coexistence with clusters of elemental Mo. Even annealing to 1000 K could not restore a long range order of MoS<sub>2</sub> nor a dissolution of elemental Mo. In contrast, after large fluence 3 keV Ar<sup>+</sup> ion irradiation of bulk MoS<sub>2</sub>, Baker *et al.* [297] found a homogeneous single amorphous surface with reduced sulfur content.

Here, a new approach is taken to investigate ion irradiation induced changes in monolayer MoS<sub>2</sub>, enabling us to induce a crystalline to amorphous phase transformation at ion fluences of the order of  $1 \times 10^{14}$  ions/cm<sup>2</sup>, 2-3 orders of magnitude lower than in previous experiments. A grazing incidence irradiation geometry is chosen, such that the ion beam has a maximized interaction with the MoS<sub>2</sub> monolayer, but no interaction with the substrate on which the layer is resting on. This implies the absence of undesirable effects like substrate damage, substrate sputtering, ion implantation, and intermixing, which is a precondition for the reversibility of the ion-induced transformation of the atomic structure. The MoS<sub>2</sub> monolayer material is synthesized, irradiated and analyzed all in situ under ultra-high vacuum (UHV) without ever exposing the sample to ambient conditions. Thereby, an ultra-clean start material with a marginal point defect density is obtained and well controlled experiments give rise to unambiguous results. An unexpected finding is that the ion-induced amorphization of monolayer MoS<sub>2</sub> is fully reversible by thermal annealing. The structural phase transformations from the crystalline-to-amorphous-to-crystalline state are accompanied by transitions from semiconducting-to-metallic-to-semiconducting properties. STM/STS are chosen as tools to visualize the morphological and electronic changes due to amorphization with a high resolution, LEED as a probe for the crystallinity of the layer, as well as PL and Raman spectroscopy to probe sensitively defects and structural changes in the material. Combined with MD simulations, which provide atomistic insights into the mechanisms at hand, our results are complemented into a comprehensive picture.

## 5.2 Amorphization and recrystallization

### Scanning tunneling microscopy and low-energy electron diffraction

The key experiment of the present work is visualized in Figure 5.1(a)-(c). The STM topograph of Figure 5.1(a) displays a coalesced monolayer MoS<sub>2</sub> on which already small hexagonal-shaped second layer MoS<sub>2</sub> islands nucleated. The edges of the monolayer and bilayer islands are metallic [298] and appear bright in the STM topograph. Additionally, bright lines are visible inside the monolayer,

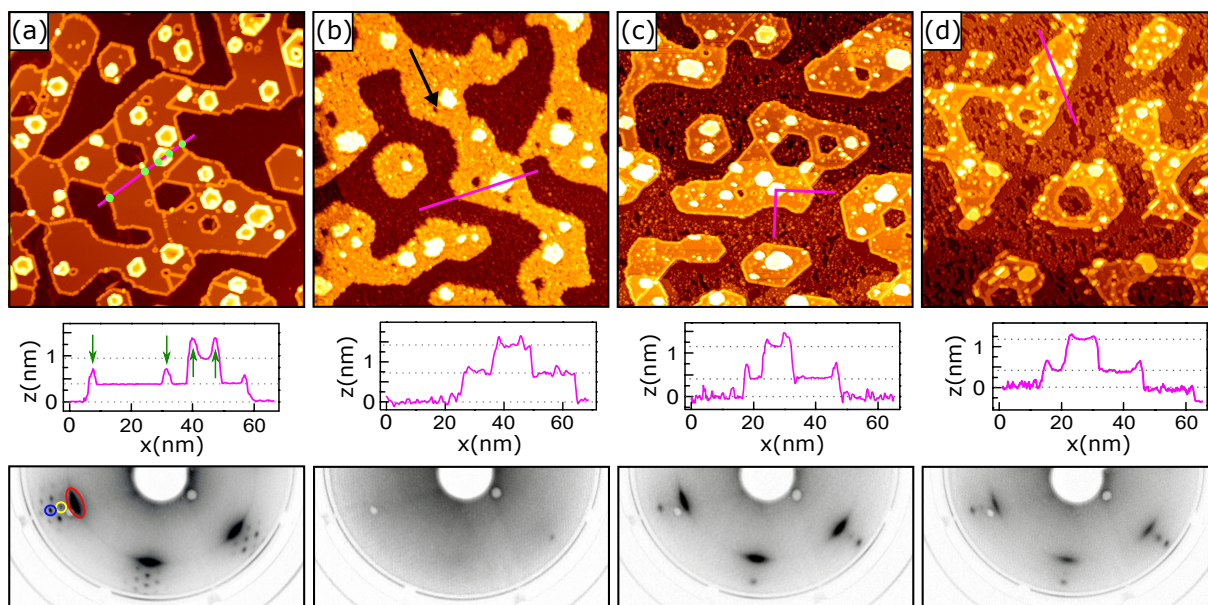


**Figure 5.1:** STM topographs, STM height profiles, and LEED patterns of (a) pristine MoS<sub>2</sub> on Gr/Ir(111); (b) of sample shown in (a) after exposure to a fluence of  $1.5 \times 10^{14}$  ions/cm<sup>2</sup> 500 eV Xe<sup>+</sup> at 300 K; (c) of sample shown in (b) after additional isochronal annealing steps of 300 s at 700 K, 875 K and 1050 K in a sulfur background pressure; (d) of sample shown in (c), after an additional ion fluence of  $1.5 \times 10^{14}$  ions/cm<sup>2</sup> 500 eV Xe<sup>+</sup> and subsequent annealing for 300 s at 1050 K, but in the absence of a sulfur background pressure. Height profiles are taken along purple lines. Black arrow in (b) indicates projection of the ion beam onto the surface. Image sizes: 164 nm × 164 nm; LEED energy: 80 eV.

which are also metallic. They are mirror twin and other lower symmetry grain boundaries [104, 299]. Metallic edges and boundaries appear bright in the STM topograph, because tunneling is conducted at  $U_t = -1.5$  V, inside the MoS<sub>2</sub> band gap which ranges from -1.76 eV to +0.77 eV [11] on Gr/Ir(111). Due to the lack of states in the MoS<sub>2</sub> band gap, the tip has to approach closer to the sample to reach the set point current giving rise to a reduced apparent height, while the metallic edge and boundary states provide tunneling electrons, such that their apparent height is close to the geometric thickness of the layer. The height profile taken along the purple line visualizes the situation: the monolayer apparent height is 0.4 nm, while the apparent height of the edges is 0.7 nm, close to the geometric height of 0.62 nm of a monolayer MoS<sub>2</sub> [300]. Note also that the height difference between the monolayer and the bilayer is 0.6 nm in good agreement with the expectations. Finally, tiny vacancy islands and a few point defects are visible through their bright rim or as bright dots. We note that angle resolved photoemission measurements of a similar sample fully confirmed excellent epitaxy and the monolayer nature of our sample [231]. The LEED pattern in Figure 5.1(a) corresponding to the sample visualized by the STM topograph displays first order Gr and Ir spots, of which example spots are marked with blue and yellow circles, respectively. The spots surrounding them are the moiré spots characteristic for single crystal epitaxial Gr/Ir(111) [124]. The intense, elongated spots (example spot encircled red) aligned with Gr and Ir(111) reflections are first order MoS<sub>2</sub> reflections. The full width at half maximum (FWHM) along the circle defined by a constant wave vector  $k$  is

$\pm 7^\circ$ . The spot broadening represents the scatter of the MoS<sub>2</sub> grain orientations with respect to the dense packed Gr and Ir(111) rows.

After irradiation of the described sample by a fluence of  $1.5 \times 10^{14}$  ions/cm<sup>2</sup> (0.1 MLE) of 500 eV Xe<sup>+</sup> at  $\theta = 75^\circ$  and at 300 K, the morphology changes as depicted by the STM topograph in Figure 5.1(b). The projection of the ion beam onto the surface is indicated by an arrow in Figure 5.1(b) and within  $\pm 5^\circ$  parallel to a dense-packed [110] direction of Ir(111). The initial morphology consisting of a coalesced monolayer MoS<sub>2</sub> and small hexagonal second layer islands can still be recognized after irradiation. However, the roughness measured on the MoS<sub>2</sub> terraces increased from 0.01 nm for the pristine case (disregarding edges and twin boundaries) to 0.1 nm after irradiation. The surface undulations after irradiation are on the atomic length scale. Enhanced roughness is present not only on monolayer and bilayer MoS<sub>2</sub>, but also on the uncovered Gr layer. The roughness is attributed to atom relocation and sputtering caused by the ion impacts. Remarkably, the bright edge and boundary lines have vanished and the apparent height of the MoS<sub>2</sub> layer is now uniform with an average around 0.7 nm, *i.e.*, the same height as the initial metallic edge and boundary states displayed [compare height profile along purple line in Figure 5.1(a)]. These changes indicate a substantial modification of the electronic structure of the MoS<sub>2</sub> layer towards an increased conductivity at the imaging voltage. The MoS<sub>2</sub> coverage decreased from 0.71 ML to 0.60 ML through sputtering. Two sputtering mechanisms need to be distinguished: (i) ions impinge on the illuminated step edge, either directly or through reflection at the Gr layer, and may cause violent sputtering through small impact parameters [40]. This mechanism is operative and can be recognized through the rough and rounded appearance of the illuminated MoS<sub>2</sub> edges in Figure 5.1(b) (compare also Figure 5.2), while along the shadowed edges still straight portions and characteristic 60° angles can be recognized. (ii) Ions impinge on the terraces of MoS<sub>2</sub> islands and cause sputtering. Whether such events contribute to the loss of coverage is investigated in the following section 5.3. Strikingly, the LEED pattern in Figure 5.1(b) displays no more first order MoS<sub>2</sub> or Gr reflections. Only a faint Ir first order reflection encircled yellow is present, indicative of a still crystalline Ir substrate. The lack of MoS<sub>2</sub> and Gr reflections has an evident interpretation: MoS<sub>2</sub> and the uncovered Gr are ion beam amorphized, inhibiting the formation of diffraction spots. Whether the Gr underneath the MoS<sub>2</sub> is damaged or not through the ion beam, cannot be judged on the basis of the LEED pattern. Due to the surface sensitivity of LEED, the strong scattering of Mo (large electron density), and the much weaker of carbon (low electron density) - even for an intact Gr lattice underneath a MoS<sub>2</sub> layer - no diffraction spots are expected.

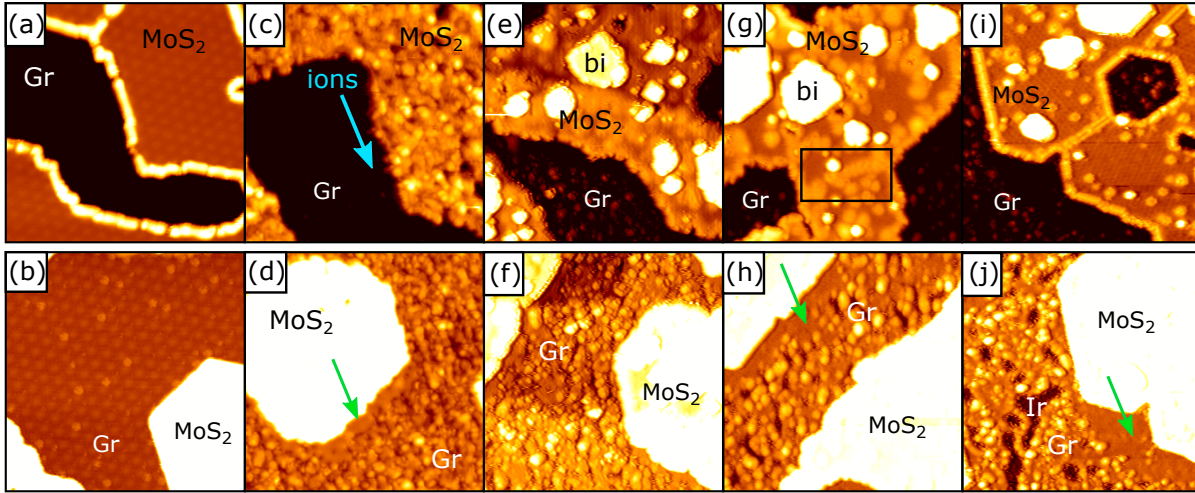
After irradiation, the sample was successively annealed in S vapor in isochronal steps of 300 s at 700 K, 875 K and 1050 K resulting in the morphology presented in the STM topograph of Figure 5.1(c). The STM data on the intermediate annealing steps of 700 K and 875 K together with well resolved images of the Gr damage are provided in Figure 5.2. The MoS<sub>2</sub> has reorganized and displays a similar appearance as after growth. Defect annealing was stimulated by both picking up S vapor atoms and vacancy migration, as previous studies [301] indicated that the migration barriers of

vacancies drop when their concentration increases and vacancies should be mobile at the annealing temperatures used in our experiments. Edge and boundary states reappeared and the height profile along the purple line in Figure 5.1(c) displays again the reduced apparent MoS<sub>2</sub> layer height characteristic for the semiconducting MoS<sub>2</sub>. The MoS<sub>2</sub> islands re-exhibit a smooth surface, though tiny vacancy islands and a substantially larger number of bright point defects are present, when compared to the pristine case as shown by the STM topograph in Figure 5.1(a). By annealing, the coverage of MoS<sub>2</sub> decreased only marginally from 0.60 ML for the amorphized layer to 0.58 ML for the crystalline layer. In the corresponding LEED pattern of Figure 5.1(c), the first order MoS<sub>2</sub> spots reappear in similar intensity and with similar angular spread as for pristine MoS<sub>2</sub> (an example spot is encircled red). The reappearance of the MoS<sub>2</sub> spots makes the recrystallization of the ion beam amorphized MoS<sub>2</sub> obvious. Also Gr spots reappear (an example spot is encircled blue) while the moiré reflections are missing. For Gr, the annealing temperature is sufficient to regain crystallinity, but not sufficient to develop the level of regularity needed for the development of a moiré, consistent with previous experiments on amorphization and recrystallization of Gr on Ir(111) [29]. The STM topograph of Figure 5.1(c) reveals in the areas of uncovered Gr indeed disorder caused by vacancy islands and a large number of bright dots indicative of C atoms still displaced.

When this sample is irradiated again and subsequently annealed with the same succession of isochronal steps in the *absence* of an S vapor, the sample restores again to the crystalline state as visible in Figure 5.1(d). Compared to the annealing in an S vapor [compare Figure 5.1(c)] two characteristic differences are present: (i) a large number of clusters of larger height are apparent at the MoS<sub>2</sub> island rims and (ii) through annealing the total MoS<sub>2</sub> coverage decreases substantially from 0.48 ML (measured after irradiation and before annealing) to 0.42 ML, much stronger than in the presence of an S vapor. These two differences may be rationalized by assuming that preferential loss of sulfur due to sputtering and subsequent annealing causes excess Mo to aggregate as small metallic clusters at the island rims, thereby giving rise to the MoS<sub>2</sub> coverage decrease. In contrast, annealing in an S vapor largely replenishes sputtered sulfur and prevents losses during heating.

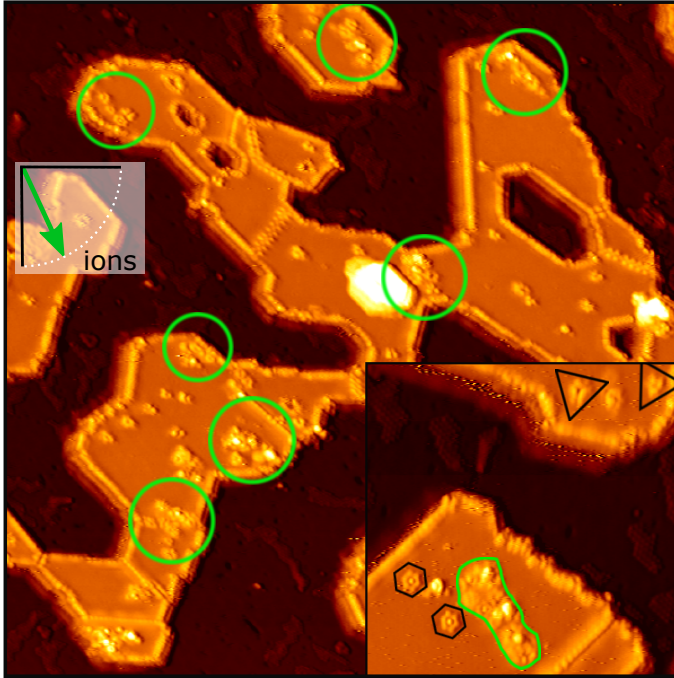
### Details of the annealing series in STM topographs

Figure 5.2 presents STM topographs of the pristine, irradiated, and annealed samples in larger magnification and additional annealing steps in order to provide a more detailed view of the structural changes during the amorphization and recrystallization process. In the upper row the color contrast is adjusted to highlight the internal structure of the MoS<sub>2</sub>, while the contrast of the bottom row shows the evolving structures in the Gr layer. As depicted in Figure 5.2(a), the pristine MoS<sub>2</sub> is free of any defects while the interior of the island shows a periodicity of 2.5 nm, which can be associated with the underlying moiré of Gr/Ir(111) [124]. Compared to a Gr layer without additional MoS<sub>2</sub> growth, small bright spots are present in the Gr layer as shown in Figure 5.2(b). They can be tentatively attributed to intercalated sulfur.



**Figure 5.2:** STM topographs showing close-ups of the sample morphology with the contrast adjusted to highlight the MoS<sub>2</sub> in the upper and Gr in the lower row. (a,b) pristine MoS<sub>2</sub> on Gr/Ir(111), (c,d) sample of (a) irradiated with a fluence of  $1.5 \times 10^{14}$  ions/cm<sup>2</sup> 500 eV Xe<sup>+</sup>, (e,f) sample of (c) annealed sample at 700 K, (g,h) sample of (e) annealed to 875 K, and (i,j) sample of (g) annealed to 1050 K. "MoS<sub>2</sub>", "Gr" and "bi" indicate monolayer MoS<sub>2</sub> islands, graphene, and bilayer MoS<sub>2</sub> islands, respectively. The blue arrow represents the azimuthal ion beam direction, the green arrows point to areas shadowed from ion impacts, the black box highlights a recovering grain boundary. Image sizes are 41 nm × 41 nm.

The close-up STM image of the irradiated MoS<sub>2</sub> in Figure 5.2(c) reveals that no crystalline structure is left within the MoS<sub>2</sub> island, which coincides with the amorphous LEED pattern of Figure 5.1(b). The blue arrow indicates the azimuthal direction of the incoming ion beam. The morphology of Figure 5.2(d) shows that the Gr also has no distinct structure left. The green arrow in Figure 5.2(d) points to a MoS<sub>2</sub> step edge along which a stripe of graphene is shadowed by the MoS<sub>2</sub> island, because of its grazing incidence at  $\theta = 75^\circ$ . The graphene appears undamaged in this stripe. Figure 5.2(e) shows that after annealing the sample to 700 K the overall MoS<sub>2</sub> becomes flat again. Besides a small bilayer island (marked with 'bi') the MoS<sub>2</sub> is covered with a high density of bright protrusions. Moreover, no signs of edge states or grain boundaries are visible. The Gr exhibits thin, dark trenches and bright protrusions, which can be attributed to agglomerated vacancy-like defects and implanted gas, respectively [see Figure 5.2(f)]. At 875 K [see Figure 5.2(g)] the MoS<sub>2</sub> inhibits a decreased number of protrusions and areas of homogeneous height become apparent. While number of smaller protrusion is still large, a recovering grain boundary becomes visible, which is marked with the black box. The Gr remains mainly unchanged, a shadowed region is marked by the green arrow [see Figure 5.2(h)]. At the highest annealing temperature of 1050 K [Figure 5.2(i)], distinct edge states and grain boundaries reappeared in the MoS<sub>2</sub>. Some small protrusions are still present, which we attribute to point defects. The uncovered Gr defect structures continue to ripen [see Figure 5.2(j) and Figure 5.2(h)]. Large vacancy islands reveal areas of bare Ir and regions of flat Gr close to the MoS<sub>2</sub> island are visible.

Single ion impacts of highly energetic  $\text{Xe}^+$  ions

**Figure 5.3:** STM topographs of  $\text{MoS}_2/\text{Gr}/\text{Ir}(111)$  after single ion impacts of 5 keV  $\text{Xe}^+$  at room temperature. Impacts and its defect structures are highlighted by green circles and adjusted contrast. Image sizes are 92 nm $\times$ 92 nm; inset: 30 nm $\times$ 30 nm. Sketch shows averaged azimuthal angle of sputter trails.

highlighted with the green circles. They evolve with preferred directions, mimicking the azimuthal angle of the incoming ion beam. The average azimuthal angle of the ion tracks yields about  $(115 \pm 5)^\circ$ , as indicated by the sketch on the left side. The close-up STM topograph in the inset of Figure 5.3 provides a highly resolved image displaying different kinds of evolving defects. A sputter trail [26,35], *i.e.* a broad line of defects, has formed as highlighted by the green lines. Additionally, defects exhibiting flower like patterns, are marked by black hexagons. This kind of defects has a hexagonal symmetry and a bright spot in its center. Moreover, defects of trigonal symmetry are present (black triangles) with two possible orientations within one domain of  $\text{MoS}_2$  which are rotated by  $180^\circ$  to each other. It should be noted here, that the intercalated sulfur shows well resolved structures at areas of uncovered Gr.

Compared to literature, Addou *et al.* show ring like defect structures, cluster-like defects with depression in its center, which they correlate to impurities in natural  $\text{MoS}_2$  [302]. For a similar system, Barja *et al.* show simulated STM images indicating that for  $\text{MoSe}_2$  on Gr top-Se-vacancies appear as a depression while bottom-Se-vacancies show up as protrusions in STM [303]. Additionally, six- and three-fold symmetries are discussed, which they correlate to a bias dependency, which can be ruled out for this system as we find both symmetrical defects for the same bias and STM-

To elucidate the defect formation of a single impinging ion, we performed low-fluence, high-energy ion irradiation experiments. Pristine  $\text{MoS}_2$  on  $\text{Gr}/\text{Ir}(111)$  was exposed highly energetic  $\text{Xe}^+$ -ions of 5 keV at a low fluence of  $1 \times 10^{-4}$  MLE at room temperature and an angle of incidence of  $75^\circ$ . As apparent from the STM topographs in Figure 5.3, showing the morphology of the irradiated sample, distinct structural changes can be observed which can be associated with single ion collision events. The large scale topograph in Figure 5.3(a) depicts large  $\text{MoS}_2$  islands with the typical edge states and grain boundaries well visible. Compared to the pristine  $\text{MoS}_2$  of Figure 5.1(a), few small defects as well as agglomerations of protrusion are present. Within the range of this topograph multiple ion impacts are visible as

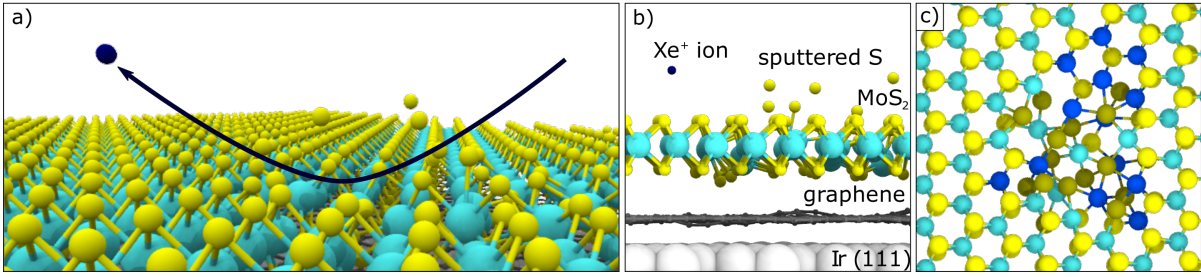


**Figure 5.4:** MD simulation event for a 500 eV Xe<sup>+</sup> impinging on MoS<sub>2</sub>/Gr/Ir(111) with a polar angle  $\theta = 75^\circ$  and an azimuthal angle of  $\phi = 27.5^\circ$ . (a) Perspective view of the event 3.6 ps after the impact, when sputtering has ceased. The yellow, blue, and dark blue balls represent the S, and Mo atoms, and the primary ion. The ion-trajectory is highlighted. (b) Side view of (a) highlighting the absence of damage in Gr and the Ir substrate. (c) Top view of impact area after 20 ps, when impact energy has dissipated. Undercoordinated Mo and S atoms are colored dark blue and brown, respectively.

tip. Interestingly, Marion *et al.* presented simulated STM images for different defect structures for supported and freestanding MoS<sub>2</sub> [304]. Although, there is no direct evidence for the origin of the defect structures, it can be argued that the flower like defect pattern resembles well the simulated STM image of the freestanding MoS<sub>2</sub> with a bottom-S-vacancy. Additionally, the trigonal defect resembles the simulation of a top-S-vacancy for freestanding MoS<sub>2</sub>. High temperature STM on Ar<sup>+</sup> bombarded bulk MoS<sub>2</sub> also revealed hexagonal shaped defects, however, they are surrounded by a dark region and show no protrusion within its hexagonal core [305]. How irradiation can cause a bottom-S-vacancy in supported MoS<sub>2</sub> still remains an open question. MD simulations as presented in the next section 5.3 provide further insight.

### 5.3 Molecular dynamics simulations

To obtain insight into the ion-induced structure transformation of the MoS<sub>2</sub> layer and its surprising ability to restore crystallinity upon annealing, we performed molecular dynamics simulations of 500 eV Xe<sup>+</sup> impacts onto MoS<sub>2</sub> on Gr/Ir(111). Both the polar angle  $\theta$  ( $\theta = 75^\circ$  in experiment) and the azimuthal angle  $\phi$  ( $\phi = 30^\circ \pm 7^\circ$  in experiment) were varied. For the simulations, a  $130 \times 75 \times 25 \text{ \AA}^3$  supercell was used, which consists of graphene [1806 formula units (f.u.)] stacked on three Ir(111) layers (1466 f.u. per layer) forming a Ir(111)/Gr=(9×9)/(10×10) supercell with 0.01 % strain on graphene. On top of that  $42 \times 28$  unit cells of MoS<sub>2</sub> (1176 f.u.) were placed, which yields 0.08 % strain on the MoS<sub>2</sub>. It was checked that for the 500 eV Xe ion under grazing incidence the ion cannot pass the relatively thin substrate. Figure 5.4(a) displays a snapshot of an event with  $\theta = 75^\circ$  and  $\phi = 27.5^\circ$  just after the impact of the ion. The impact resulted in sputtering of 7 sulfur atoms (the highest yield observed in a single event). All sputtered S atoms stem from the top S layer. Neither Mo atoms nor C atoms from the Gr layer underneath were sputtered. The primary ion was reflected as evident from the ion trajectory schematically indicated by the curved arrow, Figure 5.4(a). The side view of Figure 5.4(b) makes plain that damage in the underlying Gr layer and in the Ir substrate

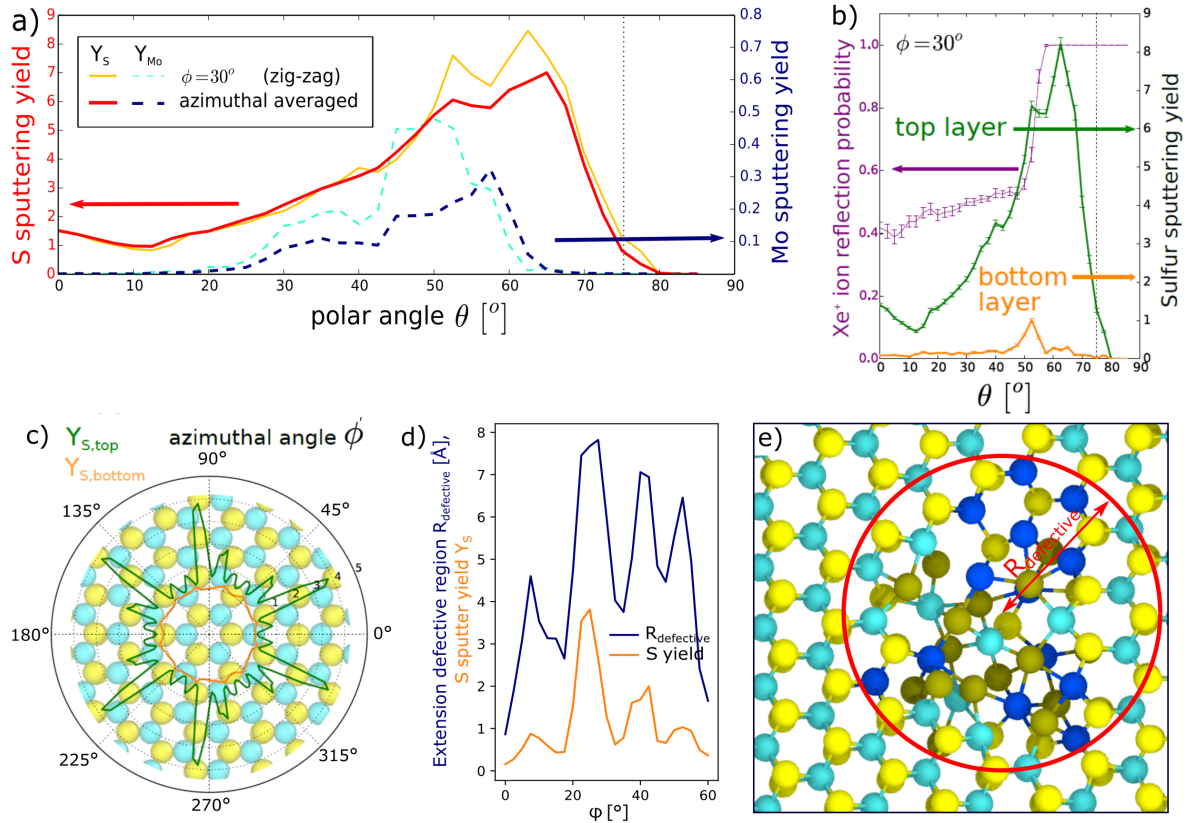


**Figure 5.5:** (a) Dependence of the sputtering yields  $Y_S$  and  $Y_{Mo}$  on the polar angle  $\theta$  for the azimuthal angle  $\phi = 30^\circ$  (yellow and dashed light blue lines) and the average over  $0^\circ$ ,  $30^\circ$ ,  $60^\circ$  (red and dashed dark blue lines). (b) Sulfur sputtering yields  $Y_{S,top}$  (green line, right axis) and  $Y_{S,bottom}$  (orange line, right axis) for top and bottom layer S atoms, respectively, as a function of polar angle  $\theta$  for  $\phi = 30^\circ$ . Also shown is the ion reflection probability (blue line, left axis) as a function of  $\theta$ . (c) Polar plot of the dependence of  $Y_{S,top}$  (green line) and  $Y_{S,bottom}$  (orange line) on  $\phi$  at fixed  $\theta = 75^\circ$  displayed on top of the ball model visualizing the geometry. (d) Defect radius  $R_{defect}$  as a function of azimuthal angle  $\phi$  at  $\theta = 75^\circ$ . (e) Visualizes the definition of  $R_{defect}$  through the disc around an impact point that contains all displaced atoms.

is absent. Figure 5.4(c) is a top view of the damaged area 20 ps after the impact, a sufficient time to dissipate the energy of the impact over the whole system, so that the atomic configuration does not more change, unless thermal annealing is done. Undercoordinated Mo atoms (dark blue) and undercoordinated S atoms (brown) are distributed in a beam-amorphized area with a radius  $R_{defective} \approx 8 \text{ \AA}$ . In conclusion, a substantial number of top layer S atoms are sputtered away and the MoS<sub>2</sub> layer is amorphized in a small area centered at the ion impact. The movie of this and similar events are available in the Supporting Information of Ref [284].

To see how representative the event visualized in Figure 5.4 is and how the sputtering evolves with  $\theta$ , Figure 5.5(a) displays the sputtering yield  $Y_S$  for S (yellow and red lines) and  $Y_{Mo}$  for Mo (light and dark blue dashed lines) as a function of the polar angle  $\theta$ . The MD results for  $\phi = 30^\circ$  (yellow,

light blue) and the average (red, dark blue) over the three investigated high symmetry directions ( $\phi = 0^\circ, 30^\circ, 60^\circ$ ) are plotted.  $Y_S$  has a broad maximum between  $50^\circ$  to  $65^\circ$ , while  $Y_{Mo}$  has a maximum at somewhat lower angles between  $40^\circ$  to  $60^\circ$ . Quantitatively,  $Y_S$  is larger by at least a factor of 20 compared to  $Y_{Mo}$ . The vertical dotted line in Figure 5.5(a) marks the experimental angle  $\phi = 75^\circ$ . It is apparent that  $Y_{Mo}$  is zero at  $\theta = 75^\circ$ . In contrast, sulfur sputtering is still substantial at  $\theta = 75^\circ$ . It is  $Y_S = 1.3$  for  $\phi = 30^\circ$ .

With Figure 5.5(b), we now take a closer look at the origin of the sputtered sulfur atoms and distinguish sputtered S atoms originating from the top S layer ( $Y_{S,top}$ , green line, right axis) and sputtered S atoms originating from the bottom S layer ( $Y_{S,bottom}$ , orange line, right axis) as a function of polar angle  $\theta$ . As expected on the basis of previous MD simulations [244], the overwhelming majority of all sputtered S atoms stems from the top layer. Only for  $\theta$  around  $50^\circ$  a non-negligible fraction of about 10% originates from the bottom layer. At the experimental angle of  $\theta = 75^\circ$  we find  $Y_{S,bottom} \approx 0$ , while  $Y_{S,top} = 1.3$ . The purple curve in Figure 5.5(b) additionally represents the ion reflectivity as a function of polar angle  $\theta$ . At the grazing experimental angle of  $\theta = 75^\circ$  all ions are reflected, consistent with the absence of sputtering for C, Mo, and bottom S. Only at angles below  $60^\circ$  the ion reflectivity drops below 1 and ion penetration of the MoS<sub>2</sub> takes place. In the small angular range around  $\theta = 50^\circ$ , ion penetration is associated with sputtering of S atoms in the bottom layer.

As the MoS<sub>2</sub> islands display scatter of  $\pm 7^\circ$  around the dense-packed orientation corresponding to  $\phi = 30^\circ$  our picture is not complete yet, as averaging over the azimuthal angle is necessary to obtain an appropriate estimate of the yields. Figure 5.5(c) presents the dependence of  $Y_{S,top}$  and  $Y_{S,bottom}$  on  $\phi$  at fixed polar angle of  $\theta = 75^\circ$  (compare Tab. 5.1). Apparently, the sputtering yield varies strongly with  $\phi$ . Averaging the yield for an angular range between  $\phi = 22.5^\circ$  and  $\phi = 37.5^\circ$  corresponding to the angular scatter of the MoS<sub>2</sub> layer yields  $\bar{Y}_{S,top} = 2.01$  and  $\bar{Y}_{S,bottom} = 0.04$  for bottom sulfur. The ratio 50:1 of top to bottom sulfur sputtering indicates almost exclusive sputtering of top layer S. We use the same averaging to obtain an effective ion beam amorphized region with a radius depending on the azimuthal angle, as shown by the graph presented in Figure 5.5(d) and the corresponding visualization in Figure 5.5(e).

**Table 5.1:** Azimuthal angle  $\phi$  dependence on the sulfur sputtering yield for top and bottom layer at a fixed polar angle of  $75^\circ$ .

$\phi [^\circ]$	$Y_{up}$	$Y_{low}$	$\phi [^\circ]$	$Y_{up}$	$Y_{low}$
0.0	0.13	0.02	32.5	0.56	0.06
2.5	0.21	0.07	35.0	0.72	0.07
5.0	0.49	0.04	37.5	1.54	0.07
7.5	0.82	0.06	40.0	1.57	0.11
10.0	0.66	0.11	42.5	1.82	0.17
12.5	0.46	0.13	45.0	0.53	0.17
15.0	0.27	0.16	47.5	0.40	0.26
17.5	0.38	0.07	50.0	0.78	0.18
20.0	1.49	0.02	52.5	0.91	0.12
22.5	3.53	0.01	55.0	0.88	0.07
25.0	3.81	0.00	57.5	0.45	0.05
27.5	2.63	0.02	60.0	0.34	0.02
30.0	1.25	0.03	avg.	1.07	0.08

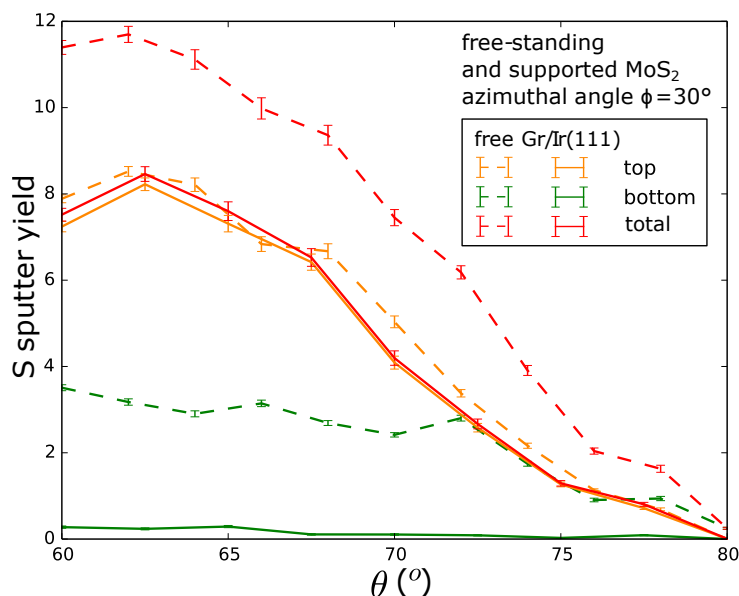


**Figure 5.6:** Comparison for S sputtering yield for freestanding and supported MoS<sub>2</sub> depending on the angle of incidence ranging from 60° to 80°. The dotted lines represent the data for freestanding MoS<sub>2</sub>, while the solid lines show the data for the supported MoS<sub>2</sub>, respectively.

Additionally, to address the important effect of the substrate on the sputtering yield, we aimed at matching the experimental setup as closely as possible by including the substrate. The main effect of the substrate is to strongly reduce sputtering from the bottom layer. This is evident from the comparison of the presented data in Figure 5.5(b) to data for freestanding flakes in Figure 4(b) of Ref. 244 and to the additional calculations carried out for freestanding MoS<sub>2</sub> irradiated with 500 eV Xe ions with the incidence angle range between  $\theta = 60^\circ$  and  $\theta = 80^\circ$  as shown in Figure 5.6. While for supported MoS<sub>2</sub> the total bottom S sputtering yield is 0 (solid green line) it becomes significant for freestanding MoS<sub>2</sub> (dotted green line) for  $\theta < 80^\circ$ .

With the help of the MD simulations, the following picture can be drawn. The primary ion beam removes S atoms from the MoS<sub>2</sub> top layer and creates an amorphized area with undercoordinated and misplaced Mo and S atoms, whereby the LEED pattern vanishes. Due to the only weak interaction of the ion beam with the Mo atoms as well as the bottom S layer and the absence of sputtering from there, the MoS<sub>2</sub> layer is not disrupted entirely. The S atoms in the MoS<sub>2</sub> layer are still coordinated to metallic Mo. This is consistent with the presence of an amorphized layer with an apparent STM height close to the geometrical height of the MoS<sub>2</sub> in Figure 5.1(b). Though the Gr layer in between the MoS<sub>2</sub> islands is subject to sputtering and C atom relocation, our simulations provide evidence that the Gr layer underneath the MoS<sub>2</sub> is not sputtered and remains largely intact. Upon annealing the layer recrystallizes, irrespective of whether S is provided or not. The additional S during annealing heals the S deficiency resulting from the top layer loss during sputtering, while without S supply the excess Mo forms metallic clusters. The recrystallization of the amorphized MoS<sub>2</sub> on Gr to a high degree of perfection is further evidence for the absence of substantial irradiation damage in the Gr

layer underneath. Otherwise strong bonds between Mo and C would have formed, as in irradiated graphene on iridium [26], impeding recrystallization.

According to this picture, ions impinging on the MoS<sub>2</sub> layer terraces [mechanism (ii) mentioned above] should not cause a shrinkage of the coverage. The only caveat to this conclusion is the fact that when considering the ion dose of  $1.5 \times 10^{14}$  ions/cm<sup>2</sup>, we must assume ions to impinge in the later stages of the exposure time interval onto pre-damaged areas. In contrast, every MD event starts with a perfectly crystalline surface. Therefore, sputtering of bottom S layer and Mo in the experiment cannot be ruled out entirely, and thus this mechanism can still contribute to coverage loss. This effect might be enhanced with increasing ion energy, as it was shown by single ion-impacts of 3 keV ions, different vacancy-defect structures appear that might indicate damage in the bottom-S-layer. Nevertheless, the dominant amount of coverage loss is attributed to mechanism (i) mentioned above, namely to sputtering of the illuminated step edges. Considering that the step edge yield may be more than an order of magnitude larger than the terrace yield determined in our MD simulations [40], and taking into account that the flux in a stripe of width 4.6 nm is focused on the illuminated edge, the substantial decrease of coverage becomes understandable. The width of the stripe focusing the flux to the edge is calculated using the geometric model outlined in Ref. 40.

### 5.4 Evolution of electronic and optical properties with amorphization and recrystallization

#### Scanning tunneling spectroscopy

The ion-induced amorphization must be accompanied by changes in the electronic structure of the MoS<sub>2</sub> layer. We analyze these changes using  $dI/dV$  STS point spectra, of which the intensity corresponds to first approximation to the local density of states (LDOS). For reference, Figure 5.7(a) displays the constant current  $dI/dV$  tunneling spectrum of pristine MoS<sub>2</sub>. The gap between the valence band and the conduction band ranges from -1.8 V to 0.8 V as indicated by vertical dotted lines. The measured gap position and magnitude of 2.6 eV is in-line with our earlier work [11]. Note that the STS measured gap is between the  $\Gamma$ -point valence band maximum and the  $K$ -point conduction band minimum. This gap is larger by about 0.1 eV than the direct band gap between the  $K$ -point extrema (see Ref. 11 for a detailed discussion). For amorphized MoS<sub>2</sub>, the gap largely disappears in the  $dI/dV$  spectrum shown Figure 5.7(b). The logarithmic representation of the data  $dI/dV$  data in the inset of Figure 5.7(b) in fact suggests metallic behavior, though with a low density of states at the Fermi level. One may therefore conclude that the crystalline, large band gap semiconductor was transformed to an amorphous metal. Also prominent in the  $dI/dV$  spectrum is the increase in the  $dI/dV$ -signal below  $-0.5$  eV, which culminates in a new peak in the LDOS around  $-2.25$  V. The enhanced conductivity at  $U_t = -1.5$  V is consistent with the disappearance of the metallic edge states in the STM topograph of Figure 5.1(b) and the increased apparent height of the entire layer through amorphization. Zhu *et al.* [119] induced a phase transformation from

the 2H to the 1T' phase of MoS<sub>2</sub> through mild Ar plasma treatment with energies well below the displacement threshold for S. Here, we expose MoS<sub>2</sub> to a substantial fluence of ions with energy *large* compared to the displacement threshold, resulting in S sputtering and atom relocation consistent with the absence of any 1T' phase.

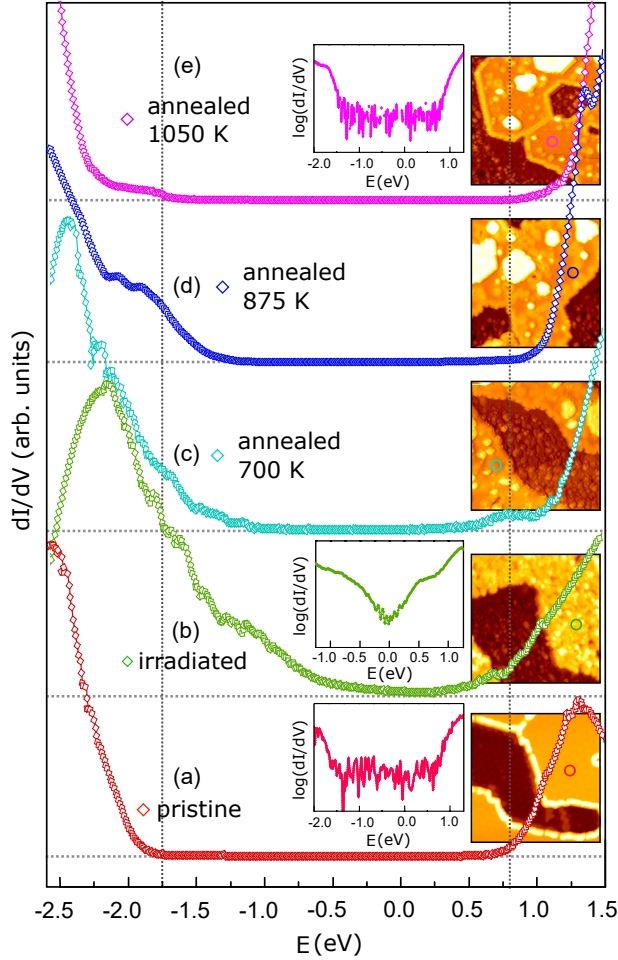


**Figure 5.7:** Evolution of the MoS<sub>2</sub> constant current  $dI/dV$  tunneling spectra with ion irradiation and annealing. The tip was stabilized at  $I_{\text{stab}} = 2 \text{ nA}$  and  $U_{\text{stab}} = -2.5 \text{ V}$ . Spectra were taken at 300 K. From bottom to top: (a) pristine MoS<sub>2</sub> on Gr/Ir(111); (b) sample after exposure to a fluence of  $1.5 \times 10^{14} \text{ ions/cm}^2$  500 eV Xe<sup>+</sup>; (c) sample of (b) annealed for 300 s at 700 K; (d) sample of (c) annealed for 300 s to 875 K; (e) sample of (d) annealed for 300 s to 1050 K. Right insets show STM topographs of size 42 nm × 42 nm, where locations of point spectra recording are indicated by empty circles. Middle insets in (a), (b) and (e) display logarithmic  $dI/dV$  spectra.

develops an S-deficiency which may be rationalized to first approximation as S-vacancies. For an ion fluence of  $1.5 \times 10^{14} \text{ ions/cm}^2$  and with  $Y_S \approx 2$ , we obtain a S-deficiency of 13 % as an order of

Annealing the sample to subsequently higher temperatures reestablishes the band gap gradually, as is apparent from the spectra of Figure 5.7(c) after annealing to 700 K and of Figure 5.7(d) after annealing to 875 K. The final annealing step to 1050 K gives rise to a  $dI/dV$  point spectrum shown in Figure 5.7(e) with a gap of the same size as in the pristine sample [compare Figure 5.7(a)]. We note that after the final annealing step still the point spectra show in-gap states when taken close to remaining defects. It was already noted by Yong *et al.* [306] and Kodama *et al.* [307] that S-vacancy formation in MoS<sub>2</sub> is associated with discrete localized in-gap states. Theoretically, Li *et al.* [15] investigated the effect of ordered S-vacancy structures on band structure and found new vacancy derived bands in the gap, that moved closer to the Fermi level with increasing vacancy concentration, until with 25% vacancies the MoS<sub>2-x</sub> sample becomes metallic. Similar results were also obtained by Iberi *et al.* [288] for the sister compound MoSe<sub>2</sub>. As the 500 eV Xe<sup>+</sup> irradiation of MoS<sub>2</sub> at  $\theta = 75^\circ$  applied by us gives rise to S sputtering, the sample certainly de-

magnitude estimate, a magnitude where in fact substantial effects are expected. The closure of the MoS<sub>2</sub> band gap upon ion irradiation is therefore in line with the above mentioned work. However, preferential sputtering of S and thus S-vacancy creation is not the only effect of ion irradiation. Disorder in lattice, S-bonding and S-concentration are effects not included in the above picture. The disorder will cause a smearing of S-vacancy derived states in energy and in dependence of their precise environment. This explains why we see a continuous extension of the LDOS from the band edges into the gap, rather than an in-gap peak as one might expect for an ordered S-vacancy superstructure. Even disorder alone, without S-deficiency might give rise to a smearing of the band edges into the gap. After annealing the amorphized layer at 700 K in S-vapor, the stoichiometry of the MoS<sub>2</sub> layer will be very close to nominal. However, as visible in Figure 5.7(c) still the LDOS extends into the gap.

In the present experiment, with MoS<sub>2</sub> resting on well conducting Gr, STM measures inherently only the conductivity through, rather than along the two dimensional (2D) material. Although the larger apparent height of the MoS<sub>2</sub> and the LDOS within the band gap after irradiation clearly indicate an enhanced conductivity through the layer at low voltages, disrupted periodicity and disorder will make this material itself unsuitable for lateral transport and diminish its mobility. However, graded ion irradiation underneath contacts with zero irradiation in the channel region or selective amorphization of the topmost layer underneath contacts of a bilayer device might have beneficial effects for the contact resistance, as is made plausible by the work of Cheng *et al.* [286] or Zhu *et al.* [119].

### Optical properties and Raman spectroscopy

In order to investigate the effect of the ion irradiation on the optical properties, we conducted ultra-high vacuum photoluminescence (UHV-PL) experiments and compare the spectra of the pristine (light blue), irradiated (violet), and annealed (green) sample in Figure 5.8(a). The as-grown MoS<sub>2</sub> on Gr/Ir(111) has a PL peak at 1.95 eV and a narrow FWHM of 13 meV at 10 K, in line with previous work [231]. Ion-induced amorphization quenches PL in agreement to previous observations on MoS<sub>2</sub> and MoSe<sub>2</sub> monolayers grown on SiO<sub>2</sub>/Si by CVD [287, 288], as well as on mechanically exfoliated MoS<sub>2</sub> flakes on SiO<sub>2</sub>/Si [291].

After annealing, PL does not recover in our sample in spite of the fact that PL of CVD-grown MoS<sub>2</sub> on SiO<sub>2</sub>/Si was shown to recover after annealing [287]. We believe that this difference stems from the morphologies and environments of the two MoS<sub>2</sub> samples under consideration. The present MoS<sub>2</sub>/Gr/Ir(111) sample grows epitaxially and has a very narrow PL line-width compared to the PL linewidth of CVD-grown MoS<sub>2</sub> on SiO<sub>2</sub>/Si which has PL FWHM of 53 meV. The narrow PL observed here is an indication of good sample quality. Nevertheless, the intensity (peak area) of the CVD-grown MoS<sub>2</sub> on SiO<sub>2</sub>/Si is  $\sim 6000$  times larger than the PL of MBE-grown MoS<sub>2</sub>/Gr/Ir(111) sample measured under identical conditions. This is a consequence of the metallic substrate and the small island size in MBE-grown sample. The mechanism for PL reduction that relates to the island

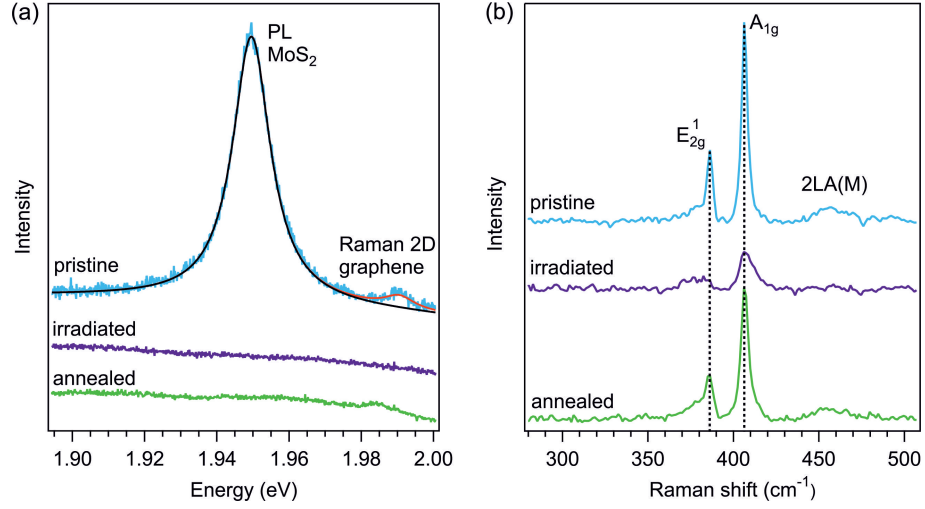


**Figure 5.8:** (a) PL spectra of a pristine MoS<sub>2</sub> on Gr/Ir(111) (light blue line), after irradiation at 300 K with 500 eV Xe<sup>+</sup> at  $\theta = 75^\circ$  (violet line), and after subsequent annealing to 970 K (green line). Black line: fit to the PL peak of the pristine sample by a Lorentzian with a full width at half maximum of 13 meV and center at 1.95 eV. The small red peak is the 2D Raman peak of the Gr substrate. (b) Raman spectra of the same sample with identical color code for the preparation conditions. The  $E_{2g}^1$ , the  $A_{1g}$  and the 2LA(M) modes are indicated. Vertical dash lines indicate the positions of the  $E_{2g}^1$  and  $A_{1g}$  modes in the pristine sample.

size is the fact that excitons can diffuse on the island and recombine non-radiatively when reaching the metallic edge of the island. The size of MoS<sub>2</sub> islands of the present MBE-grown sample is smaller compared to the island size of CVD-grown MoS<sub>2</sub>/SiO<sub>2</sub>. Exciton diffusion depends critically on the exciton density [308] and temperature [309]. The relevant PL experiments have been performed on exfoliated TMDC flakes that are freestanding or supported by SiO<sub>2</sub> [308, 309] and therefore a direct quantitative comparison of diffusion lengths in the present system is difficult. Nevertheless, for encapsulated WSe<sub>2</sub> monolayers, diffusion lengths between 360 nm (300 K) and 1.5  $\mu\text{m}$  have been reported [309]. We believe that this process could be particularly important for the present MoS<sub>2</sub>/Gr/Ir(111) samples, because the typical island diameter is at least one order of magnitude smaller than the reported diffusion lengths of the exciton. The metallic edge of an MoS<sub>2</sub> island might therefore provide an effective quenching site for the excitons.

The small MoS<sub>2</sub> islands in the present sample are also more sensitive to residual damage after annealing. This is so because the exciton is confined to the island and if the island size is sufficiently small, a single defect does not leave an unperturbed area with a size that allows hosting an exciton. We thus need to compare the average defect separations to the exciton's wavefunction diameter. If the two numbers are equal to each other, we can expect a change of the PL or even quenching of the PL.

The defect density was estimated by STM and we found that it depends on the annealing temperature. For 875 K annealing temperature we observed one defect within an MoS<sub>2</sub> area of 3.2 nm  $\times$  3.2 nm. For a larger annealing temperature of 1050 K we observe one defect in an area of

4.5 nm × 4.5 nm. The annealing temperature was 970 K for the sample whose PL and Raman spectra are shown in Figure 5.8. This means that our defect separation will be in between these two values. Let us now compare this separation to the spatial extent of the exciton wavefunction. There are no experimental or theoretical data on the present system but the extent of the exciton wavefunction of a related system (h-BN encapsulated WS<sub>2</sub>) has been studied [310]. An exciton of WS<sub>2</sub> in the 1s ground state has a diameter of 4 nm [310]. Thus, the average separation between two defects is in the order of the exciton wavefunction and we speculate that the defect density we have is already sufficient to quench PL. It should be noted that the exciton wavefunction depends strongly on the substrate's dielectric constant and the atomic details of the MoS<sub>2</sub>/Gr/Ir(111) system. Thus, for the precise estimation of the exciton wavefunction of the present system, a detailed calculation that takes into account these issues would be needed.

Let us now look to the effect of sputtering and annealing on the Raman spectra. In Figure 5.8(b), we compare the 10 K Raman spectra of the pristine sample (light blue line) with the irradiated (violet line) and annealed (green line) sample. Pristine MoS<sub>2</sub> exhibits two pronounced Raman-active modes – the in-plane  $E_{2g}^1$  mode at 386.3 cm<sup>-1</sup> and the out-of-plane  $A_{1g}$  mode at 406.5 cm<sup>-1</sup> [311], as well as a broad Raman band associated with the double-resonance longitudinal acoustic mode 2LA(M) at 458 cm<sup>-1</sup> [312]. The observed relative Raman shift between the  $E_{2g}^1$  and the  $A_{1g}$  modes of 20.2 cm<sup>-1</sup> is in line with previous results for monolayer MoS<sub>2</sub> on Gr/Ir(111) [231]. Upon irradiation, the 2LA(M) mode vanishes, the  $E_{2g}^1$  peak transforms into a broad feature just above the noise level and centered at about 378.5 cm<sup>-1</sup>, and the  $A_{1g}$  drops strongly in intensity becoming broader (with a center at ~ 408 cm<sup>-1</sup>) due to an asymmetry towards higher energy. The intensity drop of all MoS<sub>2</sub> Raman modes indicates structural disorder consistent with amorphization. The observed red-shift of the  $E_{2g}^1$  and the blue-shift of the  $A_{1g}$  phonon frequency was previously reported for MoS<sub>2</sub> in the presence of sulfur vacancies, and it was explained by the modification of the restoring force constant and the total mass of the system [313], as well as by the phonon confinement effect [314, 315]. The characteristic  $E_{2g}^1$  and  $A_{1g}$  phonon modes of MoS<sub>2</sub> recover almost to the initial strength upon annealing [green line in Figure 5.8(b)], consistent with amorphization and recrystallization. Noteworthy, after annealing there is still an asymmetry of the  $E_{2g}^1$  peak toward lower energies and of the  $A_{1g}$  peak toward higher energies. This points towards the defects still present after the recrystallization process.

## 5.5 Conclusions

MD simulations show that at  $\theta = 75^\circ$  grazing incidence of a 500 eV Xe<sup>+</sup> beam on MoS<sub>2</sub> terraces selective sputtering of the top S-layer takes place, while the Mo-layer and the bottom S-layer become disordered, but not sputtered. The supporting Gr layer remains intact and since the Xe<sup>+</sup> projectile is reflected with 100% probability no implantation of Xe atoms takes place. In consequence, we observe already for ion fluences as low as  $1.5 \times 10^{14}$  ions/cm<sup>2</sup> amorphization of a MoS<sub>2</sub> monolayer on Gr/Ir(111) as evidenced by LEED, but without disruption of the monolayer as an entity: the

original island structure is preserved in the amorphous state as visible in the STM topography. In the amorphous state, the semiconducting gap of the monolayer is shown by STS to be largely closed by a continuum of in-gap states due to disorder and sulfur deficit. The PL peak of the pristine layer with a FWHM of only 13 meV is fully quenched in the amorphous state and Raman modes either disappear or are strongly diminished. Due to the island structure of the MoS<sub>2</sub> layer and the grazing incidence of the impinging ion beam, in addition to terrace sputtering investigated in our MD simulations, illuminated MoS<sub>2</sub> edges are efficiently sputtered. This effect largely accounts for the decrease of MoS<sub>2</sub> island coverage, but does not change the global picture. It would be absent for a complete MoS<sub>2</sub> layer. As evidenced by the single ion impacts, at higher ion energies Xe ions can penetrate the MoS<sub>2</sub> layer, which might enable implantation of Xe atoms and sputtering also in the bottom-S-layer.

As the amorphous phase is homogeneous without disruption, as its sulfur deficit is only moderate, and since the graphene underneath the MoS<sub>2</sub> remained intact upon amorphization, the MoS<sub>2</sub> recovers to the crystalline state by thermal annealing. After treatment at 1050 K, the residual point defect density is 0.05 defects/nm<sup>2</sup> (corresponding to about 4.5 nm separation), the semiconducting gap is fully re-established, and all phonon modes are in intensity again close to the initial value. However, PL does not recover. We have qualitatively explained the absence of PL in the annealed sample by comparing the defect-defect separation to the spatial extent of the exciton wavefunction. The absence of PL is also not at variance with the observation of a fully restored STS curve that we show in Figure 5.7. This is so because the STS was measured locally in a defect free region. In the PL measurements a larger region is probed, because of the spatial extent of the exciton. Therefore PL reacts sensitively to defects. Finally, the amorphous state recovers to a crystalline semiconducting state, irrespective of whether the thermal annealing is conducted in an S-vapor or not. In the later case additional metallic clusters are created due to the S-deficit in the amorphous phase, or the loss of sulfur during annealing, or both.

To sum up, we demonstrated that it is possible to selectively change the defect concentration or even amorphize the top layer of a heterostructure assembled from 2D materials, without disturbing or damaging the rest of the stack. In a combination with a thermal treatment and a reactive vapor this opens the possibilities to tune the properties of a single 2D layer in a stack in a wide range. This finding is likely to have relevance for future experiments with stacks of 2D layers or even in device prototyping based on such stacks. The method presented here might also provide a path to synthesize so-called Janus material with a MoSSe stoichiometry that has S (Se) on the upper (lower) plane with respect to Mo as realized by Ma *et al.* [285] and Lu *et al.* [316]. Such a material could be synthesized by low-energy grazing incidence ion irradiation resulting in sputtering of the upper S layer from a MoS<sub>2</sub> sample and subsequently selenizing it.



## CHAPTER 6

# Self-limited vacancy cluster growth in 2D material moirés

*The work presented in this chapter is not published yet. Publication is intended and a manuscript is in preparation [317]. It contains contributions from P. Valerius, C. Speckmann, N. Atodiresei, B. V. Senkovskiy, A. Grüneis, and T. Michely. I was responsible for the design of the experiments, carried out most of the STM and LEED measurements and data analysis. I wrote the draft of the manuscript with T. Michely. DFT calculations were provided by N. Atodiresei. C. Speckmann conducted experiments with h-BN on Pt(111) under my guidance as part of his bachelor thesis. I performed the Raman spectroscopy measurements under the guidance of B. V. Senkovskiy and A. Grüneis.*

### 6.1 Motivation

One key property of graphene and other 2D materials is the possibility of hosting nanopores in their lattices while offering atomic thicknesses. Both properties are requirements in order to fabricate ultimately thin filter membranes as barriers used for separation processes such as size selective mass transport. As discussed above, theoretical [17–19] and experimental [20–25] investigations predict a huge impact of graphene on filter membranes, because Gr is ultimately thin and able to host a dense array of nanometer-sized pores. Depending on the pore size a large variety of separation processes are applicable, e.g., atoms and molecules from gas mixtures [55], molecules or ions from solutions [20–22, 24, 25, 318] (compare Figure 1.10) and extraction of macro molecules such as DNA [319, 320]. We refer to recent review articles for additional information on the different types and possibilities on the production of such state of the art filter membranes based on graphene [27, 321–324].

Recently it was shown that low-energy ion irradiation of metal supported Gr at elevated temperatures can lead to the formation of a graphene nanomesh [26]. Compared to standard perforation techniques, such as etching or bottom-up synthesis [20, 27], the moiré based GNM yields a well-ordered and homogeneously distributed pore lattice with an outstanding pore density of  $10^{12}$  per  $\text{cm}^2$ . The pore diameters are in the range of 1 nm, which is a critical pore size necessary for molecular sieving processes and essential for water purification purposes [27]. The Gr/Ir(111) moiré superlattice [124]

has a periodicity about 10 times larger than the Ir unit cell. The binding strength of defects [26,140] depend on position within the moiré unit cell. For example in Gr on Ir(111), a tetra-vacancy placed at the FCC/HCP site is energetically favored by about 4 eV compared to the TOP site [26]. For a different supercell h-BN on Al(111), the energetic variation depending on the vacancy cluster position is about 6 eV [140].

In this chapter, we want to exploit the nanomesh formation mechanism in h-BN on Ir(111) and report on an improved regularity, ordering, and density compared to existing data in literature of graphene on Ir(111) [26]. We use low-energy He<sup>+</sup> ion irradiation on supported monolayers of h-BN on Ir(111) in order to induce single vacancy defects [82,83] while reducing implantation of foreign gas atoms in the substrate [254]. At elevated temperatures vacancies in supported 2D materials become mobile and coalesce to vacancy clusters [251,325]. These vacancy-like clusters are trapped at specific positions of the h-BN/Ir(111) moiré [26,140], resulting in a well ordered and ultimately dense array of nanopores, which is highly desirable for upcoming filtering devices [17]. During the investigation we have observed that the vacancy clusters growth ceases and the cluster size stagnates with increasing ion fluence. Apparently, clusters are unable to grow beyond a magic size. Instead, excess vacancies are expelled from the mesh and a far reaching migration is enabled towards domain boundaries or defects. We propose a bimodal growth model of vacancy structures: (i) vacancy clusters trapped in the moiré cell, and (ii) large vacancy islands with large lateral separation. Additionally, we explain how to optimize the cluster arrays and how they depend on parameters like temperature, ion fluence, ion energy, and ion species. Finally, it is demonstrated that vacancy cluster membranes can be detached from their metallic substrate holding the promise of application.

## 6.2 Vacancy cluster arrays in h-BN and Gr on Ir(111)

### Low-energy He<sup>+</sup> ion irradiation of h-BN on Ir(111) at elevated temperatures

One key factor for the realization of the Gr nanomesh is based on the potential landscape, which originates from the moiré with the Ir substrate [26]. Changing the size of the moiré unit cell could lead to the formation of differently spaced nanopores in the nanomesh. In this section we introduce the qualitative features of vacancy cluster arrays by high temperature 500 eV He<sup>+</sup> irradiation in a different moiré setup of hexagonal boron nitride on Ir(111), while a close comparison to Gr/Ir(111) will be drawn. As shown by Farwick *et al.* in Ref. 190, h-BN on Ir(111) forms an incommensurate (11.7 × 11.7) on (10.7 × 10.7) super cell, where the h-BN is strongly corrugated by 1.5 Å. The valley atoms are chemisorbed to Ir(111), while the h-BN in the surrounding mesas is physisorbed to Ir [186].

The STM topograph in Figure 6.1(a) shows a pristine h-BN layer on Ir(111) at a negative tunneling bias (compare the tunneling parameters in the box), where the moiré super cell with the periodicity of 2.9 nm is visible through a regular array of depressions (valleys). The moiré unit cell is indicated in the inset as a rhombus with the valley in its center. The STM topograph shown in Figure 6.1(b) displays the same area but recorded at a positive bias. Changing the polarity leads to a contrast

## 6.2 Vacancy cluster arrays in h-BN and Gr on Ir(111)

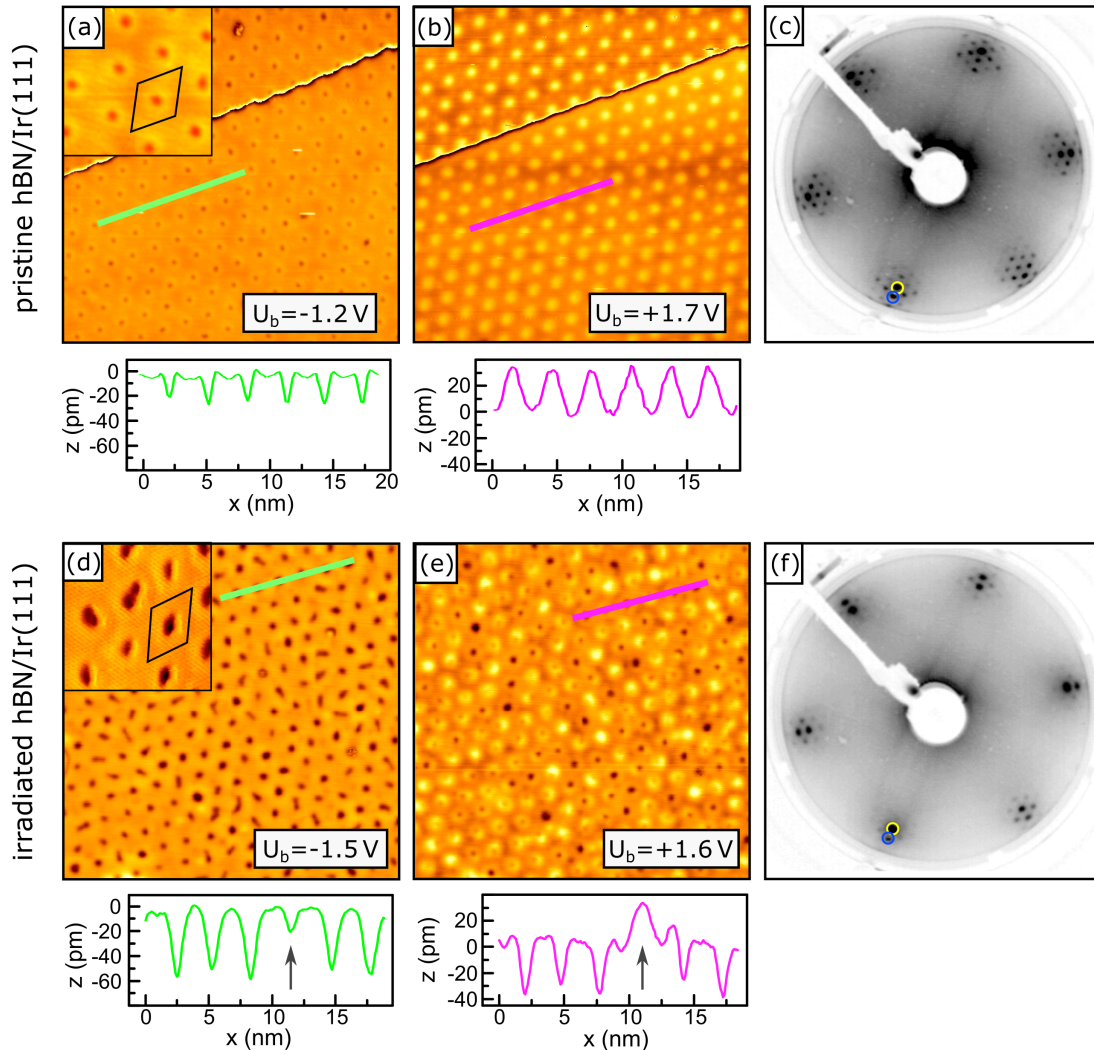


**Figure 6.1:** STM topographs, associated height profiles, and LEED measurements at 68 eV of (a-c) pristine h-BN/Ir(111) and (d-f) after exposure to 0.75 MLE 500 eV  $\text{He}^+$  at 1200 K. The blue and yellow circles in the LEED data highlight the first order h-BN and Ir-substrate spot, respectively. Insets in (a,d) are magnified views of the same sample. Image sizes are 45 nm  $\times$  45 nm and 11 nm  $\times$  11 nm for the insets. The tunneling bias  $U_t$  is stated in each topograph.

inversion in the topographs [189], where the valley sites appear as bright bumps. The apparent height corrugation changed from 20 pm to 40 pm (compare associated height profiles). The STM topograph in Figure 6.1(d) depicts the h-BN/Ir(111) sample after irradiation with 0.75 MLE of 500 eV  $\text{He}^+$  ions at 1200 K. The dark valley regions appear slightly larger compared to the pristine sample, while the apparent depth increased from about 20 pm to 60 pm as can be seen in the height profiles in Figure 6.1(a) and (d). Only one valley still shows a depth of 20 pm. The inset shows a magnified and atomically resolved region of the same sample. Identification of vacancy clusters is more reliable at positive bias, where valleys without vacancy clusters appear as protrusions with a

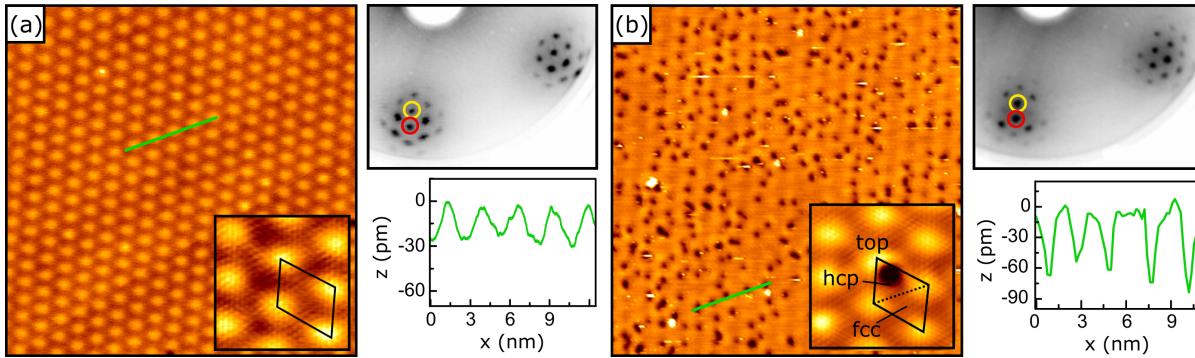


**Figure 6.2:** STM topographs, associated height profiles, and LEED measurement at 68 eV of (a) pristine Gr/Ir(111) and (b) sample shown in (a) after irradiation with 0.75 MLE 500 eV  $\text{He}^+$  at 1150 K. The red and yellow circle in the LEED data highlight the first order Gr and Ir-substrate spot, respectively. Insets in (a) and (b) are magnified views of the associated sample. The black rhombus indicates the moiré unit cell. Image sizes are 45 nm $\times$ 45 nm and 9 nm $\times$ 9 nm for the insets.

height of about 25 pm [compare Figure 6.1(b)]. As evidenced by the STM topograph in Figure 6.1(e) and the associated height profile, the vacancy clusters appear as dark spots with depths of about 40 pm, making their identification unambiguous. The valley sites that do not host a vacancy cluster still show an apparent height of 25 pm. The shapes of the vacancy islands are compact and circular. Due to their smallness, their convolution with the STM tip shape, and the contrast being determined also by electronic effects, it is not possible to give a reliable estimate about their shape and size. The LEED pattern for pristine h-BN shown in Figure 6.1(c) displays two orders of moiré reflexes, where the first order Ir and h-BN spots are highlighted by a yellow and blue circle, respectively. The high order of moiré reflexes indicates a perfect long-range order of the h-BN layer with respect to the Ir substrate. Upon irradiation the number of surrounding moiré reflections decreases [compare Figure 6.1(f)]. Consistent with the real space view, the moiré is preserved, though its perfection is decreased.

### Low-energy $\text{He}^+$ ion irradiation of Gr on Ir(111) at elevated temperatures

A similar self-organization process takes place for ion irradiation of Gr on Ir(111) which forms a moiré with a periodicity of 2.5 nm and a unit cell as depicted in the inset of Figure 6.2(a). We grew a complete monolayer as described in section 3.3. The pristine graphene sample morphology is shown in Figure 6.2(a). The STM topograph displays a well ordered moiré superlattice with barely any defects visible. The apparent height corrugation in the pristine moiré is about 30 pm (compare associated height profile).

We repeated the procedure for the nanomesh formation in h-BN/Ir(111) now for the Gr sample. The STM topograph in Figure 6.2(b) depicts the resulting morphology after exposing the sample shown in (a) to 500 eV 0.75 MLE  $\text{He}^+$  ions at 1150 K. A large number of vacancy clusters have formed in the majority of the moiré unit cells. As shown by the associated height profile, the vacancy

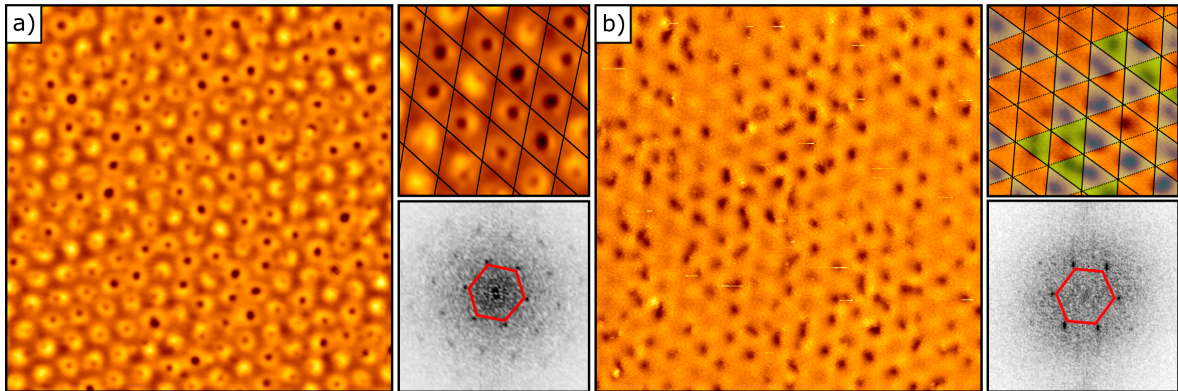


**Figure 6.3:** (a-c) STM topographs and FFT of h-BN/Ir(111) and (d-f) of Gr/Ir(111) exposed to 0.75 MLE 500 eV He ions at 1200 K and 1150 K, respectively. Image sizes are 36 nm  $\times$  36 nm and 13 nm  $\times$  13 nm for the magnified views. The moiré lattices of both systems are highlighted. The blue and green triangles mark the HCP and FCC areas in the Gr/Ir(111) superlattice that are hosting a vacancy cluster.

clusters have apparent depths of up to 90 pm and are laterally separated by 2.5 nm.<sup>1</sup> This significantly increases the height variation compared to pristine graphene. Some regularity in the arrangement of the vacancy clusters is apparent, but they are less accurately positioned as for h-BN/Ir(111). The reason for this is that there are two preferential vacancy cluster binding sites in each moiré cell, which are depicted by the centers of the two triangles as shown in the inset of Figure 6.2(b). The different regions of the moiré unit cell, that are the TOP, FCC, and HCP site are highlighted. Both HCP and FCC sites are populated by vacancy clusters, while they are absent in the bright areas in the corners of the moiré unit cell (TOP regions). The LEED pattern of the pristine Gr shows sharp Gr and Ir substrate spots, accompanied by the typical moiré satellites up to second-order [compare Figure 6.2(a)]. After irradiation, the LEED pattern reveals barely any change, except of a slightly reduced intensity of higher-order moiré satellites [compare Figure 6.2(b)], indicating that the moiré of the irradiated Gr is still very well ordered.

Figure 6.3 provides a side-by-side comparison of STM topographs and Fourier transformed (FFT) images of the nanomesh formed in (a) h-BN/Ir(111) and (b) Gr/Ir(111). The large-scale STM topographs in Figure 6.3(a) and (b) depict the h-BN and Gr samples after irradiation to 0.75 MLE of 500 eV He<sup>+</sup> irradiation at elevated temperatures, as discussed above. The black lattices in the magnified views indicate the moiré superlattices. It can be noted that the ordering of vacancy clusters in h-BN is very high. The vacancy clusters are solely located at the valley sites. By comparing the STM topographs in Figure 6.3(a) and (b) it can be directly noted that the vacancy clusters are less ordered in Gr/Ir(111). To determine the position of the vacancy clusters, we split the moiré lattice of Gr/Ir(111) into two different triangles. The up-pointing one represents the HCP and the down-pointing one the FCC region. We measured that around 59 % of the vacancy clusters populate a HCP region (blue triangles), 34 % an FCC region (green triangles), and 7 % a TOP region. The ratio of

<sup>1</sup>We note that the depths of vacancy clusters are not a reliably measure. In STM the apparent height of Gr on Ir(111) is 1.7 Å, while the geometrical adsorption height is 3.4 Å [126].

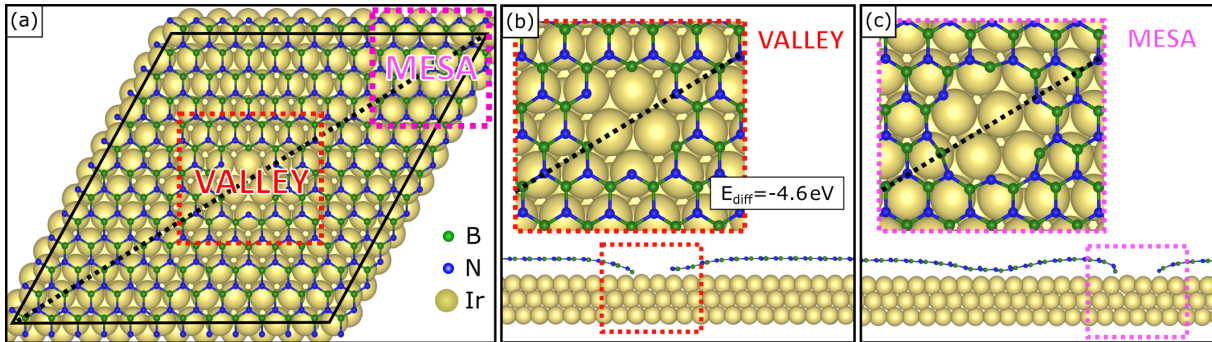


**Figure 6.4:** Ball model representation of relaxed DFT calculated vacancy structures within a commensurate  $(12 \times 12)_{\text{h-BN}}$  on  $(11 \times 11)_{\text{Ir}}$  supercell. (a) h-BN layer on Ir(111) containing a hexagonal shaped vacancy cluster with 6 atoms missing located at the valley site. The valley and mesa site are highlighted by a red and pink box, respectively. Green, blue, and yellow balls represent the B, N, and Ir atoms. (b) and (c) provide close up images of the defect structures within the marked regions in (a) and corresponding side views of a cut along the diagonal as marked by the black dashed line.

HCP : FCC : TOP occupation is about 8 : 5 : 1. To quantify the long-range order of the two systems, Fourier transformed images of both samples are provided. In Figure 6.3(a) the FFT image shows hexagonal spots at the edges of the red hexagon that correspond to the h-BN/Ir(111) moiré lattice. The higher-order spots indicate an exceptional ordering. In (b) the FFT image shows intense first order spots, while second- or higher-order spots are barely visible. Therefore, the ordering vacancy clusters in the moiré superlattice of h-BN/Ir(111) is clearly higher compared to in Gr/Ir(111).

### 6.3 Mechanism of vacancy cluster array formation in h-BN/Ir(111)

This chapter is dedicated to provide a model for the nanomesh formation mechanism in h-BN/Ir(111). An understanding of vacancy cluster array formation as described above is obtained by explaining why the vacancy clusters are observed only in the valley sites of the moiré. We analyze this observation with the help of DFT calculations for h-BN/Ir(111) of which examples are shown by the atomic models in Figure 6.4. The models represent the moiré with three B- and three N-atoms missing in the valley [red box in Figure 6.4(a) and (b)] and in the mesa [pink box in Figure 6.4(c)]. For reference, top and side views of the moiré unit cell without any vacancy cluster are provided in Figure 1.14(b). Figure 6.4(a) provides an overview of the approximated  $(12 \times 12)_{\text{h-BN}}$  on  $(11 \times 11)_{\text{Ir}}$  supercell marked by the black rhombus. As apparent from the top-view of Figure 6.4(c), some hexagons at the created h-BN edge are distorted and the h-BN bonds differ significantly from the optimum binding angles of  $120^\circ$ . The presented side views correspond to a cut along the diagonal indicated by the black dashed line. As apparent from the side view of Figure 6.4(b), the vacancy cluster in the valley does not cause a substantial disturbance of the h-BN flake. Only some valley atoms that have become the edge atoms move slightly closer to the Ir substrate due to the formation of new bonds. The remaining h-BN layer is completely flat. The situation is considerably different for the vacancy cluster in the mesa as shown in Figure 6.4(c). The edge atoms of the created vacancy cluster moved down

### 6.3 Mechanism of vacancy cluster array formation in h-BN/Ir(111)

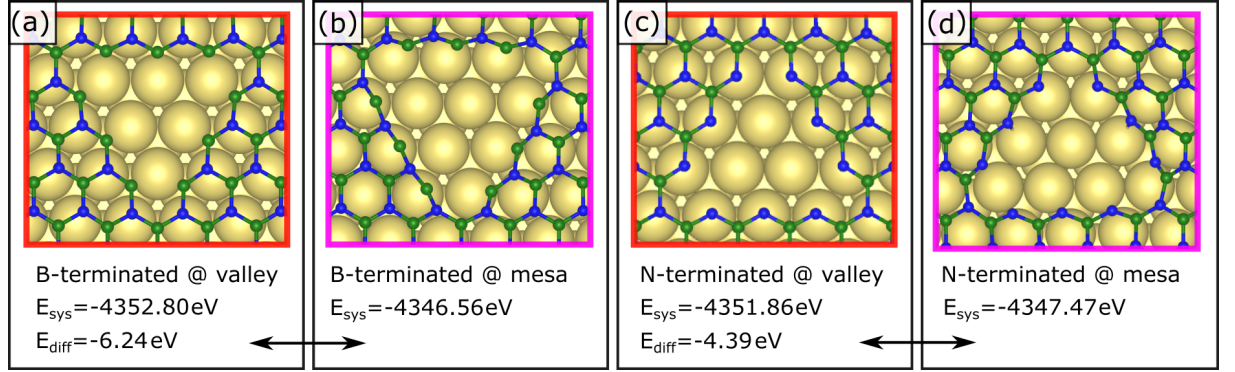


**Figure 6.5:** (a-d) Relaxed DFT calculated vacancy structures with nine atoms missing in the h-BN layer. In (a) and (b) three are B atoms and six N atoms were removed and vice versa in (c) and (d). The resulting edge termination is indicated. The red and pink box indicate whether the vacancy cluster is located in the valley or mesa, respectively. The system energies are given.

significantly from their initial mesa position in order to form bonds with Ir, causing a substantial deformation of the h-BN flake in their surrounding and a lowering of other atom positions. The downward movement of atoms that do not form additional bonds with Ir implies a drastic energy penalty. The height of the mesa atoms was determined by the equilibrium of vdW attraction and Pauli repulsion [compare Figure 1.14 and Ref. 190]. As they are dragged down by the vacancy cluster edge atoms, repulsive forces are acting on them. This repulsion is also reflected in the difference of the systems energy  $E_{\text{sys}}$  which is higher by 4.6 eV compared to the vacancy cluster located in the valley. The difference in system energy  $E_{\text{diff}}$  is defined as

$$E_{\text{diff}} = -(E_{\text{sys}}^{\text{valley}} - E_{\text{sys}}^{\text{mesa}}), \quad (6.1)$$

where  $E_{\text{sys}}^{\text{valley}}$  is the total energy of the relaxed vacancy structure located at the h-BN/Ir(111) valley site, and  $E_{\text{sys}}^{\text{mesa}}$  denotes the total energy of the h-BN layer including the vacancy structure located at the mesa site.

Figure 6.5 depicts additional atomic models of vacancy clusters with nine atoms missing, of which either three are B atoms and six are N atoms as shown in Figure 6.5(a) and (b)] or vice versa in Figure 6.5(c) and (d). The resulting edge termination is of zigzag type either terminated by B atoms or N atoms, respectively. The relaxed vacancy structures are triangular shaped. The red and pink box indicate whether the vacancy cluster is located in the valley or the mesa region, respectively. The vacancy structures located in the mesa are distorted with many in-plane bonds differing from the  $120^\circ$  binding angles. Interestingly, the system energies of the respective N-terminated vacancy structures are about 1 eV higher compared to the B-terminated ones. This could be an indication that B-edges are energetically preferred, which stands in line with the observation that B-terminated h-BN nano-flakes and intercalated h-BN flakes on Ir(111) are energetically favored [190, 251].<sup>2</sup> The

<sup>2</sup>We note that the energy difference for the vacancy structures is on the one hand smaller compared to h-BN nano

flake size investigated here is considerably larger compared to the h-BN flakes from the literature and we attribute the smaller energy difference to the smaller edge size or edge-to-flake ratio. The total energies of various vacancy structures as investigated within the scope of this work are shown in Table 6.1. The total energy is a negative quantity per definition, for reference we state the total energy of the pristine h-BN/Ir(111) supercell with no vacancy cluster. The corresponding vacancy structures are shown in Figure A.3 and Figure A.4 of the Scientific Appendix.

To conclude, based on our DFT calculations we can identify the valley region as the energetically preferred site to create a vacancy cluster. Even the energy difference between small vacancy clusters located in the valley or mesa is significant. This explains our experimental observations that we observe the formation of an array of vacancy clusters that are solely located at the valley sites.

## 6.4 Influence of the ion fluence and temperature on the nanomesh formation

In this section we investigate the influence of the ion fluence and irradiation temperature on the nanomesh formation. We aim to investigate the correlation between (i) ion fluence and vacancy cluster sizes and (ii) irradiation temperature and cluster density. A possible fluence-induced size tuning is of particular interest. The variation of irradiation temperature might improve the regularity of the nanomesh. Finally, we will conclude on the optimal irradiation conditions on how to form a regular nanomesh with a small size distribution of vacancy clusters.

**Table 6.1:** Calculated energies of different vacancy structures. The vacancy cluster size indicates the number of removed atoms, where B and N stands for the amount of B and N atoms removed. If applicable, (M) or (V) denote the mesa or valley site where the vacancy cluster was created.  $E_{\text{sys}}$  is the total energy of the system.

size-B-N	$E_{\text{sys}}$ [eV]
0-0-0	-4426.86
6-3-3 (M)	-4372.37
6-3-3 (V)	-4376.99
9-3-6 (M)	-4346.56
9-3-6 (V)	-4352.80
9-6-3 (M)	-4347.47
9-6-3 (V)	-4351.86
24-12-12	-4234.40
30-12-18	-4187.58
30-18-12	-4180.85
54-27-27	-3998.69

flakes, where the energy gain for B-terminated over N-terminated edges is about 0.45 eV per edge atom (here it is about 0.11 eV) and on the other hand the energy difference could stem from different internal energies, as the total number of B and N atoms vary.

## 6.4 Influence of the ion fluence and temperature on the nanomesh formation

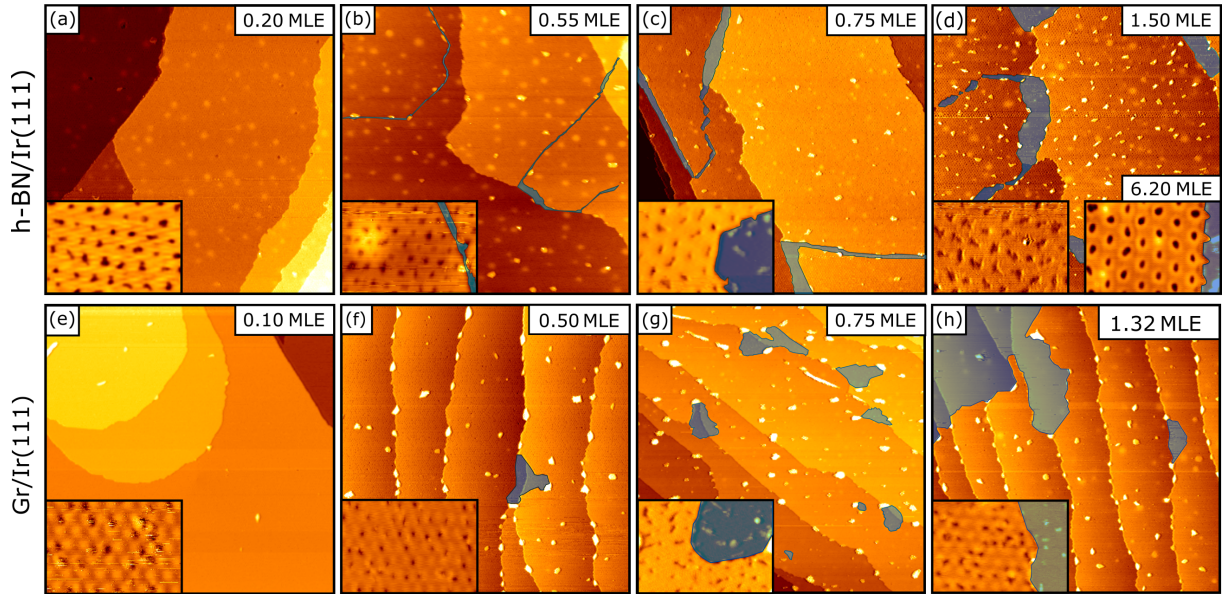


**Figure 6.6:** STM topographs with associated magnified views of an ion fluence series of (a-d) h-BN/Ir(111) and (e-h) Gr/Ir(111) exposed to 500 eV He<sup>+</sup> ions at 1200 K and 1150 K, respectively. The ion fluence is given in each image and ranges from 0.10 MLE to 1.50 MLE. Large vacancy islands are highlighted by blue coloring. Image sizes are 300 nm × 300 nm and 22 nm × 16 nm for the magnified topographs, respectively. The right inset in (d) corresponds to a sample irradiated with an ion fluence of 6.2 MLE.

### Variation of the ion fluence

The STM topographs in Figure 6.6(a)-(d) depict the surface morphologies of h-BN/Ir(111) irradiated with He<sup>+</sup> ions at 1200 K for different ion doses, as stated in the image. The STM topograph in Figure 6.6(a) shows the sample morphology irradiated with a relatively low ion dose of 0.2 MLE. Several Ir terraces are covered with a closed h-BN layer. Smooth bulges are visible, which can be attributed to implanted gas bubbles near the surface region of the Ir bulk [29, 251]. The inset shows a magnification of the same sample and reveals that vacancy clusters are located solely at the valleys. Figure 6.6(b) depicts the surface morphology after an ion dose of 0.55 MLE. Bright protrusions form on the terraces that can be identified as gas filled blisters at the h-BN/Ir(111) interface. Additionally, we observe dark stripes which are highlighted by the blue coloring. The dark stripes are attributed to vacancy islands which consecutively grow in size with increasing ion fluence [compare Figure 6.6(b)-(d)]. They form at the positions of domain boundaries which form between the two differently oriented h-BN grains [185]. The h-BN edge itself is a large scale defect that acts as a sink for mobile vacancies within the h-BN layer at elevated temperatures. Vacancies that attach to the h-BN edge widen the grain boundary significantly. The formation and widening of the dark stripes suggests a substantial erosion of the h-BN layer for large ion doses [compare STM topograph in Figure 6.6(d)]. The magnified views shown in the insets of Figure 6.6(b), (c), and (d) display

typical h-BN edges. Interestingly, the vacancy clusters do not increase in size for higher ion fluences, although more and more vacancies are created during the ion beam induced sputtering. The right inset in Figure 6.6(d) shows a magnified topograph of a much higher fluence of 6.2 MLE. Even for this very high ion dose, the vacancy size did not increase considerably.

In a similar manner, a fluence series for Gr/Ir(111) is presented in the STM topographs of Figure 6.6(e)-(h). The large scale STM topograph in Figure 6.6(f) shows the formation of large vacancy islands at an ion fluence of 0.5 MLE. The islands grow in size with increasing ion fluence [compare Figure 6.6(f)-(h)]. However, the shapes are different compared to h-BN/Ir(111) and can be explained by the absence of grain boundaries. Therefore, vacancies agglomerate at different sites, such as pre-existing blisters, wrinkles, or substrate step edges. Once a vacancy island has formed, it acts as a sink for additional vacancies. This is confirmed by the findings in Figure 6.6(h), where a very large vacancy island of the order of several hundred nm in diameter can be found after the exposure to 1.32 MLE. The insets of Figure 6.6(e)-(h) show that the size of vacancy cluster also stagnates for Gr/Ir(111) with larger ion fluences, similar to our findings for ion irradiation of h-BN/Ir(111).

The graphs shown in Figure 6.7 present the vacancy number density  $n$  per moiré unit cell and the amount of sputtered area depending on the ion fluence in (a) h-BN and (b) Gr on Ir(111). The amount of sputtered area is given with respect to a full monolayer and was determined by measuring the fractional areas of the large vacancy islands. The cluster number density represents how many vacancy clusters are present per moiré cell. Figure 6.7(a) and (b) display a gradual increase in  $n$  (full red dots) with ion fluence, until  $n$  saturates approaching unity. For Gr/Ir(111),  $n$  reaches its maximum at about 0.75 MLE of  $\text{He}^+$  ions. Remarkably for both cases, we observe an onset of substantial h-BN and Gr erosion after an ion dose of about 0.5 MLE, which is indicated by the kink in the blue dashed lines. For ion doses below 0.5 MLE, the sputtered area remains nearly 0, because we do not observe any large vacancy islands. This means that irradiating the h-BN/Ir(111) and Gr/Ir(111) sample with low ion doses leads solely to the formation of nanopores. In other words, the amount of vacancies created by 0.5 MLE 500 eV  $\text{He}^+$  ions are distributed within the nanomesh, without introducing large defects in the 2D layer. For ion doses above 0.5 MLE the vacancy cluster density only slightly increases, accompanied by the formation of larger vacancy islands.

The constant slope of the blue curves suggests that the pore size does not depend on the ion dose - and with that on the number of vacancies created in the 2D layer - once it reaches a critical size. It is rather a dynamic process that is balanced between created vacancies and vacancies that are expelled from the vacancy cluster at the high temperature. It is itself fascinating, that vacancy clusters can nucleate at temperatures above 1000 K, as vacancies are extremely mobile. Still many vacancy clusters survive the extreme high temperatures, indicating that the valley is a strong nucleation site for vacancy clusters, which is mediated through the formation of stable bonds between the h-BN and Gr edges with the Ir(111) surface.

We denote the removal of a vacancy (as a single or double vacancy) from a vacancy cluster as a re-evaporation process. An equilibrium hole size is reached when the number of created and re-evaporated vacancies within one moiré cell is identical. This means that the rate of re-evaporation

## 6.4 Influence of the ion fluence and temperature on the nanomesh formation

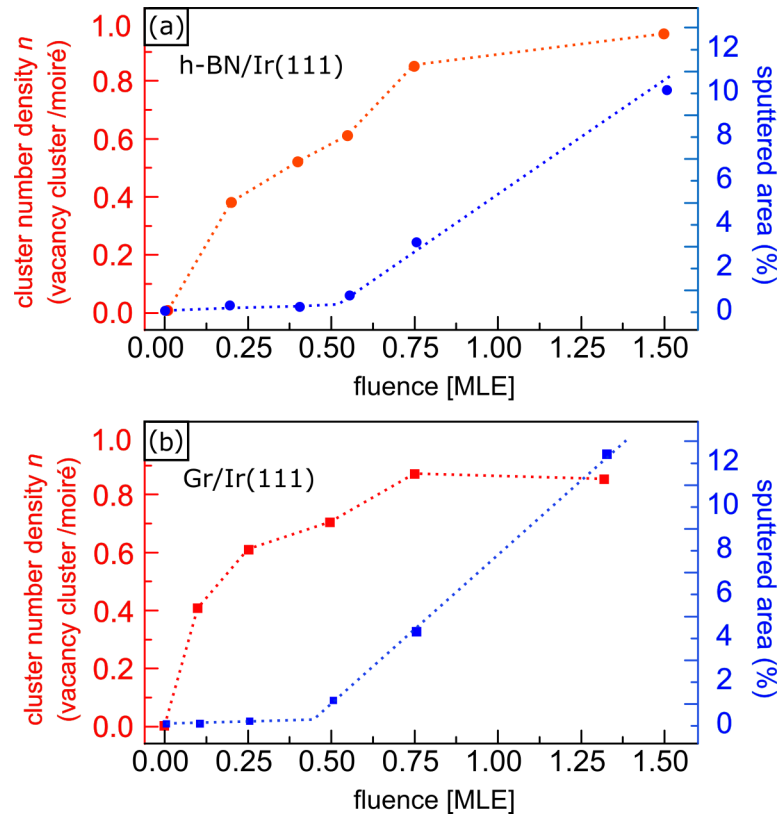


**Figure 6.7:** Evolution of the vacancy cluster number density  $n$  per moiré cell (red) and of the sputtered area (blue) for (a) h-BN/Ir(111) and (b) Gr/Ir(111) with the ion fluence of 500 eV He at 1200 K and 1150 K, respectively. With increasing ion fluence the number of moiré cells populated by a vacancy cluster increases until it saturates around 0.75 MLE. The formation of large vacancy islands in h-BN and Gr only sets in after an ion dose of about 0.5 MLE.

increases with cluster size or that the vapor pressure (of vacancies) increases with the size of a vacancy cluster, which is counter-intuitive. For instance, water droplets with smaller sizes (larger curvature) have higher vapor pressures than larger ones. Therefore, we assume that the edge energy is lower for larger vacancy clusters, that facilitates the diffusion of vacancies.

For Gr the nanopore formation and saturation of pore size happen in a similar way as for h-BN. The blue curve in Figure 6.7(b) indicates that the formation of large vacancy islands sets in at a slightly smaller ion dose of about 0.4 MLE. At the same, the slope of the blue curve for ion fluences ranging from 0.50 MLE to 1.50 MLE is steeper compared to h-BN. This means that the sputtering yield of 500 eV He<sup>+</sup> ions is larger for Gr/Ir(111). From the relation between the sputtered area and ion fluence (linear slope of the blue curves) we can determine a sputtering yield, which is  $Y_{\text{h-BN}} = 0.25$  for 500 eV He<sup>+</sup> for h-BN/Ir(111) and  $Y_{\text{Gr}} = 0.33$  for Gr/Ir(111), respectively. Compared to calculated sputtering yields of  $Y_{\text{h-BN}}^{\text{cal}} = 0.30$  and  $Y_{\text{Gr}}^{\text{cal}} = 0.20$ , these values are reasonable. We calculated the sputtering yields for 500 eV He<sup>+</sup> ions impinging on a graphitic carbon layer and a BN-compound layer on an Ir slab using the SRIM code [31]. Using the experimentally determined sputtering yields, we can estimate the average size of a vacancy cluster in the h-BN and Gr nanomesh to consist of

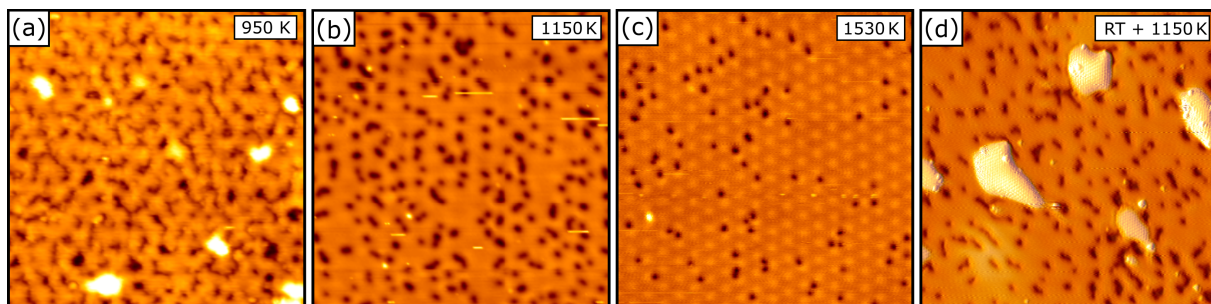


**Figure 6.8:** STM topographs of Gr/Ir(111) exposed to 0.75 MLE 500 eV He<sup>+</sup> at (a) 950 K, (b) 1150 K, (c) 1530 K, and (d) at room temperature and subsequently annealed to 1150 K. Image sizes are 30 nm × 30 nm.

15 and 12 atoms missing, respectively. To conclude, we have shown that the vacancy cluster size stagnates with large ion doses. There is an onset for the formation of large vacancy island, indicating a bimodal growth model of vacancies in the 2D moiré system. First, the vacancies are locally trapped at the valley sites, until nearly each moiré cell hosts a vacancy cluster of a certain size. Then, excess vacancies agglomerate towards global sinks which are given by large scale defects or substrate edges and form vacancy islands. We note that large vacancy islands are detrimental to filtering processes.

### Variation of the irradiation temperature for the nanomesh formation

As presented above, He<sup>+</sup> ion irradiation of Gr and h-BN on Ir(111) at elevated temperatures leads to the formation of a nanomesh. Based on our DFT results, the total energy of the system can be significantly lowered when the vacancy cluster is located at the valley. Therefore, the irradiation temperature plays a key role in the nanomesh formation process, as the provided thermal energy activates the effective diffusion of vacancies towards the valley site within each moiré unit cell. Additionally, we have observed that the vacancy cluster size stagnates with ion fluence - through re-evaporating of excess vacancies. Therefore, the vacancy size might be controllable through a temperature variation. In this section we investigate the influence of irradiation temperature first on the nanomesh formation in Gr, then compare the results to the nanomesh formation in h-BN.

### 500eV He<sup>+</sup> ion irradiation of Gr/Ir(111) at various temperatures

The STM topographs in Figure 6.8 represents a series of the Gr/Ir(111) sample after exposure to 0.75 MLE He<sup>+</sup> ions at different temperatures. The topograph in Figure 6.8(a) shows the Gr surface after ion irradiation at a temperature of 950 K. Dark trenches can be observed that have formed along several moiré cells. They can be attributed to vacancy clusters of different moiré cells that coalesced to larger dendritic vacancy cluster aggregates. Additionally, bright protrusions appear which are due to implanted ions at the Gr/Ir(111) interface [29]. It can be argued that due to the low sample temperature, the noble gas atoms were not able to escape from the interface region into the vacuum. Repeating the irradiation experiment at a higher temperature of 1150 K shows that

## 6.4 Influence of the ion fluence and temperature on the nanomesh formation

the dark trenches disappear [see STM topograph in Figure 6.8(b)]. Only small and roundly shaped depressions are left, distinctly located at the FCC/HCP sites of the moiré. As apparent from the STM topograph in Figure 6.8(c), at a very high irradiation temperature of 1530 K, large areas exhibit an unperturbed Gr/Ir(111) moiré. The defect density has drastically decreased. We have also conducted the irradiation experiment at room temperature and subsequently annealed the sample to 1150 K. The resulting morphology is shown in the topograph of Figure 6.8(d). The amount of He filled blisters at the Gr/Ir interface is significantly higher compared to the sample shown in Figure 6.8(b), which was irradiated at 1150 K. The increased blister density is due to a higher trapping efficiency of noble gas atoms at lower temperatures [29]. However, the number of vacancy clusters is similar. We find that some vacancy clusters near blisters are elongated and spread out over several moiré cells. We presume that blisters locally induce stress and deformation in the Gr sheet and therefore influence the vacancy agglomeration.

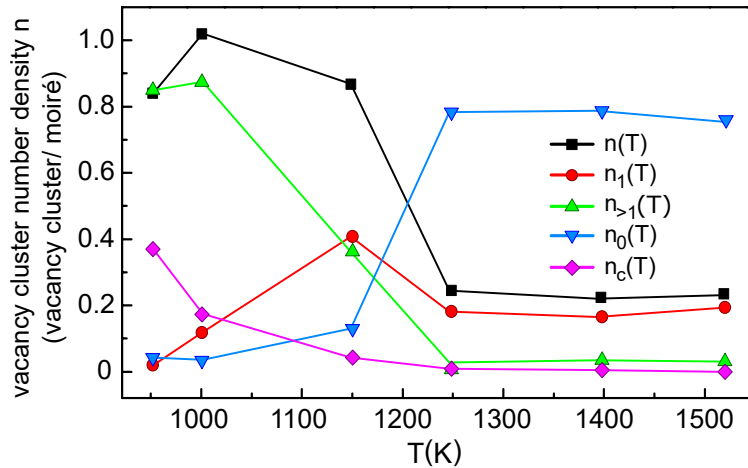


**Figure 6.9:** Analysis of vacancy cluster number density  $n$  per moiré unit cell, moiré cells with exactly one vacancy cluster  $n_1$ , more than one  $n_{>1}$ , without any  $n_0$ , and with a coalesced cluster  $n_c$  as a function of temperature  $T$ . Ion fluence for all data points is  $F = 0.75$  MLE.

The graph shown in Figure 6.9 analyzes the total vacancy cluster number density  $n$  (black curve) as a function of temperature. In order to understand it quantitatively we also compare the number of moiré cells containing exactly one  $n_1$  (red curve), none  $n_0$  (blue curve), more than one  $n_{>1}$  (green curve), and multiple coalesced  $n_c$  (pink curve) vacancy clusters. The overall vacancy density  $n$  initially increases from 950 K to 1150 K. For irradiation temperatures above 1250 K the vacancy density drastically reduces to 0.3 and stays constant for even higher temperatures. The initial in-

crease of the total vacancy density can be explained by the decrease of coalesced clusters  $n_c$ . That split up into several smaller clusters. The dark trenches visible after irradiation at 950 K [Figure 6.8(a)] form as either the mobility of vacancies within the Gr lattice is too small to arrange within one moiré unit cell or to migrate beyond towards a global sink. Therefore, the vacancy clusters also appear in the energetically unfavorable TOP region, which ultimately enables coalescence with vacancy cluster from the neighboring HCP or FCC region from the same and/or the adjacent moiré cell. With increasing irradiation temperature, the created vacancies have enough energy to migrate freely within the moiré cell and finally agglomerate at the HCP/FCC site to form stable clusters. At 1250 K the total number density  $n$  displays a pronounced drop. This drop is due to a step-like reduction in nucleation probability, which consequently reduces the number of occupied moiré cells  $n$ , while the number of moiré cells without defects  $n_0$  increases significantly. This indicates

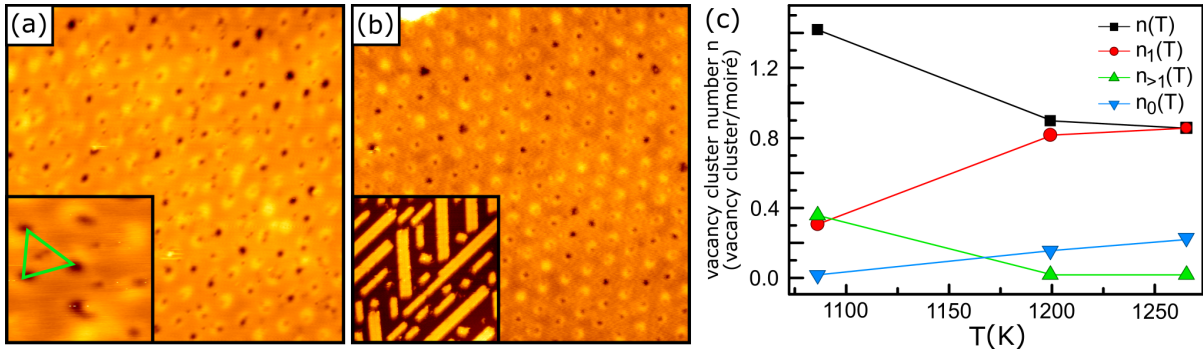


**Figure 6.10:** STM topographs shown with positive tunneling bias of h-BN on Ir(111) irradiated with 0.75 MLE 500 eV He<sup>+</sup> at (a) 1073 K and (b) 1270 K. (c) Analysis of total vacancy cluster density  $n$ , moiré cells containing exactly one vacancy cluster  $n_1$ , moiré cells containing more than one  $n_{>1}$ , and moiré cells without vacancy cluster  $n_0$  for irradiated h-BN on Ir(111) as a function of temperature  $T$ . Image sizes are 40 nm × 40 nm, for the inset in (a) it is 8 nm × 8 nm, and in (b) it is 62 nm × 62 nm.

that vacancy migration beyond one moiré unit cell to the next is possible. Vacancies ultimately heal out at Gr edges or large defects, such as substrate step edges and wrinkles [325]. It should be noted that for lower temperatures we also observe formation of large vacancy islands, but only for larger ion doses. From Figure 6.9 it becomes apparent that  $n_1$ , the density of moiré cells containing exactly one vacancy cluster per moiré cell, has a maximum at 1150 K. From this we conclude that ion irradiation of Gr/Ir(111) around 1150 K yields the optimal condition for the purpose of creating a highly ordered nanomesh with the highest possible density of vacancy clusters. For lower temperatures the pore size is larger, but the number and ordering is hardly controllable due to coalescence of vacancy clusters. For higher temperatures the number of vacancy clusters drastically reduces, resulting in a less dense array of nanopores.

### 500eV He<sup>+</sup> ion irradiation of h-BN/Ir(111) at various temperatures

Due to the hetero-elemental composition in h-BN, vacancy migration is suppressed to some extent compared to Gr [92]. However, in previous a experiment we have shown that bond re-organization and vacancy migration is still possible, resulting in a perfect recrystallization of the h-BN after largely destroying it [251]. These effects might result in a very different behavior than what was found for Gr/Ir(111) which will be addressed in this section. The STM topograph in Figure 6.10(a) shows h-BN/Ir(111) after He<sup>+</sup> irradiation at 1073 K at a positive tunneling bias. As shown previously, a high amount of valley sites appear dark in the center, indicating the formation of vacancy clusters. Additionally, small dark spots have formed between three adjacent valleys, as shown by the higher resolved topograph in the inset (see green triangle). The irradiation at a reduced temperature yields a very high vacancy cluster density, but the exceptional ordering by having exactly one vacancy cluster at the valley site is lost [compare Figure 6.1(d) and (e)]. The STM topograph in Figure 6.10(b) depicts the sample surface irradiated at 1273 K. While vacancy clusters are still present at the valley locations in a high number, already a significant amount of moiré cells are free of any defects. Addi-

## 6.5 Influence of ion species and grazing incidence on the nanomesh formation

tionally, defects at interstitial sites are abundant. Therefore, as argued before, the interstitial defects are the result of a reduced migration mobility within the moiré unit cell, for larger temperatures, vacancy clusters are solely present at center of the valley region. However, as shown by the inset, at temperatures of 1273 K, areas covered with striped islands appear, which can be assigned to decomposed h-BN [191, 251].

Figure 6.10 shows again the evolution of the vacancy cluster density with the irradiation temperature. As shown by the black curve in the graph of Figure 6.10(c), the total vacancy cluster number density  $n$  is higher for lower temperatures. The ordering of vacancy clusters in h-BN nanomeshes peaks around 1270 K, evidenced by the maximized number of moiré cells containing exactly one vacancy cluster  $n_1$  (red curve), while the number of moiré cells containing more than one vacancy defect  $n_{>1}$  is reduced (green curve). At 1270 K all populated moiré cells contain exactly one vacancy cluster (black and red curve cross). Additionally, a considerable amount of moiré cells are free of any defects [compare  $n_0$  (blue curve)], indicating that vacancies can migrate into neighboring moiré unit cells. However, the thermal instability of the h-BN layer for temperatures above 1200 K leads to a decomposition of the layer into striped islands. Disregarding decomposition, the highest temperature of irradiation appears optimum, but in terms of reproducibility it seems mandatory to a safe distance in temperature from decomposition conditions. Therefore, the most promising irradiation temperature in order to fabricate a well-ordered h-BN nanomesh membrane is at 1200 K, which is noticeably higher than for Gr/Ir(111).

## 6.5 Influence of ion species and grazing incidence on the nanomesh formation

In this section we want to address the influence of different ion species on the formation of the nanomesh. With our initial approach we used  $\text{He}^+$  ions, as for He the tendency to form blisters is expected to be minimal [212]. Additionally, solely the formation of single vacancies upon collision is to be expected. Ions with larger radii, such as  $\text{Xe}^+$ , are expected to induce more complex vacancy structures in Gr and h-BN even for low ion energies [82, 83]. Compared to single vacancies, the mobility of complex defect structures will be drastically lower, which might have detrimental effects on the nanomesh formation. On the other hand, the increased sputtering yield of larger noble gas ions increases the flux<sup>3</sup> of created vacancies. A higher vacancy flux could enable the formation of larger vacancy clusters, as it will be discussed in more detail in the following.

The STM topographs in Figure 6.11 show a series for irradiated h-BN/Ir(111) for varying ion species, energies, and irradiation temperature. The morphology shown in Figure 6.11(a) is the previously shown nanomesh after exposing h-BN/Ir(111) to 500 eV  $\text{He}^+$  ions at 1200 K. These irradiation parameters resemble a high re-evaporation rate of individual vacancies (high temperature) and a low

<sup>3</sup>We denote the number of created vacancy per time interval as the vacancy flux. A low ion flux of low-energy  $\text{He}^+$  ions creates less vacancies compared to a high ion flux and therefore corresponds to a low vacancy flux. Additionally, larger ions at similar ion fluxes would create more vacancies per ion incident and thus yield a larger vacancy flux.

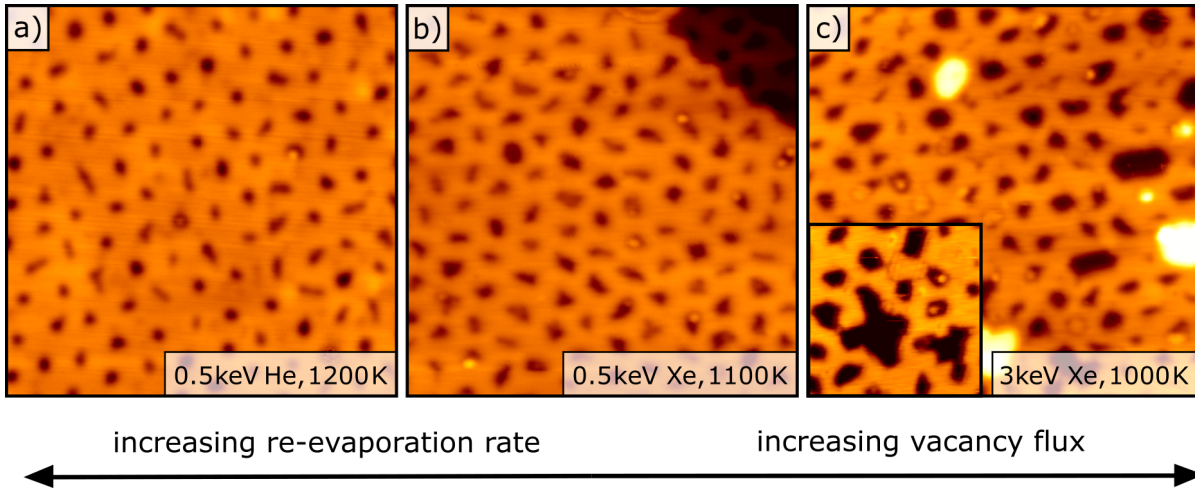


**Figure 6.11:** Comparison of STM topographs of h-BN/Ir(111) for different ion species and irradiation temperatures. The sample shown in (a) was exposed to 500 eV 0.8 MLE He<sup>+</sup> ions at 1200 K, (b) to 500 eV 0.1 MLE Xe<sup>+</sup> ions at 1100 K, and (c) to 3 keV 0.1 MLE Xe<sup>+</sup> ions at 1000 K. The arrow indicates higher irradiation temperatures to the left (higher re-evaporation rate of vacancies) and larger amounts of created vacancies per ion to the right. The inset in (c) is a magnified view of the same sample. Image sizes are 50 nm×50 nm and 15 nm×13 nm for the inset.

flux of induced vacancies (low ion energy, low ion mass). The arrow indicates a higher re-evaporation rate of vacancies from the vacancy cluster to the left. The number of created vacancies increases with ion mass and ion energy, which is highlighted by the arrow pointing to the right. The resulting vacancy clusters order well with the moiré and show a narrow size distribution. Figure 6.11(b) displays the sample morphology after exposing h-BN/Ir(111) to 500 eV Xe<sup>+</sup> at 1100 K. The nanomesh is still well-ordered and the vacancy clusters are limited to the moiré cell. It appears that the average hole size has increased. Due to the higher ion mass, the sputtering of B and N atoms increases. Therefore a larger number of vacancies are created upon ion impact, giving rise to larger holes. We note that the ion flux measured with the Faraday cup was similar for the He<sup>+</sup> ions (1.8 nA) and Xe<sup>+</sup> ions (1.5 nA). To further increase the effect of higher vacancy flux and lower re-evaporation rate, we repeated the process with a much larger ion energy and even lower temperature. The STM topograph in Figure 6.11(c) depicts the h-BN/Ir(111) surface exposed to 3 keV Xe<sup>+</sup> ions at 1000 K. Clearly, the size of the vacancy clusters has increased with some extending over more than one moiré cell. The combination of a higher vacancy flux and lower re-evaporation rate indeed leads to larger hole sizes. However, the overall ordering has reduced, which is in line with the lower irradiation temperature, as discussed above. The inset in Figure 6.11(c) is a magnified view of the same sample surface, showing vacancy clusters which extend over several moiré cells. We conclude that the vacancy cluster size is controllable by adjusting the irradiation parameters, *i.e.*, larger vacancy fluxes or lower irradiation temperatures yield larger vacancy clusters. Additionally, it has been shown that vacancy clusters coalesce, when their expansion is no longer confined within one moiré unit cell.

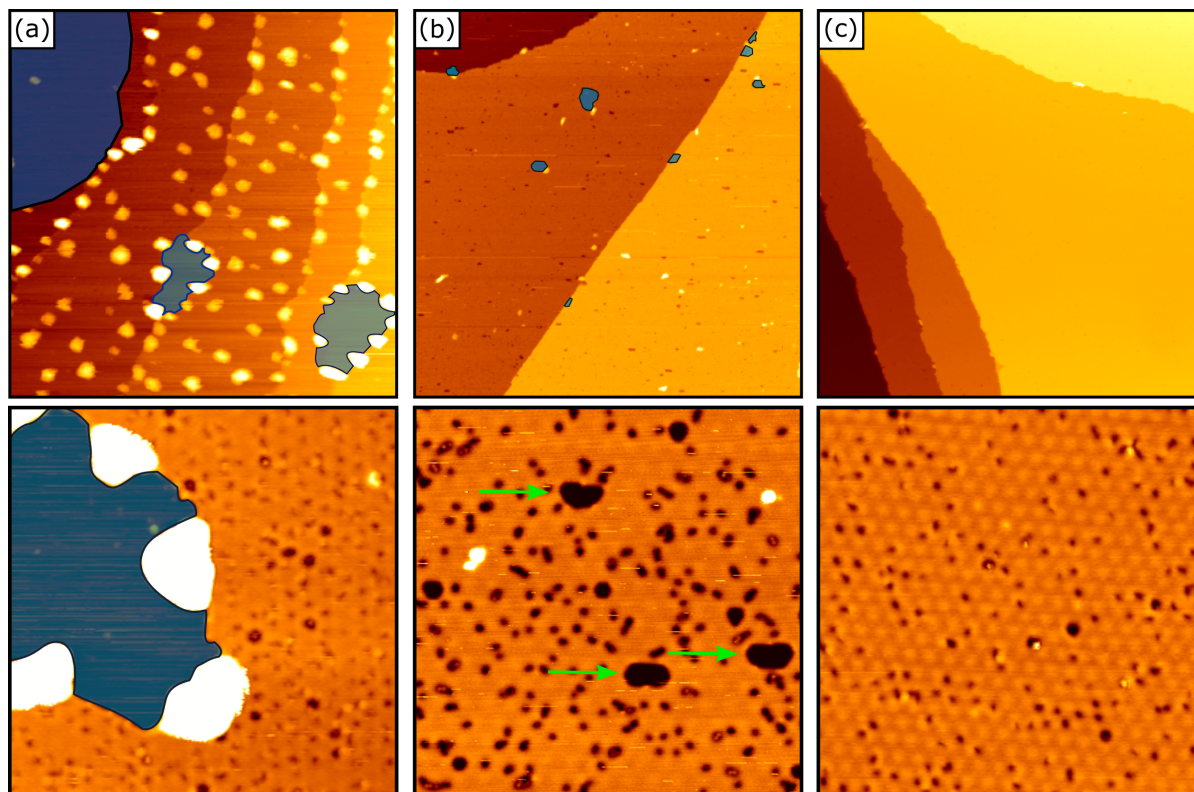


**Figure 6.12:** STM topographs with associated magnified views of Gr/Ir(111) exposed to (a) 0.50 MLE 500 eV Xe at normal incidence at 1150 K. (b) Same as (a) but with the ion beam  $75^\circ$  off normal. Vacancy islands are marked in a blue color. Green arrows indicate azimuthal ion beam direction and highlight extended vacancy clusters. (c) Same as (b) but with a lower ion fluence of 0.2 MLE. Image sizes are  $355\text{ nm} \times 355\text{ nm}$  and  $50\text{ nm} \times 50\text{ nm}$  for the magnified views.

### Nanomesh formation in Gr/Ir(111) under grazing ion incidence

Next we will focus on the effect of different ion species on the nanomesh formation in Gr/Ir(111). Figure 6.12 represents the Gr/Ir(111) surfaces irradiated with  $\text{Xe}^+$  ions at 1150 K for varying ion incidence angles and ion fluences. The STM topograph shown in Figure 6.12(a) displays the Gr/Ir(111) morphology after irradiation with 0.50 MLE 500 eV  $\text{Xe}^+$  ions at normal incidence. The sample is covered with gas filled blisters, which are preferentially located at Ir step edges or vacancy island edges. Compared to prior experiments these blister are larger in size. Moreover, large vacancy islands are present, indicating substantial erosion of the Gr sheet. The close up image depicts small vacancy clusters within the Gr, while also exposing some gas blisters at the vacancy island edge. The large vacancy islands and the large number of blisters are not beneficial for creating a well-ordered nanomesh. As reported by Herbig *et al.* in Ref. 254, blister formation is drastically reduced for ion beams at grazing incidence. Therefore, we repeated the experiment with a different polar angle of the incoming ion beam, now  $75^\circ$  off the surface normal in order to reduce the blister formation. Additionally, by choosing the proper grazing angle the kinetic energy normal to the surface can be tuned to sufficiently low values, such that mostly single vacancies are created. The resulting mor-

phology is presented in the STM topograph shown in Figure 6.12(b). In fact, the amount and size of the blisters has drastically reduced and only very few and smaller vacancy islands are visible. As shown by the magnified image, the vacancy cluster density is still high, while some larger vacancy clusters are present that extend over several moiré cells. The extended clusters, as highlighted by the green arrows, grow preferentially in the azimuthal direction of the ion beam, which can be explained by the preferential step edge sputtering. To achieve a uniform nanomesh and avoid larger vacancy islands, we reduce the ion fluence of the  $\text{Xe}^+$  ions to an ion dose of 0.2 MLE. The corresponding morphology is shown in Figure 6.12(c). The large scale topograph reveals a very clean surface, free of any blisters or large vacancy islands. Nevertheless, the magnified view shows that still a considerable amount of vacancy clusters form, which however is inferior in density to the He irradiated sample. We do not observe a considerable change in size of the vacancy cluster for low ion doses, which indicates that the vacancy flux created by grazing  $\text{Xe}^+$  ions is not significantly higher compared to  $\text{He}^+$  ion at normal incidence. To conclude, low-energy  $\text{Xe}^+$  irradiation at grazing incidence yields an elegant alternative to using normal incidence  $\text{He}^+$  beams, which results in a very clean formation of a nanomesh with barely any gas implantation. While the cluster size distribution is excellent if the ion dose is limited to 0.2 MLE, the vacancy cluster density is lower compared to  $\text{He}^+$  ion irradiation.

### 6.6 Low-energy $\text{He}^+$ ion irradiation of h-BN on Pt(111) at elevated temperatures

In section 4.6, we briefly discussed the influence of the substrate on the annealing behavior of irradiated h-BN. Although the moiré pattern on h-BN/Pt(111) is similar to h-BN/Ir(111), it is not clear whether a nanomesh forms in h-BN/Pt(111). The formation of the nanomesh is based on the energy gain of a vacancy cluster when migrating towards a specific location within the moiré unit cell. Because the h-BN - Pt interaction is significantly lower than h-BN - Ir, the energy distribution is expected to be different for h-BN/Pt(111). In this section we apply the irradiation technique used in section 6.2 to investigate the possibility of creating a nanomesh in h-BN/Pt(111) and to test the generality of the nanomesh formation using the energy landscape of a 2D material moiré. Figure 6.13 displays STM topographs and LEED images of pristine h-BN/Pt(111) and h-BN/Pt(111) exposed to 500 eV  $\text{He}^+$  ions at (b) 1100 K and (c) 1200 K. The STM topograph in Figure 6.13(a) displays a well-ordered h-BN/Pt(111) moiré lattice of the  $0^\circ$  domain. Its distinct LEED pattern shows intense spots with second order moiré satellites corresponding to the  $0^\circ$ -domain, and slight intensity for  $15^\circ$  and  $30^\circ$  rotated domains, indicating an overall well-ordered h-BN layer on Pt(111).

Similarly to the recipe used for the nanomesh formation in h-BN/Ir(111), the sample shown in Figure 6.13(a) was exposed to 0.75 MLE 500 eV  $\text{He}^+$  ions at elevated temperatures. Single vacancies created upon ion impact in the h-BN layer can migrate towards the energetically most favorable position within the moiré unit cell. We reduced the irradiation temperature to 1100 K, because the substrate interaction is slightly lower compared to Ir(111) [187]. The corresponding topograph is displayed in Figure 6.13(b). The large STM topograph displays a well-ordered moiré with small

## 6.6 Low-energy He<sup>+</sup> ion irradiation of h-BN on Pt(111) at elevated temperatures

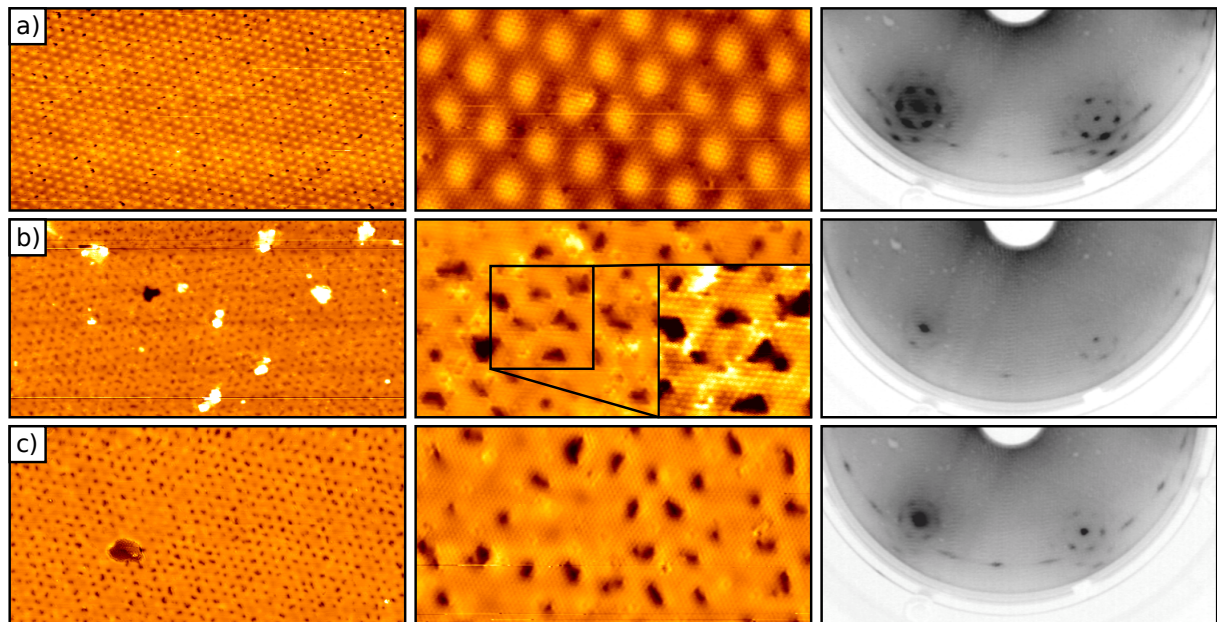


**Figure 6.13:** STM topographs and LEED measurements of (a) pristine h-BN on Pt(111). (b) Sample shown in (a) after exposure to 0.75 MLE 500 eV He<sup>+</sup> at 1100 K. (c) h-BN on Pt(111) after exposure to 0.75 MLE 500 eV He<sup>+</sup> at 1200 K. Image sizes are 90 nm×45 nm (left) and 22.5 nm×11.3 nm (middle); for the inset it is 6 nm×6 nm. LEED energy is 68 eV.

depressions in nearly each moiré cell, which indicates a successful nanomesh formation. However, some bright protrusions correlated to trapped gas atoms are present at the interface of h-BN/Pt(111). The LEED pattern still shows sharp spots for the Pt(111), the aligned, and 30° rotated h-BN domain, indicating that the h-BN integrity is still intact. The close-up image in Figure 6.13(b) confirms the formation of a regular vacancy cluster lattice. The inset provides an atomically resolved image with adjusted contrast in order to highlight the defect structures. Apparently, the vacancy clusters are not of uniform size and shape. Additionally, interstitial single vacancies are still present between the valley sites of the moiré. Suggesting that either the energy gain for a vacancy to combine at the valley site into a vacancy cluster is too small or the kinetic energy provided by heating is too low, to efficiently activate the migration of each vacancy. Therefore, in order to lower the density of the interstitial vacancies, the experiment was repeated at a higher temperature of 1200 K. The corresponding morphology is presented in Figure 6.13(c). The large scale STM topograph shows a well ordered nanomesh, with a high density of vacancy clusters. A depression close to the center of the image can be correlated with a gas filled blister. The magnified view shows a reduced amount of interstitial vacancies between the valley sites and more compact vacancy clusters. The LEED pattern indicates an overall improved ordering within the h-BN lattice. The diffraction spots for h-BN and the accompanying moiré with Pt(111) are slightly more intense compared to Figure 6.13(b).

To sum up, the nanomesh formation in h-BN/Pt(111) is indeed feasible. Besides the comparably weak substrate interaction, the vacancy clusters agglomerate only at one specific site of the moiré cell. However, single vacancy defects are present in between the valley sites. It should be noted that the experiments presented here correspond only to the aligned domain of h-BN with respect to the Pt substrate. The rotated h-BN domains, which exhibit largely different moiré superlattices were not investigated.

### 6.7 Intercalation of a h-BN sheet on Ir(111)

Prior to transferring the 2D membrane from the metal substrate, *e.g.*, by hydrogen bubbling transfer, it is helpful to weaken the substrate interaction. This can be achieved by, *e.g.*, intercalating foreign species at the interface region of the 2D sheet and its support. Therefore, we have examined the intercalation of Eu below h-BN monolayers on Ir(111). To test the generality of the process, we have expanded the investigation to the intercalation of Au at the h-BN/Ir(111) interface. As a final step a nanomesh membrane resting on Ir(111) was also tested. Figure 6.14 displays a LEED and STM series of Eu intercalation in h-BN/Ir(111). Figure 6.14(a) shows a LEED pattern of the pristine h-BN/Ir(111), where the typical moiré pattern of h-BN/Ir(111) is visible with sharp spots up to third order, indicating the successful growth of a well-ordered h-BN layer.

The sample of Figure 6.14(a) was subsequently exposed to Eu vapor at about 750 K. The high temperature during Eu exposure enables Eu intercalation. The LEED patterns in Figure 6.14(b-d) present a series of the h-BN/Ir(111) surface exposed to an increasing amount of Eu. Strikingly, the Eu forms well-ordered structures at the interface of h-BN/Ir(111). For a rather small amount of about 0.43 ML<sup>4</sup> Eu, a clear (2 × 2) superstructure with respect to Ir(111) evolves (see blue circles), which correlates to a low density phase of Eu (compare Refs. 266, 326, 327). After increasing the deposited amount of Eu to 0.86 ML, the LEED pattern in Figure 6.14(c) shows that the (2 × 2) still exists, while additional spots (green circles) appear which can be correlated to a ( $\sqrt{3} \times \sqrt{3}$ ) superstructure w.r.t. to Ir(111). This phase is more dense, compared to the (2 × 2)-phase and indicates that indeed more Eu is intercalated at the interface of h-BN/Ir(111). To check whether it is possible to reach an even denser phase, additional Eu was evaporated. The LEED pattern in Figure 6.14(d) correspond to the sample after exposure to 1.29 ML of Eu. Apparently, clear diffraction spots correlating to the dense ( $\sqrt{3} \times \sqrt{3}$ )-phase are visible, while the less dense (2 × 2)-phase is absent. This indicates that the intercalation of a homogeneous and dense phase of Eu is possible.

The STM topographs in Figure 6.14(e-h) represent the changes in the morphology of h-BN/Ir(111) for the different amounts of intercalated Eu. Figure 6.14(e) depicts the sample after depositing only a tiny amount of 0.05 ML Eu, highlighting the formation of small Eu islands and wires below the h-BN layer. After increasing the amount of Eu to 0.43 ML, the resulting morphology is shown in Figure 6.14(f). A high number of small islands ordered along the high symmetry directions of the h-

---

<sup>4</sup>Intercalated Eu amounts are specified in monolayers (ML), where 1 ML (or 100% ML) corresponds to a full (2 × 2) intercalation layer with respect to the Gr lattice.

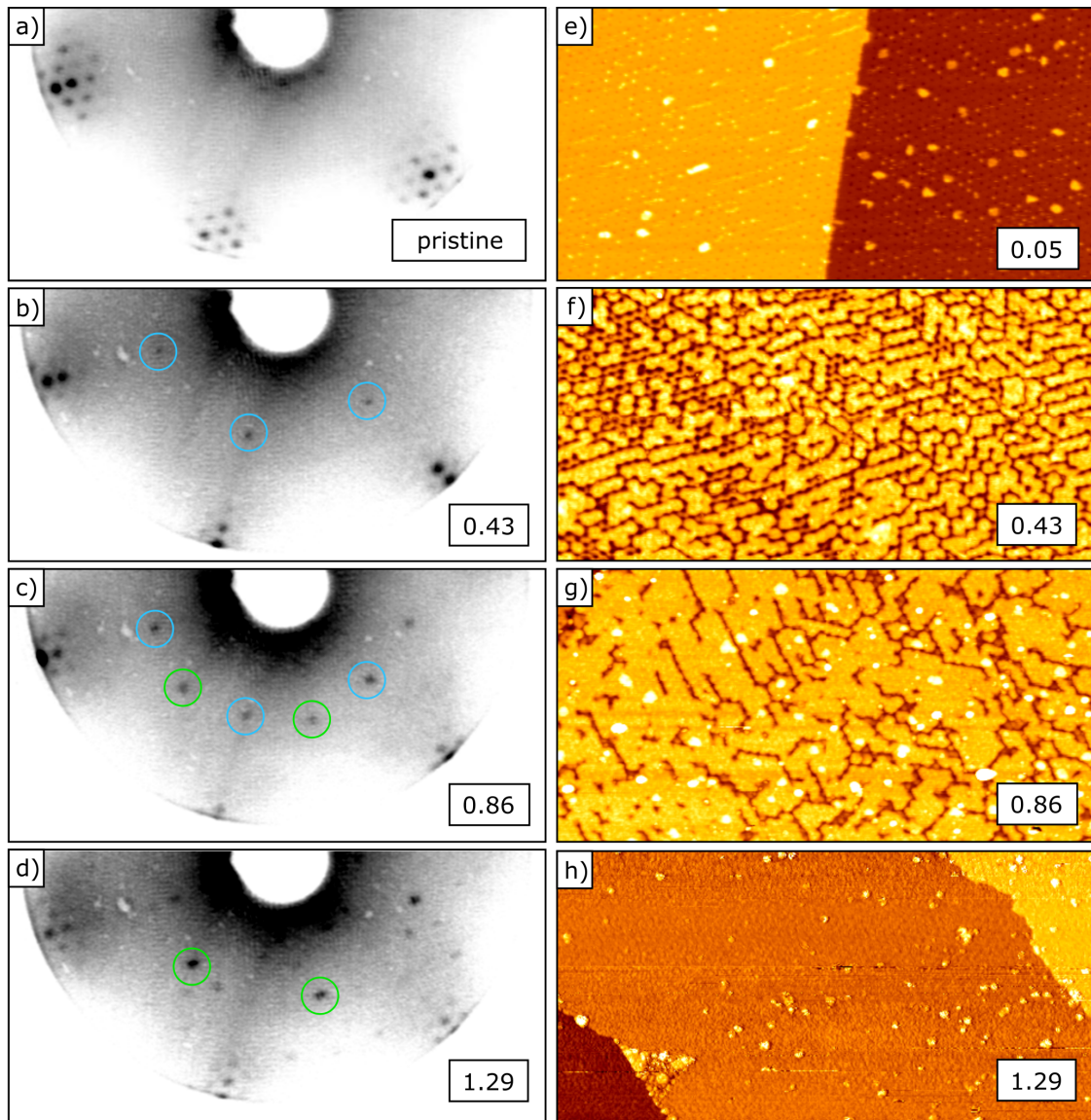


**Figure 6.14:** Eu intercalation series of h-BN/Ir(111). (a-d) LEED data and (e-h) STM topographs of h-BN/Ir(111) intercalated with Eu at 750 K; amount of Eu in ML as stated in the images. The occurring  $(2 \times 2)$  and  $(\sqrt{3} \times \sqrt{3})$  superstructures w.r.t. Ir(111) substrate are highlighted by blue and green circles, respectively. LEED energies are 72 eV and images sizes are 180 nm  $\times$  90 nm.

BN and the Ir(111) appeared on the surface (compare also Figure 6.15). These islands have different sizes and shapes, and are separated only by small dark trenches. The trenches form preferably along neighboring valleys of the h-BN/Ir(111) moiré. The island density is not homogeneously distributed, e.g., in the upper left of Figure 6.14(f), the island density is significantly lower. It is well known that intercalation of a metal supported 2D material does not occur homogeneously, but predominantly near island edges or defects [156, 266].

At areas of low Eu concentration, the intercalated Eu forms worm-like structures meandering along the wire sites of the h-BN/Ir(111) moiré (compare green tiles in Figure 6.15). It is noted, that the

trenches are ziz-zag shaped, following the morphology of the moiré lattice, by avoiding the areas where the h-BN is closely bound to the Ir substrate (valleys, red tiles in Figure 6.15). It can be assumed that a certain amount of Eu is needed before it creeps below the valley sites of the moiré. In order to do so, it must become energetically more favorable to lower the binding between h-BN and Ir at the chemisorbed valley sites than to increase the density of Eu between the valleys. Figure 6.14(g) depicts the sample surface after depositing 0.86 ML of Eu. A closed network of dense Eu islands has formed. The dark trenches forming along the valley sites of the moiré can be correlated to areas that are either not intercalated by Eu, or to a dilute Eu phase [similar to oxygen intercalation of Gr as shown in Ref. [328]]. Finally, the surface morphology becomes smooth after the deposition of 1.29 ML of Eu, as shown by the STM topograph in Figure 6.14(h). It is assumed that the whole h-BN is homogeneously intercalated by the dense ( $\sqrt{3} \times \sqrt{3}$ ) Eu-phase [compare LEED data in Figure 6.14(d)].

The following picture for Eu intercalation in h-BN/Ir(111) can be drawn, firstly low amounts of Eu form networks of worm-like structures, that is a less dense Eu-phase. This is followed by the formation of small Eu islands, *i.e.*, a more dense phase of Eu, locally unlocking the valley locations of h-BN. When the intercalation process proceeds further, the Eu islands grow laterally, until only thin dark trenches of non-intercalated regions are left. Finally, a smooth surface morphology is obtained, when Eu intercalation is saturated, and the whole h-BN layer is intercalated by the dense ( $\sqrt{3} \times \sqrt{3}$ ) Eu-phase. It should be noted that when considering Gr/Ir(111), it was shown, that an even more dense phase of Eu, a ( $\sqrt{3} \times \sqrt{3}$ )-phase w.r.t. to the Gr lattice is possible to form [266, 325]. Here, even after considerable large amounts of deposited Eu, there were no indications of a more dense ( $\sqrt{3} \times \sqrt{3}$ )-phase of Eu w.r.t. h-BN.

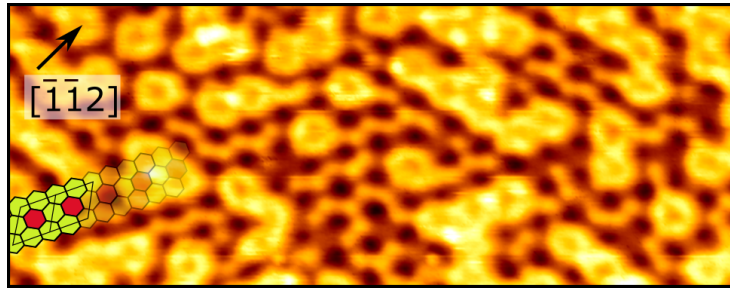


**Figure 6.15:** Eu intercalation of h-BN/Ir(111). STM topograph ( $65 \text{ nm} \times 25 \text{ nm}$ ) after intercalation of 0.43 ML Eu at 750 K. Based on the different local interaction strength of h-BN with the substrate, the moiré can be tiled into valley sites (red tiles, strong interaction) and wire sites (green, weak interaction) [compare unit cell at lower left side]. The arrow indicates the Ir $[\bar{1}\bar{1}2]$  direction [327].

### Au intercalation of h-BN/Ir(111)

Figure 6.16 depicts LEED and STM data after depositing 3 ML of Au on h-BN/Ir(111) at 723 K. Although, the moiré diffraction spots of h-BN/Ir(111) are highly suppressed, clear spots corresponding to the h-BN and Ir lattice are visible [compare LEED data in Figure 6.16(a)]. There are no visible spots corresponding to a superstructure [such as ( $\sqrt{3} \times \sqrt{3}$ ) or ( $2 \times 2$ )]. An additional spot appears, which can be correlated to the slightly larger nearest neighbor distance of Au ( $2.97 \text{ \AA}$ ) compared to Ir ( $2.73 \text{ \AA}$ ). Figure 6.16(b) shows a STM topograph of the same sample. The island

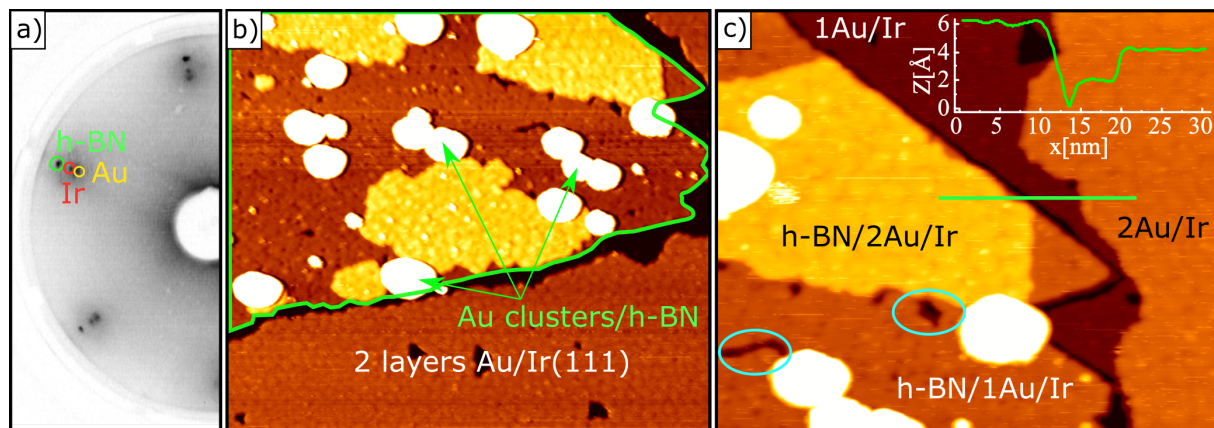


**Figure 6.16:** LEED measurement and STM topographs of Au intercalated h-BN/Ir(111). (a) LEED data and (b,c) STM topographs of h-BN/Ir(111) after depositing 3 ML of Au at 723 K. In (a) h-BN, Ir(111), and Au substrate reflections are highlighted by green, red, and yellow circles, respectively. In (b) the h-BN island is highlighted. LEED energy is 72 eV and images sizes are 180 nm  $\times$  160 nm in (a) and 90 nm  $\times$  80 nm in (b).

in the upper left corner, highlighted by the green shell, can be correlated to a Au intercalated h-BN island on Ir(111). The brighter islands within the green border can be correlated to bilayer Au islands intercalated below the h-BN. Large circular shaped protrusions (see green arrows) with heights of about 3 nm are gold clusters still resting above the h-BN layer<sup>5</sup>. Outside the green border, flat layers of Au on Ir(111) are present, with a typical reconstruction pattern, also visible through the h-BN layer [compare Figure 6.16(c)]. Figure 6.16(c) depicts a magnified view of the area in (b). Along the edge of the h-BN islands, a dark trench is visible. As shown in the associated height profile taken along the green line in Figure 6.16(c), the trench is 2 Å lower compared to the first Au layer on Ir(111). This might indicate that the edges of the h-BN layer are still bound to the Ir substrate. It should be noted that dark areas within the h-BN layer are visible (compare blue circles in Figure 6.16(c)). This either correlates to areas where h-BN is not intercalated, or to a defective h-BN layer at locations, where the Au atoms might have intercalated through.

To conclude, similar to Gr/Ir(111) [329] Au intercalation of h-BN/Ir(111) is possible. The Au below the h-BN either forms an isomorphic lattice with the Ir substrate (no additional spot in LEED), or reconstruct at the surface when additional layers of Au add up (additional Au reflections appear in LEED). However, Au still forms large clusters above the h-BN layer, which helped us to distinguish the h-BN from the Au layer. However, damage formation within the h-BN layer can not be excluded. Therefore, we believe that intercalation with Eu appears more favorable, in order to reduce the coupling strength to the Ir substrate.

<sup>5</sup>The existence of the h-BN layer is proven by the formation of Au clusters. While Au on h-BN forms clusters, it is known to wet Ir surfaces.

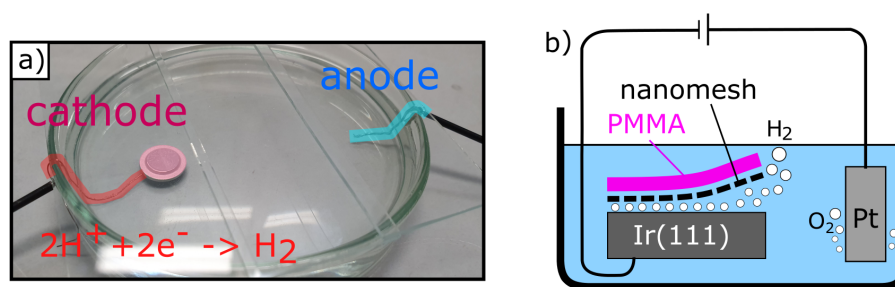


**Figure 6.17:** (a) Photograph and (b) schematics of the hydrogen bubbling transfer method. The PMMA/Gr/Ir(111) crystal is immersed in a 10 % NaOH solution and connected to the cathode. A Pt-wire serves as the anode. When a bias voltage of about 1.6 V is applied, hydrogen gas forms on the Ir surface. Hydronium ions from the NaOH solution are reduced to  $\text{H}_2(\text{g})$ . The hydrogen bubbles delaminate the Gr layer from the substrate.

## 6.8 Bubbling transfer of nanomesh membranes on Ir(111)

While applications of the vacancy cluster array on Ir(111) can be envisioned, *e.g.*, as a template, for applications like filtering it is obligatory to detach the prepared cluster lattice membrane from the Ir(111) substrate. In the past the bubbling transfer method has been applied as an etch free transfer method for Gr on Ir [278,279,330]. In this method the Gr covered metal is first coated with a polymer (*e.g.* PMMA) in order to prevent scrambling of the Gr, when it becomes detached. A photograph and schematics of the bubbling transfer are presented in Figure 6.17(a) and (b). The Ir(111) sample is used as a cathode and a Pt-electrode as an anode. Hydronium ions are reduced at the Ir surface to  $\text{H}_2$ -molecules. The hydronium ions creep in between the Gr and Ir interface and eventually form  $\text{H}_2(\text{g})$ -bubbles. The  $\text{H}_2$ -bubbling delaminates the PMMA/Gr layer from the Ir substrate, as depicted by the schematics in Figure 6.17(b). However, small vacancy clusters increase the adhesion of Gr to the Ir substrate substantially due to the strong C-Ir bonds formed by the Gr edge atoms with Ir(111) [325]. Therefore, without additional measures the bubbling transfer method is likely to fail in detaching of the vacancy cluster membrane. In order to weaken the binding of the membrane to Ir we intercalated Eu till saturation at a sample temperature of 720 K under UHV conditions such that a  $(\sqrt{3} \times \sqrt{3})$  intercalation pattern forms [266,325,326]. The corresponding LEED pattern is shown Figure 6.18(a), where the dense Eu phase is highlighted by green circles. After coating with PMMA the sample is immersed in a 10 % NaOH solution. In a first step we apply an underpotential voltage of 1.4 V for 10 h to induce intercalation of hydronium ions and its reaction with the intercalated Eu layer at the Gr/Ir(111) interface. Subsequently, the voltage is gradually increased above the onset of gas evolution until after 5 h and at a final voltage of 1.7 V the membrane lifted-off from the substrate.

The separated PMMA/Gr layer was transferred onto a  $\text{SiO}_2$ -wafer as depicted by the photograph shown in Figure 6.18(b). After the PMMA has been dissolved in acetone we use an optical microscope to identify regions that are covered with the Gr nanomesh and regions of bare  $\text{SiO}_2$ . Figure 6.18(c)

## 6.8 Bubbling transfer of nanomesh membranes on Ir(111)

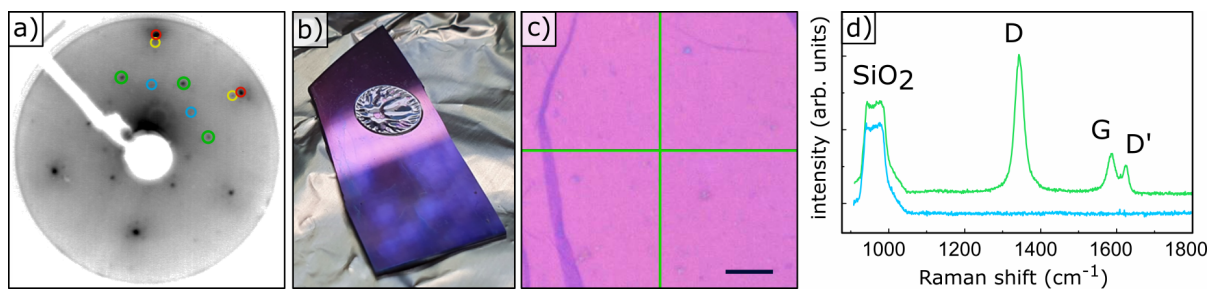


**Figure 6.18:** Raman spectroscopy of a transferred Gr nanomesh membrane on SiO<sub>2</sub>. (a) LEED pattern of the Eu intercalated Gr nanomesh at 86 eV. The diffraction spots corresponding to the Gr, Ir, ( $\sqrt{3} \times \sqrt{3}$ ), and ( $2 \times 2$ ) Eu phase are highlighted by red, yellow, green, and blue circles, respectively. (b) Photograph of a transferred Gr nanomesh membrane onto a SiO<sub>2</sub>-wafer supported by PMMA. (c) Microscopical image of a GNM covered region on SiO<sub>2</sub> using a 100x magnification lens. The scale-bar is 10  $\mu\text{m}$ . (d) Raman spectra of GNM/SiO<sub>2</sub> (green) and bare SiO<sub>2</sub> (blue) indicating a successful transfer of the GNM onto SiO<sub>2</sub>. The laser wavelength is 532 nm.

shows a microscopic image of the Gr nanomesh using a 100x magnification lens. The image shows a flat Gr layer on SiO<sub>2</sub> with a dark band in the membrane which we interpret as a fold that has formed during the transfer process.<sup>6</sup> To obtain further information on the transferred membrane we performed Raman spectroscopy at various locations of the sample. A Raman spectrum obtained from the region in the cross-hair of Figure 6.18(c) is displayed in the graph of Figure 6.18(d). The green curve shows intense G ( $E_{2g}$  phonon) and D (defect activated breathing mode) peaks at 1580  $\text{cm}^{-1}$  and 1350  $\text{cm}^{-1}$  that prove the existence of a successfully transferred Gr nanomesh membrane. The intensity ratio of the related D to G peak yields about  $I_D/I_G \approx 3.20$ . Cançado *et al.* [333] related this ratio to the average defect separation  $L_D$  between ion beam induced defects. Based on their data and for the laser wavelength of 532 nm used by us we estimate  $L_D \approx 3$  nm in decent agreement with the moiré unit cell size of 2.5 nm. From this we conclude that the introduced vacancy clusters are still present and survived the transfer process. For reference we present the Raman spectrum of bare SiO<sub>2</sub>. The reference signal of SiO<sub>2</sub> was recorded at an uncovered region of SiO<sub>2</sub>. It looks unambiguously different. Except of the Si-related vibration mode, no peaks are visible. The successful transfer of the membrane opens the door to a variety of additional experiments which are under progress, but beyond the scope of this thesis.

### Bubbling transfer of a h-BN nanomesh

Analogue to the previous section, a similar approach was taken in order to remove the h-BN nanomesh from the Ir(111) substrate. The h-BN nanomesh was created by high temperature He<sup>+</sup> ion irradiation in UHV of h-BN/Ir(111). Subsequently, the sample was intercalated by Eu and afterwards [compare LEED pattern in Figure 6.19(a)], transferred into ambient and coated with PMMA. The same bubbling method was applied as for the previous Gr nanomesh sample. The removed PMMA sheet was transferred onto SiO<sub>2</sub> and dissolved with acetone. The microscopic images in Figure 6.19(a)

<sup>6</sup>We note that the intercalation of foreign species at the interface of Gr/Ir(111) might have lead to the formation of additional wrinkles [156, 325] that are stable upon a transfer process [279, 331, 332].

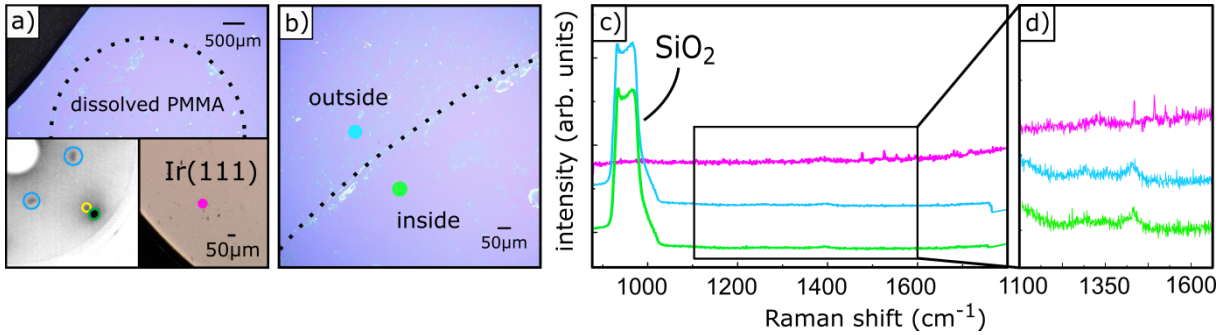


**Figure 6.19:** Raman spectroscopy of a transferred h-BN nanomesh membrane on SiO<sub>2</sub>. (a,b) Microscopical image of SiO<sub>2</sub> at the location of a transferred and dissolved PMMA layer (black dashed circle) after applying bubbling transfer on a h-BN nanomesh on Ir(111) using a 100x magnification lens. The left inset shows a LEED pattern of the Eu intercalated h-BN nanomesh on Ir(111) at 72 eV and the right inset shows a microscopy image of Ir(111) crystal after the transfer. The diffraction spots corresponding to h-BN, Ir, and ( $\sqrt{3} \times \sqrt{3}$ ) Eu phase are highlighted by green, yellow, and blue. The scale-bar is as stated in the images. (c,d) Raman spectra at indicated regions on SiO<sub>2</sub>. The laser wavelength is 532 nm.

and (b) show a residual circle where the former PMMA sheet was dissolved (inside dashed circle). However, we could not identify any regions in the magnified view of Figure 6.19(b) that indicate the presence of a transferred h-BN sheet. Therefore, it is not clear whether the transfer process was successful. Apparently, h-BN on SiO<sub>2</sub> has a much weaker optical contrast compared to Gr and is therefore hard to resolve using optical microscopy [334]. Depending on the wavelength of the microscope (using narrow bandpass filters) the maximum optical contrast is  $\approx 2\%$ , *i.e.*, significant lower than graphene's 10 %.

To gain additional insight into the transfer process, we measured Raman spectra at various positions on the SiO<sub>2</sub> and Ir sample. The green and blue dots in Figure 6.19(b) and the pink dot in the inset of Figure 6.19(a) correspond to the positions where the spectra were recorded on SiO<sub>2</sub> and Ir(111), respectively. The spectra are plotted in the graphs shown in Figure 6.19(c) and (d). The green and blue curve in Figure 6.19(c) show the significant SiO<sub>2</sub> substrate peak, while no other peak can be resolved. From literature the in-plane vibrational mode of h-BN on SiO<sub>2</sub> is expected to be around 1370 cm<sup>-1</sup> for monolayers, 1364 cm<sup>-1</sup> for bilayers, and 1366 cm<sup>-1</sup> for bulk h-BN [334, 335]. Therefore, a highly resolved spectra around this wavenumber was recorded and is shown in Figure 6.19(d). Although, there is some intensity measured around 1400 cm<sup>-1</sup>, as shown by the green curve, the absence of the expected peaks indicate an unsuccessful transfer of the h-BN nanomesh. We measure a similar peak on the bare Si surface, as shown by the blue curve. Here, no h-BN is to be expected. A further spectroscopic hunt for the h-BN nanomesh is not very promising without previous microscopic confirmation of h-BN (nanomesh) covered areas. Additionally, we checked the Ir(111) surface for any signal of h-BN, which is shown by the pink curves. Here, no response could be measured either, which however could be due to the absence of h-BN on the Ir crystal or to the luminescence of the Ir bulk, the same reason Gr on Ir(111) can not be measured with Raman spectroscopy (only Gr on Ir thin films) [336].

## 6.9 Conclusions

We have shown that the nanomesh formation in h-BN/Ir(111) upon  $\text{He}^+$  ion irradiation at elevated temperatures is feasible. This nanomesh has even superior ordering compared to the nanomesh that forms under similar irradiation conditions in Gr/Ir(111). Vacancy clusters nucleate only at one specific site of the moiré and are stable up to very high temperatures. We determined the valley-site as the energetically preferred region for vacancy agglomeration, as geometric configurations allow dangling N- and B-bonds to easily saturate with Ir substrate atoms. The size of the vacancy clusters stagnates with increasing ion fluence. Excess vacancies are expelled and migrate towards the edges of the 2D layer. The stagnation in size indicates a stable hole size that is balanced by the flux of created vacancies by the ion beam and the re-evaporation of individual vacancies from the cluster. This balance can be controlled through either increasing the vacancy flux or by reducing the rate of re-evaporation. The vacancy flux can be increased with higher ion energies, heavier noble gas ions, and larger ion fluxes. Reducing the temperature also leads to a decrease in vacancy mobility that ultimately lowers the ordering of the nanomesh. The formation of the nanomesh is also feasible for a variety of irradiation conditions, among grazing-ion incidence, different ions, and different ion energies. For h-BN/Pt(111), even though the substrate interaction is reduced, the formation of an ordered vacancy cluster array is still possible. However, small vacancies were still trapped between the valleys. Additionally, we have shown that the removal of the Gr nanomesh from its substrate is attainable by using the  $\text{H}_2$ -bubbling technique. However, the bubbling transfer of h-BN from Ir(111) does not work, even when intercalated with a full Eu layer in h-BN/Ir(111). Different transfer methods, *e.g.*, by introducing larger intercalants into the interface region of h-BN/Ir(111) might yield better results. Additional DFT calculations might uncover the hole size dependent stability, which could lead to a well-controllable hole size. TEM images of the removed membrane would deliver a smoking gun evidence, that the vacancy clusters are still present after the transfer process. Finally, this process enables the use of a removed nanomesh for mass filtration. Depending on the finite hole sizes, this membrane could significantly improve water purification processes.



## CHAPTER 7

# Suppression of wrinkle formation in graphene on Ir(111) by high-temperature, low-energy ion irradiation

*This chapter contains contributions from P. Valerius, A. Herman, and T. Michely. A. Herman conducted experiments under my guidance as part of his master thesis. I wrote most of the manuscript and I was responsible for the design of the experiments in correspondence with T. Michely. I conducted or was involved in all STM and LEED measurements, and analyzed all presented data. This work is published in Nanotechnology **30**, 085304 (2018) 325. The results are also the subject of the master thesis of A. Herman.*

### 7.1 Motivation

In CVD grown Gr, wrinkles are a persistent type of defect, typically present in the form of networks with a characteristic separation on the order of  $\mu\text{m}$  [155, 156]. They originate from the mismatch of thermal expansion coefficients of the substrate (a transition metal or SiC) and of graphene, the latter of which displays a marginal thermal expansion over an extended temperature range [157]. When Gr cools down from its growth temperature of  $\approx 1270\text{ K}$ , the Ir substrate shrinks, while Gr does not according to its thermal expansion coefficient. Therefore, compressive strain is induced into Gr. After the temperature has dropped by more than 400 K the strain exceeds a critical threshold. Wrinkle formation in Gr sets in which partly releases the strain by delamination of the Gr from the substrate. During further cool-down wrinkles grow while more and more of them are formed. The extent to which wrinkles form depends on the balance of the delamination energy, the Gr bending energy, and the elastic energy stored in the strained Gr [155]. This implies that when Gr adheres strongly to the substrate, wrinkle formation may be entirely suppressed, because the energetic cost of delamination is too high. Conversely, for weakly interacting substrates nearly all strain will be released in a wrinkle network. Even after transfer from the original growth substrate to a foreign one (e.g., an insulating substrate), the shape of the original growth substrate is preserved, as are wrinkles

and other features originating from the growth process [331, 332, 337]. This effect of "frozen" Gr morphology is presumably caused by the defects built into Gr when it conforms to irregularities of the substrate during growth, or by irreversible cracks created at locations where wrinkles intersect when Gr is cooled down from its growth temperature [156].

As wrinkles are invariably present in CVD grown graphene, it is no surprise that their effects on the properties of Gr are well investigated. Wrinkles deteriorate the electrical properties of Gr through electron scattering [158, 159], - they possess a defect resistance and give rise to a voltage drop in transport measurements [338–340]. Wrinkles also affect thermal properties of Gr and give rise to a reduced thermal conductivity [160–162, 341]. Lastly, wrinkles in Gr affect material transport in Gr membrane applications [318] and display an enhanced or reduced chemical reactivity compared to the flat material [342–345]. Since the presence of wrinkles in Gr is for most purposes detrimental, strategies for avoiding Gr wrinkle formation in CVD growth are needed. Here, we explored a strategy aimed at a tensile pre-straining of Gr still close to the Gr growth temperature, such that upon cool down the Gr relaxes to an almost unstrained material. The idea is based on previous electron microscopy work that demonstrated dislocation climb, under conditions where vacancies are created through electron impacts [80, 109, 110]. Then, the successive creation of vacancies leads not to an accumulation of defects, but only to the climb motion of the dislocation core – a pentagon-heptagon or 5-7 defect [137] – together with the creation of tensile strain. The frequency of climb events was found to substantially increase with the Gr temperature [109], suggesting that the method could be feasible at a typical Gr growth temperature of  $\approx 1270$  K. Room temperature ion irradiation of freestanding [346] and supported Gr [347] globally induces tensile strain, but causes at the same time a degradation of the material up to the amorphous state [346]. Modification of the strain state of Gr at elevated temperatures close to the Gr growth temperature has not yet been attempted. One could hope that under such conditions the irradiation-induced vacancies heal at dislocations by climb motion thereby creating tensile strain only.

In the present study we report on 500 eV He<sup>+</sup> ion irradiation of Gr grown on Ir(111) conducted at 1150 K. The use of low-energy He<sup>+</sup> was motivated by the goal of producing single vacancies [82], which are more likely to be mobile than complex and extended defect structures, *e.g.*, those caused by larger noble gas ions. Growing on Ir(111) results in epitaxial single crystal Gr [137], with a sufficient concentration of dislocations – 5-7 defects – that might climb upon vacancy incorporation. The irradiation temperature of 1150 K is still close enough to the growth temperature of 1470 K, such that wrinkles have not yet nucleated; they only nucleate about 400 K below the growth temperature [155]. Below, we will show that ion irradiation under these conditions is indeed able to suppress wrinkle formation entirely. However, the concept of tensile pre-straining by ion irradiation fails due to the interaction of vacancies with the substrate. Instead, this interaction implies effectively an enhanced adhesion – thus an enhanced delamination energy – which suppresses wrinkle formation [331].

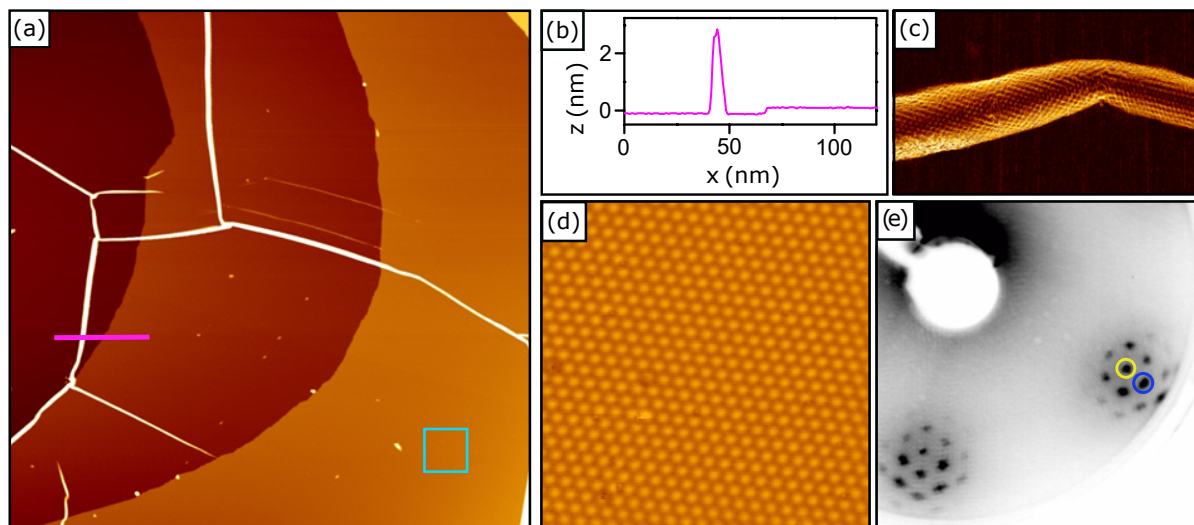


**Figure 7.1:** (a) STM topograph of Gr/Ir(111) with a wrinkle network after Gr growth at 1470 K. (b) Height profile along pink line in (a). (c) Atomically resolved Gr lattice on wrinkle. (d) Zoom into area of blue square in (a) displaying the Gr moiré with Ir(111). (e) 68 eV LEED pattern of same sample. First order Ir(111) (yellow circle) and Gr lattice (blue circle) reflections are indicated. Image sizes: (a) 720 nm  $\times$  720 nm; (c) 20 nm  $\times$  10 nm; (d) 40 nm  $\times$  40 nm.

## 7.2 High temperature Gr growth and wrinkle formation

As a reference for the wrinkle removal experiments serves the large scale STM topograph depicted in Figure 7.1 (a). It displays the sample topography after growth of a full monolayer graphene at 1470 K on Ir(111). The growth temperature was purposefully chosen high, in order to maximize the thermal mismatch strain upon cool-down and thus to create a pronounced wrinkle network. The wrinkles are visible as a network of bright lines, which display a typical height of 3 nm as exemplified in the line profile of Figure 7.1 (b), which is taken along the pink line in Figure 7.1 (a). The typical graphene nature of the wrinkles is underlined by the atomically resolved topograph of Figure 7.1 (c), where the wrinkle shows strong similarities to carbon nanotubes. In addition, two preexisting iridium substrate steps overgrown by Gr can be recognized in Figure 7.1 (a) as curved lines separating different height levels. The overall cleanliness of the sample is very high, while only few gas filled blisters are visible as bright protrusions, which have formed due to desorbing noble atoms from the Ir bulk during the high temperature growth. The close-up in Figure 7.1 (d) of the marked area in (a) displays a well ordered, nearly defect-free Gr moiré with Ir(111) with a periodicity of 2.53 nm [139], indicating that the crystallinity Gr is very high for this growth mode. The global epitaxial order of the Gr layer on Ir(111) is confirmed by the LEED pattern in Figure 7.1 (e). It displays the characteristic moiré satellites surrounding the first order Gr (blue circle) and Ir (yellow circle) reflections.

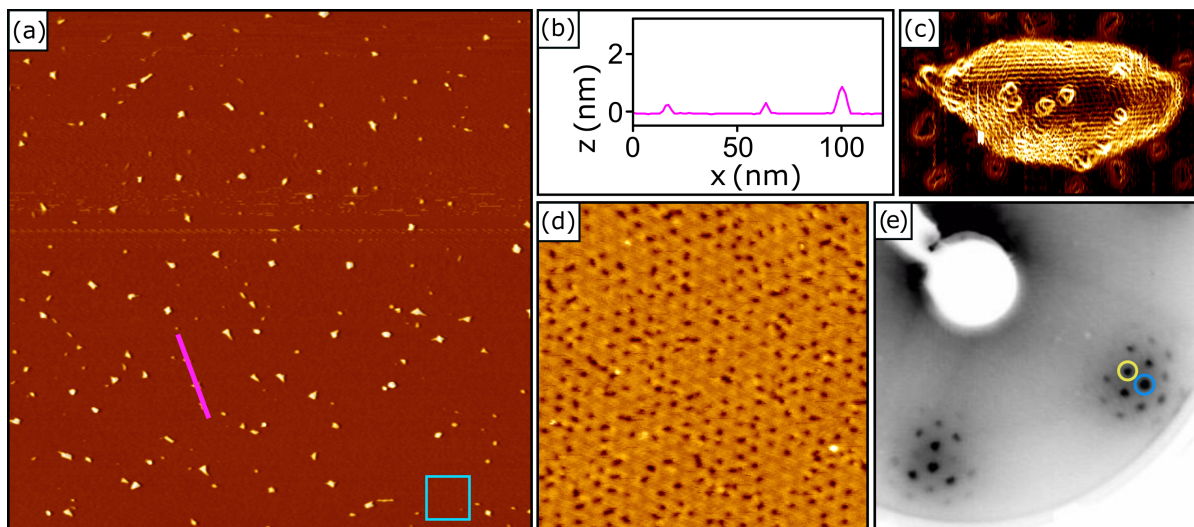


**Figure 7.2:** (a) STM topograph of sample as in (a), but with additional 0.25 MLE 500 eV  $\text{He}^+$  exposure at 1150 K. Wrinkles are absent and He blisters are present (see text). (b) Height profile along pink line in (a). (c) Atomically resolved Gr lattice on blister. (d) Zoom into area of blue square in (a). A large number of vacancy clusters is visible as dark spots. (e) 68 eV LEED pattern of same sample. Image sizes: (a) 720 nm  $\times$  720 nm; (c) 16 nm  $\times$  10 nm; (d) 40 nm  $\times$  40 nm.

### 7.3 Effect of high temperature $\text{He}^+$ ion irradiation on wrinkle formation

In order to entirely remove the thermal mismatch strain upon cooling from 1470 K to ambient of about 0.9% [155, 281]) it would be necessary to remove 1.8% of the Gr area. Using 500 eV  $\text{He}^+$  with a sputtering yield of about  $Y_{\text{Gr}}=0.33$  for Gr on Ir (compare chapter 6) we considered a fluence of 0.25 MLE as sufficient. Figure 7.2 (a) displays the topograph resulting, when additional 0.25 MLE 500 eV  $\text{He}^+$  irradiation is conducted at 1150 K prior to cool down. In agreement with the tensile pre-straining idea no wrinkles are visible in the topograph. However, bright protrusions appear in substantial number. As highlighted by the line profile displayed in Figure 7.2 (b), their typical height is below 1 nm. The topograph of Figure 7.2 (c) resolves the Gr lattice on a bright protrusion. Such bright protrusions were unambiguously identified in previous work [29, 30, 212, 213, 251, 348] as blisters of He trapped between the substrate and the Gr layer. Such blisters form unavoidably upon ion irradiation of supported Gr adhering to a substrate through trapping and aggregation of the primary ions. For He the trapping efficiency is minimal resulting only in small and shallow blisters. The close-up in Figure 7.2 (d) of the marked area in Figure 7.2 (a) shows a large amount of dark spots in stark contrast to the unirradiated case represented by Figure 7.1 (d). We identify these dark spots as vacancy clusters, which apparently reflect the moiré periodicity. About 65% of the moiré unit cells are populated by one cluster. In previous work [26] such vacancy clusters in Gr on Ir(111) were found to preferentially populate locations in the moiré, where the vacancy cluster edge bonds favorably bind to the Ir substrate atoms. Thereby, their distribution reflects the the moiré

### 7.3 Effect of high temperature He<sup>+</sup> ion irradiation on wrinkle formation

periodicity. Despite the large number of vacancy clusters, the LEED pattern in Figure 7.2 (e) still shows an intact Gr lattice. The moiré reflections are only slightly attenuated indicative of a preserved long range order.

Contrary to expectations derived from the pre-straining concept, a large amount of the ion beam created vacancies is not annealed by contributing to dislocation climb. Instead vacancies are rather pinned in the form of small clusters to the substrate as seen in Figure 7.2 (d). Therefore it is uncertain whether pre-straining took place at all and it remains open for what reason wrinkles were suppressed. In view of previous work for lower fluences and at lower temperatures the pinning of the vacancy clusters in the moiré still at 1150 K is surprising, as vacancy cluster disappearance by dissolution or diffusion was already found at 900 K [26].

#### Mechanism of wrinkle removal by high temperature ion exposure

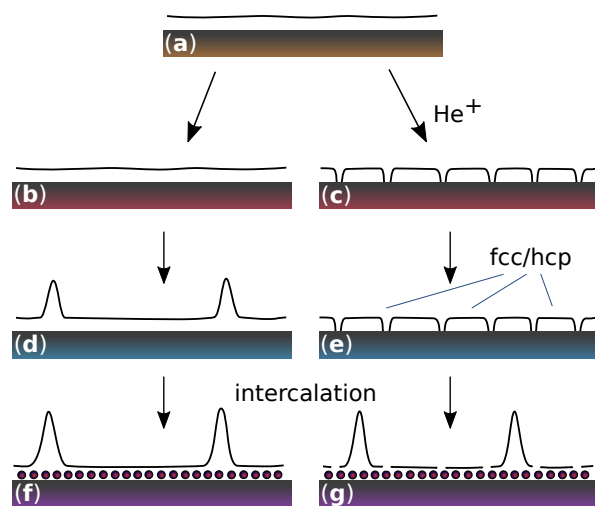


**Figure 7.3:** Schematics depicting the mechanism of wrinkle suppression by ion irradiation. (a) Pristine Gr at growth temperature. (b) Sample of (a) cooled to 1150 K. (c) Same as (b), but irradiated at 1150 K with 500 eV He<sup>+</sup> ions. Vacancies in Gr form clusters pinned in the moiré through strong bonds with the Ir substrate. (d) Sample of (b) cooled to 300 K resulting in wrinkle formation. (e) Sample of (c) cooled to 300 K without wrinkle formation due to pinning by the vacancy clusters. (f) Sample of (d) intercalated with Eu. (g) Sample of (e) after Eu intercalation. Pinning by vacancies is nullified by Eu-induced Gr decoupling from the substrate.

As mentioned in the introduction, when disregarding kinetic effects, in a simple quantitative model wrinkle formation can be understood to result from the energy minimization of the sum of strain, bending, and delamination energies [155]. When the temperature is lowered, the strain energy increases due to thermal mismatch. As it depends quadratic on strain (and the delamination energy does not), wrinkle formation will set in at some critical value of the strain (and thus temperature). Note that the energy minimum of the system is achieved by balancing the relevant energies. Thereby, a certain concentration of wrinkles together with some residual strain is present. For Gr at ambient, only weakly interacting with Ir(111), about 2/3 of the thermal mismatch is released by wrinkles, while 1/3 is still present as residual strain [155, 281].

Introducing a large number of vacancy clusters, that involve strong bonds between the C atoms at the cluster edge and Ir surface atoms effectively increases the delamination energy of Gr. Note that a Gr edge - Ir(111) bond is of the order of 5 eV [29]. A vacancy cluster consisting of a few vacancies easily doubles the delamination energy per moiré unit cell. This is evident by noting that the Gr binding energy to the substrate per moiré unit cell is 14.7 eV (per C atom it is 0.069 eV [190] and there are 213 C atoms in a unit

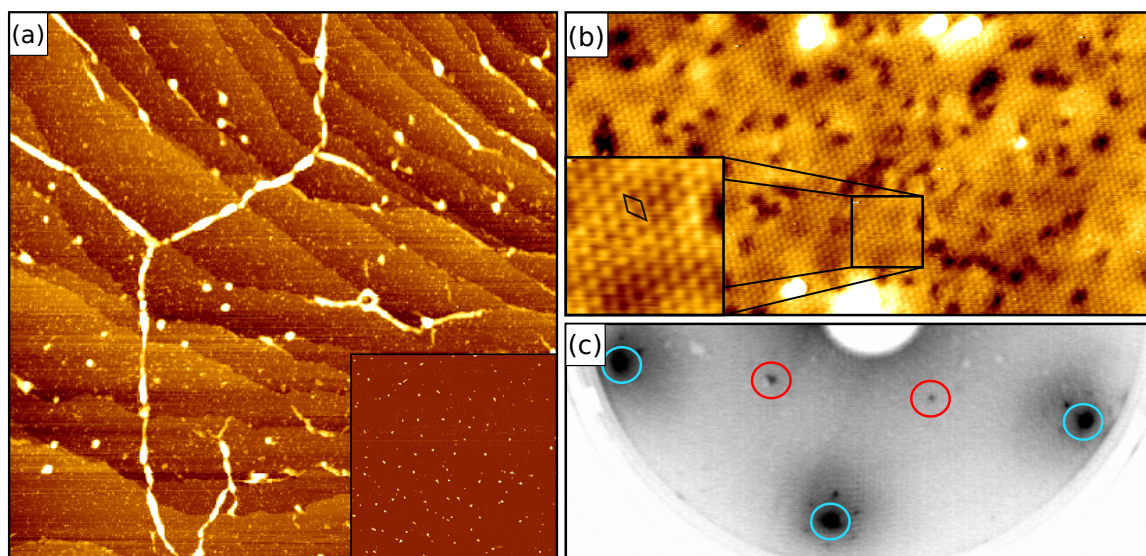


**Figure 7.4:** (a) STM topograph of Gr/Ir(111) exposed to 0.25 MLE 500 eV He<sup>+</sup> at 1150 K, cooled to ambient, and intercalated by Eu at 800 K. Inset: sample prior Eu intercalation. (b) Topograph of sample in (a) with atomically resolved  $(\sqrt{3} \times \sqrt{3})R30^\circ$  Eu structure w.r.t. Gr. Inset: Close-up with unit cell indicated. (c) 68 eV LEED pattern. First order Gr (blue circles) and  $(\sqrt{3} \times \sqrt{3})R30^\circ$  Eu superstructure (red circles) reflections are indicated. Image sizes: (a) and inset: 720 nm  $\times$  720 nm; (b) 38 nm  $\times$  19 nm.

cell [139]). Thus we hypothesize that the pinning of Gr by vacancy clusters formed upon irradiation suppresses wrinkle formation, rather than tensile pre-straining. Though dislocation climb by vacancies and thus pre-straining cannot be ruled out entirely, considering the high vacancy cluster density with a mean separation below 3 nm, escape of vacancies from cluster pinning and their diffusion and annealing to 5-7 defects appears unlikely.

The schematics in Figs. 7.3(a)-(e) summarizes our discussion. Whereas in the case without He irradiation upon cooling wrinkles form [compare Figs. 7.3(a),(b) and (d)], in the case with He irradiation the vacancy clusters created bind down to the substrate [Figure 7.3(c)], enhance the delamination energy, and thereby prevent wrinkle formation upon cool down [Figure 7.3(e)]. To test our hypothesis we consider two experiments. First, if intercalation – insertion of a foreign species in between Gr and the substrate – decouples Gr from the substrate by breaking the Gr - substrate bonds, the residual compressive strain should be released. For non-irradiated Gr this may slightly increase the wrinkle density and size through release of the 1/3 of thermal mismatch still present as residual strain [Figure 7.3(f)]. However, for the irradiated case, the sudden appearance of wrinkles upon intercalation is to be expected [Figure 7.3(g)], when the pinning of the vacancy clusters is nullified. Second, if irradiation is conducted under conditions where vacancy clusters are formed to a smaller extent – e.g., at even higher temperature – the pinning effect is reduced and thus the energy cost for delamination. In the absence of pre-straining through dislocation climb one would thus expect wrinkle formation upon cooling also in this case.

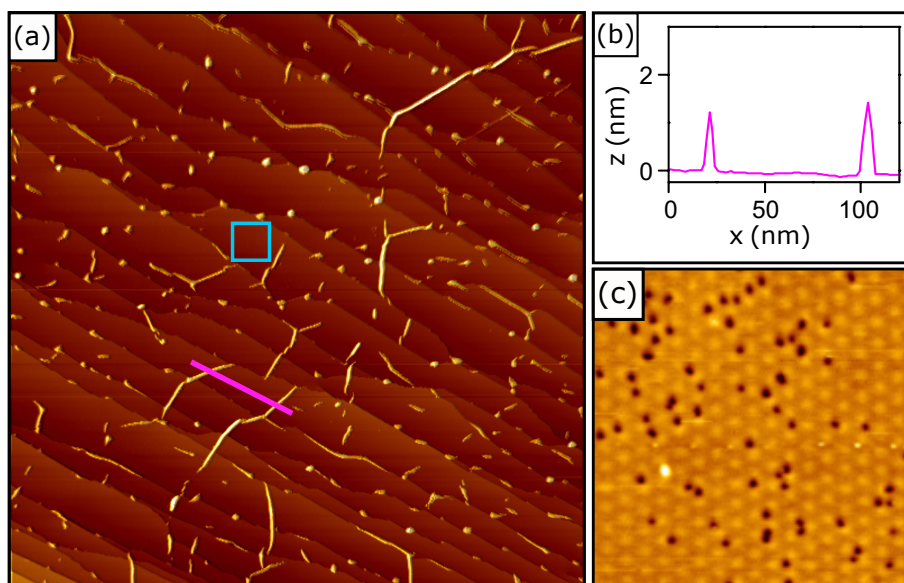


**Figure 7.5:** (a) STM topograph of Gr/Ir(111) after 0.25 MLE 500 eV He<sup>+</sup> irradiation at 1400 K. (b) Height profile along pink line in (a). (c) Zoom into area of blue square in (a), exhibiting a reduced number of vacancy defects. Image sizes are: (a) 720 nm × 720 nm; (c) 40 nm × 40 nm.

## 7.4 Unpinning of irradiated Gr by Eu intercalation

The STM topograph in Figure 7.4(a) shows Gr on Ir(111) irradiated with 500 eV He<sup>+</sup> at 1150 K, cooled to room temperature, then still free of wrinkles [see inset of Figure 7.4(a)], and subsequently exposed to Eu vapor at 800 K. The enhanced temperature during Eu exposure enables Eu intercalation [compare with Figure 7.3(e-g)]. It is obvious from Figure 7.4(a) that a wrinkle network appears in consequence of intercalation, which is in full agreement with our hypothesis that wrinkle formation is suppressed by vacancy cluster pinning and consequently enabled by unpinning. In the high resolution topograph of the same sample in Figure 7.4(b) the  $(\sqrt{3} \times \sqrt{3})R30^\circ$  Eu structure underneath the Gr layer is atomically resolved (the unit cell is indicated in the inset). The atomic resolution of the Eu intercalation layer through an apparently transparent Gr layer has already been observed before [266]. The  $(\sqrt{3} \times \sqrt{3})R30^\circ$  Eu superstructure is also supported by the LEED pattern presented in Figure 7.4(c). The  $(\sqrt{3} \times \sqrt{3})R30^\circ$  Eu superstructure is only formed under an entirely intercalated Gr layer [266], consistent with our assumption of wrinkle formation through decoupling. Also apparent in Figure 7.4(b) is a large number of dark spots, which we identify with the vacancy clusters in Gr.

### Temperature variation during irradiation

When the He<sup>+</sup> irradiation is performed at a temperature 250 K higher than in the case of Figure 7.2(a), where the formation of the wrinkle network was entirely suppressed, the morphology of Figure 7.5(a) results. Obviously, wrinkles are present in Figure 7.5(a). Their number is increased, but the wrinkles are shorter and not connected to a network. Figure 7.5(b) makes plain that the

wrinkles are now much lower in height, typically 1.5 nm instead of 3 nm as shown in Figure 7.2 (a). The close-up in Figure 7.5 (c) of the marked area in Figure 7.5 (a) shows a much smaller number of vacancy clusters as compared to Figure 7.2 (d). Instead of vacancy clusters being present in 65 % of the moiré unit cells as in Figure 7.2 (d), now they are present in only 25 % of the moiré cells (compare results of chapter 6)<sup>1</sup>. Apparently, due to the higher temperature of 1400 K the vacancy mobility is enhanced, leading to a lower number density of clusters. We also find now rare vacancy islands with a typical distance of the order of  $\mu\text{m}$  and dimension of the order of 50 nm which accumulate a large fraction of the vacancies created. Our interpretation is as follows: The smaller number density of vacancy clusters still induces pinning, which is however not sufficient to prevent wrinkle formation entirely. The residual pinning limits the wrinkle growth, that is network formation and strain release, over larger areas. The latter implies the reduced wrinkle height. Again, based on the data there is no indication for annealing of vacancies at dislocation cores.

### 7.5 Conclusions

In conclusion, our experiments demonstrate that high temperature ion irradiation may suppress wrinkle formation for Gr/Ir(111) entirely. The mechanism of this suppression is the effective increase of adhesion of Gr to its substrate and thus of the Gr delamination energy. It is caused by the ion-induced formation of a large number of small vacancy clusters, which effectively pin the Gr to the substrate through strong bonds between the vacancy cluster edges and substrate atoms. Thereby the entire thermal mismatch strain is still stored in the sample under ambient conditions, and may suddenly be released when the Gr is decoupled from the substrate, *e.g.*, by intercalation.

Our experiments indicate that for Gr/Ir(111) – even at the highest ion irradiation temperature of 1400 K – the ion beam created Gr vacancies do not give rise to dislocation climb, presumably also due to the interaction of the vacancies with the substrate. Suppression of wrinkle formation through high temperature ion irradiation, though feasible, appears not a suitable method to perfect the Gr and enhance properties like electrical or thermal conductivity: instead of being affected by a two-dimensional wrinkle network Gr is densely punctuated by small vacancy clusters and additionally by blisters. We are convinced that our arguments also apply to other supported Gr (or other 2D materials) systems, where strong bonds between Gr edge atoms and the substrate form.

---

<sup>1</sup>We note that vacancy cluster density has slightly changed compared to our published values in Ref. [325] due to access to additional data

## **PART IV**

---

# **Summary and Outlook**



In this thesis we investigated the interactions of low-energy ions impinging on 2D materials that are resting on a metal substrate. Furthermore, we studied the effect upon subsequent thermal annealing. Our investigations show that the global damage morphology, induced by  $\text{Xe}^+$  irradiation in the energy range from a few 100 eV to a few 1000 eV, and its annealing of h-BN resting on a Ir(111) slab result in some unique features. Among such, we were able to directly image Xe, which becomes efficiently trapped at the interface of h-BN/Ir(111). The Xe atoms exhibit solid structures of monolayer and bilayer thickness through the blister cover, which presumably is enabled by the strong adhesion and thus comparatively higher pressure in h-BN blisters as compared to Gr ones. We thereby provide a direct proof for the high pressures in irradiation-induced noble gas blisters under 2D-layers on a metal. At sufficiently high annealing temperatures stand-alone blisters sealed only to the metal substrate form. We identified the onset of 2D-layer decomposition as the key condition for the creation of stand-alone blisters. Visually, an appealing effect of the hetero-elemental binding in h-BN is the development of pronounced triangular shapes in the entire morphology, which is traced back to the strong and preferential binding of B-terminated zigzag edges to Ir(111).

Strikingly, the experiments bear strong similarities to irradiated Gr on Ir(111), involving irradiation-induced structural disintegration, reestablishment of lattice and moiré pattern, blister and nanomesh (ordered positioning of vacancy clusters) formation, and finally the collapse of the vacancy clusters into large vacancy islands at the highest annealing temperature. Despite the dissimilarity of the electron irradiation damage in the freestanding materials, these similarities for the supported materials arise from the strong binding of the 2D-layer edges to the Ir(111) substrate. We believe that this feature is of general relevance and expect for any 2D-layer on a substrate, to which its edges bind strongly, a similar set of phenomena after irradiation and annealing, as described here. However, the list of 2D materials is vastly growing and interesting phenomena are to be expected when these materials interact with energetic ions or when annealed up to very high temperatures. For instance, we have observed the formation of 2D boron, often denoted as borophene, which is known to have metallic character. New emerging phases upon thermal disintegration of h-BN on Ir(111), and structural and electronic changes that might occur consequent to ion irradiation are certainly topics of high interest. As 2D boron is polymorphic [277], and hence different synthesis substrates can have a significant influence on its structure and properties, it is worthwhile to investigate the growth on various substrates, along with different synthesis methods.

Moreover, we have shown that high temperature ion irradiation may suppress wrinkle formation for Gr/Ir(111) entirely. The mechanism of this suppression is the effective increase of adhesion of Gr to its substrate and thus of the Gr delamination energy. It is caused by the ion-induced formation of a large number of small vacancy clusters, which effectively pin the Gr to the substrate. Thereby the entire thermal mismatch strain is still stored in the sample under ambient conditions. Suppression of wrinkle formation through high temperature ion irradiation, though feasible, appears not a suitable

---

method to perfect the Gr and enhance properties like electrical or thermal conductivity: instead of being affected by a two-dimensional wrinkle network Gr is densely punctuated by small vacancy clusters. We are convinced that our arguments also apply to other supported Gr and other 2D material systems, where strong bonds between edge atoms and the substrate form. However, the controlled introduction of strain is highly desirable to change mechanic and electronic properties of 2DM [15], and our investigations might open a path to intentionally induce and control strain by deliberately choosing a growth temperature and carefully enhance adhesion through defects.

We found that the nanomesh formation in h-BN/Ir(111) upon  $\text{He}^+$  ion irradiation at elevated temperatures is possible. It is also feasible for a variety of irradiation conditions, among grazing-ion incidence, different ions, different ion energies, and different substrates such as Pt(111). The uniqueness of vacancy cluster pinning makes h-BN on Ir(111) from the fundamental point of view superior to Gr/Ir(111) and may thus enable the formation of much better ordered arrays of vacancy clusters. The moiré based nanomesh formation result in stable hole sizes that are balanced by the flux of created vacancies by the ion beam and the re-evaporation of individual vacancies. We successfully removed the Gr nanomesh from its substrate by using the  $\text{H}_2$ -bubbling technique. However, the bubbling transfer of h-BN from Ir(111) does not yet work. The implementation of the nanomesh for mass filtration is still an open task and depending on the finite hole sizes, this membrane could be tested for various mass separation processes.

Furthermore, we demonstrated that it is possible to selectively change the defect concentration or even amorphize the top layer of a heterostructure assembled from 2D materials, without disturbing or damaging the rest of the stack. In combination with a thermal treatment and a reactive vapor this opens the possibilities to tune the properties of a single 2D layer in a stack in a wide range. This finding is likely to have relevance for future experiments with stacks of 2D layers or even in device prototyping based on such stacks. We have observed that  $\text{MoS}_2$  flakes on Gr/Ir(111) are wrapped by edge states showing distinct electronic properties that differ from the interior of the  $\text{MoS}_2$  islands. Depending on the irradiation geometry we could show that edges facing the incoming ion beam are selectively sputtered. A selective ion beam treatment of edge states might open or close these electronic circuits and could therefore play a role in upcoming nano-devices. In order to gain additional insight into the importance of the substrate in the semiconductor-to-metal transition in irradiated  $\text{MoS}_2$  on Gr/Ir(111), this experiment could be performed on a strongly insulating substrate such as h-BN/Ir(111). First growth experiments have already shown that the formation of  $\text{MoS}_2$ /h-BN/Ir(111) is indeed feasible. Additionally, the method presented in chapter 5 might also provide a path to synthesize so-called Janus materials with a  $\text{MoSSe}$  stoichiometry that has S (Se) on the upper (lower) plane with respect to Mo as realized by Ma et al. [285] and Lu et al. [316]. Such a material could be synthesized by low-energy grazing incidence ion irradiation resulting in sputtering of the upper S layer from a  $\text{MoS}_2$  sample and subsequently selenizing it. As large as the family of

TDMC materials is, the possibilities of creating interchanges of Mo or other transition metals with chalcogenides such as S, Se, Te, and so on, are endless and many fascinating properties, such as charge density waves and superconductivity, are to be expected.



## **PART V**

---

### **Appendix**



# APPENDIX A

## Scientific Appendix

*The scientific appendix discusses additional experiments on the topic of low-energy ion interactions with 2D materials that, however, deviated from the main concept of part III.*

### A.1 Low-energy Xe<sup>+</sup> ion irradiation and thermal annealing of Gr on Ir(110)

Structural phenomena that occur upon ion irradiation of supported 2DMs and subsequent annealing strongly depend on the substrate interaction. A strong aspect is the underlying crystal symmetry, which for Ir(111), results in hexagonal and threefold symmetric defect structures for Gr and h-BN. A possible route to exhibit new defect structures is to lower the system's symmetry. For instance, the lowest-index face Ir(110) shows a twofold symmetry. Interestingly, Gr/Ir(110) has proven to be a suitable substrate to introduce preferential ordering in organo-metallic wire complexes, which lack a global orientation when deposited on Gr/Ir(111). Here, a Gr/Ir(110) sample is irradiated by low-energy Xe<sup>+</sup> ions and annealed stepwise. The changes in crystallinity and the formation of defect structures are tracked by LEED and STM measurements.

The Gr sample was grown via CVD of ethylene at 1400 K on an unreconstructed Ir(110) substrate. Ir(110) alone is an unstable surface that reconstructs into a faceted surface, with facets that are of (331) and (33 $\bar{1}$ ) type [349]. The unreconstructed surface was obtained by cooling the crystal from 1400 K to room temperature in an oxygen background of about  $1 \times 10^{-7}$  mbar. Excess oxygen will be removed during Gr growth by reacting with C into CO or CO<sub>2</sub>. Figure A.1(a) shows the LEED pattern after exposing a clean Ir(110) to ethylene at 1400 K. Although the reflection pattern is rich, the relevant spots corresponding to Gr and the unreconstructed Ir substrate are marked by blue and red circles, respectively. All additional spots can be correlated to mixing of Gr and Ir substrate lattice vectors and will not be further discussed here. A more detailed description of Gr growth on Ir(110) can be found in Ref. 350.

The large scale STM topograph of Figure A.1(b) shows the pristine Gr/Ir(110) surface. Stripes along the ( $\bar{1}10$ ) are apparent, exhibiting high plateaus and low plains separated by substrate step bunches. The formation of step bunches was also observed for Gr/Ir(332) [351]. The higher-

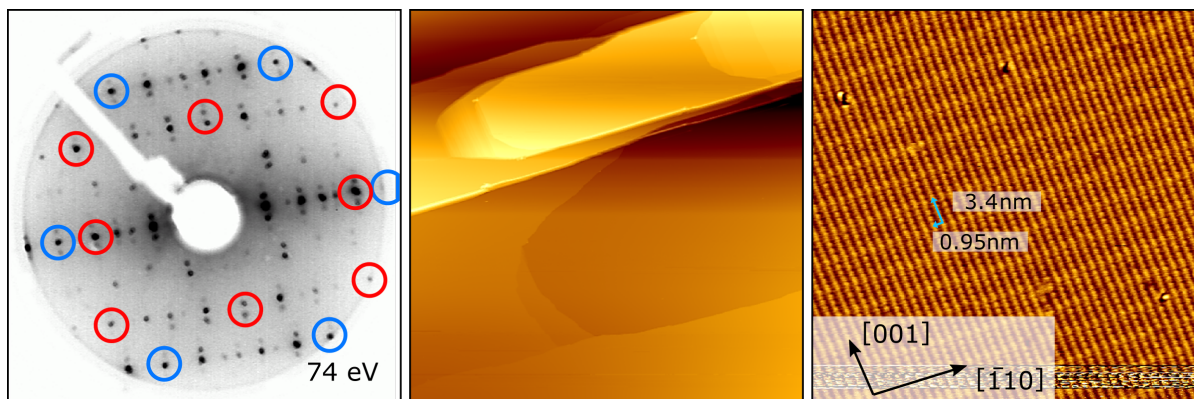


**Figure A.1:** LEED and STM measurements after growth of Gr on Ir(110). (a) LEED pattern of Gr/Ir(110) taken at 74 eV, after ethylene exposure of Ir(110) at 1400 K. Spots of the unreconstructed Ir(110) are marked by red circles, and of the Gr with corresponding moiré spots by blue circles. All other spots correspond to the superposition of Gr and Ir substrate lattice vectors. Image sizes are (b) 360 nm  $\times$  360 nm and (c) 45 nm  $\times$  45 nm.

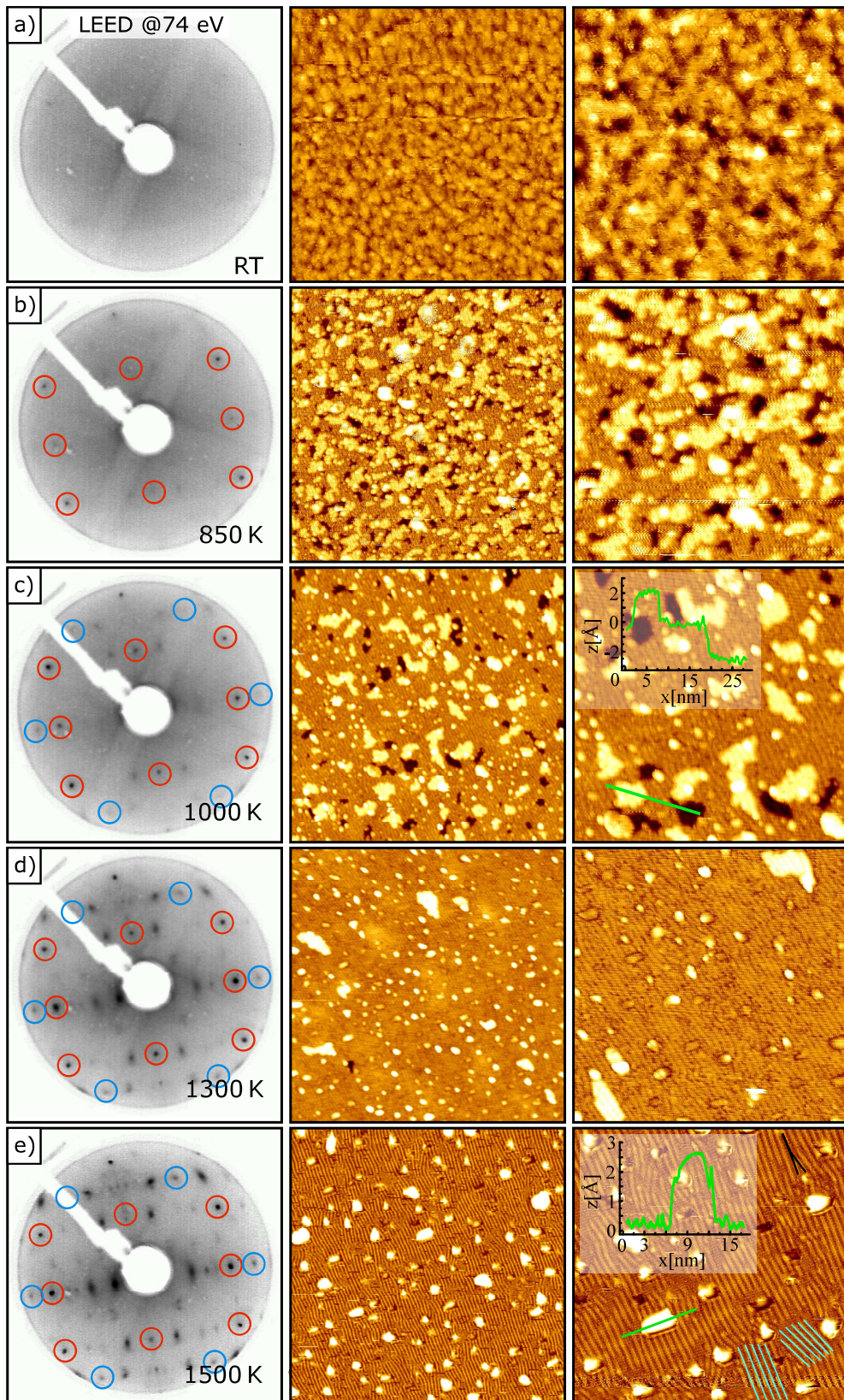
resolution STM image in Figure A.1(c) exhibits the moiré superstructure of Gr/Ir(110) and only very few defects. The moiré unit cell is rectangular with a short periodicity in the  $[\bar{1}10]$  direction of about 0.95 nm and a long periodicity of 3.5 nm in the  $[001]$  direction, as indicated by the blue arrows.

Figure A.2 depicts LEED and STM measurements for the amorphization and subsequent annealing series of Gr/Ir(110). As apparent from Figure A.2(a), the LEED pattern shows barely any diffraction spots, after directly exposing the Gr/Ir(110) sample to 0.1 MLE 3 keV Xe ions at room temperature. The STM topographs reveal a very rough surface with small scale protrusions and depressions, with a total corrugations of about 4 Å. No signs of moiré can be recognized. The roughness can be correlated to induced damage, such as Ir adatoms, surface vacancies, and implanted Xe atoms.

LEED and STM measurements presented in A.2(b) depicts the sample shown in Figure A.2(a) annealed to 850 K. The LEED pattern exhibits clear diffraction spots which correlate to the Ir substrate, while barely any diffraction intensity from the Gr lattice can be seen. The morphology is still rough, while three distinct height levels can be observed. The darkest regions can be interpreted as the bare Ir surface or vacancy islands within the first Ir surface layer (compare height profile in Figure A.2(c)). The bright regions, about 2 Å high, can be correlated with intact Gr intercalated either by Xe atoms or adatom islands of Ir. The base level corresponds to intact Gr on smooth areas of Ir(110).

The next annealing steps were performed at 1000 K, 1300 K, and 1500 K and the corresponding measurements are shown in Figure A.2(c-e). The LEED pattern gradually changes, while the Ir substrate spots become very sharp and more intense with increasing annealing temperature (compare red circles). The change in morphology reveals that the dark areas become less frequent until they disappear at 1300 K. This leads to the assumption that the dark regions were vacancy islands within the Ir substrate layer. They recombined with Ir adatoms, which perfectly agrees with the fact that the number of bright islands has decreased as well (see Figure A.2(d,e)). The bright protrusions still

## A.1 Low-energy Xe<sup>+</sup> ion irradiation and thermal annealing of Gr on Ir(110)



**Figure A.2:** Amorphization and recrystallization series of Gr/Ir(110). (a) LEED and STM measurements of Gr on Ir(110) exposed to 0.1 MLE 3 keV Xe at RT. (b) Sample of (a) subsequently annealed to 850 K, (c) to 1000 K, (d) to 1300 K, and (e) to 1500 K. LEED energy is 74 eV and image sizes are (mid) 90 nm × 90 nm and (right) 45 nm × 45 nm.

present after annealing at 1500 K, show a larger height of 3 Å and can be correlated to Xe filled blister at the interface of Gr/Ir(110). These blisters show clear differences in appearance compared to similar formed blisters in Gr/Ir(111) [29], as they are smaller in size and show a rather two-fold than six-fold symmetry.

Interestingly, the a clear moiré superstructure becomes visible again. However, small patches of a slightly misoriented moiré are also visible, which deviate by about 16° [compare blue lines in Figure A.2(e)]. Furthermore, correlated to the slightly rotated rows of the moiré are additional rows that form at large scale defects such as blisters. One example is highlighted by the black line in upper right corner of Figure A.2(e), which resembles an edge dislocation. The misalignment can be due to slightly rotated Gr or rotated regions within Ir substrate, where for instance Ir adatom and vacancy islands have recombined.

### **A.2 DFT calculated structures of various vacancy cluster configurations in the h-BN on Ir(111) supercell**

This section provides an overview of the relaxed vacancy structures calculated for h-BN resting on three layers of Ir, as discussed in chapter 6. The atomic models presented in Figures A.3 and A.4 are ordered with increasing number of missing atoms, while the number of B and N atoms are also stated. For small vacancies with nine or less atoms missing also the position of the vacancy was changed within the unit cell, as stated in the figure. Apparently, a systematic variation of the vacancy size can be quite complex, as with size also the geometry changes quite significantly. However, vacancies with 6, 24, and 54 atoms missing show a very similar hexagonal symmetry.

## A.2 DFT calculated vacancy cluster configurations in h-BN on Ir(111)

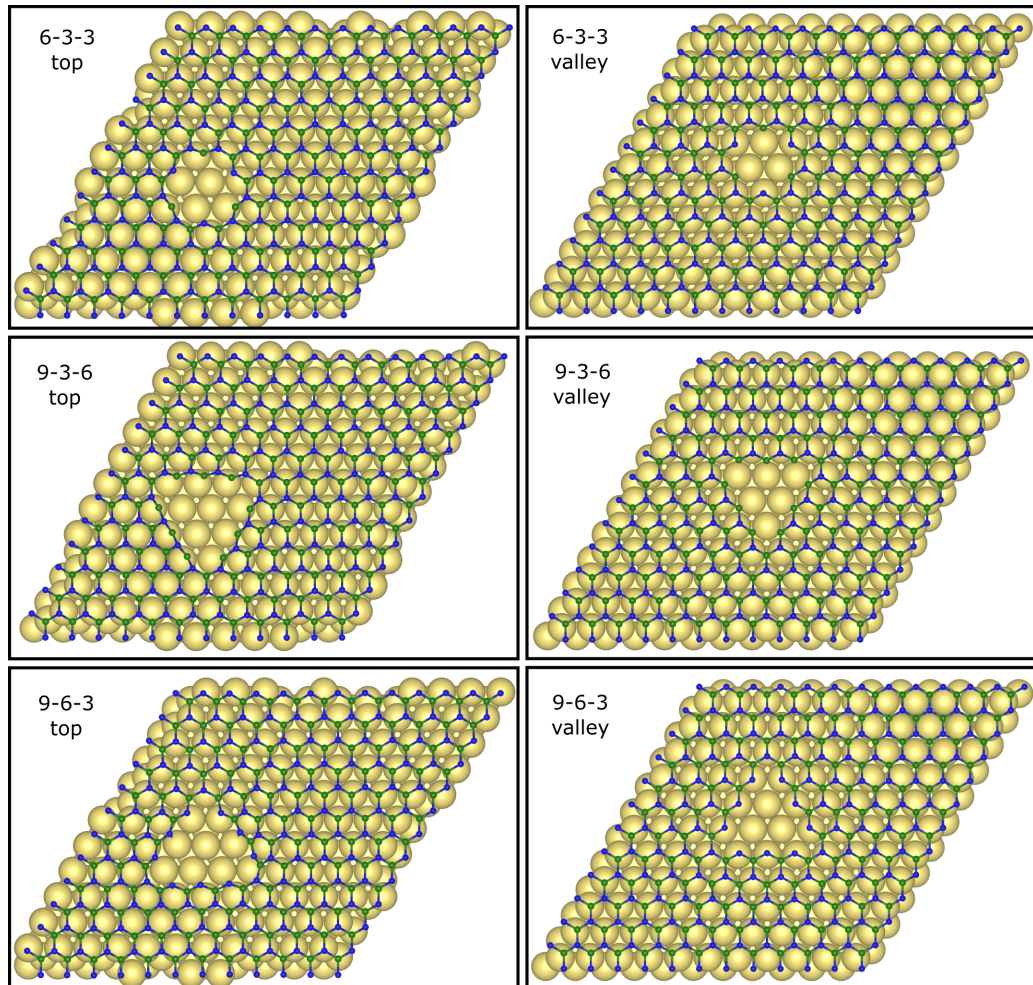


**Figure A.3:** Relaxed vacancy structures in h-BN/Ir(111) based on DFT calculations. The nomenclature is as follows, the first number defines the total amount of atoms missing, the second number counts the B atoms, and the third the missing N atoms (,e.g.  $atoms_{tot} - B - N$ ).

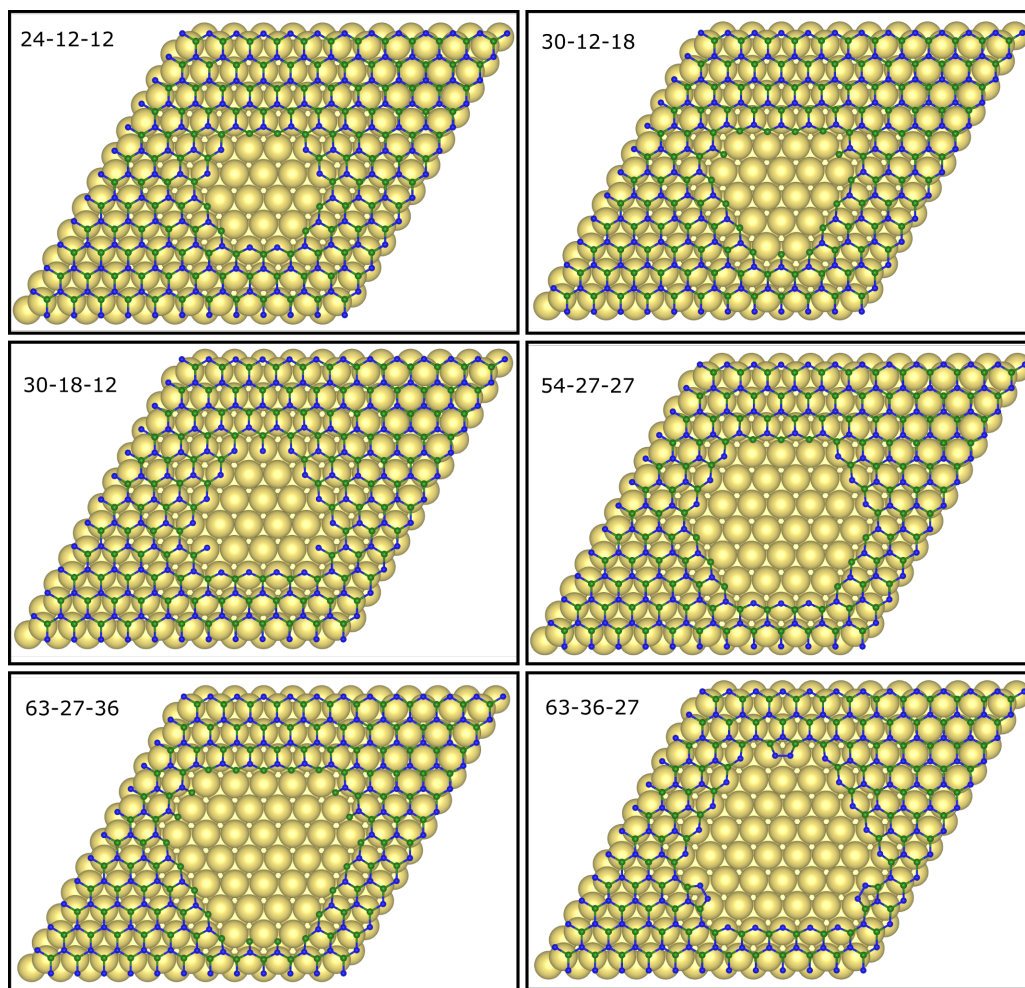


**Figure A.4:** Relaxed vacancy structures in h-BN/Ir(111) based on DFT calculations. The nomenclature is as follows, the first number indicates the total amount of atoms missing, the second number the amount of B atoms, and the third amount of N atoms (e.g.,  $atoms_{tot} - B - N$ ).

## **APPENDIX B**

### **Appendix**

In this chapter images are presented that I recorded during measurements or digitally created using a 3D rendering software. These images do not necessarily contribute to the scientific thread of this thesis. The left image in Figure B.1 was published in Ref. [352] as part of the graphical abstract (TOC figure).

#### **B.1 3D rendered interpretation of the Gr/Ir(111) moiré based metal cluster superlattice**

#### **B.2 Interference effects of visible light in PMMA/Gr-membranes transferred on SiO<sub>2</sub>**

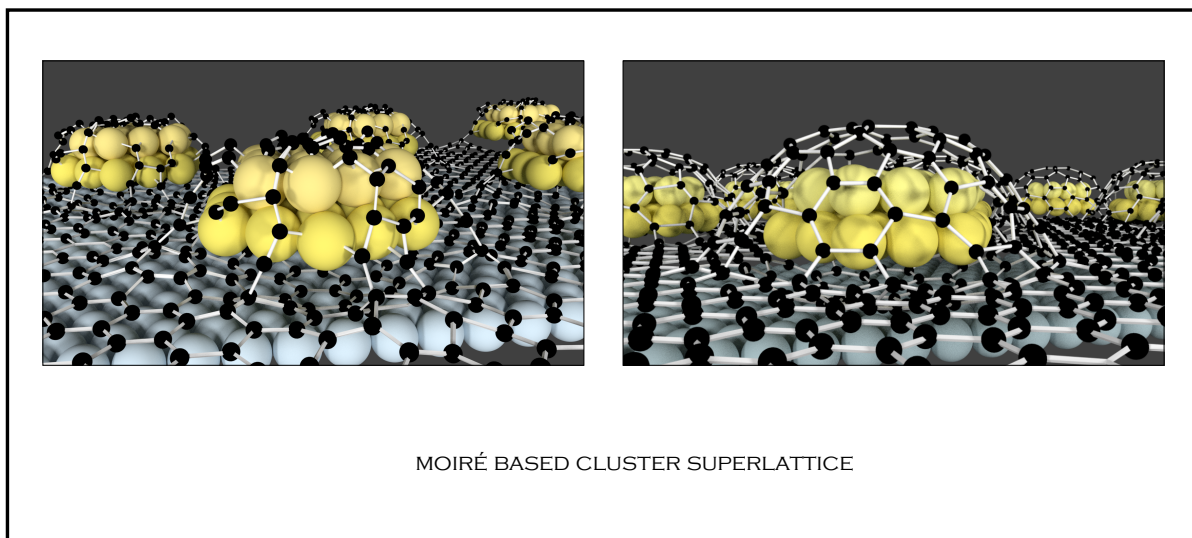


**Figure B.1:** 3D rendered interpretation of the Gr/Ir(111) moiré cluster superlattice embedded by C. The left side shows C radicals that bind preferably to metal atoms of the ordered cluster lattice and by this improve their thermal stability significantly [352]. When this sample is thermally annealed, the adsorbed carbon atoms on the metal clusters form a fullerene like cap, which can bind to underlying Gr sheet.

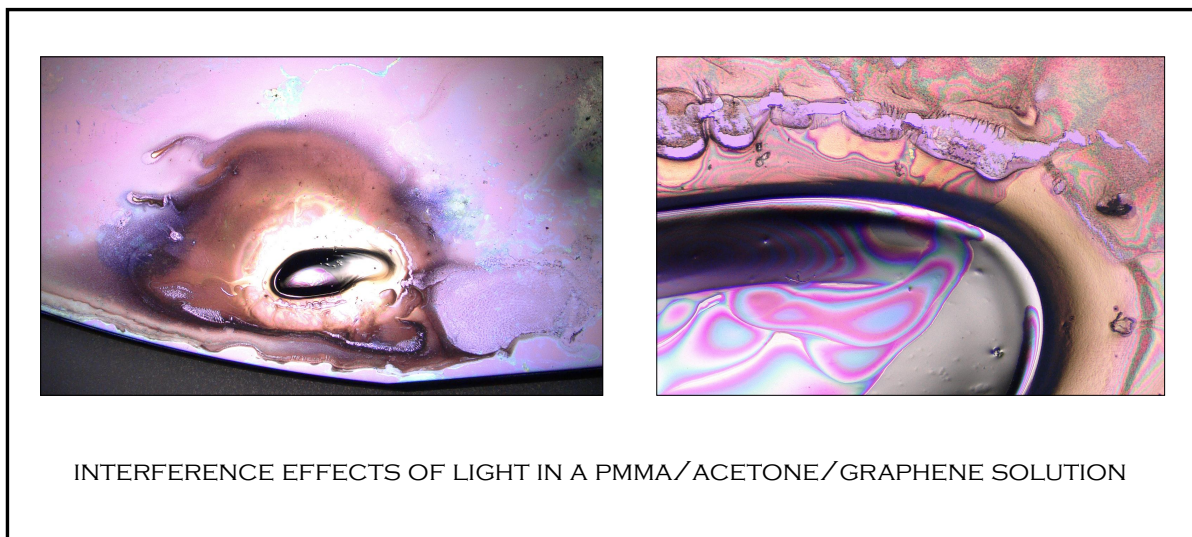


**Figure B.2:** Optical microscopy images of a PMMA-Gr membrane dissolving in pure acetone on a SiO<sub>2</sub> substrate. The zoom on the left side shows interference effects of light on the remaining PMMA and on residuals of dissolved PMMA. The field of view is 17.4 mm left and 1.7 mm right.

## B.2 Interference effects of visible light in PMMA/Gr-membranes transferred on SiO<sub>2</sub>

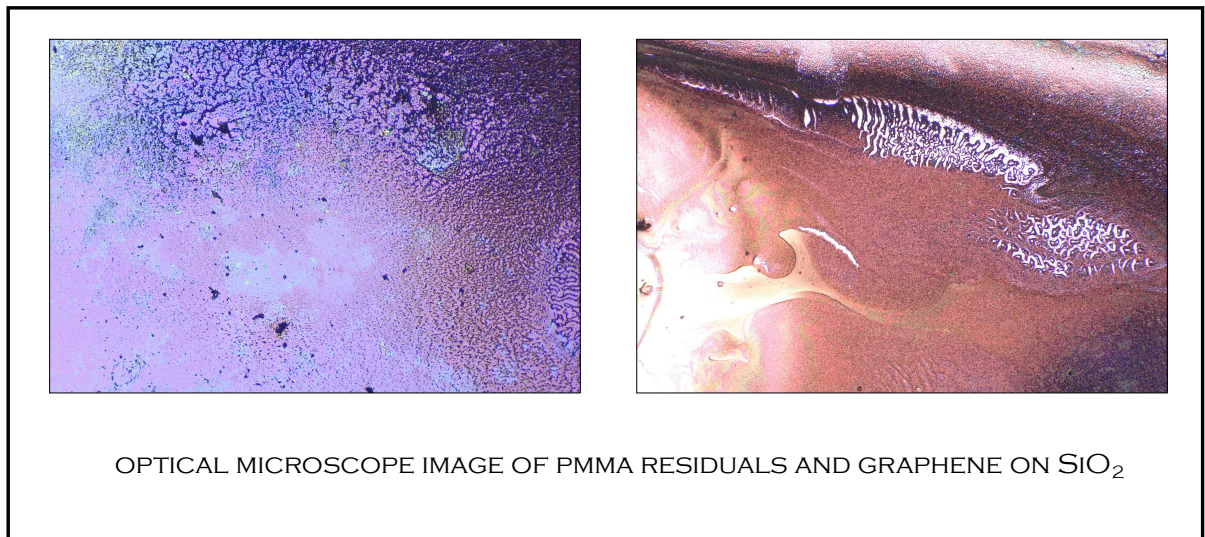


**Figure B.3:** Optical microscopy images of a PMMA-Gr membrane dissolving in pure acetone on a SiO<sub>2</sub> substrate. The residuals after PMMA dissolution resembles dune like structures. When the dissolved PMMA is still wet, the structures appear bright as shown in the right image. Field of view is 1.7 mm each.

## APPENDIX C

### Liste der Teilpublikationen (*List of Publications*)

---

Teile dieser Arbeit wurden als Bestandteil der folgenden Artikel in Fachzeitschriften bereits veröffentlicht:

*Parts of the results presented in this thesis can be found in the following publications:*

- [252] K. Omambac, M. Petrovic, **P. Valerius**, P. Bampoulis, T. Michely, M. Horn von Hoegen, and F. Meyer zu Heringdorf  
*Thermal dispersion of h-BN and formation of borophene on Ir(111)*  
in preparation, (2020)
- [317] **P. Valerius**, C. Speckmann, N. Atodiresei, B. V. Senkovskiy, A. Grüneis, and T. Michely  
*Growth stagnation in a magic vacancy cluster mesh*  
in preparation, (2020)
- [284] **P. Valerius**, S. Kretschmer, B. V. Senkovskiy, S. Wu, J. Hall, A. Herman, N. Ehlen, M. Ghorbani-Asl, A. Grüneis, A. V. Krasheninnikov, and T. Michely  
*Reversible crystalline-to-amorphous phase transformation in monolayer MoS<sub>2</sub> under grazing ion irradiation*  
2D Materials, **07** (2020), 025005
- [325] **P. Valerius**, A. Herman, and T. Michely  
*Suppression of wrinkle formation in graphene on Ir(111) by high-temperature, low-energy ion irradiation*  
Nanotechnology, **30** (2018), 011006
- [251] **P. Valerius**, C. Herbig, M. Will, M. A. Arman, J. Knudsen, V. Caciuc, N. Atodiresei, and T. Michely  
*Annealing of ion-irradiated hexagonal boron nitride on Ir(111)*  
Phys. Rev. B., **96** (2017), 235410

---

**Weitere Publikationen:**

*Further publications:*

- [352] M. Will, P. Bampoulis, T. Hartl, **P. Valerius**, and T. Michely  
*Conformal Embedding of Cluster Superlattices with Carbon*  
ACS Applied Materials & Interfaces, **11** (2019), 40524-40532
- [192] M. Will, N. Atodiresei, V. Caciuc, **P. Valerius**, C. Herbig, and T. Michely  
*A Monolayer of Hexagonal Boron Nitride on Ir(111) as a Template for Cluster Superlattices*  
ACS Nano, **12** (2018), 6871-6880

## Appendix C Liste der Teilpublikationen (*List of Publications*)

---

### Konferenzbeiträge als präsentierender Autor:

*Conference contributions as presenting author:*

- 2019/08** International Conference on Ion-Surface Interactions (ISI), Moscow (Russia), invited talk, *Reversible crystalline-to-amorphous phase transformation in monolayer MoS<sub>2</sub> under grazing ion irradiation*
- 2019/03** DPG Spring Meeting Section Condensed Matter, Regensburg (Germany), talk, *Reversible crystalline-to-amorphous phase transformation in monolayer MoS<sub>2</sub>*
- 2018/07** European Workshop on Epitaxial Graphene and 2D Materials, Salamanca (Spain), poster, *Supported 2D materials under low-energy He ion irradiation*
- 2018/03** DPG Spring Meeting, Berlin (DE), poster, *Epitaxially grown 2D materials under He ion irradiation: towards one atom thick membranes*
- 2017/09** International Workshop on Inelastic Ion-Surface Collisions (IISC), Dresden (Germany), poster, *Ion irradiation of h-BN and Gr on Ir(111)*
- 2017/02** Toward Reality in Nanoscale Materials X (TRNM), Levi (Finland), talk, *Epitaxially grown h-BN on Ir(111): A one atomic thick layer under ion irradiation*
- 2016/07** EWE G/2D, Bergisch Gladbach (Germany), poster, *Crystalline Xe underneath a monolayer of hexagonal boron nitride*
- 2016/03** DPG Spring Meeting, Regensburg (Germany), poster, *Crystalline Xe underneath a monolayer of hexagonal boron nitride*

## Bibliography

- [1] M. Ashton, J. Paul, S. B. Sinnott and R. G. Hennig, 'Topology-scaling identification of layered solids and stable exfoliated 2D materials', *Phys Rev Lett* **118**, 106101 (2017). Cited on page(s) 3 and 13
- [2] A. Zurutuza and C. Marinelli, 'Challenges and opportunities in graphene commercialization', *Nat Nanotechnol* **9**, 730 (2014). Cited on page(s) 3
- [3] A. C. Ferrari *et al.*, 'Science and technology roadmap for graphene, related two-dimensional crystals, and hybrid systems', *Nanoscale* **7**, 4598 (2015). Cited on page(s) 3
- [4] M. F. El-Kady, Y. Shao and R. B. Kaner, 'Graphene for batteries, supercapacitors and beyond', *Nat Rev Mater* **1**, 1 (2016). Cited on page(s) 3
- [5] Y. Cao, V. Fatemi, S. Fang, K. Watanabe, T. Taniguchi, E. Kaxiras and P. Jarillo-Herrero, 'Unconventional superconductivity in magic-angle graphene superlattices', *Nature* **556**, 43 (2018). Cited on page(s) 3 and 16
- [6] M. Yankowitz, S. Chen, H. Polshyn, Y. Zhang, K. Watanabe, T. Taniguchi, D. Graf, A. F. Young and C. R. Dean, 'Tuning superconductivity in twisted bilayer graphene', *Science* **363**, 1059 (2019). Cited on page(s) 3 and 16
- [7] A. K. Geim and I. V. Grigorieva, 'Van der Waals heterostructures', *Nature* **499**, 419 (2013). Cited on page(s) 3
- [8] A. C. Neto, F. Guinea, N. M. Peres, K. S. Novoselov and A. K. Geim, 'The electronic properties of graphene', *Rev Mod Phys* **81**, 109 (2009). Cited on page(s) 3
- [9] M. Topsakal, E. Aktürk and S. Ciraci, 'First-principles study of two- and one-dimensional honeycomb structures of boron nitride', *Phys Rev B* **79**, 115442 (2009). Cited on page(s) 3 and 14
- [10] K. Kobayashi and J. Yamauchi, 'Electronic structure and scanning-tunneling-microscopy image of molybdenum dichalcogenide surfaces', *Phys Rev B* **51**, 17085 (1995). Cited on page(s) 3 and 14
- [11] C. Murray, W. Jolie, J. A. Fischer, J. Hall, C. van Efferen, N. Ehlen, A. Grüneis, C. Busse and T. Michely, 'Comprehensive tunneling spectroscopy of quasifreestanding MoS<sub>2</sub> on graphene on Ir(111)', *Phys Rev B* **99**, 115434 (2019). Cited on page(s) 3, 15, 18, 75, and 84
- [12] L. Britnell *et al.*, 'Field-effect tunneling transistor based on vertical graphene heterostructures', *Science* **335**, 947 (2012). Cited on page(s) 3 and 16
- [13] F. Withers *et al.*, 'Light-emitting diodes by band-structure engineering in van der Waals heterostructures', *Nat Mater* **14**, 301 (2015). Cited on page(s) 3 and 16
- [14] K. Gopinadhan, Y. Shin, R. Jalil, T. Venkatesan, A. Geim, A. Neto and H. Yang, 'Extremely large magnetoresistance in few-layer graphene/boron-nitride heterostructures', *Nat Commun* **6**, 8337 (2015). Cited on page(s) 3 and 16
- [15] H. Li *et al.*, 'Activating and optimizing MoS<sub>2</sub> basal planes for hydrogen evolution through the formation of strained sulphur vacancies', *Nat Mater* **15**, 48 (2016). Cited on page(s) 3, 15, 18, 20, 73, 85, and 130
- [16] S. McDonnell, R. Addou, C. Buie, R. M. Wallace and C. L. Hinkle, 'Defect-dominated doping and contact resistance in MoS<sub>2</sub>', *ACS Nano* **8**, 2880 (2014). Cited on page(s) 3, 20, and 73
- [17] D. Cohen-Tanugi and J. Grossman, 'Water desalination across nanoporous graphene', *Nano Lett* **12**, 3602 (2012). Cited on page(s) 3, 68, 91, and 92

## Bibliography

---

- [18] M. E. Suk and N. R. Aluru, 'Water transport through ultrathin graphene', *J Phys Chem Lett* **1**, 1590 (2010). Cited on page(s) 3 and 91
- [19] K. Sint, B. Wang and P. Král, 'Selective ion passage through functionalized graphene nanopores', *J Am Chem Soc* **130**, 16448 (2008). Cited on page(s) 3 and 91
- [20] S. P. Surwade, S. N. Smirnov, I. V. Vlassiuk, R. R. Unocic, G. M. Veith, S. Dai and S. M. Mahurin, 'Water desalination using nanoporous single-layer graphene', *Nat Nanotechnol* **10**, 459 (2015). Cited on page(s) 3 and 91
- [21] P. Sun, M. Zhu, K. Wang, M. Zhong, J. Wei, D. Wu, Z. Xu and H. Zhu, 'Selective ion penetration of graphene oxide membranes', *ACS Nano* **7**, 428 (2012). Cited on page(s) 3 and 91
- [22] P. R. Kidambi, M. S. Boutilier, L. Wang, D. Jang, J. Kim and R. Karnik, 'Selective nanoscale mass transport across atomically thin single crystalline graphene membranes', *Adv Mater* **29**, 1605896 (2017). Cited on page(s) 3 and 91
- [23] J. Abraham *et al.*, 'Tunable sieving of ions using graphene oxide membranes', *Nat Nanotechnol* **12**, 546 (2017). Cited on page(s) 3 and 91
- [24] S. C. O'Hern, C. A. Stewart, M. S. Boutilier, J.-C. Idrobo, S. Bhaviripudi, S. K. Das, J. Kong, T. Laoui, M. Atieh and R. Karnik, 'Selective molecular transport through intrinsic defects in a single layer of CVD graphene', *ACS Nano* **6**, 10130 (2012). Cited on page(s) 3 and 91
- [25] S. C. O'Hern, M. S. Boutilier, J.-C. Idrobo, Y. Song, J. Kong, T. Laoui, M. Atieh and R. Karnik, 'Selective ionic transport through tunable subnanometer pores in single-layer graphene membranes', *Nano Lett* **14**, 1234 (2014). Cited on page(s) 3 and 91
- [26] S. Standop, O. Lehtinen, C. Herbig, G. Lewes-Malandrakis, F. Craes, J. Kotakoski, T. Michely, A. V. Krashennnikov and C. Busse, 'Ion impacts on graphene/Ir(111): interface channeling, vacancy funnels, and a nanomesh', *Nano Lett* **13**, 1948 (2013). Cited on page(s) 4, 21, 25, 43, 46, 47, 68, 79, 84, 91, 92, 122, and 123
- [27] L. Wang, M. S. Boutilier, P. R. Kidambi, D. Jang, N. G. Hadjiconstantinou and R. Karnik, 'Fundamental transport mechanisms, fabrication and potential applications of nanoporous atomically thin membranes', *Nat Nanotechnol* **12**, 509 (2017). Cited on page(s) 4, 18, and 91
- [28] C. Herbig and T. Michely, 'Graphene: the ultimately thin sputtering shield', *2D Mater* **3**, 025032 (2016). Cited on page(s) 4, 25, and 43
- [29] C. Herbig, E. Åhlgren, U. Schröder, A. Martínez-Galera, M. Arman, J. Kotakoski, J. Knudsen, A. Krashennnikov and T. Michely, 'Xe irradiation of graphene on Ir(111): From trapping to blistering', *Phys Rev B* **92**, 085429 (2015). Cited on page(s) 4, 25, 43, 44, 46, 52, 53, 56, 59, 68, 69, 77, 99, 102, 103, 122, 123, and 138
- [30] R. Larciprete, S. Colonna, F. Ronci, R. Flammini, P. Lacovig, N. Apostol, A. Politano, P. Feulner, D. Menzel and S. Lizzit, 'Self-assembly of graphene nanoblister sealed to a bare metal surface', *Nano Lett* **16**, 1808 (2016). Cited on page(s) 4, 25, 43, 56, 69, and 122
- [31] J. Ziegler, M. Ziegler and J. Biersack, 'SRIM—The stopping and range of ions in matter', *Nucl Instr Meth Phys Res Sec B* **268**, 1818 (2010). Cited on page(s) 8, 70, and 101
- [32] K. Oura, A. Zotov, V. Lifshits, A. Saranin and M. Katayama, 'Surface Science' (Springer-Verlag, Berlin Heidelberg, 2003). Cited on page(s) 9, 10, 28, 29, and 33
- [33] R. S. Williams, in 'Quantitative Intensity Analysis of Low-Energy Scattering and Recoiling from Crystal Surfaces', edited by J. W. Rabalais (Wiley, New York, 1994), Pages 1–54. Cited on page(s) 10
- [34] L. C. Feldman, J. W. Mayer and S. T. Picraux, 'Materials analysis by ion channeling: submicron crystallography' (Academic Press, New York, 2012). Cited on page(s) 10

- [35] A. Redinger, S. Standop, T. Michely, Y. Rosandi and H. M. Urbassek, 'Trails of kilovolt ions created by subsurface channeling', *Phys Rev Lett* **104**, 075501 (2010). Cited on page(s) 10 and 79
- [36] A. Redinger, S. Standop, Y. Rosandi, H. Urbassek and T. Michely, 'Making channeling visible: keV noble gas ion trails on Pt (111)', *New J Phys* **13**, 013002 (2011). Cited on page(s) 11
- [37] A. Redinger, 'Surface damage through grazing incidence ions investigated by scanning tunneling microscopy', Dissertation, University of Cologne, 2009. Cited on page(s) 11
- [38] M. A. Nastasi and J. W. Mayer, 'Ion implantation and synthesis of materials' (Springer, Berlin, 2006), Vol. 80. Cited on page(s) 12
- [39] R. Behrisch, 'Sputtering by particle bombardment' (Springer Verlag, Berlin-Heidelberg, 1981). Cited on page(s) 12
- [40] H. Hansen, C. Polop, T. Michely, A. Friedrich and H. M. Urbassek, 'Step edge sputtering yield at grazing incidence ion bombardment', *Phys Rev Lett* **92**, 246106 (2004). Cited on page(s) 12, 13, 76, and 84
- [41] W. Meng, P. Okamoto, L. Thompson, B. Kestel and L. Rehn, 'Hydrogen-induced crystal to glass transformation in  $Zr_3Al$ ', *Appl Phys Lett* **53**, 1820 (1988). Cited on page(s) 13
- [42] D. Luzzi and M. Meshii, 'The crystalline to amorphous transition of intermetallic compounds under electron irradiation-a review', *Res Mechanica* **21**, 207 (1987). Cited on page(s) 13
- [43] M. Tsai and B. Streetman, 'Recrystallization of implanted amorphous silicon layers. I. Electrical properties of silicon implanted with  $BF_2^+$  or  $Si^+ + B^+$ ', *J Appl Phys* **50**, 183 (1979). Cited on page(s) 13
- [44] E. Gerstner, 'Nobel prize 2010: Andre Geim & Konstantin Novoselov', *Nat Phys* **6**, 836 (2010). Cited on page(s) 14
- [45] C.-H. Chang, X. Fan, S.-H. Lin and J.-L. Kuo, 'Orbital analysis of electronic structure and phonon dispersion in  $MoS_2$ ,  $MoSe_2$ ,  $WS_2$ , and  $WSe_2$  monolayers under strain', *Phys Rev B* **88**, 195420 (2013). Cited on page(s) 14
- [46] T. Yokoya, T. Kiss, A. Chainani, S. Shin, M. Nohara and H. Takagi, 'Fermi surface sheet-dependent superconductivity in  $2H-NbSe_2$ ', *Science* **294**, 2518 (2001). Cited on page(s) 14
- [47] X. Xi, Z. Wang, W. Zhao, J.-H. Park, K. T. Law, H. Berger, L. Forró, J. Shan and K. F. Mak, 'Ising pairing in superconducting  $NbSe_2$  atomic layers', *Nat Phys* **12**, 139 (2016). Cited on page(s) 14
- [48] E. Navarro-Moratalla *et al.*, 'Enhanced superconductivity in atomically thin  $TaS_2$ ', *Nat Commun* **7**, 1 (2016). Cited on page(s) 14
- [49] H. Dil, J. Lobo-Checa, R. Laskowski, P. Blaha, S. Berner, J. Osterwalder and T. Greber, 'Surface trapping of atoms and molecules with dipole rings', *Science* **319**, 1824 (2008). Cited on page(s) 15
- [50] F. Schulz, R. Drost, S. Hämäläinen and P. Liljeroth, 'Templated self-assembly and local doping of molecules on epitaxial hexagonal boron nitride', *ACS Nano* **7**, 11121 (2013). Cited on page(s) 15 and 23
- [51] P. Gehring, B. Gao, M. Burghard and K. Kern, 'Growth of high-mobility  $Bi_2Te_2Se$  nanoplatelets on hBN sheets by van der Waals epitaxy', *Nano Lett* **12**, 5137 (2012). Cited on page(s) 15
- [52] C. Dean *et al.*, 'Boron nitride substrates for high-quality graphene electronics', *Nat Nanotechnol* **5**, 722 (2010). Cited on page(s) 15
- [53] D. Golberg, Y. Bando, Y. Huang, T. Terao, M. Mitome, C. Tang and C. Zhi, 'Boron nitride nanotubes and nanosheets', *ACS Nano* **4**, 2979 (2010). Cited on page(s) 15
- [54] W. Lei, D. Portehault, D. Liu, S. Qin and Y. Chen, 'Porous boron nitride nanosheets for effective water cleaning', *Nat Commun* **4**, 1777 (2013). Cited on page(s) 15

## Bibliography

---

- [55] J. Azamat, A. Khataee and F. Sadikoglu, 'Separation of carbon dioxide and nitrogen gases through modified boron nitride nanosheets as a membrane: insights from molecular dynamics simulations', *RSC Adv* **6**, 94911 (2016). Cited on page(s) 15, 68, and 91
- [56] M. Yamaguchi, J. Bernhardt, K. Faerstein, D. Shtansky, Y. Bando, I. Golovin, H. Sinning and D. Golberg, 'Fabrication and characteristics of melt-spun Al ribbons reinforced with nano/micro-BN phases', *Acta Mater* **61**, 7604 (2013). Cited on page(s) 15
- [57] J. Martin, C. Donnet, T. Le Mogne and T. Epicier, 'Superlubricity of molybdenum disulphide', *Phys Rev B* **48**, 10583 (1993). Cited on page(s) 15 and 73
- [58] B. C. Windom, W. Sawyer and D. W. Hahn, 'A Raman spectroscopic study of MoS<sub>2</sub> and MoO<sub>3</sub>: applications to tribological systems', *Tribol Lett* **42**, 301 (2011). Cited on page(s) 15 and 73
- [59] K. Chang, Z. Mei, T. Wang, Q. Kang, S. Ouyang and J. Ye, 'MoS<sub>2</sub>/graphene cocatalyst for efficient photocatalytic H<sub>2</sub> evolution under visible light irradiation', *ACS Nano* **8**, 7078 (2014). Cited on page(s) 15 and 73
- [60] Y. Li, H. Wang, L. Xie, Y. Liang, G. Hong and H. Dai, 'MoS<sub>2</sub> nanoparticles grown on graphene: an advanced catalyst for the hydrogen evolution reaction', *J Am Chem Soc* **133**, 7296 (2011). Cited on page(s) 15 and 73
- [61] B. Radisavljevic, A. Radenovic, J. Brivio, i. Giacometti and A. Kis, 'Single-layer MoS<sub>2</sub> transistors', *Nat Nanotechnol* **6**, 147 (2011). Cited on page(s) 15 and 73
- [62] Q. H. Wang, K. Kalantar-Zadeh, A. Kis, J. N. Coleman and M. S. Strano, 'Electronics and optoelectronics of two-dimensional transition metal dichalcogenides', *Nat Nanotechnol* **7**, 699 (2012). Cited on page(s) 15 and 73
- [63] Z. Yin, H. Li, H. Li, L. Jiang, Y. Shi, Y. Sun, G. Lu, Q. Zhang, X. Chen and H. Zhang, 'Single-layer MoS<sub>2</sub> phototransistors', *ACS Nano* **6**, 74 (2011). Cited on page(s) 15 and 73
- [64] D. Lien, M. Amani, S. B. Desai, G. H. Ahn, K. Han, J.-H. He, J. W. Ager, M. C. Wu and A. Javey, 'Large-area and bright pulsed electroluminescence in monolayer semiconductors', *Nat Commun* **9**, 1229 (2018). Cited on page(s) 15 and 73
- [65] J. Kim *et al.*, 'Observation of ultralong valley lifetime in WSe<sub>2</sub>/MoS<sub>2</sub> heterostructures', *Sci Adv* **3**, e1700518 (2017). Cited on page(s) 15 and 73
- [66] K. F. Mak, C. Lee, J. Hone, J. Shan and T. F. Heinz, 'Atomically thin MoS<sub>2</sub>: a new direct-gap semiconductor', *Phys Rev Lett* **105**, 136805 (2010). Cited on page(s) 15
- [67] G.-B. Liu, W.-Y. Shan, Y. Yao, W. Yao and D. Xiao, 'Three-band tight-binding model for monolayers of group-VIB transition metal dichalcogenides', *Phys Rev B* **88**, 085433 (2013). Cited on page(s) 15
- [68] Z. M. Wang, 'MoS<sub>2</sub>: materials, physics, and devices' (Springer Science & Business Media, Chengdu People's Republic of China, 2013), Vol. 21. Cited on page(s) 16
- [69] K. F. Mak, K. He, J. Shan and T. F. Heinz, 'Control of valley polarization in monolayer MoS<sub>2</sub> by optical helicity', *Nat Nanotechnol* **7**, 494 (2012). Cited on page(s) 16
- [70] D. Xiao, G.-B. Liu, W. Feng, X. Xu and W. Yao, 'Coupled spin and valley physics in monolayers of MoS<sub>2</sub> and other group-VI dichalcogenides', *Phys Rev Lett* **108**, 196802 (2012). Cited on page(s) 16
- [71] C. J. Chen, 'Introduction to scanning tunneling microscopy' (Oxford University Press on Demand, New York, 1993), Vol. 4. Cited on page(s) 16
- [72] X. Li *et al.*, 'Large-area synthesis of high-quality and uniform graphene films on copper foils', *Science* **324**, 1312 (2009). Cited on page(s) 16 and 21
- [73] F. Hao, D. Fang and Z. Xu, 'Mechanical and thermal transport properties of graphene with defects', *Appl Phys Lett* **99**, 041901 (2011). Cited on page(s) 17

- [74] G. He *et al.*, 'Conduction mechanisms in CVD-grown monolayer MoS<sub>2</sub> transistors: from variable-range hopping to velocity saturation', *Nano Lett* **15**, 5052 (2015). Cited on page(s) 17
- [75] B. Akdim, R. Pachter and S. Mou, 'Theoretical analysis of the combined effects of sulfur vacancies and analyte adsorption on the electronic properties of single-layer MoS<sub>2</sub>', *Nanotechnology* **27**, 185701 (2016). Cited on page(s) 17
- [76] F. Banhart, J. Kotakoski and A. V. Krasheninnikov, 'Structural defects in graphene', *ACS Nano* **5**, 26 (2011). Cited on page(s) 17
- [77] J. Kotakoski, J. Meyer, S. Kurasch, D. Santos-Cottin, U. Kaiser and A. Krasheninnikov, 'Stone-Wales-type transformations in carbon nanostructures driven by electron irradiation', *Phys Rev B* **83**, 245420 (2011). Cited on page(s) 17
- [78] J. Kotakoski, A. Krasheninnikov, U. Kaiser and J. Meyer, 'From point defects in graphene to two-dimensional amorphous carbon', *Phys Rev Lett* **106**, 105505 (2011). Cited on page(s) 17, 19, and 20
- [79] J. C. Meyer, C. Kisielowski, R. Erni, M. D. Rossell, M. Crommie and A. Zettl, 'Direct imaging of lattice atoms and topological defects in graphene membranes', *Nano Lett* **8**, 3582 (2008). Cited on page(s) 17 and 43
- [80] O. Lehtinen, S. Kurasch, A. Krasheninnikov and U. Kaiser, 'Atomic scale study of the life cycle of a dislocation in graphene from birth to annihilation', *Nat Commun* **4**, 2098 (2013). Cited on page(s) 17, 19, 43, and 120
- [81] O. Lehtinen, I.-L. Tsai, R. Jalil, R. R. Nair, J. Keinonen, U. Kaiser and I. V. Grigorieva, 'Non-invasive transmission electron microscopy of vacancy defects in graphene produced by ion irradiation', *Nanoscale* **6**, 6569 (2014). Cited on page(s) 17
- [82] O. Lehtinen, J. Kotakoski, A. Krasheninnikov, A. Tolvanen, K. Nordlund and J. Keinonen, 'Effects of ion bombardment on a two-dimensional target: atomistic simulations of graphene irradiation', *Phys Rev B* **81**, 153401 (2010). Cited on page(s) 17, 92, 105, and 120
- [83] O. Lehtinen, E. Dumur, J. Kotakoski, A. Krasheninnikov, K. Nordlund and J. Keinonen, 'Production of defects in hexagonal boron nitride monolayer under ion irradiation', *Nucl Instr Meth Phys Res B* **269**, 1327 (2011). Cited on page(s) 17, 47, 60, 92, and 105
- [84] Y. H. Lee, S. G. Kim and D. Tománek, 'Catalytic growth of single-wall carbon nanotubes: an ab initio study', *Phys Rev Lett* **78**, 2393 (1997). Cited on page(s) 17
- [85] L. Zhao *et al.*, 'Visualizing individual nitrogen dopants in monolayer graphene', *Science* **333**, 999 (2011). Cited on page(s) 17
- [86] A. Lherbier, A. R. Botello-Mendez and J.-C. Charlier, 'Electronic and transport properties of unbalanced sublattice N-doping in graphene', *Nano Lett* **13**, 1446 (2013). Cited on page(s) 17
- [87] Y. Wang, Y. Huang, Y. Song, X. Zhang, Y. Ma, J. Liang and Y. Chen, 'Room-temperature ferromagnetism of graphene', *Nano Lett* **9**, 220 (2008). Cited on page(s) 17
- [88] M. Vozmediano, M. López-Sancho, T. Stauber and F. Guinea, 'Local defects and ferromagnetism in graphene layers', *Phys Rev B* **72**, 155121 (2005). Cited on page(s) 17
- [89] C. Jin, F. Lin, K. Suenaga and S. Iijima, 'Fabrication of a freestanding boron nitride single layer and its defect assignments', *Phys Rev Lett* **102**, 195505 (2009). Cited on page(s) 17, 20, and 69
- [90] J. Meyer, A. Chuvilin, G. Algara-Siller, J. Biskupek and U. Kaiser, 'Selective sputtering and atomic resolution imaging of atomically thin boron nitride membranes', *Nano Lett* **9**, 2683 (2009). Cited on page(s) 17, 20, 43, and 69
- [91] A. Krasheninnikov, P. Lehtinen, A. Foster and R. Nieminen, 'Bending the rules: contrasting vacancy energetics and migration in graphite and carbon nanotubes', *Chem Phys Lett* **418**, 132 (2006). Cited on page(s) 17 and 43

## Bibliography

---

- [92] A. Zobelli, C. Ewels, A. Gloter and G. Seifert, 'Vacancy migration in hexagonal boron nitride', *Phys Rev B* **75**, 094104 (2007). Cited on page(s) 17, 43, and 104
- [93] J. A. Fürst, J. G. Pedersen, C. Flindt, N. A. Mortensen, M. Brandbyge, T. G. Pedersen and A.-P. Jauho, 'Electronic properties of graphene antidot lattices', *New J Phys* **11**, 095020 (2009). Cited on page(s) 17
- [94] I. Naumov and A. Bratkovsky, 'Semiconducting graphene nanomeshes', *Phys Rev B* **85**, 201414 (2012). Cited on page(s) 17
- [95] J. Eroms and D. Weiss, 'Weak localization and transport gap in graphene antidot lattices', *New J Phys* **11**, 095021 (2009). Cited on page(s) 17
- [96] X. Liang, Y.-S. Jung, S. Wu, A. Ismach, D. L. Olynick, S. Cabrini and J. Bokor, 'Formation of bandgap and subbands in graphene nanomeshes with sub-10 nm ribbon width fabricated via nanoimprint lithography', *Nano Lett* **10**, 2454 (2010). Cited on page(s) 17
- [97] C. J. Russo and J. A. Golovchenko, 'Atom-by-atom nucleation and growth of graphene nanopores', *PNAS* **109**, 5953 (2012). Cited on page(s) 18
- [98] Z. Wang, 'Structure and electronic properties of boron nitride sheet with grain boundaries', *J Nanopart Res* **14**, 1 (2012). Cited on page(s) 18
- [99] H. Liu, M. Si, S. Najmaei, A. T. Neal, Y. Du, P. M. Ajayan, J. Lou and P. D. Ye, 'Statistical study of deep submicron dual-gated field-effect transistors on monolayer chemical vapor deposition molybdenum disulfide films', *Nano Lett* **13**, 2640 (2013). Cited on page(s) 18
- [100] K.-K. Liu *et al.*, 'Growth of large-area and highly crystalline MoS<sub>2</sub> thin layers on insulating substrates', *Nano Lett* **12**, 1538 (2012). Cited on page(s) 18
- [101] J. Hong *et al.*, 'Exploring atomic defects in molybdenum disulphide monolayers', *Nat Commun* **6**, 6293 (2015). Cited on page(s) 18
- [102] Y.-C. Lin, D. O. Dumcenco, H.-P. Komsa, Y. Niimi, A. V. Krasheninnikov, Y.-S. Huang and K. Suenaga, 'Properties of individual dopant atoms in single-layer MoS<sub>2</sub>: atomic structure, migration, and enhanced reactivity', *Adv Mater* **26**, 2857 (2014). Cited on page(s) 18
- [103] W. Zhou, X. Zou, S. Najmaei, Z. Liu, Y. Shi, J. Kong, J. Lou, P. M. Ajayan, B. I. Yakobson and J.-C. Idrobo, 'Intrinsic structural defects in monolayer molybdenum disulfide', *Nano Lett* **13**, 2615 (2013). Cited on page(s) 18
- [104] W. Jolie *et al.*, 'Tomonaga-Luttinger Liquid in a Box: Electrons Confined within MoS<sub>2</sub> Mirror-Twin Boundaries', *Phys Rev X* **9**, 011055 (2019). Cited on page(s) 18 and 75
- [105] J. Kotakoski, C. Jin, O. Lehtinen, K. Suenaga and A. Krasheninnikov, 'Electron knock-on damage in hexagonal boron nitride monolayers', *Phys Rev B* **82**, 113404 (2010). Cited on page(s) 19, 20, and 43
- [106] O. V. Yazyev, I. Tavernelli, U. Rothlisberger and L. Helm, 'Early stages of radiation damage in graphite and carbon nanostructures: A first-principles molecular dynamics study', *Phys Rev B* **75**, 115418 (2007). Cited on page(s) 19
- [107] J. C. Meyer *et al.*, 'Accurate measurement of electron beam induced displacement cross sections for single-layer graphene', *Phys Rev Lett* **108**, 196102 (2012). Cited on page(s) 19
- [108] H.-P. Komsa, J. Kotakoski, S. Kurasch, O. Lehtinen, U. Kaiser and A. V. Krasheninnikov, 'Two-dimensional transition metal dichalcogenides under electron irradiation: defect production and doping', *Phys Rev Lett* **109**, 035503 (2012). Cited on page(s) 19
- [109] C. Gong, A. W. Robertson, K. He, G.-D. Lee, E. Yoon, C. S. Allen, A. I. Kirkland and J. H. Warner, 'Thermally induced dynamics of dislocations in graphene at atomic resolution', *ACS Nano* **9**, 10066 (2015). Cited on page(s) 19 and 120

- [110] J. H. Warner, E. R. Margine, M. Mukai, A. W. Robertson, F. Giustino and A. I. Kirkland, 'Dislocation-driven deformations in graphene', *Science* **337**, 209 (2012). Cited on page(s) 19, 43, and 120
- [111] P. Willke, J. A. Amani, A. Sinterhauf, S. Thakur, T. Kotzott, T. Druga, S. Weikert, K. Maiti, H. Hofsäss and M. Wenderoth, 'Doping of graphene by low-energy ion beam implantation: structural, electronic, and transport properties', *Nano Lett* **15**, 5110 (2015). Cited on page(s) 19
- [112] E. Åhlgren, S. Hämäläinen, O. Lehtinen, P. Liljeroth and J. Kotakoski, 'Structural manipulation of the graphene/metal interface with Ar<sup>+</sup> irradiation', *Phys Rev B* **88**, 155419 (2013). Cited on page(s) 20, 25, and 43
- [113] E. Gruber *et al.*, 'Ultrafast electronic response of graphene to a strong and localized electric field', *Nat Commun* **7**, 1 (2016). Cited on page(s) 20
- [114] J. Hopster, R. Kozubek, B. Ban-d'Etat, S. Guillous, H. Lebius and M. Schleberger, 'Damage in graphene due to electronic excitation induced by highly charged ions', *2D Mater* **1**, 011011 (2014). Cited on page(s) 20
- [115] L. Madauß, O. Ochedowski, H. Lebius, B. Ban-d'Etat, C. H. Naylor, A. C. Johnson, J. Kotakoski and M. Schleberger, 'Defect engineering of single- and few-layer MoS<sub>2</sub> by swift heavy ion irradiation', *2D Mater* **4**, 15034 (2017). Cited on page(s) 20 and 73
- [116] N. Alem, R. Erni, C. Kisielowski, M. D. Rossell, W. Gannett and A. Zettl, 'Atomically thin hexagonal boron nitride probed by ultrahigh-resolution transmission electron microscopy', *Phys Rev B* **80**, 155425 (2009). Cited on page(s) 20
- [117] B. Huang, H. Xiang, J. Yu and S.-H. Wei, 'Effective control of the charge and magnetic states of transition-metal atoms on single-layer boron nitride', *Phys Rev Lett* **108**, 206802 (2012). Cited on page(s) 20
- [118] D. S. Fox *et al.*, 'Nanopatterning and electrical tuning of MoS<sub>2</sub> layers with a subnanometer helium ion beam', *Nano Lett* **15**, 5307 (2015). Cited on page(s) 20 and 73
- [119] J. Zhu *et al.*, 'Argon plasma induced phase transition in monolayer MoS<sub>2</sub>', *J Am Chem Soc* **139**, 10216 (2017). Cited on page(s) 20, 73, 74, 84, and 86
- [120] A. K. Geim and K. S. Novoselov, 'The rise of graphene', *Nat Mater* **6**, 183 (2007). Cited on page(s) 20
- [121] A. Pakdel, Y. Bando and D. Golberg, 'Plasma-assisted interface engineering of boron nitride nanostructure films', *ACS Nano* **8**, 10631 (2014). Cited on page(s) 20
- [122] P. Sutter, J. T. Sadowski and E. Sutter, 'Graphene on Pt(111): Growth and substrate interaction', *Phys Rev B* **80**, 245411 (2009). Cited on page(s) 21
- [123] M. Gao, Y. Pan, L. Huang, H. Hu, L. Zhang, H. Guo, S. Du and H.-J. Gao, 'Epitaxial growth and structural property of graphene on Pt(111)', *Appl Phys Lett* **98**, 033101 (2011). Cited on page(s) 21
- [124] A. N'Diaye *et al.*, 'Structure of epitaxial graphene on Ir(111)', *New J Phys* **10**, 043033 (2008). Cited on page(s) 21, 75, 77, and 91
- [125] I. Pletikosić, M. Kralj, P. Pervan, R. Brako, J. Coraux, A. N'diaye, C. Busse and T. Michely, 'Dirac cones and minigaps for graphene on Ir(111)', *Phys Rev Lett* **102**, 056808 (2009). Cited on page(s) 21
- [126] C. Busse *et al.*, 'Graphene on Ir(111): physisorption with chemical modulation', *Phys Rev Lett* **107**, 036101 (2011). Cited on page(s) 21, 22, and 95
- [127] S. K. Hämäläinen, M. P. Boneschanscher, P. H. Jacobse, I. Swart, K. Pussi, W. Moritz, J. Lahtinen, P. Liljeroth and J. Sainio, 'Structure and local variations of the graphene moiré on Ir(111)', *Phys Rev B* **88**, 201406 (2013). Cited on page(s) 21
- [128] R. Addou, A. Dahal, P. Sutter and M. Batzill, 'Monolayer graphene growth on Ni(111) by low temperature chemical vapor deposition', *Appl Phys Lett* **100**, 021601 (2012). Cited on page(s) 21

## Bibliography

---

- [129] A. Dahal and M. Batzill, 'Graphene–nickel interfaces: a review', *Nanoscale* **6**, 2548 (2014). Cited on page(s) 21
- [130] A. V. De Parga, F. Calleja, B. Borca, M. Passeggi Jr, J. Hinarejos, F. Guinea and R. Miranda, 'Periodically rippled graphene: growth and spatially resolved electronic structure', *Phys Rev Lett* **100**, 056807 (2008). Cited on page(s) 21
- [131] W. Moritz, B. Wang, M.-L. Bocquet, T. Brugger, T. Greber, J. Wintterlin and S. Günther, 'Structure determination of the coincidence phase of graphene on Ru(0001)', *Phys Rev Lett* **104**, 136102 (2010). Cited on page(s) 21
- [132] L. Gao, J. R. Guest and N. P. Guisinger, 'Epitaxial graphene on Cu(111)', *Nano Lett* **10**, 3512 (2010). Cited on page(s) 21
- [133] T. Niu, M. Zhou, J. Zhang, Y. Feng and W. Chen, 'Growth intermediates for CVD graphene on Cu(111): carbon clusters and defective graphene', *J Am Chem Soc* **135**, 8409 (2013). Cited on page(s) 21
- [134] E. N. Voloshina, Y. S. Dedkov, S. Torbrügge, A. Thissen and M. Fonin, 'Graphene on Rh(111): Scanning tunneling and atomic force microscopy studies', *Appl Phys Lett* **100**, 241606 (2012). Cited on page(s) 21
- [135] B. Wang, M. Caffio, C. Bromley, H. Früchtl and R. Schaub, 'Coupling epitaxy, chemical bonding, and work function at the local scale in transition metal-supported graphene', *ACS Nano* **4**, 5773 (2010). Cited on page(s) 21
- [136] J. Knudsen, P. J. Feibelman, T. Gerber, E. Grånäs, K. Schulte, P. Stratmann, J. N. Andersen and T. Michely, 'Clusters binding to the graphene moiré on Ir(111): X-ray photoemission compared to density functional calculations', *Phys Rev B* **85**, 035407 (2012). Cited on page(s) 21 and 22
- [137] J. Coraux, A. N'Diaye, C. Busse and T. Michely, 'Structural coherency of graphene on Ir(111)', *Nano Lett* **8**, 565 (2008). Cited on page(s) 21, 36, and 120
- [138] J. Coraux *et al.*, 'Growth of graphene on Ir(111)', *New J Phys* **11**, 023006 (2009). Cited on page(s) 21
- [139] A. N'Diaye *et al.*, 'Two-dimensional Ir cluster lattice on a graphene moiré on Ir(111)', *Phys Rev Lett* **97**, 215501 (2006). Cited on page(s) 21, 22, 121, and 124
- [140] A. Krasheninnikov, N. Berseneva, D. Kvashnin, J. Enkovaara, T. Björkman, P. Sorokin, D. Shtansky, R. Nieminen and D. Golberg, 'Toward Stronger Al–BN Nanotube Composite Materials: Insights into Bonding at the Al/BN Interface from First-Principles Calculations', *J Phys Chem C* **118**, 26894 (2014). Cited on page(s) 21 and 92
- [141] C. Vo-Van, S. Schumacher, J. Coraux, V. Sessi, O. Fruchart, N. B. Brookes, P. Ohresser and T. Michely, 'Magnetism of cobalt nanoclusters on graphene on iridium', *Appl Phys Lett* **99**, 142504 (2011). Cited on page(s) 22
- [142] R. Baltic, M. Pivetta, F. Donati, C. Wäckerlin, A. Singha, J. Dreiser, S. Rusponi and H. Brune, 'Superlattice of single atom magnets on graphene', *Nano Lett* **16**, 7610 (2016). Cited on page(s) 22
- [143] C. Herbig, T. Knispel, S. Simon, U. A. Schröder, A. J. Martínez-Galera, M. A. Arman, C. Teichert, J. Knudsen, A. V. Krasheninnikov and T. Michely, 'From Permeation to Cluster Arrays: Graphene on Ir(111) Exposed to Carbon Vapor', *Nano Lett* **17**, 3105 (2017). Cited on page(s) 22
- [144] T. Gerber, J. Knudsen, P. J. Feibelman, E. Granas, P. Stratmann, K. Schulte, J. N. Andersen and T. Michely, 'CO-induced Smoluchowski ripening of Pt cluster arrays on the graphene/Ir(111) moiré', *ACS Nano* **7**, 2020 (2013). Cited on page(s) 22
- [145] D. Mousadacos, M. Pivetta, H. Brune and S. Rusponi, 'Sm cluster superlattice on graphene/Ir(111)', *New J Phys* **19**, 123021 (2017). Cited on page(s) 22
- [146] A. N'Diaye, T. Gerber, C. Busse, J. Mysliveček, J. Coraux and T. Michely, 'A versatile fabrication method for cluster superlattices', *New J Phys* **11**, 103045 (2009). Cited on page(s) 22

- [147] J. Mao, H. Zhang, Y. Jiang, Y. Pan, M. Gao, W. Xiao and H.-J. Gao, 'Tunability of supramolecular kagome lattices of magnetic phthalocyanines using graphene-based moiré patterns as templates', *J Am Chem Soc* **131**, 14136 (2009). Cited on page(s) 22
- [148] H. Zhang *et al.*, 'Assembly of iron phthalocyanine and pentacene molecules on a graphene monolayer grown on Ru(0001)', *Phys Rev B* **84**, 245436 (2011). Cited on page(s) 22
- [149] S. K. Hamalainen, M. Stepanova, R. Drost, P. Liljeroth, J. Lahtinen and J. Sainio, 'Self-assembly of cobalt-phthalocyanine molecules on epitaxial graphene on Ir(111)', *J Phys Chem C* **116**, 20433 (2012). Cited on page(s) 22
- [150] P. Järvinen, S. K. Hämäläinen, M. Ijäs, A. Harju and P. Liljeroth, 'Self-assembly and orbital imaging of metal phthalocyanines on a graphene model surface', *J Phys Chem C* **118**, 13320 (2014). Cited on page(s) 22
- [151] S. Barja, M. Garnica, J. J. Hinarejos, A. L. V. de Parga, N. Martín and R. Miranda, 'Self-organization of electron acceptor molecules on graphene', *Chem Commun* **46**, 8198 (2010). Cited on page(s) 22
- [152] S. Standop, T. Michely and C. Busse, 'H<sub>2</sub>O on graphene/Ir(111): A periodic array of frozen droplets', *J Phys Chem C* **119**, 1418 (2015). Cited on page(s) 22
- [153] A. Kumar, K. Banerjee and P. Liljeroth, 'Molecular assembly on two-dimensional materials', *Nanotechnology* **28**, 082001 (2017). Cited on page(s) 22
- [154] M. Petrović, J. Sadowski, A. Šiber and M. Kralj, 'Wrinkles of graphene on Ir(111): Macroscopic network ordering and internal multi-lobed structure', *Carbon* **94**, 856 (2015). Cited on page(s) 22
- [155] A. N'Diaye *et al.*, 'In situ observation of stress relaxation in epitaxial graphene', *New J Phys* **11**, 113056 (2009). Cited on page(s) 22, 36, 119, 120, 122, and 123
- [156] M. Petrović *et al.*, 'The mechanism of caesium intercalation of graphene', *Nat Commun* **4**, 2772 (2013). Cited on page(s) 22, 111, 115, 119, and 120
- [157] D. E. Gray *et al.*, in 'American Institute of Physics handbook: Section editors: Bruce H. Billings [and others] Coordinating editor: Dwight E. Gray', edited by D. E. G. American Institute of Physics (McGraw-Hill Companies, University of Michigan, 1972). Cited on page(s) 22 and 119
- [158] M. Ahmad, H. An, Y. Kim, J. Lee, J. Jung, S.-H. Chun and Y. Seo, 'Nanoscale investigation of charge transport at the grain boundaries and wrinkles in graphene film', *Nanotechnology* **23**, 285705 (2012). Cited on page(s) 22 and 120
- [159] W. Zhu, T. Low, V. Perebeinos, A. Bol, Y. Zhu, H. Yan, J. Tersoff and P. Avouris, 'Structure and electronic transport in graphene wrinkles', *Nano Lett* **12**, 3431 (2012). Cited on page(s) 22 and 120
- [160] C. Wang, Y. Liu, L. Li and H. Tan, 'Anisotropic thermal conductivity of graphene wrinkles', *Nanoscale* **6**, 5703 (2014). Cited on page(s) 22 and 120
- [161] L. Cui, X. Du, G. Wei and Y. Feng, 'Thermal conductivity of graphene wrinkles: a molecular dynamics simulation', *J Phys Chem C* **120**, 23807 (2016). Cited on page(s) 22 and 120
- [162] S. Chen, Q. Li, Q. Zhang, Y. Qu, H. Ji, R. Ruoff and W. Cai, 'Thermal conductivity measurements of suspended graphene with and without wrinkles by micro-Raman mapping', *Nanotechnology* **23**, 365701 (2012). Cited on page(s) 22 and 120
- [163] M. Corso, W. Auwärter, M. Muntwiler, A. Tamai, T. Greber and J. Osterwalder, 'Boron nitride nanomesh', *Science* **303**, 217 (2004). Cited on page(s) 22
- [164] R. Laskowski and P. Blaha, 'Unraveling the structure of the h-BN/Rh(111) nanomesh with ab initio calculations', *J Phys Condens Matter* **20**, 064207 (2008). Cited on page(s) 22
- [165] S. Berner *et al.*, 'Boron nitride nanomesh: Functionality from a corrugated monolayer', *Angew Chem Int Edit* **46**, 5115 (2007). Cited on page(s) 22

## Bibliography

---

- [166] A. Preobrajenski, S. Krasnikov, A. Vinogradov, M. L. Ng, T. Käämbre, A. Cafolla and N. Mårtensson, 'Adsorption-induced gap states of h-BN on metal surfaces', *Phys Rev B* **77**, 085421 (2008). Cited on page(s) 22
- [167] R. Laskowski, P. Blaha, T. Gallauner and K. Schwarz, 'Single-layer model of the hexagonal boron nitride nanomesh on the Rh(111) surface', *Phys Rev Lett* **98**, 106802 (2007). Cited on page(s) 22
- [168] G. Dong, E. B. Fourré, F. C. Tabak and J. W. Frenken, 'How boron nitride forms a regular nanomesh on Rh(111)', *Phys Rev Lett* **104**, 096102 (2010). Cited on page(s) 22
- [169] D. Martoccia, S. Pauli, T. Brugger, T. Greber, B. Patterson and P. Willmott, 'h-BN on Rh(111): Persistence of a commensurate 13-on-12 superstructure up to high temperatures', *Surf Sci* **604**, L9 (2010). Cited on page(s) 22
- [170] A. Goriachko, Y. He, M. Knapp, H. Over, M. Corso, T. Brugger, S. Berner, J. Osterwalder and T. Greber, 'Self-assembly of a hexagonal boron nitride nanomesh on Ru(0001)', *Langmuir* **23**, 2928 (2007). Cited on page(s) 22
- [171] P. Sutter, J. Lahiri, P. Albrecht and E. Sutter, 'Chemical vapor deposition and etching of high-quality monolayer hexagonal boron nitride films', *ACS Nano* **5**, 7303 (2011). Cited on page(s) 22
- [172] J. Lu, P. Yeo, Y. Zheng, H. Xu, C. Gan, M. Sullivan, A. Castro Neto and K. Loh, 'Step flow versus mosaic film growth in hexagonal boron nitride', *J Am Chem Soc* **135**, 2368 (2013). Cited on page(s) 22
- [173] W. Auwärter, M. Muntwiler, T. Greber and J. Osterwalder, 'Co on h-BN/Ni(111): from island to island-chain formation and Co intercalation', *Surf Sci* **511**, 379 (2002). Cited on page(s) 22 and 23
- [174] W. Auwärter, T. Kreutz, T. Greber and J. Osterwalder, 'XPD and STM investigation of hexagonal boron nitride on Ni(111)', *Surf Sci* **429**, 229 (1999). Cited on page(s) 22
- [175] W. Auwärter, M. Muntwiler, J. Osterwalder and T. Greber, 'Defect lines and two-domain structure of hexagonal boron nitride films on Ni(111)', *Surf Sci* **545**, L735 (2003). Cited on page(s) 22, 55, and 69
- [176] G. Grad, P. Blaha, K. Schwarz, W. Auwärter and T. Greber, 'Density functional theory investigation of the geometric and spintronic structure of h-BN/Ni (111) in view of photoemission and STM experiments', *Phys Rev B* **68**, 085404 (2003). Cited on page(s) 22
- [177] S. Joshi, D. Ecija, R. Koitz, M. Iannuzzi, A. Seitsonen, J. Hutter, H. Sachdev, S. Vijayaraghavan, F. Bischoff and K. Seufert, 'Boron nitride on Cu(111): an electronically corrugated monolayer', *Nano Lett* **12**, 5821 (2012). Cited on page(s) 22 and 44
- [178] C. Brülke, T. Heepenstrick, N. Humberg, I. Krieger, M. Sokolowski, S. Weiß, F. S. Tautz and S. Soubatch, 'Long Vertical Distance Bonding of the Hexagonal Boron Nitride Monolayer on the Cu(111) Surface', *J Phy Chem C* **121**, 23964 (2017). Cited on page(s) 22
- [179] M. Schwarz *et al.*, 'Corrugation in the weakly interacting hexagonal-BN/Cu(111) system: Structure determination by combining noncontact atomic force microscopy and x-ray standing waves', *ACS Nano* **11**, 9151 (2017). Cited on page(s) 22 and 23
- [180] Q. Zhang, J. Yu, P. Ebert, C. Zhang, C.-R. Pan, M.-Y. Chou, C.-K. Shih, C. Zeng and S. Yuan, 'Tuning band gap and work function modulations in monolayer hBN/Cu(111) heterostructures with moiré patterns', *ACS Nano* **12**, 9355 (2018). Cited on page(s) 22
- [181] Q. Li, X. Zou, M. Liu, J. Sun, Y. Gao, Y. Qi, X. Zhou, B. I. Yakobson, Y. Zhang and Z. Liu, 'Grain boundary structures and electronic properties of hexagonal boron nitride on Cu(111)', *Nano Lett* **15**, 5804 (2015). Cited on page(s) 22
- [182] E. Čavar, R. Westerström, A. Mikkelsen, E. Lundgren, A. Vinogradov, M. L. Ng, A. Preobrajenski, A. Zakharov and N. Mårtensson, 'A single h-BN layer on Pt(111)', *Surface Science* **602**, 1722 (2008). Cited on page(s) 22, 61, and 62

- [183] M. Paffett, R. Simonson, P. Papin and R. Paine, 'Borazine adsorption and decomposition at Pt(111) and Ru(001) surfaces', *Surf Sci* **232**, 286 (1990). Cited on page(s) 22
- [184] A. Nagashima, N. Tejima, Y. Gamou, T. Kawai and C. Oshima, 'Electronic structure of monolayer hexagonal boron nitride physisorbed on metal surfaces', *Phys Rev Lett* **75**, 3918 (1995). Cited on page(s) 22 and 23
- [185] F. Orlando, R. Larciprete, P. Lacovig, I. Boscarato, A. Baraldi and S. Lizzit, 'Epitaxial growth of hexagonal boron nitride on Ir(111)', *J Phys Chem C* **116**, 157 (2011). Cited on page(s) 22, 49, 50, and 99
- [186] F. Orlando, P. Lacovig, L. Omiciuolo, N. Apostol, R. Larciprete, A. Baraldi and S. Lizzit, 'Epitaxial growth of a single-domain hexagonal boron nitride monolayer', *ACS Nano* **8**, 12063 (2014). Cited on page(s) 22, 55, and 92
- [187] A. Preobrajenski, M. Nesterov, M. L. Ng, A. Vinogradov and N. Mårtensson, 'Monolayer h-BN on lattice-mismatched metal surfaces: On the formation of the nanomesh', *Chem Phys Lett* **446**, 119 (2007). Cited on page(s) 22, 23, 60, and 108
- [188] D. Usachov, A. Fedorov, O. Vilkov, V. Adamchuk, L. Yashina, L. Bondarenko, A. Saranin, A. Grüneis and D. Vyalikh, 'Experimental and computational insight into the properties of the lattice-mismatched structures: Monolayers of h-BN and graphene on Ir(111)', *Phys Rev B* **86**, 155151 (2012). Cited on page(s) 22, 50, 64, and 69
- [189] F. Schulz, R. Drost, S. Hämäläinen, T. Demonchaux, A. Seitsonen and P. Liljeroth, 'Epitaxial hexagonal boron nitride on Ir(111): A work function template', *Phys Rev B* **89**, 235429 (2014). Cited on page(s) 22, 23, 44, 57, 66, and 93
- [190] F. Farwick zum Hagen *et al.*, 'Structure and Growth of Hexagonal Boron Nitride on Ir(111)', *ACS Nano* **10**, 11012 (2016). Cited on page(s) 22, 23, 44, 47, 48, 49, 50, 54, 55, 57, 58, 69, 92, 97, and 123
- [191] M. Petrović, U. Hagemann, M. Horn-von Hoegen and F.-J. M. zu Heringdorf, 'Microanalysis of single-layer hexagonal boron nitride islands on Ir(111)', *Appl Surf Sci* **420**, 504 (2017). Cited on page(s) 22, 63, 64, 65, and 105
- [192] M. Will, N. Atodiresei, V. Caciuc, P. Valerius, C. Herbig and T. Michely, 'A monolayer of hexagonal boron nitride on Ir(111) as a template for cluster superlattices', *ACS Nano* **12**, 6871 (2018). Cited on page(s) 22, 23, and 145
- [193] W. Auwärter, 'Hexagonal boron nitride monolayers on metal supports: Versatile templates for atoms, molecules and nanostructures', *Surface Science Reports* **74**, 1 (2019). Cited on page(s) 23
- [194] A. Preobrajenski, A. Vinogradov and N. Mårtensson, 'Monolayer of h-BN chemisorbed on Cu(111) and Ni(111): The role of the transition metal 3d states', *Surf Sci* **582**, 21 (2005). Cited on page(s) 23
- [195] A. Preobrajenski, M. L. Ng, A. Vinogradov and N. Mårtensson, 'Controlling graphene corrugation on lattice-mismatched substrates', *Phys Rev B* **78**, 073401 (2008). Cited on page(s) 23
- [196] M. Iannuzzi, F. Tran, R. Widmer, T. Dienel, K. Radican, Y. Ding, J. Hutter and O. Gröning, 'Site-selective adsorption of phthalocyanine on h-BN/Rh(111) nanomesh', *Phys Chem Chem Phys* **16**, 12374 (2014). Cited on page(s) 23
- [197] S. Joshi *et al.*, 'Control of molecular organization and energy level alignment by an electronically nanopatterned boron nitride template', *ACS Nano* **8**, 430 (2013). Cited on page(s) 23
- [198] M. C. Patterson, B. F. Habenicht, R. L. Kurtz, L. Liu, Y. Xu and P. T. Sprunger, 'Formation and stability of dense arrays of Au nanoclusters on hexagonal boron nitride/Rh(111)', *Phys Rev B* **89**, 205423 (2014). Cited on page(s) 23
- [199] F. Wu, D. Huang, Y. Yue and L. Liu, 'Template growth of Au, Ni and Ni-Au nanoclusters on hexagonal boron nitride/Rh(111): a combined STM, TPD and AES study', *RSC Adv* **7**, 44169 (2017). Cited on page(s) 23

## Bibliography

---

- [200] W. C. McKee, M. C. Patterson, J. R. Frick, P. T. Sprunger and Y. Xu, 'Adsorption of transition metal adatoms on h-BN/Rh(111): Implications for nanocluster self-assembly', *Catal* **280**, 220 (2017). Cited on page(s) 23
- [201] W. McKee, M. Patterson, D. Huang, J. Frick, R. Kurtz, P. Sprunger, L. Liu and Y. Xu, 'CO adsorption on Au nanoparticles grown on hexagonal boron nitride/Rh(111)', *J Phys Chem C* **120**, 10909 (2016). Cited on page(s) 23
- [202] J. N. Coleman *et al.*, 'Two-dimensional nanosheets produced by liquid exfoliation of layered materials', *Science* **331**, 568 (2011). Cited on page(s) 23
- [203] Y.-H. Lee *et al.*, 'Synthesis of large-area MoS<sub>2</sub> atomic layers with chemical vapor deposition', *Adv Mater* **24**, 2320 (2012). Cited on page(s) 23
- [204] S. G. Sørensen, H. G. Führtbauer, A. K. Tuxen, A. S. Walton and J. V. Lauritsen, 'Structure and electronic properties of in situ synthesized single-layer MoS<sub>2</sub> on a gold surface', *ACS Nano* **8**, 6788 (2014). Cited on page(s) 23
- [205] J. A. Miwa, S. Ulstrup, S. G. Sørensen, M. Dendzik, A. G. Čabo, M. Bianchi, J. V. Lauritsen and P. Hofmann, 'Electronic structure of epitaxial single-layer MoS<sub>2</sub>', *Phys Rev Lett* **114**, 046802 (2015). Cited on page(s) 23
- [206] J. Hall, B. Pielic, C. Murray, W. Jolie, T. Wekking, C. Busse, M. Kralj and T. Michely, 'Molecular beam epitaxy of quasi-freestanding transition metal disulphide monolayers on van der Waals substrates: a growth study', *2D Mater* **5**, 025005 (2018). Cited on page(s) 23 and 36
- [207] M. M. Ugeda, I. Brihuega, F. Guinea and J. M. Gómez-Rodríguez, 'Missing atom as a source of carbon magnetism', *Phys Rev Lett* **104**, 096804 (2010). Cited on page(s) 25
- [208] M. Ugeda, D. Fernández-Torre, I. Brihuega, P. Pou, A. Martínez-Galera, R. Pérez and J. Gómez-Rodríguez, 'Point defects on graphene on metals', *Phys Rev Lett* **107**, 116803 (2011). Cited on page(s) 25
- [209] M. M. Ugeda, I. Brihuega, F. Hiebel, P. Mallet, J.-Y. Veuillen, J. M. Gómez-Rodríguez and F. Ynduráin, 'Electronic and structural characterization of divacancies in irradiated graphene', *Phys Rev B* **85**, 121402 (2012). Cited on page(s) 25
- [210] H. Cun, M. Iannuzzi, A. Hemmi, J. Osterwalder and T. Greber, 'Ar implantation beneath graphene on Ru(0001)', *Surf Sci* **634**, 95 (2015). Cited on page(s) 25 and 43
- [211] H. Kim *et al.*, 'Nanoscale control of phonon excitations in graphene', *Nat Commun* **6**, 7528 (2015). Cited on page(s) 25 and 43
- [212] C. Herbig, E. Åhlgren, W. Jolie, C. Busse, J. Kotakoski, A. Krashennnikov and T. Michely, 'Interfacial Carbon Nanoplatelet Formation by Ion Irradiation of Graphene on Iridium(111)', *ACS Nano* **8**, 12208 (2014). Cited on page(s) 25, 43, 47, 69, 105, and 122
- [213] C. Herbig *et al.*, 'Comment on "Interfacial Carbon Nanoplatelet Formation by Ion Irradiation of Graphene on Iridium(111)"', *ACS Nano* **9**, 4664 (2015). Cited on page(s) 25, 43, and 122
- [214] G. Zamborlini, M. Imam, L. Patera, T. Menten, G. Comelli and A. Locatelli, 'Nanobubbles at GPa Pressure under Graphene', *Nano Lett* **15**, 6162 (2015). Cited on page(s) 25, 43, 46, and 56
- [215] F. Späth, K. Gotterbarm, M. Amende, U. Bauer, C. Gleichweit, O. Höfert, H. Steinrück and C. Papp, 'Keeping argon under a graphene lid - Argon intercalation between graphene and nickel(111)', *Surf Sci* **643**, 222 (2016). Cited on page(s) 25, 43, 56, and 69
- [216] H. Cun, M. Iannuzzi, A. Hemmi, S. Roth, J. Osterwalder and T. Greber, 'Immobilizing individual atoms beneath a corrugated single layer of boron nitride', *Nano Lett* **13**, 2098 (2013). Cited on page(s) 25, 44, and 70

- [217] H. Cun, M. Iannuzzi, A. Hemmi, J. Osterwalder and T. Greber, 'Two-Nanometer Voids in Single-Layer Hexagonal Boron Nitride', *ACS Nano* **8**, 7423 (2014). Cited on page(s) 25, 44, and 70
- [218] H. Cun, M. Iannuzzi, A. Hemmi, J. Osterwalder and T. Greber, 'Implantation Length and Thermal Stability of Interstitial Ar Atoms in Boron Nitride Nanotents', *ACS Nano* **8**, 1014 (2013). Cited on page(s) 25, 44, 46, and 70
- [219] H. Cun *et al.*, 'Centimeter-sized single-orientation monolayer hexagonal boron nitride with or without nanovoids', *Nano Lett* **18**, 1205 (2018). Cited on page(s) 25 and 70
- [220] M. Iannuzzi, 'Ar Implantation at the hBN/Rh(111) Nanomesh by ab initio Molecular Dynamics', *J Phys Chem B* **119**, 22198 (2015). Cited on page(s) 25, 44, and 70
- [221] G. Binnig and H. Rohrer, 'Scanning tunneling microscopy', *Surface science* **126**, 236 (1983). Cited on page(s) 27
- [222] J. Tersoff and D. R. Hamann, 'Theory of the Scanning Tunneling Microscope', *Phys Rev B* **31**, 805 (1985). Cited on page(s) 28
- [223] J. Bardeen, 'Tunnelling from a many-particle point of view', *Phys Rev Lett* **6**, 57 (1961). Cited on page(s) 28
- [224] N. Ehlen, Diplomarbeit, Universität zu Köln, 2019. Cited on page(s) 31
- [225] M. Fox, 'Optical properties of solids (2ed Ed.)' (AAPT, Oxford University Press Inc., New York, 2010). Cited on page(s) 31
- [226] D. Förster, 'EuO and Eu on metal crystals and graphene: interface effects and epitaxial films', Dissertation, Universität zu Köln, 2011. Cited on page(s) 34
- [227] R. Nyholm, J. Andersen, U. Johansson, B. Jensen and I. Lindau, 'Beamline I311 at MAX-LAB: a VUV/soft X-ray undulator beamline for high resolution electron spectroscopy', *Nucl Instr Meth Phys Res A* **467**, 520 (2001). Cited on page(s) 35 and 37
- [228] R. van Gastel, A. N'Diaye, D. Wall, J. Coraux, C. Busse, N. Buckanie, F.-J. Meyer zu Heringdorf, M. Horn von Hoegen, T. Michely and B. Poelsema, 'Selecting a single orientation for millimeter sized graphene sheets', *Appl Phys Lett* **95**, 121901 (2009). Cited on page(s) 36
- [229] I. Horcas, R. Fernández, J. Gomez-Rodriguez, J. Colchero, J. Gómez-Herrero and A. Baro, 'WSXM: a software for scanning probe microscopy and a tool for nanotechnology', *Rev Sci Instr* **78**, 013705 (2007). Cited on page(s) 37
- [230] B. V. Senkovskiy *et al.*, 'Semiconductor-to-Metal Transition and Quasiparticle Renormalization in Doped Graphene Nanoribbons', *Adv Electron Mater* **3**, 1600490 (2017). Cited on page(s) 37
- [231] N. Ehlen *et al.*, 'Narrow photoluminescence and Raman peaks of epitaxial MoS<sub>2</sub> on graphene/Ir(111)', *2D Mater* **6**, 011006 (2018). Cited on page(s) 37, 75, 86, and 88
- [232] K. Burke, 'Perspective on density functional theory', *J Chem Phys* **136**, 150901 (2012). Cited on page(s) 38
- [233] P. Hohenberg and W. Kohn, 'Inhomogeneous Electron Gas', *Phys Rev* **136**, B864 (1964). Cited on page(s) 38
- [234] P. E. Blöchl, 'Projector augmented-wave method', *Phys Rev B* **50**, 17953 (1994). Cited on page(s) 38
- [235] G. Kresse and J. Hafner, 'Ab initio molecular dynamics for liquid metals', *Phys Rev B* **47**, 558 (1993). Cited on page(s) 38
- [236] G. Kresse and J. Furthmüller, 'Efficient iterative schemes for *ab initio* total-energy calculations using a plane-wave basis set', *Phys Rev B* **54**, 11169 (1996). Cited on page(s) 38
- [237] G. Kresse and D. Joubert, 'From ultrasoft pseudopotentials to the projector augmented-wave method', *Phys Rev B* **59**, 1758 (1999). Cited on page(s) 38

## Bibliography

---

- [238] J. P. Perdew, K. Burke and M. Ernzerhof, 'Generalized Gradient Approximation Made Simple', *Phys Rev Lett* **77**, 3865 (1996). Cited on page(s) 38
- [239] K. Lee, E. D. Murray, L. Kong, B. I. Lundqvist and D. C. Langreth, 'Higher-accuracy van der Waals density functional', *Phys Rev B* **82**, 081101(R) (2010). Cited on page(s) 38
- [240] I. Hamada, 'van der Waals density functional made accurate', *Phys Rev B* **89**, 121103(R) (2014). Cited on page(s) 38
- [241] K. Momma and F. Izumi, 'VESTA 3 for three-dimensional visualization of crystal, volumetric and morphology data', *J Appl Crystallogr* **44**, 1272 (2011). Cited on page(s) 38
- [242] B. J. Alder and T. E. Wainwright, 'Studies in molecular dynamics. I. General method', *J Chem Phys* **31**, 459 (1959). Cited on page(s) 38
- [243] S. Plimpton, 'Fast Parallel Algorithms for Short-Range Molecular Dynamics', *J Comput Phys* **117**, 1 (1995). Cited on page(s) 38
- [244] M. Ghorbani-Asl, S. Kretschmer, D. E. Spearot and A. V. Krasheninnikov, 'Two-dimensional MoS<sub>2</sub> under ion irradiation: from controlled defect production to electronic structure engineering', *2D Mater* **4**, 025078 (2017). Cited on page(s) 38, 82, and 83
- [245] J. Knudsen, P. Feibelman, T. Gerber, E. Grånäs, K. Schulte, P. Stratmann, J. Andersen and T. Michely, 'Clusters binding to the graphene moiré on Ir(111): X-ray photoemission compared to density functional calculations', *Phys Rev B* **85**, 035407 (2012). Cited on page(s) 38 and 50
- [246] S. Kretschmer, M. Maslov, S. Ghaderzadeh, M. Ghorbani-Asl, G. Hlawacek and A. V. Krasheninnikov, 'Supported Two-Dimensional Materials under Ion Irradiation: The Substrate Governs Defect Production', *ACS Appl Mater Interfaces* **10**, 30827 (2018). Cited on page(s) 38
- [247] J.-w. Jiang, H. S. Park and T. Rabczuk, 'Molecular dynamics simulations of single-layer molybdenum disulphide and thermal conductivity', *J Appl Phys* **114**, 64307 (2013). Cited on page(s) 39
- [248] J. F. Ziegler, J. P. Biersack, M. D. Ziegler and J. P. Biersack, 'Nucl Instruments Methods Phys Res Sect B' (MA: Springer, Boston, 1985), Vol. 268, Pages 1818–1823. Cited on page(s) 39
- [249] S. Munetoh, T. Motooka, K. Moriguchi and A. Shintani, 'Interatomic potential for Si–O systems using Tersoff parameterization', *Comput Mater Sci* **39**, 334 (2007). Cited on page(s) 39
- [250] S. M. Foiles, M. I. Baskes and M. S. Daw, 'Embedded-atom-method functions for the fcc metals Cu, Ag, Au, Ni, Pd, Pt, and their alloys', *Phys Rev B* **33**, 7983 (1986). Cited on page(s) 39
- [251] P. Valerius, C. Herbig, M. Will, M. Arman, J. Knudsen, V. Caciuc, N. Atodiresei and T. Michely, 'Annealing of ion-irradiated hexagonal boron nitride on Ir(111)', *Phys Rev B* **96**, 235410 (2017). Cited on page(s) 43, 63, 64, 92, 97, 99, 104, 105, 122, and 144
- [252] K. Omambac, M. Petrovic, P. Valerius, P. Bampoulios, T. Michely, M. Horn von Hoegen and F. Meyer zu Heringdorf, 'Thermal dispersion of h-BN and formation of borophene on Ir(111)', *in preparation* **0**, 0 (2020). Cited on page(s) 43 and 144
- [253] A. Robertson, G. Lee, K. He, E. Yoon, A. Kirkland and J. Warner, 'Stability and Dynamics of the Tetravacancy in Graphene', *Nano Lett* **14**, 1634 (2014). Cited on page(s) 43
- [254] C. Herbig, E. H. Åhlgren and T. Michely, 'Blister-free ion beam patterning of supported graphene', *Nanotechnology* **28**, 055304 (2016). Cited on page(s) 47, 92, and 107
- [255] K. Ueda *et al.*, 'Adsorption and Reaction of CO and NO on Ir(111) Under Near Ambient Pressure Conditions', *Topics in Catalysis* **59**, 487 (2016). Cited on page(s) 50
- [256] A. Santra, B. Min, C. Yi, K. Luo, T. Choudhary and D. Goodman, 'Decomposition of NH<sub>3</sub> on Ir(100): A temperature programmed desorption study', *J Phys Chem B* **106**, 340 (2002). Cited on page(s) 50, 63, and 69

- [257] J. Cornish and N. Avery, 'Adsorption of N<sub>2</sub>, O<sub>2</sub>, N<sub>2</sub>O and NO on Ir(111) by EELS and TPD', *Surf Sci* **235**, 209 (1990). Cited on page(s) 50 and 63
- [258] C. Wagner, L. Davis and W. Riggs, 'The energy dependence of the electron mean free path', *Surf Interface Anal* **2**, 53 (1980). Cited on page(s) 52
- [259] M. Seah and W. Dench, 'Quantitative electron spectroscopy of surfaces: a standard data base for electron inelastic mean free paths in solids', *Surf Interface Anal* **1**, 2 (1979). Cited on page(s) 52
- [260] S. Tanuma, C. Powell and D. Penn, 'Calculations of electron inelastic mean free paths (IMFPs). IV. Evaluation of calculated IMFPs and of the predictive IMFP formula TPP-2 for electron energies between 50 and 2000 eV', *Surf Interface Anal* **20**, 77 (1993). Cited on page(s) 52
- [261] S. Donnelly, 'A thermal evolution study of the trapping and release of inert gases in nickel', *Vacuum* **28**, 163 (1978). Cited on page(s) 52 and 53
- [262] A. R. Lahrood, T. de Los Arcos, M. Prenzel, A. von Keudell and J. Winter, 'X-ray photoelectron spectroscopy on implanted argon as a tool to follow local structural changes in thin films', *Thin Solid Films* **520**, 1625 (2011). Cited on page(s) 52
- [263] P. Mallet, F. Varchon, C. Naud, L. Magaud, C. Berger and J. Veuillen, 'Electron states of mono- and bilayer graphene on SiC probed by scanning-tunneling microscopy', *Phys Rev B* **76**, 041403 (2007). Cited on page(s) 56
- [264] A. Martínez-Galera, I. Brihuega and J. Gómez-Rodríguez, 'Ethylene irradiation: a new route to grow graphene on low reactivity metals', *Nano Lett* **11**, 3576 (2011). Cited on page(s) 56
- [265] A. Martínez-Galera, U. Schröder, F. Huttmann, W. Jolie, F. Craes, C. Busse, V. Caciuc, N. Atodiresei, S. Blügel and T. Michely, 'Oxygen orders differently under graphene: new superstructures on Ir(111)', *Nanoscale* **8**, 1932 (2016). Cited on page(s) 56
- [266] S. Schumacher *et al.*, 'Europium underneath graphene on Ir(111): Intercalation mechanism, magnetism, and band structure', *Phys Rev B* **90**, 235437 (2014). Cited on page(s) 56, 110, 111, 112, 114, and 125
- [267] P. Granfors, A. Macrander and R. Simmons, 'Crystalline xenon: Lattice parameters, thermal expansion, thermal vacancies, and equation of state', *Phys Rev B* **24**, 4753 (1981). Cited on page(s) 57
- [268] K. Schubert, 'Ein Modell für die Kristallstrukturen der chemischen Elemente', *Acta Crystallogr Sect B* **30**, 193 (1974). Cited on page(s) 57
- [269] D. A. Young, 'Phase diagrams of the elements' (Univ of California Press, California, US, 1991). Cited on page(s) 57
- [270] Y. Zhang, X. Weng, H. Li, H. Li, M. Wei, J. Xiao, Z. Liu, M. Chen, Q. Fu and X. Bao, 'Hexagonal boron nitride cover on Pt (111): a new route to tune molecule-metal interaction and metal-catalyzed reactions', *Nano Lett* **15**, 3616 (2015). Cited on page(s) 62
- [271] C. Oshima and A. Nagashima, 'Ultra-thin epitaxial films of graphite and hexagonal boron nitride on solid surfaces', *J Phys Condens Matter* **9**, 1 (1997). Cited on page(s) 62
- [272] A. J. Mannix *et al.*, 'Synthesis of borophenes: Anisotropic, two-dimensional boron polymorphs', *Science* **350**, 1513 (2015). Cited on page(s) 64, 66, and 67
- [273] B. Feng, J. Zhang, Q. Zhong, W. Li, S. Li, H. Li, P. Cheng, S. Meng, L. Chen and K. Wu, 'Experimental realization of two-dimensional boron sheets', *Nat Chem* **8**, 563 (2016). Cited on page(s) 64 and 66
- [274] I. Boustani, 'Systematic ab initio investigation of bare boron clusters: Determination of the geometry and electronic structures of B<sub>n</sub> (n = 2–14)', *Phys Rev B* **55**, 16426 (1997). Cited on page(s) 66
- [275] Z. A. Piazza, H.-S. Hu, W.-L. Li, Y.-F. Zhao, J. Li and L.-S. Wang, 'Planar hexagonal B<sub>36</sub> as a potential basis for extended single-atom layer boron sheets', *Nat Commun* **5**, 3113 (2014). Cited on page(s) 66

## Bibliography

---

- [276] X.-F. Zhou, X. Dong, A. R. Oganov, Q. Zhu, Y. Tian and H.-T. Wang, 'Semimetallic two-dimensional boron allotrope with massless Dirac fermions', *Phys Rev Lett* **112**, 085502 (2014). Cited on page(s) 66
- [277] E. S. Penev, S. Bhowmick, A. Sadrzadeh and B. I. Yakobson, 'Polymorphism of two-dimensional boron', *Nano Lett* **12**, 2441 (2012). Cited on page(s) 66 and 129
- [278] E. Koren, E. Sutter, S. Bliznakov, F. Ivars-Barcelo and P. Sutter, 'Isolation of high quality graphene from Ru by solution phase intercalation', *Appl Phys Lett* **103**, 121602 (2013). Cited on page(s) 68 and 114
- [279] I. Rakić, D. Čapeta, M. Plodinec and M. Kralj, 'Large-scale transfer and characterization of macroscopic periodically nano-rippled graphene', *Carbon* **96**, 243 (2016). Cited on page(s) 68, 114, and 115
- [280] D. Cohen-Tanugi, L. Lin and J. Grossman, 'Multilayer Nanoporous Graphene Membranes for Water Desalination', *Nano Lett* **16**, 1027 (2016). Cited on page(s) 68
- [281] H. Hattab *et al.*, 'Growth temperature dependent graphene alignment on Ir(111)', *Appl Phys Lett* **98**, 141903 (2011). Cited on page(s) 69, 122, and 123
- [282] S. Nie, A. Walter, N. Bartelt, E. Starodub, A. Bostwick, E. Rotenberg and K. McCarty, 'Growth from below: Graphene bilayers on Ir(111)', *ACS Nano* **5**, 2298 (2011). Cited on page(s) 69
- [283] E. Loginova, N. Bartelt, P. Feibelman and K. McCarty, 'Factors influencing graphene growth on metal surfaces', *New J Phys* **11**, 063046 (2009). Cited on page(s) 69
- [284] P. Valerius *et al.*, 'Reversible crystalline-to-amorphous phase transformation in monolayer MoS<sub>2</sub> under grazing ion irradiation', *2D Mater* **7**, 025005 (2019). Cited on page(s) 73, 81, and 144
- [285] Q. Ma *et al.*, 'Postgrowth tuning of the bandgap of single-layer molybdenum disulfide films by sulfur/selenium exchange', *ACS Nano* **8**, 4672 (2014). Cited on page(s) 73, 89, and 130
- [286] Z. Cheng *et al.*, 'Convergent ion beam alteration of 2D materials and metal-2D interfaces', *2D Mater* **6**, 034005 (2019). Cited on page(s) 73 and 86
- [287] Q. Ma *et al.*, 'Controlled argon beam-induced desulfurization of monolayer molybdenum disulfide', *J Phys Condens Matter* **25**, 252201 (2013). Cited on page(s) 73 and 86
- [288] V. Iberi *et al.*, 'Nanoforging single layer MoSe<sub>2</sub> through defect engineering with focused helium ion beams', *Sci Rep* **6**, 30481 (2016). Cited on page(s) 73, 85, and 86
- [289] K. Haynes, R. Murray, Z. Weinrich, X. Zhao, D. Chiappe, S. Sutar, I. Radu, C. Hatem, S. Perry and K. Jones, 'Modulating the resistivity of MoS<sub>2</sub> through low energy phosphorus plasma implantation', *Appl Phys Lett* **110**, 262102 (2017). Cited on page(s) 73
- [290] Y. Chen *et al.*, 'Tuning electronic structure of single layer MoS<sub>2</sub> through defect and interface engineering', *ACS Nano* **12**, 2569 (2018). Cited on page(s) 73
- [291] S. Bertolazzi, S. Bonacchi, G. Nan, A. Pershin, D. Beljonne and P. Samorì, 'Engineering Chemically Active Defects in Monolayer MoS<sub>2</sub> Transistors via Ion-Beam Irradiation and Their Healing via Vapor Deposition of Alkanethiols', *Adv Mater* **29**, 1606760 (2017). Cited on page(s) 73 and 86
- [292] G.-Y. Zhao, H. Deng, N. Tyree, M. Guy, A. Lisfi, Q. Peng, J.-A. Yan, C. Wang and Y. Lan, 'Recent Progress on Irradiation-Induced Defect Engineering of Two-Dimensional 2H-MoS<sub>2</sub> Few Layers', *Appl Sci* **9**, 678 (2019). Cited on page(s) 73
- [293] R. Kozubek *et al.*, 'Perforating Freestanding Molybdenum Disulfide Monolayers with Highly Charged Ions', *J Phys Chem Lett* **10**, 904 (2019). Cited on page(s) 73
- [294] M. G. Stanford *et al.*, 'Focused helium-ion beam irradiation effects on electrical transport properties of few-layer WSe<sub>2</sub>: enabling nanoscale direct write homo-junctions', *Sci Rep* **6**, 27276 (2016). Cited on page(s) 73

- [295] B. C. Bayer, R. Kaindl, M. Reza Ahmadpour Monazam, T. Susi, J. Kotakoski, T. Gupta, D. Eder, W. Waldhauser and J. C. Meyer, 'Atomic-scale in situ observations of crystallization and restructuring processes in two-dimensional MoS<sub>2</sub> films', *ACS Nano* **12**, 8758 (2018). Cited on page(s) 74
- [296] J. R. Lince, T. B. Stewart, M. M. Hills, P. D. Fleischauer, J. A. Yarmoff and A. Taleb-Ibrahimi, 'Chemical effects of Ne<sup>+</sup> bombardment on the MoS<sub>2</sub> (0001) surface studied by high-resolution photoelectron spectroscopy', *Surf Sci* **210**, 387 (1989). Cited on page(s) 74
- [297] M. Baker, R. Gilmore, C. Lenardi and W. Gissler, 'XPS investigation of preferential sputtering of S from MoS<sub>2</sub> and determination of MoS<sub>x</sub> stoichiometry from Mo and S peak positions', *Appl Surf Sci* **150**, 255 (1999). Cited on page(s) 74
- [298] M. Bollinger, J. Lauritsen, K. W. Jacobsen, J. K. Nørskov, S. Helveg and F. Besenbacher, 'One-dimensional metallic edge states in MoS<sub>2</sub>', *Phys Rev Lett* **87**, 196803 (2001). Cited on page(s) 74
- [299] H.-P. Komsa and A. V. Krasheninnikov, 'Engineering the Electronic Properties of Two-Dimensional Transition Metal Dichalcogenides by Introducing Mirror Twin Boundaries', *Adv Electron Mater* **3**, 1600468 (2017). Cited on page(s) 75
- [300] V. Petkov, S. Billinge, P. Larson, S. Mahanti, T. Vogt, K. Rangan and M. G. Kanatzidis, 'Structure of nanocrystalline materials using atomic pair distribution function analysis: Study of LiMoS<sub>2</sub>', *Phys Rev B* **65**, 092105 (2002). Cited on page(s) 75
- [301] H.-P. Komsa, S. Kurasch, O. Lehtinen, U. Kaiser and A. V. Krasheninnikov, 'From point to extended defects in two-dimensional MoS<sub>2</sub>: Evolution of atomic structure under electron irradiation', *Phys Rev B* **88**, 035301 (2013). Cited on page(s) 76
- [302] R. Addou, L. Colombo and R. M. Wallace, 'Surface defects on natural MoS<sub>2</sub>', *ACS Appl Mater Interfaces* **7**, 11921 (2015). Cited on page(s) 79
- [303] S. Barja *et al.*, 'Identifying substitutional oxygen as a prolific point defect in monolayer transition metal dichalcogenides with experiment and theory', *arXiv preprint arXiv:1810.03364* (2018). Cited on page(s) 79
- [304] I. D. Marion, D. Čapeta, B. Pelić, F. Faraguna, A. Gallardo, P. Pou, B. Biel, N. Vujičić and M. Kralj, 'Atomic-scale defects and electronic properties of a transferred synthesized MoS<sub>2</sub> monolayer', *Nanotechnology* **29**, 305703 (2018). Cited on page(s) 80
- [305] N. Sengoku and K. Ogawa, 'Investigations of electronic structures of defects introduced by an ion bombardments on MoS<sub>2</sub> by scanning tunneling microscopy', *Jpn J Appl Phys* **34**, 3363 (1995). Cited on page(s) 80
- [306] K. S. Yong, D. M. Otalvaro, I. Duchemin, M. Saeys and C. Joachim, 'Calculation of the conductance of a finite atomic line of sulfur vacancies created on a molybdenum disulfide surface', *Phys Rev B* **77**, 205429 (2008). Cited on page(s) 85
- [307] N. Kodama, T. Hasegawa, T. Tsuruoka, C. Joachim and M. Aono, 'Electronic State Formation by Surface Atom Removal on a MoS<sub>2</sub> Surface', *Jpn J Appl Phys* **51**, 06FF07 (2012). Cited on page(s) 85
- [308] M. Kulig, J. Zipfel, P. Nagler, S. Blanter, C. Schüller, T. Korn, N. Paradiso, M. M. Glazov and A. Chernikov, 'Exciton Diffusion and Halo Effects in Monolayer Semiconductors', *Phys Rev Lett* **120**, 207401 (2018). Cited on page(s) 87
- [309] F. Cadiz, C. Robert, E. Courtade, M. Manca, L. Martinelli, T. Taniguchi, K. Watanabe, T. Amand, A. C. H. Rowe, D. Paget, B. Urbaszek and X. Marie, 'Exciton diffusion in WSe<sub>2</sub> monolayers embedded in a van der Waals heterostructure', *Appl Phys Lett* **112**, 152106 (2018). Cited on page(s) 87
- [310] J. Zipfel, J. Holler, A. A. Mitioglu, M. V. Ballottin, P. Nagler, A. V. Stier, T. Taniguchi, K. Watanabe, S. A. Crooker, P. C. M. Christianen, T. Korn and A. Chernikov, 'Spatial extent of the excited exciton states in WS<sub>2</sub> monolayers from diamagnetic shifts', *Phys Rev B* **98**, 075438 (2018). Cited on page(s) 88

## Bibliography

---

- [311] J. Ribeiro-Soares, R. M. Almeida, E. B. Barros, P. T. Araujo, M. S. Dresselhaus, L. G. Cançado and A. Jorio, 'Group theory analysis of phonons in two-dimensional transition metal dichalcogenides', *Phys Rev B* **90**, 115438 (2014). Cited on page(s) 88
- [312] B. R. Carvalho, Y. Wang, S. Mignuzzi, D. Roy, M. Terrones, C. Fantini, V. H. Crespi, L. M. Malard and M. A. Pimenta, 'Intervalley scattering by acoustic phonons in two-dimensional MoS<sub>2</sub> revealed by double-resonance Raman spectroscopy', *Nat Commun* **8**, 14670 (2017). Cited on page(s) 88
- [313] W. M. Parkin, A. Balan, L. Liang, P. M. Das, M. Lamparski, C. H. Naylor, J. A. Rodríguez-Manzo, A. T. C. Johnson, V. Meunier and M. Drndić, 'Raman Shifts in Electron-Irradiated Monolayer MoS<sub>2</sub>', *ACS Nano* **10**, 4134 (2016). Cited on page(s) 88
- [314] S. Mignuzzi, A. J. Pollard, N. Bonini, B. Brennan, I. S. Gilmore, M. A. Pimenta, D. Richards and D. Roy, 'Effect of disorder on Raman scattering of single-layer MoS<sub>2</sub>', *Phys Rev B* **91**, 195411 (2015). Cited on page(s) 88
- [315] J. Klein, A. Kuc, A. Nolinder, M. Altzschner, J. Wierzbowski, F. Sigger, F. Kreupl, J. J. Finley, U. Wurstbauer, A. W. Holleitner and M. Kaniber, 'Robust valley polarization of helium ion modified atomically thin MoS<sub>2</sub>', *2D Mater* **5**, 011007 (2017). Cited on page(s) 88
- [316] A.-Y. Lu *et al.*, 'Janus monolayers of transition metal dichalcogenides', *Nat Nanotechnol* **12**, 744 (2017). Cited on page(s) 89 and 130
- [317] P. Valerius, C. Speckmann, N. Atodiresei, B. V. Senkovskiy, A. Grüneis and T. Michely, 'Growth stagnation in a magic vacancy cluster mesh', *in preparation* **0**, 0 (2020). Cited on page(s) 91 and 144
- [318] P. R. Kidambi, R. A. Terry, L. Wang, M. S. Boutilier, D. Jang, J. Kong and R. Karnik, 'Assessment and control of the impermeability of graphene for atomically thin membranes and barriers', *Nanoscale* **9**, 8496 (2017). Cited on page(s) 91 and 120
- [319] C. A. Merchant *et al.*, 'DNA translocation through graphene nanopores', *Nano Lett* **10**, 2915 (2010). Cited on page(s) 91
- [320] G. F. Schneider, S. W. Kowalczyk, V. E. Calado, G. Pandraud, H. W. Zandbergen, L. M. Vandersypen and C. Dekker, 'DNA translocation through graphene nanopores', *Nano Lett* **10**, 3163 (2010). Cited on page(s) 91
- [321] S. Dervin, D. D. Dionysiou and S. C. Pillai, '2D nanostructures for water purification: graphene and beyond', *Nanoscale* **8**, 15115 (2016). Cited on page(s) 91
- [322] P. Goh and A. Ismail, 'Graphene-based nanomaterial: the state-of-the-art material for cutting edge desalination technology', *Desalination* **356**, 115 (2015). Cited on page(s) 91
- [323] T. Humplik *et al.*, 'Nanostructured materials for water desalination', *Nanotechnology* **22**, 292001 (2011). Cited on page(s) 91
- [324] K. A. Mahmoud, B. Mansoor, A. Mansour and M. Khraisheh, 'Functional graphene nanosheets: The next generation membranes for water desalination', *Desalination* **356**, 208 (2015). Cited on page(s) 91
- [325] P. Valerius, A. Herman and T. Michely, 'Suppression of wrinkle formation in graphene on Ir(111) by high-temperature, low-energy ion irradiation', *Nanotechnology* **30**, 085304 (2018). Cited on page(s) 92, 104, 112, 114, 115, 119, 126, and 144
- [326] S. Schumacher, 'Europium-Intercalated Graphene, Cluster Lattices, and Polar Oxide Bilayers', Dissertation, Universität zu Köln, 2014. Cited on page(s) 110 and 114
- [327] S. Schumacher, D. F. Förster, M. Rösner, T. O. Wehling and T. Michely, 'Strain in epitaxial graphene visualized by intercalation', *Phys Rev Lett* **110**, 086111 (2013). Cited on page(s) 110 and 112
- [328] E. Granas, J. Knudsen, U. A. Schröder, T. Gerber, C. Busse, M. A. Arman, K. Schulte, J. N. Andersen and T. Michely, 'Oxygen intercalation under graphene on Ir(111): energetics, kinetics, and the role of graphene edges', *ACS Nano* **6**, 9951 (2012). Cited on page(s) 112

- [329] U. Schröder, 'Changing graphene's properties. Etching, intercalation, and deuteration.', Dissertation, Universität zu Köln, 2016. Cited on page(s) 113
- [330] L. Gao *et al.*, 'Repeated growth and bubbling transfer of graphene with millimetre-size single-crystal grains using platinum', *Nat Commun* **3**, 699 (2012). Cited on page(s) 114
- [331] B. Deng *et al.*, 'Wrinkle-Free Single-Crystal Graphene Wafer Grown on Strain-Engineered Substrates', *ACS Nano* **11**, 12337 (2017). Cited on page(s) 115 and 120
- [332] J. Kraus, S. Böcklein, R. Reichelt, S. Günther, B. Santos, T. Menteş and A. Locatelli, 'Towards the perfect graphene membrane?—Improvement and limits during formation of high quality graphene grown on Cu-foils', *Carbon* **64**, 377 (2013). Cited on page(s) 115 and 120
- [333] L. G. Cançado, A. Jorio, E. M. Ferreira, F. Stavale, C. A. Achete, R. B. Capaz, M. V. d. O. Moutinho, A. Lombardo, T. Kulmala and A. C. Ferrari, 'Quantifying defects in graphene via Raman spectroscopy at different excitation energies', *Nano Lett* **11**, 3190 (2011). Cited on page(s) 115
- [334] R. V. Gorbachev *et al.*, 'Hunting for monolayer boron nitride: optical and Raman signatures', *Small* **7**, 465 (2011). Cited on page(s) 116
- [335] R. Arenal, A. Ferrari, S. Reich, L. Wirtz, J.-Y. Mevellec, S. Lefrant, A. Rubio and A. Loiseau, 'Raman spectroscopy of single-wall boron nitride nanotubes', *Nano letters* **6**, 1812 (2006). Cited on page(s) 116
- [336] C. Vo-Van, A. Kimouche, A. Reserbat-Plantey, O. Fruchart, P. Bayle-Guillemaud, N. Bendiab and J. Coraux, 'Epitaxial graphene prepared by chemical vapor deposition on single crystal thin iridium films on sapphire', *Appl Phys Lett* **98**, 181903 (2011). Cited on page(s) 116
- [337] I. Š. Rakić, D. Čapeta, M. Plodinec and M. Kralj, 'Large-scale transfer and characterization of macroscopic periodically nano-rippled graphene', *Carbon* **96**, 243 (2016). Cited on page(s) 120
- [338] K. W. Clark, X.-G. Zhang, I. V. Vlassiuk, G. He, R. M. Feenstra and A.-P. Li, 'Spatially resolved mapping of electrical conductivity across individual domain (grain) boundaries in graphene', *ACS Nano* **7**, 7956 (2013). Cited on page(s) 120
- [339] P. Willke, M. Schneider and M. Wenderoth, 'Electronic Transport Properties of 1D-Defects in Graphene and Other 2D-Systems', *Annalen der Physik* **529**, 1700003 (2017). Cited on page(s) 120
- [340] P. Willke, T. Kotzott, T. Pruschke and M. Wenderoth, 'Magnetotransport on the nano scale', *Nat Commun* **8**, 15283 (2017). Cited on page(s) 120
- [341] S. Chen *et al.*, 'Raman measurements of thermal transport in suspended monolayer graphene of variable sizes in vacuum and gaseous environments', *ACS Nano* **5**, 321 (2010). Cited on page(s) 120
- [342] E. Starodub, N. Bartelt and K. McCarty, 'Oxidation of graphene on metals', *J Phys Chem C* **114**, 5134 (2010). Cited on page(s) 120
- [343] Q. Wu *et al.*, 'Selective surface functionalization at regions of high local curvature in graphene', *Chem Commun* **49**, 677 (2012). Cited on page(s) 120
- [344] Y. Zhang, Q. Fu, Y. Cui, R. Mu, L. Jin and X. Bao, 'Enhanced reactivity of graphene wrinkles and their function as nanosized gas inlets for reactions under graphene', *Physical Chemistry Chemical Physics* **15**, 19042 (2013). Cited on page(s) 120
- [345] J. Park, A. Akbari-Sharbat, S. Ezugwu, R. Bauld and G. Fanchini, 'Direct synthesis of highly conducting graphene nanoribbon thin films from graphene ridges and wrinkles', *Acta Mater* **107**, 96 (2016). Cited on page(s) 120
- [346] C.-T. Pan, J. Hinks, Q. Ramasse, G. Greaves, U. Bangert, S. Donnelly and S. Haigh, 'In-situ observation and atomic resolution imaging of the ion irradiation induced amorphisation of graphene', *Sci Rep* **4**, 6334 (2014). Cited on page(s) 120
- [347] N. Blanc, F. Jean, A. V. Krasheninnikov, G. Renaud and J. Coraux, 'Strains induced by point defects in graphene on a metal', *Phys Rev Lett* **111**, 085501 (2013). Cited on page(s) 120

## Bibliography

---

- [348] S. Yoo, E. Åhlgren, J. Seo, W. Kim, S. Chiang and J. Kim, 'Growth kinetics of Kr nano structures encapsulated by graphene', *Nanotechnology* **29**, 385601 (2018). Cited on page(s) 122
- [349] R. Koch, M. Borbonus, O. Haase and K. Rieder, 'New aspects on the Ir (110) reconstruction: surface stabilization on mesoscopic scale via (331) facets', *Phys Rev Lett* **67**, 3416 (1991). Cited on page(s) 135
- [350] F. Huttmann, 'Graphene on iridium with aromatic molecules and 3d or 4f metals: binding, doping, magnetism, and organometallic synthesis', Dissertation, Universität zu Köln, 2017. Cited on page(s) 135
- [351] I. Šrut, V. M. Trontl, P. Pervan and M. Kralj, 'Temperature dependence of graphene growth on a stepped iridium surface', *Carbon* **56**, 193 (2013). Cited on page(s) 135
- [352] M. Will, P. Bampoulis, T. Hartl, P. Valerius and T. Michely, 'Conformal Embedding of Cluster Superlattices with Carbon', *ACS Appl Mater Interfaces* **11**, 40524 (2019). Cited on page(s) 141, 142, and 145

# Danksagung

## *(Acknowledgements)*

---

An dieser Stelle möchte ich meinen Dank an die vielen Personen aussprechen, die mich in den letzten dreieinhalb Jahren unterstützt haben und auf unterschiedlicher Weise zum Gelingen dieser Arbeit beigetragen haben. *Finally, i would like to thank all the people who helped me during the last three and a half years. Without your help i would not have realized this thesis.*

An erster Stelle möchte ich Prof. Dr. Thomas Michely danken. Danke, dass Du mich als Doktorand aufgenommen hast und maßgeblich sowohl auf fachlicher als auch persönlicher Ebene zum Erfolg dieser Arbeit beigetragen hast. Durch Dich konnte ich einen vielseitigen Einblick in die Welt der Wissenschaft bekommen, spannende Forschungsreisen unternehmen und informative Tagungen in verschiedenen Städten dieser Welt besuchen. Hier erlebte ich interessante Begegnungen und führte angeregte Unterhaltungen. Allerdings gilt es auch zu erwähnen, dass ich mich anfänglich nicht leicht damit tat, bei diesen Tagungen aufzutreten. Letzten Endes kann ich sagen, dass dies für die Entwicklung meines persönlichen Horizonts von großer Bedeutung war. Danke das du an meine Arbeit und Fähigkeit geglaubt hast.

Anschließend möchte ich besonders Assoz. Prof. Jani Kotakoski dafür danken, meine Dissertation als Zweitprüfer zu lesen - *I would like to thank especially Assoz. Prof. Jani Kotakoski for accepting to be the second referee for this thesis.* Herrn Prof. Dr. Klas Lindfors gilt mein Dank für die Übernahme des Vorsitzes meiner Prüfungskommission. Dr. Pantelis Bampoulis möchte ich für die Übernahme des Prüfungsbeisitzes danken.

Des Weiteren möchte ich mich bei allen Personen bedanken, die durch ihre Kooperationen zu dieser Arbeit einen großen Teil beigetragen haben. Charlotte Herbig, Pantelis Bampoulis, Moritz Will und Joshua Hall danke ich für die Zusammenarbeit während meiner Messungen in den Laboren der Universität zu Köln. Mohammed A. Arman und Jan Knudsen möchte ich für die Unterstützung am Synchrotron in Lund danken. Boris V. Senkvoskiy, Niels Ehlen, Shilong Wu, und Alex Grüneis danke ich für Unterstützung mit spektroskopischen Messungen an MoS<sub>2</sub>. Für die Bereitstellung von theoretischen Rechnungen und atomistischen Simulationen danke ich Silvan Kretschmer, Mahdi Ghorbani-Asl, Arkady V. Krasheninnikov vom Helmholtz-Zentrum in Dresden und Nicolae Atodiresei und Vasile Caciuc vom Forschungszentrum in Jülich. Ebenso danke ich Norbert Henn und Pascal Hurth und allen Mitarbeiter\*innen der Mechanik- und Elektronikwerkstatt, die auf technischer Seite zum Gelingen dieser Arbeit beigetragen haben.

## **Danksagung (*Acknowledgements*)**

---

Ich danke Carsten Speckmann und Alexander Herman, die durch ihre jeweiligen Bachelor- und Masterarbeiten zu einem Teil meines Promotionsprojektes beigetragen haben. Außerdem bedanke ich mich für das Korrekturlesen der geschriebenen Arbeit bei Pantelis Bampoulis, Moritz Will, Clifford Murray, Stefan Kraus, Timo Knispel, und Camiel van Efferen. Generell möchte ich mich bei allen Mitgliedern der AG Michely bedanken – danke für die nette Arbeitsatmosphäre, Gespräche, leckeren Kaffee (entkoffeiniert), auch ein paar Kölsch, Käsefondues und vieles mehr, wat wor dat dann en superjeile Zick. Wenn mich mittags die Nostalgie überkommen sollte, werde ich euch mit Sicherheit mal in der Mensa besuchen.

Ich möchte auch meiner Familie und meinen Freunden danken, die mich stets daran erinnern, was neben der Promotion noch wichtig im Leben ist und mir emotionalen Halt gegeben haben. Ich danke besonders meiner Mutter Emi Valerius, meiner Partnerin Sarah Meier und meinem guten Freund Nicolas Engelbarts.

# Erklärung gemäß Promotionsordnung

---

Ich versichere, dass ich die von mir vorgelegte Dissertation selbstständig angefertigt, die benutzten Quellen und Hilfsmittel vollständig angegeben und die Stellen der Arbeit - einschließlich Tabellen, Karten und Abbildungen -, die anderen Werken im Wortlaut oder dem Sinn nach entnommen sind, in jedem Einzelfall als Entlehnung kenntlich gemacht habe; dass diese Dissertation noch keiner anderen Fakultät oder Universität zur Prüfung vorgelegen hat; dass sie - abgesehen von den angegebenen Teilpublikationen - noch nicht veröffentlicht worden ist, sowie, dass ich eine solche Veröffentlichung vor Abschluss des Promotionsverfahrens nicht vornehmen werde. Die Bestimmungen der Promotionsordnung sind mir bekannt. Die von mir vorgelegte Dissertation ist von Prof. Dr. Thomas Michely betreut worden.

Köln, den 26.02.2020

Philipp Valerius

# Lebenslauf (*Curriculum Vitae*)

---

## Persönliche Daten

Name	Valerius
Vorname	Philipp Lucas Taka
Geburtstag	09.07.1990
Geburtsort	Wickede (Ruhr)
Staatsangehörigkeit	deutsch

## Ausbildung

08/2016 – 05/2020	Promotionsstudium II. Physikalisches Institut, Universität zu Köln Arbeitsgruppe Prof. Dr. T. Michely
10/2013 – 05/2016	M. Sc. Physik, Universität zu Köln Durchschnittsnote: 1,6 <b>Masterarbeit</b> " <i>A hexagonal boron nitride layer on Ir(111): Trapping of Xe underneath and growth of C clusters on top</i> " (Note: 1,4) angefertigt am II. physikalischen Institut, Universität zu Köln
10/2010 – 10/2013	B. Sc in Physik, Universität zu Köln Durchschnittsnote: 2,5 <b>Bachelorarbeit</b> " <i>Einfluss von Sauerstoff auf die Dynamik von Mikrokolonien von Neisseria gonorrhoeae</i> " (Note: 1,3) angefertigt am Institut für Biophysik, Universität zu Köln
07/2001 – 07/2010	Allgemeine Hochschulreife, Marien-Gymnasium Werl Durchschnittsnote: 1,9